



**UNIVERSITÀ
DI TRENTO**

**Department of
Industrial Engineering**

Doctoral School in Materials, Mechatronics
and Systems Engineering

XXXIV cycle

Smart coatings for energy saving buildings

Author:

Andrea Rosati

Supervisors:

Prof. Stefano Rossi

Prof. Michele Fedel

Preface

This dissertation is an original intellectual product of the author, *Andrea Rosati*.

- The Chapter 1 is focused on the motivation and aim of this dissertation.
- The Chapter 2 is devoted to a complete analysis of building cooling strategies and a critical review of the most used pigments for cool coatings application. A section of Chapter 2 has been published [Rosati, A., Fedel, M., & Rossi, S. (2021). NIR reflective pigments for cool roof applications: A comprehensive review. *Journal of Cleaner Production*, 313, 127826.].
- The Chapter 3 is devoted to the methods description. All the methods described in the Chapter 3, to perform measurements of heat release or retention, together with NIR reflectance, are well underlined in the following published paper: "Rosati, A., Fedel, M., & Rossi, S. (2021). Laboratory scale characterization of cool roof paints: Comparison among different artificial radiation sources. *Progress in Organic Coatings*, 161, 106464".
- The Chapter 4 is devoted to an accurate analysis of the results of the pigments and of the derived coatings. Part of the results described in Chapter 4 was deepened in the following published paper: "Rosati, A., Fedel, M., & Rossi, S. (2021). $\text{YIn}_{0.9}\text{Mn}_{0.1}\text{O}_3\text{-ZnO}$ NIR reflective nano-pigment exhibiting three different colors: ochre, cyan blue, and deep blue. *Journal of Solid State Chemistry*, 299, 122176".

- A side project is based on the employment of a group of synthesized pigments to understand their photocatalytic ability. At the present date the manuscript research paper entitled “Sol-Gel derived yellow $\text{YIn}_{0.9}\text{Fe}_{0.1}\text{O}_3\text{-ZnO}$ pigments showing Near Infra Red (NIR) reflectance and photocatalytic activity” is submitted to the journal Material Chemistry and Physics .The current status is “with editor”. The pigments and strategy devoted to photocatalytic measurements of pigments, and derived coatings, are shown in Chapter 5.
- As concluding chapters, there are the Chapter 6 and the Chapter 7. In the Chapter 6 are compared the best results to find the best pigment and derived coating. In the Chapter 7 are discussed the conclusions of this work.

Summary

<i>Acknowledgements</i>	7
1 Motivation and aim	8
2 Theoretical background	10
2.1 Urban heat island effect	10
2.2 Urban cooling strategies	12
2.3 Cool coatings	13
2.4 The behavior and features of Near Infrared (NIR) Reflective pigments	15
2.5 Synthesis route of Near Infrared Reflective pigments	16
2.5.1 Overview on yellow pigments	21
2.5.1.1 Sol-Gel route	25
2.5.1.2 Solid state route	29
2.5.1.3 Hydrothermal and precipitation route	32
2.5.1.4 Advantageous aspects of the synthesis processes	35
2.5.2 Overview on red pigments	36
2.5.2.1 Sol-Gel route	38
2.5.2.2 Solid state route	40
2.5.2.3 Hydrothermal and precipitation route	41
2.5.2.4 Advantageous aspects of the synthesis processes	43
2.5.3 Overview on blue pigments	44
2.5.3.1 Sol-Gel route	47
2.5.3.2 Solid state route	51
2.5.3.3 Hydrothermal and precipitation route	53
2.5.3.4 Advantageous aspects of the synthesis processes	57
2.5.4 An evaluation of the best synthesis techniques	58
2.5.5 Environmentally friendly syntheses route of Near Infrared (NIR) Reflective pigments	59
2.5.5.1 Hydrothermal synthesis	59
2.5.5.2 Sol-Gel Synthesis	62
2.5.5.3 Pigments based on YInO_3	70
2.6 Review on colorimetry fundamentals	76

2.6.1	Principle of colorimetry and spectrophotometry	78
3	Materials and methods	82
3.1	Materials	82
3.1.1	Pigments precursors	82
3.1.2	Coatings precursors	82
3.2	Methods	83
3.2.1	Synthesis of $\text{YIn}_{0.9}\text{M}(\text{Mn, Fe, Cu})_{0.1}\text{O}_3\text{-ZnO}$ pigments	83
3.2.2	Deposition of obtained coatings from pigments	87
3.2.3	Characterization techniques of pigments	92
3.2.3.1	Thermogravimetric (TGA) and differential scanning calorimetry (DSC)	92
3.2.3.2	Fourier transform infrared (FT-IR) spectroscopy	93
3.2.3.3	Powder X-ray diffraction analysis	93
3.2.3.4	Colorimetric measurements	94
3.2.3.5	Near-infrared reflectance (700-2500 nm)	95
3.2.3.6	SEM observation and analysis	96
3.2.4	Characterization techniques of coatings	96
3.2.4.1	Near-infrared reflectance (700-2500 nm)	97
3.2.4.2	Thermal behavior	97
3.2.4.3	Exposure to sun radiation	97
3.2.4.4	Exposure to artificial radiation sources	101
4	Results & Discussion	105
4.1	Analysis performed on obtained pigments	105
4.1.1	Termogravimetry (TGA) and Differential scanning calorimetry (DSC)	105
4.1.1.1	YInMnO-ZnO pigments	105
4.1.1.2	YInCuO-ZnO pigments	108
4.1.1.3	YInFeO-ZnO pigments	109
4.1.2	Fourier transform infrared spectroscopy (FT-IR)	112
4.1.2.1	YInMnO-ZnO pigments	112
4.1.2.2	YInCuO-ZnO pigments	114
4.1.2.3	YInFeO-ZnO pigments	116
4.1.3	Powder X-ray diffraction analysis	117
4.1.3.1	X-ray diffraction as function of temperature	117
4.1.4	X-ray diffraction of calcined dried gels used as pigments	123
4.1.4.1	YInMnO-ZnO pigments	123
4.1.4.2	YInCuO-ZnO pigments	125

4.1.4.3	YInFeO-ZnO pigments	128
4.1.5	Colorimetric analysis on pigments	132
4.1.5.1	YInMnO-ZnO pigments	132
4.1.5.2	YInCuO-ZnO pigments	134
4.1.5.3	YInFeO-ZnO pigments.....	137
4.1.6	SEM Observation and analysis.....	139
4.1.6.1	YInMnO-ZnO pigments	139
4.1.6.2	YInCuO-ZnO pigments	142
4.1.6.3	YInFeO-ZnO pigments.....	144
4.1.7	Near Infrared Reflectance of pigments	148
4.1.7.1	YInMnO-ZnO pigments.....	148
4.1.7.2	YInCuO-ZnO pigments	151
4.1.7.3	YInFeO-ZnO pigments.....	153
4.1.7.4	YInM(Mn, Cu, Fe)O-ZnO pigments: comparison of different reflective values.	155
4.2	Analysis performed on pigmented coatings	158
4.2.1	NIR reflectance.....	158
4.2.1.1	Coatings with YInMnO-ZnO pigments	158
4.2.1.2	Coatings with YInCuO-ZnO pigments.....	161
4.2.1.3	Coatings with YInFeO-ZnO pigments	163
4.2.1.4	Discussion of compared values of reflectance	166
4.2.2	Thermal performances analysis.....	169
4.2.2.1	Preliminary analysis on coatings having YInMnO-ZnO based pigments.....	169
4.2.2.2	Thermal performances analysis with artificial radiation source	172
4.2.2.3	Analysis on coatings having YInCuO-ZnO pigments	181
4.2.2.4	Analysis on coatings with YInFeO-ZnO pigments.....	183
4.2.3	Comparison among different temperature data.....	185
5	Investigation of photocatalytic properties of YInFeO-ZnO pigments	189
5.1	Introduction	189
5.2	Pigments and materials used for photocatalytic test.....	191
5.3	Deposition and characterization of corresponding coatings	193
5.4	Characterization techniques	195
5.4.1	Structural and morphological analysis	195
5.4.2	Color properties	196
5.4.3	Powder X-ray diffraction analysis.....	199
5.4.4	Near-infrared reflectance of investigated pigments.....	201

5.4.5	Photocatalytic test of obtained pigments	203
5.4.6	Near-infrared reflectance of coatings	205
5.4.7	Photocatalytic test of coatings derived from pigments.....	208
5.4.8	Effect of coatings under xenon radiation source	210
5.5	Observations on properties of YInFeO–ZnO pigments and corresponding coatings	213
6	Comparison among significant results	215
7	Conclusions.....	219
8	References	222

Acknowledgements

I feel obliged to thank my supervisors: **Stefano Rossi** and **Michele Fedel**, who welcomed me to Trento, teaching me the values and ethics of their research group.

Thanks to **Stefano**, whose creativity and flair in scientific research helped me to look for different perspectives to enhance my work to the maximum.

Thanks to **Michele**, rational, determined and with an insatiable appetite for knowledge. I hope he passed on at least one of these qualities to me.

Thanks to **Francesco Parrino** and **Marcello Picollo**. Their knowledge and availability were crucial to achieving the results presented in this research project.

Special thanks go to **Luca Benedetti**. With extreme availability and a smile on his lips, he helped me to face every obstacle.

Thanks to my mother **Rossella**, my father **Fabio** and my brother **Alessandro**. I have a wonderful family who guided and supported me in every choice and made me strong when I felt weak.

During this path, three special people stopped walking beside me, but I would not be here without their teachings. They are my grandparents: **Raffaele**, **Franca** and **Maria**.

Therefore thanks to **Raffaele**. Your actions have inspired me. You made me understand who I am through the valors of our ancestors.

Thanks to **Franca**. Your will and determination have been invaluable in getting here.

Thanks to **Maria**. You taught me that freedom is knowledge. You made me the Man I am by teaching me only virtues. Through you, I also met my grandfather **Alvaro** and his virtues.

Finally, thanks to **Martina**, the woman with whom I have been sharing my life for almost twelve years. I cannot describe the strength that her love gives me. I will have many research projects to think and all very interesting but our projects remain the best!

1 Motivation and aim

The present thesis is devoted to synthesis, through the environmentally friendly citrate sol-gel route, of $\text{YIn}_{0.9}\text{O}_3$ –ZnO near infrared reflective based pigments, having different chromophore elements (Mn, Cu, Fe), with the aim to add in binder and obtaining cool coatings. A “cool” coating for roofing consists of paint (or glaze) containing color pigments, which do not absorb the infrared portion of the solar spectrum. Cool coatings applied over buildings surface provide an effective solution for passive cooling of building indoors and influencing local outdoor microclimate, mitigating urban heat islands effect (UHIE).

The primary purpose is to produce pigments according to an environmentally friendly route, using non-toxic raw materials, as well as short times and low temperatures for synthesis, and without residual waste. The resulting pigments must have high reflectance in the near-infrared so that they can be used in the field of cold paints. To realize the corresponding coatings, pigments were dispersed in two different binders (standard PMMA and industrial binder). For the most interesting pigments, in terms of NIR reflectance, other property, was decided to explore, which define these NIR reflective pigments as smart pigments for building application: the photocatalytic ability.

The experimental part of the thesis can be divided in two main part:

1. Synthesis and characterization of pigments. Pigments were synthesized and characterized according to chemical physical analysis, as Fourier transform

infrared spectroscopy (FT-IR), SEM-EDXS observations, X ray diffraction and identification in CIE-1976L*a*b* color space according to colorimetric measurements. The near infrared (NIR) reflectance ability was tested with NIR reflectance measurements.

2. Preparation of coatings and characterization. The pigments were dispersed in two different binders and the obtained coatings were characterized and tested. The capability of coatings to act as cool surfaces was assessed by NIR reflectance measurements and irradiating the surface of coatings by using different radiation sources and find out what is the radiation source approximating that of sun.

The significant advancements made to the technical field can be summarized in the following key points:

- (a) Improvement of the citrate based sol-gel route for $\text{YIn}_{0.9}\text{O}_3$ -ZnO based pigments, decreasing times and temperatures conventionally employed, and improving properties of the final product by changing elements in base structure.
- (b) Make possible application of pigments currently employed only in academia in industrial field. The pigments were dispersed in two different binders: a standard PMMA and an industrial acrylic binder.
- (c) find a light source that could be a model that best approximates solar radiation.

2 Theoretical background

2.1 Urban heat island effect

In 2018, around 55% of population resides in urban areas, and this share is expected to rise further, from 81% today to nearly 88% in 2050 [1]. This high population density is responsible of an increasing in the thermal emissions derived from anthropogenic activities, especially those related to transport and industrial processes [2] and the massive use of environmental comforts technologies in buildings, the so-called Heating, Ventilation and Air Conditioning (HVAC), that account for the 40% of buildings energetic consumption [3,4]. HVAC systems reduce thermal stresses indoor but outdoor remain. Moreover, thermal stresses will increase as a result of a global temperature rise, and an increase in hot extremes and heat waves. Combined with urban thermal emissions from anthropogenic activities, these conditions are likely to result in uncomfortable and unhealthy heat stresses, and more alarmingly, a significant increase in heat-related mortality. The heat wave in the summer of 2006 caused about a thousand heat-related deaths [5]. Another dangerous effect of higher temperatures is the stimulation of the formation of ground-level ozone in urban areas, which can lead to or aggravate cardio-respiratory diseases such as lunging flammation and decreased lung functionality [6]. The International Panel on Climate Change [7] has predicted a global surface air warming of between 1.1 and 6.4 °C for the 21st century, and an increase in hot extremes and heat waves. The Royal Netherlands Meteorological Institute (KNMI) predicts for the climate in the Netherlands in 2050 a decrease in the number of days with precipitation in summer and warmer summers and winters. The accuracy of these

predictions is based on the development of human activities in the future, considering greenhouse gas concentrations in the atmosphere and land use, and the response of the climate system to these changes.

Besides anthropogenic emissions and HVAC also the materials employed in urban environment (such asphalt, concrete, lime and plasters) influence urban overheating due to the high heat adsorption and retention capacity [8] and the low reflectance of solar radiation (low albedo). These materials change the heat and moisture exchange between the surface and the atmosphere affecting the urban areas' thermal environment. Asphalt pavement absorbs up to 90% of solar radiation [9] and the warming effect is amplified by absorption of short-wave radiation from the sun in low albedo materials and trapping by multiple reflections between buildings and street surface. The short wave radiations in the near infrared, NIR, (700-2500 nm) are in fact 52% of the solar radiation, while 5% is on ultra-violet (UV) and 43% of visible radiation. Therefore, a relevant amount of adsorbed heat is due to the near-infrared component of solar radiation. Anthropogenic thermal emissions, urban thermophysical and geometrical characteristics, together with low reflective materials of buildings, imply that urban climates differ from those of rural areas.

The loss of vegetation reduces the albedo, decreasing reflection of short-wave radiation, and more importantly reduces evapotranspiration, decreasing the cooling due to the transfer of latent heat. The urban centers can consequently be up to 7 °C warmer than the surrounding rural areas [10]. This phenomenon is known as the urban heat island (UHI)

effect [11–15]. Accordingly, the urban air temperature is higher than that of the surrounding rural environment.

To limit the human health and environmental problems related to the warming of cities a strategy is to conceive new models of urban expansion as well as adapt existing urban environments, considering urban warming.

2.2 Urban cooling strategies

To tackle the environmental and economic issues derived from the UHI effect, many technological solutions have been investigated: vegetation, phase change materials (PCM) [16,17], smart glazing films [18] and reflective coatings for claddings and roofing components [19]. Vegetation [20] is one of the most effective UHI mitigation strategies, especially for built-up urban areas [21].

Vegetation achieves the cooling effect increasing latent heat flux and decreases sensible heat. The main role of vegetation in cooling strategy consists in the decrease of the mean radiant temperature, which has a critical effect in human thermal comfort [22]. Besides vegetation of urban areas, in order to come to a sustainable built environment, the building industry requires new energy saving solutions.

One strategy is the use of Phase Change Materials (PCM), which are “latent” thermal storage materials possessing a large amount of heat energy stored during their phase change. The energy required to change the phase of a substance is known as latent heat, which can absorb and release thermal energy at a specific temperature [23]. The principle of the phase change material (PCM) is simple. As the temperature increases, the material

changes phase from solid to liquid. The reaction being endothermic, the PCM absorbs heat. Similarly, when the temperature decreases, the material changes phase from liquid to solid. The reaction being exothermic, the PCM desorbs heat [24]. Most used phase change materials are waxes [24,25] and hydrated salts [23,26] incorporated in concretes. Increasing the latent heat thermal energy storage capacity of concrete using PCMs has positive effects on the energy efficiency of a building as it contributes to a reduction in temperature fluctuations and reduces thermal loads. One issue with the use of PCMs integrated with building materials is that is difficult to perform intrusive maintenance on PCM system. When PCM has stopped being effective, it is difficult to replace the PCM without performing any destructive methods to access it [27].

2.3 Cool coatings

Another important strategy to mitigate the UHI effect is the use of cool coatings technology. A cool surface is characterized by increased reflectance in the non-visible regions (UV and/or NIR) compared to a conventional surface with the same visual appearance. The group of cool materials includes “cool tiles [28]”, “cool façade coatings [29]” and “cool roof paintings [3]”. A “cool” coating for roofing consists of paint (or glaze [18]) containing color pigments, which do not absorb the infrared portion of the solar spectrum.

In particular, the use of roof coatings with high near infrared (NIR) reflectance has been demonstrated to be an effective alternative to mitigate the UHI effect. In buildings, roof plays a vital role in controlling and cooling loads and protects the interior space from

harsh climatic conditions. Roof is a critical part of building envelopes that accounts for a large amount of solar radiation in hot and dry climates. The cool roof reduces the heat transfer to the building through the roofs as compared to the traditional roofs. Most of the solar radiation on a cool roof surface is reflected due to the higher reflectivity of the roof. This cool roof phenomenon makes it most convenient when solar radiation's intensity is very high, and maximum diurnal variation occurs [30]. Increasing the roof solar reflectance could potentially lead to an increase in heating energy demand. Studies have shown that this increase is far less important than the corresponding cooling energy savings, resulting into positive net savings for warm/moderate climatic conditions [31,32]. This is explained by the fact that during winter, the sun is much lower in the sky, and solar radiation arriving at a horizontal surface less intense. There is a higher probability of overcast sky and less solar availability (fewer hours of sunshine), so less total energy arrives on a surface to be absorbed or reflected over the same time as during the summer [33]. So we can conclude that cool coatings have become a well-known measure to reduce electricity consumption from HVAC systems and to improve thermal comfort in not conditioned buildings [33,34].

To address the environmental issues due to the increasing energy demand for HVAC, "cool" coatings for roofing are a promising solution both in terms of cost, performance and, therefore, feasibility. The Pisello's review paper [35] deals with the progress and development of the roofing materials to mitigate the UHI effect. Pisello [35] demonstrated that cool coatings' effectiveness to mitigate urban overheating is a well-established fact. In particular, in this section is well underlined that pigments play a decisive role in the design of a cool coating with high-performing cooling properties and reflectance towards solar

radiation. The chemical and physical properties of pigments to be tailored to well-designed cool coatings, towards solar radiation are reported also in a previous work of Brady et al. published in 1992 [36].

2.4 The behavior and features of Near Infrared (NIR) Reflective pigments

The so-called “NIR reflective pigments” (to underline their capability to reflect the near-infrared portion of the solar spectrum) do not have electronic transitions for wavelengths >700 nm. Reflection is located in the infrared region and in a portion of visible light; however, reflectivity and absorptivity of the pigment are independent: thus, NIR pigments may have any color.

Thanks to their specific structure, the NIR pigments promote a diffuse reflection of the incident NIR wavelengths. Along with a specific crystallographic structure, the particle size of the pigment and particle size distribution [37,38] of pigments are critical parameters. According to literature [39], the particle size should be more than half the light’s wavelength to be reflected to provide effective NIR reflectivity. Thus, to reflect infrared radiation in the range of 700-1100 nanometers wavelength (i.e. the heat production region) particle size should be at least 0.35 to 0.55 micrometers [39]. Recently, experimental findings have suggested that the particle size and particle size distribution of the pigments do not affect significantly the NIR reflectance. There are several works devoted to the understanding of the intrinsic structure effect on NIR reflective behavior of pigments [40–42]. In paper by Song et al. [42] was underlined how changes the NIR reflectance adding different elements (M = Cr, Mn, Fe, Co, Al, Ga and In) in pigments having a $YMn_{0.9}M_{0.1}O_3$ formulation,

considering also different amounts of doping elements. The authors concluded that the NIR reflectance was tuned according to the number of unpaired electrons of doping elements, maintaining the same amount of doping elements. However, obtaining high performance NIR reflective pigments is closely related to the synthesis process, as synthesis route influence the agglomeration, homogeneity and degree of crystallinity of pigments.

2.5 Synthesis route of Near Infrared Reflective pigments

Cool pigments are obtained mainly by subjecting mixtures of metal hydroxides, nitrates, acetates, and oxides, to different synthesis methods. NIR reflective pigments in the last decade were mainly based on the reflective properties of white pigments, in particular TiO_2 (rutile and anatase) [43–45]. TiO_2 particles were used to be mixed with other pigments to increase the near-infrared reflectance [44,46].

Recent literature reports focus on the developing innovative NIR pigments alternative to titanium dioxide. The effectiveness of zinc oxide (ZnO) [47], zirconium dioxide (ZrO_2) [48], bismuth vanadate (BiVO_4) [49] and rare earths, such as neodymium (Nd), [50] yttrium (Y) and indium (In) oxides [51,52] was explored. Also clay minerals, as kaolin, have been demonstrated to act as NIR reflective pigments [53,54].

Many effective NIR reflective pigments with good processing properties (e.g., the dispersibility in aqueous media, low synthesis temperature, and good compatibility with many different doping elements) are based on toxic elements such as chromium and cobalt [55–57]. In particular, hexavalent chromium (CrVI) compounds are classified as

carcinogenic to humans [58]. Cobalt effects on human health include hematological and endocrine dysfunctions [59].

To address the actual restrictions on the use of confirmed or suspected toxic/cancerogenic compounds, research on NIR reflective pigments is focusing on both environmentally friendly and not harmful to human health aspects.

Many publications consider pigments synthesized from non-toxic reagents among environmentally friendly pigments, but the production route can also affect environmental harmfulness. A low energy consumption synthesis may significantly improve a pigment's eco-sustainability. The scientific community's approach to decrease energy consumption, required for synthesizing the NIR reflective pigments, relies mainly on reducing processing time and temperature. In this frame, Primo et al. [55] synthesized a Co-doped zinc oxide green pigment ($\text{Co}_x\text{Zn}_{1-x}\text{O}$) by gelatinization and calcination of starch colloidal suspension. Highly crystallized single phases were obtained with an energy-saving process (at the temperature of 800-1000 °C), but the reagents necessary for the production of these pigments (cobalt nitrate, cobalt acetate, and cobalt chloride) are toxic and dangerous to humans. Ding et al. [57] made a series of pigments with the formula $\text{Bi}_{1-x}\text{Cr}_x\text{PO}_4$, by hydrothermal method. This synthesis method requires relatively low temperature reducing the environmental impact. However, the employed raw materials included, among the other, chromium nitrate nonahydrate ($\text{Cr}(\text{NO}_3)_3 \cdot 9\text{H}_2\text{O}$), which is a strong oxidizer and may cause fires (even if it is not as dangerous to human health as any precursor based on Cr^{6+}). These last examples highlight that a careful selection of environmentally friendly raw materials for the synthesis

is crucial for developing NIR reflective pigments, which are not harmful to the environment or human health. Of course, an environmentally friendly route is also given by a low energy cost and safe synthesis route. Procedures such as the solid-state method have known an interesting development in the synthesis of pigments based on non-toxic precursors. However, those procedures imply high temperatures and prolonged thermal treatments to obtain the final pigments [60–63]. Solid-state synthesis techniques also require mechanical mixing, high temperatures and long soaking times. In general calcination process in solid-state route requires temperatures higher than 1000 °C [60,64,65] and times near to 24 h [66,67].

Of course, as it appears from the examples described above it is not clear how to pursue the aim of realizing environmentally friendly pigments. A part of research aims just to improve well known synthesis procedures reducing times and/or temperatures employed, maintaining toxic precursors; while other research parts are oriented towards pigments synthesis based on non-toxic reagents with high temperatures and long times.

The role of this section is to understand if research is orienting towards environmentally friendly procedures based on the low energy consumption, in terms of time and temperatures, considering low environmental impact precursors. In this section, the most promising NIR pigments are reviewed, together with the appearance properties and the efficiency in terms of the NIR reflectance effect of three widely used cool pigments: yellow, red, and shades tending to blue [52]. The aim is to make, as far as possible, a rapid consultation about the state of the art of NIR reflective pigments according to their chemical

composition, synthesis method, color, and NIR reflectance values. Therefore, we have summarized the features described above according to three tables (**Table 2. 1**, **Table 2. 2**, **Table 2. 3**) as will be seen later.

An approximation is necessary when pigments are grouped according to the color coordinates. For what concerns red and yellow pigments, it is sometimes impossible to clearly discern between both colors and the relative shades, mainly when reddish or yellowish pigments are obtained. The difference between dark shades of yellow or light shades of red is sometimes very slight and a matter of subjective opinion from one observer to another. Usually, the experimental approach in the literature of NIR reflective pigments is to evaluate the effect of different parameters as doping elements, temperature of calcination in the synthesis route of the resulting pigments. Literature focuses on what is the effect of different parameters aiming at the transition from one color to another. Therefore, the tables below showing yellow and red pigments represent also pigments having white shades, as they are comparative or starting material to obtain final pigments, yellowish or reddish. This representation has the aim to underline how just a single parameter (as temperature used during synthesis or a change in doping elements) change the color.

Regarding the production method, four main synthesis routes have been identified and reported: sol-gel, solid-state, hydrothermal methods and precipitation route. The last two methods were grouped in the same section, considering that many authors are used to applying both in sequence.

The surface appearance for each cited pigment is reviewed and given in terms of colorimetric coordinates according to CIE $L^*a^*b^*$ system [68], where L^* is the color lightness ($L^*=0$ for black and $L^*=100$ for white), a^* is the green (-)/ red (+) axis, and b^* is the blue (-)/yellow (+) axis. L^* , a^* and b^* parameters are used to identify and discriminate color, especially in the case of reddish and yellowish shades.

The reflectance data in the literature are expressed according to the NIR reflectance (%) and after are changed to NIR solar reflectance, R^* (%) [40–42]. The spectral solar reflectance gives the total reflectance (diffuse and specular) as a function of the wavelength and considering the solar spectrum (from 300 to 2500 nm). R^* is used to compute the total solar reflectance through the standard solar spectrum. This parameter is a quantity derived from the following equation:












$$R^* = \frac{\int_{700}^{2500} r(\lambda)i(\lambda)d(\lambda)}{\int_{700}^{2500} i(\lambda)d(\lambda)} \quad (2.1)$$



















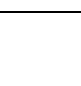
Where $r(\lambda)$ is the experimentally obtained spectral reflectance ($W\ m^{-2}$) and $i(\lambda)$ is the solar spectral irradiance ($W\ m^{-2}\ nm^{-1}$), obtained following ASTM standards (as E891-87, G159-98, G173-03). Therefore, we can compare different NIR reflectance data only having the same ASTM data sheets. For this reason, in reviewed data of NIR reflectance, we decided to show the raw data obtained in the reviewed publications by spectrophotometer analysis in the NIR range (700-2500 nm). In this way, the data collected by the different authors become comparable, considering that the instrument employed in all publications is a UV-vis-NIR spectrophotometer with standards used as the white standards (as MgO, BaSO₄) [69,70]. Reflectance measurement is a relative measurement since reflectance value is




















obtained with respect to the standard sample. In addition, the reflectance values are subjected to change based on the standard. Therefore, also in this case, we need to consider minor errors due to specific employed equipment.

















2.5.1 Overview on yellow pigments





Table 2. 1. Color coordinates, NIR reflectance of the powdered yellow pigments and the synthesis method employed.

Chemical compound	Synthesis route	Color coordinates			Color from color coordinates [®]	NIR Reflectance (R %)	Reference
		<i>L</i> *	<i>a</i> *	<i>b</i> *			
BiVO ₄	Sol-Gel	82.43	4.25	76.26		75.94	[71]
50% BiVO ₄ -ZnO 1g	Sol-Gel	89.06	-1.34	76.64		95.37	[71]
25% BiVO ₄ -ZnO 3g	Sol-Gel	91.53	-6.28	76.45		98.33	[71]
5% BiVO ₄ -ZnO 5.6g	Sol-Gel	86.79	4.92	53.50		99.64	[71]
10% BiVO ₄ -ZnO 9g	Sol-Gel	90.87	-2.88	41.81		98.3	[71]
BiVO ₄ -TiO ₂	Sol-Gel	89.84	-2.67	72.41		92.43	[71]
BiVO ₄ -SiO ₂	Sol-Gel	89.15	-3.83	72.90		87.75	[71]
BiVO ₄ -Al ₂ O ₃	Sol-Gel	87.42	-3.88	62.42		90.98	[71]
CeO ₂	Sol-Gel	90.30	-6.69	31.80		≈85.00*	[70]
CeBi ₅ O ₉	Sol-Gel	84.69	0.30	42.65		≈84.00*	[70]
CeBi ₁₀ O ₁₇	Sol-Gel	83.38	4.14	49.02		≈86.00*	[70]

CeBi ₁₅ O ₂₄	Sol-Gel	80.51	6.62	52.26		≈87.00*	[70]
CeBi ₂₀ O ₃₂	Sol-Gel	82.07	4.34	40.12		≈88.00*	[70]
La ₂ Ce ₂ O ₇	Sol-Gel	94.18	-1.26	9.93		95.95	[61]
La ₂ Ce _{1.99} Pr _{0.01} O ₇	Sol-Gel	74.32	11.6 4	22.94		90.54	[61]
La ₂ Ce _{1.95} Pr _{0.05} O ₇	Sol-Gel	64.62	14.83	22.80		89.34	[61]
La ₂ Ce _{1.9} Pr _{0.1} O ₇	Sol-Gel	60.35	15.61	21.46		86.95	[61]
La ₂ Ce _{1.8} Pr _{0.2} O ₇	Sol-Gel	54.29	16.16	19.18		83.52	[61]
La ₂ Ce _{1.7} Pr _{0.3} O ₇	Sol-Gel	50.23	14.88	16.43		81.00	[61]
La ₂ Ce _{1.6} Pr _{0.4} O ₇	Sol-Gel	49.35	14.55	15.88		76.06	[61]
La ₂ Ce _{1.5} Pr _{0.5} O ₇	Sol-Gel	46.87	13.50	13.40		75.30	[61]
La ₂ Ce _{1.99} Tb _{0.01} O ₇	Sol-Gel	75.14	12.24	25.28		93.06	[61]
La ₂ Ce _{1.95} Tb _{0.05} O ₇	Sol-Gel	66.73	15.92	24.89		95.17	[61]
La ₂ Ce _{1.9} Tb _{0.1} O ₇	Sol-Gel	61.93	15.36	22.02		94.34	[61]
La ₂ Ce _{1.9} Tb _{0.2} O ₇	Sol-Gel	57.34	15.88	20.80		89.72	[61]
La ₂ Ce _{1.9} Tb _{0.3} O ₇	Sol-Gel	55.77	16.71	19.93		92.93	[61]
La ₂ Ce _{1.9} Tb _{0.4} O ₇	Sol-Gel	54.33	16.38	19.43		88.79	[61]
La ₂ Ce _{1.9} Tb _{0.5} O ₇	Sol-Gel	51.35	15.9 4	17.57		90.77	[61]
Yb ₆ Mo ₂ O ₁₅	Solid-state	88.70	-6.60	55.00		93.70	[72]
Yb ₆ MoO ₁₂	Solid-state	95.20	-11.70	28.30		93.10	[72]

$\text{Yb}_6\text{Mo}_{1.7}\text{Na}_{0.3}\text{O}_{15-\delta}$	Solid-state	90.50	-8.10	59.60		/	[72]
$\text{Yb}_{5.4}\text{Na}_{0.6}\text{Mo}_2\text{O}_{15-\delta}$	Solid-state	89.20	-5.90	67.50		/	[72]
$\text{Yb}_6\text{Mo}_{1.7}\text{Fe}_{0.3}\text{O}_{15-\delta}$	Solid-state	64.60	20.50	48.90		/	[72]
$\text{Yb}_6\text{Mo}_{1.6}\text{Fe}_{0.4}\text{O}_{15-\delta}$	Solid-state	60.10	18.90	39.00		90.40	[72]
$\text{Yb}_6\text{MoNbO}_{15-\delta}$	Solid-state	96.70	-11.00	44.20		99.70	[72]
$\text{Yb}_6\text{Mo}_{1.7}\text{Co}_{0.3}\text{O}_{15-\delta}$	Solid-state	41.20	11.10	18.90		/	[72]
$\text{Yb}_6\text{Mo}_{1.7}\text{Bi}_{0.3}\text{O}_{15-\delta}$	Solid-state	86.90	1.80	58.20		/	[72]
$\text{Yb}_6\text{Na}_{0.3}\text{Mo}_{1.7}\text{O}_{15-\delta}$	Solid-state	90.50	-8.10	59.60		/	[72]
$\text{Yb}_{5.4}\text{Ca}_{0.6}\text{Mo}_2\text{O}_{15-\delta}$	Solid-state	92.10	-8.80	61.10		/	[72]
$\text{Yb}_5\text{TiMo}_2\text{O}_{15+\delta}$	Solid-state	95.50	-11.00	46.90		99.40	[72]
$\text{Yb}_{4.8}\text{Bi}_{1.2}\text{Mo}_2\text{O}_{15}$	Solid-state	82.90	3.20	60.50		91.40	[72]
$\text{Bi}_2\text{YCe}_2\text{O}_7$	Solid-state	82.91	5.44	48.76		90.20	[73]
$\text{Bi}_{1.75}\text{Y}_{0.25}\text{Ce}_2\text{O}_7$	Solid-state	83.36	3.52	51.36		91.60	[73]
$\text{Bi}_{1.50}\text{Y}_{0.50}\text{Ce}_2\text{O}_7$	Solid-state	76.85	13.33	47.97		91.90	[73]
$\text{Bi}_{1.25}\text{Y}_{0.75}\text{Ce}_2\text{O}_7$	Solid-state	77.14	11.32	48.63		89.80	[73]
BiYCe_2O_7	Solid-state	79.82	8.17	46.70		90.90	[73]
$\text{Bi}_{0.75}\text{Y}_{1.25}\text{Ce}_2\text{O}_7$	Solid-state	78.61	8.18	45.18		89.40	[73]
$\text{Bi}_{0.50}\text{Y}_{1.50}\text{Ce}_2\text{O}_7$	Solid-state	83.15	5.49	43.78		93.60	[73]
$\text{Bi}_2\text{Ce}_2\text{O}_7$	Solid-state	82.91	5.44	48.76		90.20	[73]

$\text{BiCe}_{1.75}\text{Tb}_{0.25}\text{O}_7$	Solid-state	70.75	12.11	32.49		86.80	[73]
$\text{BiCe}_{1.50}\text{Tb}_{0.50}\text{O}_7$	Solid-state	62.26	15.01	32.07		87.70	[73]
$\text{BiCe}_{1.25}\text{Tb}_{0.75}\text{O}_7$	Solid-state	55.66	14.36	26.62		84.20	[73]
BiCeTbO_7	Solid-state	50.37	13.08	22.98		80.80	[73]
$\text{BiCe}_{0.75}\text{Tb}_{1.25}\text{O}_7$	Solid-state	46.09	11.23	18.61		75.10	[73]
$\text{BiCe}_{0.5}\text{Tb}_{1.50}\text{O}_7$	Solid-state	42.01	10.37	15.83		70.30	[73]
$\text{Al}_{0.97}\text{Fe}_{0.03}\text{PO}_4$	Precipitation	75.76	12.46	23.70		$\approx 84.00^*$	[74]
$\text{Al}_{0.95}\text{Fe}_{0.05}\text{PO}_4$	Precipitation	68.76	15.93	27.28		$\approx 80.00^*$	[74]
$\text{Al}_{0.92}\text{Fe}_{0.08}\text{PO}_4$	Precipitation	62.99	16.54	30.11		$\approx 67.00^*$	[74]
$\text{Ni}_2\text{P}_2\text{O}_7$	Precipitation	78.61	13.5	66.80		/	[75]
$\text{Ni}_2\text{P}_2\text{O}_7$	Hydrothermal	87.50	1.99	46.20		/	[75]
$\text{Ni}_2\text{P}_2\text{O}_7$	Precipitation	77.43	5.53	4.21		/	[75]
$\text{Ni}_2\text{P}_2\text{O}_7$	Precipitation	92.37	1.23	-1.22		/	[75]
$\text{Mn}_2\text{P}_2\text{O}_7$	Hydrothermal	92.37	1.23	-1.22		/	[75]
$\text{Mn}_{1.5}\text{Ni}_{0.5}\text{P}_2\text{O}_7$	Hydrothermal	70.23	1.87	7.15		/	[75]
$\text{Mn}_{1.0}\text{Ni}_{1.0}\text{P}_2\text{O}_7$	Hydrothermal	84.80	1.34	16.96		/	[75]
$\text{Mn}_{0.5}\text{Ni}_{1.5}\text{P}_2\text{O}_7$	Hydrothermal	86.58	1.23	27.20		/	[75]
$\text{Ni}_2\text{P}_2\text{O}_7$	Hydrothermal	87.50	1.99	46.20		/	[75]
$\text{Mn}_2\text{P}_2\text{O}_7$	Precipitation	77.43	5.53	4.21		/	[75]

$Mn_{1.5}Ni_{0.5}P_2O_7$	Precipitation	67.85	1.79	13.15		/	[75]
$Mn_{1.0}Ni_{1.0}P_2O_7$	Precipitation	87.02	3.32	27.57		/	[75]
$Mn_{0.5}Ni_{1.5}P_2O_7$	Precipitation	78.52	2.15	41.91		/	[75]
$Ni_2P_2O_7$	Precipitation	78.61	13.54	66.83		/	[75]

Legend:

- [®] : The color represented is obtained matching color coordinates
- * : Extrapolated from fig.3 (a) of [70]
- / : Data not showed in the paper

From **Table 2. 1** is possible to have an overview of which yellow NIR reflective pigments are currently most used. A series of publications regarding yellow shades of pigments, is focused on the effect of doping and/or coupling elements in changing color shades and the effect of modulation of NIR reflectance. About this, the study of Thejus and Nishanth [71] is a good example to represent an improvement toward eco-friendly synthesis technique (sol-gel citrate method) involving the use of nontoxic raw material ($BiVO_4$) [71] coupled with the two most widely used NIR reflective oxides: TiO_2 and ZnO .

2.5.1.1 Sol-Gel route

The study of Thejus and Nishanth [71] synthesized of $BiVO_4$ - ZnO complex pigments starting from the following procedure: solution of $Bi(NO_3)_3 \cdot 5H_2O$ and citric acid were mixed with distilled water under a continuous stirring. Subsequently, 50 mL NH_4VO_3 solution was added dropwise under vigorous stirring. The resultant solution was heated at 150 °C for 1 h after the slow addition of different well-known NIR reflective pigments: Al_2O_3 , ZnO , TiO_2 ,

SiO₂. The resultant solution was kept to dry to get solid xerogel form and ground well, afterward calcined at 500 °C for 3 h under air atmosphere . White pigments presented above were added to the vanadate solution (NH₄VO₃) with respect to the following BiVO₄ amounts (weight of white pigments is shown in parenthesis): 50 wt% BiVO₄-ZnO (1 g), 25 wt% BiVO₄-ZnO (3 g), 15 wt% BiVO₄-ZnO (5.6 g), 10 wt% BiVO₄-ZnO (9 g). Other pigments were produced employing 25 wt% of BiVO₄ and TiO₂, SiO₂, Al₂O₃.

The appearance properties of all the prepared pigments are listed in **Table 2. 1**. Appealing yellow shades were obtained for 50 wt% BiVO₄-ZnO (1 g) and 25 wt% BiVO₄-ZnO (3 g). This is due to the very high value of *b** coordinate (76.64 and 76.45) and the negative value of *a**(-1.34 and -6.28). The highest color intensity is obtained for 25 wt% BiVO₄-ZnO (3 g) (*L** = 91.53). Pigments based on SiO₂ (BiVO₄-SiO₂) and Al₂O₃ (BiVO₄-Al₂O₃) show comparable yellow intensities as demonstrated by color coordinates *b** of BiVO₄-SiO₂ (72.90) and BiVO₄-Al₂O₃ (62.42). Zinc oxide is confirmed to increase the NIR reflectance to higher values, as shown by NIR reflectance of BiVO₄-ZnO compounds (>95%).

BiVO₄ was revealed to be an interesting hosting base material for doping elements. Sandhya Kumari et al. [49] investigated the substitution of V with Ta/P in BiVO₄, which is responsible of a lattice distortion giving a more bright yellow pigment with high NIR reflectance [49]. In the optimized sol-gel procedure (low temperature sol-gel synthesis) by Jose et al [70] the yellow hue of the pigments increases with increase in Bi³⁺ concentration in CeO₂ based structure. The sol-gel synthesis method used by Jose et al. [70], for the synthesis of bismuth-doped cerium oxide yellow nano-pigments, was based on the realization of a Ce(OH)₄ precipitate obtained from Ce(NO₃)₃·6H₂O solution in water and 20–30% of

ammonia. The precipitate was dispersed in 1000 mL of water and 10% of HCl was added to maintain pH 2. Four different ratios of Bi³⁺ doped ceria [(100:5), (100:10), (100:15) and (100:20)] were obtained. A weighed amount of bismuth nitrate (Bi(NO)₃·5H₂O) was added to ceria sol and the resultant bismuth-doped ceria sol was treated into an autoclave at 150 °C for 24 h, followed by a 150 °C drying process. The yellow hue of the pigments increases with increase in Bi³⁺ concentration in Ce based structure up to the 15 mol % of Bi. From 20 mol % there is a decrease in the yellow intensity. However, by increasing the amount of Bi an increment in the saturation of each pigment is observed (*L** decreases). With the increasing amount of Bi³⁺, a rise in NIR reflectance values is clear visible (from ≈85.00 to ≈88.00). Cerium oxides and cerium complex metal oxides were confirmed as highly performing NIR reflecting pigments. In particular Y₂Ce₂O₇ and Sm₂Ce₂O₇ were revealed to be interesting for their bright yellow shades [61]. Also in the case of complex cerium oxides the sol-gel route based on citric acid revealed to be an highly performing process giving interesting results, as confirmed by in La₂Ce₂O₇ synthesized by Huang et al [61]. The authors obtained a wide range of colors (from yellow ochre to reddish) just by changing the doping elements, Tb and Pr, in the starting oxide: La₂Ce₂O₇ .

The raw materials employed by Huang et al [61] were La (NO₃)₃·6H₂O, Ce(NO₃)₃·6H₂O, Pr(NO₃)₃·6H₂O, Tb(NO₃)₃·6H₂O, ethylene glycol (2 mL) and citric acid (1.78 g). Using the sol-gel method the stoichiometric quantities of raw materials, according to the formula of La₂Ce_{2-x}M_xO₇ (M = Pr or Tb; x = 0, 0.01, 0.05, 0.1, 0.2, 0.3, 0.4, 0.5) were dissolved in the adequate ethylene glycol, where citric acid was added as the chelating agent. The solution was dissolved employing ultrasonication and heated at 80 °C under continuous

stirring promoting the polymerization reaction. The wet gel was dried at 80 °C for 10 h and the obtained xerogel was ground into a powder. Finally, the obtained powder was calcined at 900 °C for 10 h to prepare the samples.

For the pigments synthesized by Huang et al [61], the reported data reveal that Pr decreases the brightness of pigments: L^* value decreases from 94.18 (in $\text{La}_2\text{Ce}_2\text{O}_7$) to 46.87 in $\text{La}_2\text{Ce}_{1.9}\text{Pr}_{0.5}\text{O}_7$. The same decreasing trend is observed for b^* coordinates. The general trend of the coordinates, including a^* , underlines that the hue tends to a red shade.

The lightness of Tb^{4+} doped pigments is gradually decreased with the increased amount of dopant. The substitution of Tb^{4+} for Ce^{4+} decreases L^* values from 94.18 to 51.35. The b^* value is also regularly increased from 9.93 to 25.28. Then it decreases with further addition of Tb^{4+} (0.1 mol %), which promotes a decrease in yellowness. The same trend characterizes L^* and b^* of Pr^{4+} and Tb^{4+} : L^* decreases progressively with the increasing amount of Pr^{4+} or Tb^{4+} . b^* increases up to 0.01 mol % of the doping element, then decreases from 0.05 mol % of doping element. NIR reflectance values are significantly reduced from 95.95 % to 75.30 % with the addition of Pr in $\text{La}_2\text{Ce}_2\text{O}_7$ structure. More reduction in NIR reflectance parameter is observed when Tb replaces part of Ce: the NIR reflectance changes from 95.95 % to 90.77 %. Looking at the NIR reflectance data of Jose et al [70] reported in **Table 2. 1**, an increasing amount of Bi achieves the increase in NIR reflectance. The increasing trend in NIR reflectance was also obtained also by Huang et al [61]. Jose et al [70] enhancing the brightness (L^* value) of yellow color by adding an increasing amount of bismuth; however, the yellow component reaches a maximum with the intermediate amount of bismuth. The substitution of Ce with Pr demonstrates that the latter decreases

the NIR reflectance more than Tb. Comparing NIR reflectance values of CeO₂, obtained by Jose et al [70] with La₂Ce₂O₇ synthesized by Huang et al. [61], La increases NIR reflectance from about 85.00% to 95.95%.

In the case of sol-gel synthesized yellow pigments based on CeO₂, Bi is the doping element able to increase NIR reflectance, as demonstrated by Jose et al. [70]. Thejus and Nishanth [71] obtained NIR reflectance data confirming increased NIR reflectance by Bi, obtaining the highest value for NIR reflectance and yellow component *b**. The potential of rare earth oxides are also explored using another popular route in pigments synthesis: the solid state route [72].

2.5.1.2 Solid state route

The solid-state reaction method, or ceramic method, is a well-known processing route for obtaining thermodynamically stable phases at high temperatures through solid-state diffusion [76]. It implies high temperatures and long time thermal treatments to obtain the final pigments. Schildhammer et al. [72] produced cool yellow pigments using rare earth oxides, with the general formulas Yb_{6-x}D_xMo₂O_{15±δ} (D=Na, Ca, Ti, Bi) and Yb₆Mo_{2-x}M_xO_{15-δ} (M=Na, Fe, Co, Nb, Bi). Pigments with the formula Yb₆MoO₁₂ were used as comparative material. For the preparation of the new pigment Yb₆Mo₂O₁₅ and comparative pigment Yb₆MoO₁₂, the following reagents were used as starting material: Yb₂O₃ and (NH₄)₆Mo₇O₂₄·4H₂O. The reagents were ground with the addition of acetone in an agate mortar. After the evaporation of the residual acetone, the finally ground powders were

poured into corundum crucibles and placed in an electric furnace. After 20 h at 1350 °C, the yellow/red powder was ground manually in an agate mortar.

Molybdenum's presence straightforwardly influences the b^* value (yellow component): the b^* value increases from 28.3 for $\text{Yb}_6\text{MoO}_{12}$ to 55.0 for $\text{Yb}_6\text{Mo}_2\text{O}_{15}$. From the pigments $\text{Yb}_6\text{-xD}_x\text{Mo}_2\text{O}_{15\pm\delta}$ (D=Na, Ca, Ti, Bi), two candidates, namely $\text{Yb}_{4.8}\text{Bi}_{1.2}\text{Mo}_2\text{O}_{15}$ and $\text{Yb}_5\text{TiMo}_2\text{O}_{15+\delta}$, have been selected by authors to study the NIR reflectivity. The Bi^{3+} doped compound was chosen, as it displays the highest b^* value (60.50) and is thus the most promising candidate for application as a cool yellow pigment. The Bi^{3+} doped compound possesses a NIR reflectance (91.40 %), similar to $\text{Yb}_6\text{Mo}_2\text{O}_{15}$ (93.70 %). $\text{Yb}_5\text{TiMo}_2\text{O}_{15+\delta}$ shows a reflectivity near to 100 % (99.40 %). Doping with Bi^{3+} results in the strongest red shift, but the a^* value, which is responsible for red and green color hue, changes from 6.60 for $\text{Yb}_6\text{Mo}_2\text{O}_{15}$ to 3.20 for $\text{Yb}_{4.8}\text{Bi}_{1.2}\text{Mo}_2\text{O}_{15}$.

Schildhammer et al. [69] selected two pigments for the NIR reflectance analysis from the class of materials including $\text{Yb}_6\text{Mo}_{2-x}\text{M}_x\text{O}_{15-\delta}$ (M=Na, Fe, Co, Nb, and Bi) pigments: $\text{Yb}_6\text{Mo}_{1.6}\text{Fe}_{0.4}\text{O}_{15-\delta}$ and $\text{Yb}_6\text{MoNbO}_{15-\delta}$. $\text{Yb}_6\text{Mo}_{1.6}\text{Fe}_{0.4}\text{O}_{15-\delta}$ show a NIR reflectance of 90.40 % and the red component is one of the highest ($a^*=18.90$) considering both classes of pigments. This behaviour is due to the presence of the Fe chromophore, as observed for the $\text{Yb}_6\text{Mo}_{1.7}\text{Fe}_{0.3}\text{O}_{15-\delta}$ pigment ($a^*=20.50$). By Nb doping, $\text{Yb}_6\text{MoNbO}_{15-\delta}$ increases the NIR reflectance (99.70 %) but significantly decreases the yellow component ($b^*=44.2$) with respect to the undoped reference pigments ($\text{Yb}_6\text{Mo}_2\text{O}_{15}$ and $\text{Yb}_6\text{MoO}_{12}$).

$\text{Yb}_6\text{Mo}_2\text{O}_{15}$ can be used for yellow pigments of different intensities and shades. $\text{Yb}_6\text{Mo}_2\text{O}_{15}$ displays an intense yellow color defined by $L^*=88.70$, $a^*=6.6$, $b^*=55.00$. Ti^{4+} and

Nb⁵⁺ doping of Yb₆Mo₂O₁₅, with values of 99.40 % and 99.70 %, respectively, achieved an increase of the NIR reflectance. These findings suggest the potential of Nb⁵⁺ as a doping agent in cool pigments, in agreement with the high reflectance values of the pigments obtained by Schildhammer et al. [72].

Raj et al. [73] focused the attention on the active role of rare earth oxides to increase NIR reflectance, In this case the resulting pigment is an oxide formed by different rare earths and bismuth. The precursors consist in rare earth oxides (CeO₂, Y₂O₃ and Tb₄O₇.) and Bi₂O₃. The precursors were added in the stoichiometric ratio and homogenized by wet mixing with acetone in an agate mortar until to obtain a slurry. The slurry was dried in an air oven at a temperature of 100 °C. A homogenous mixture was obtained after a cycle of mixing and drying. The mixed product was then calcined in a platinum crucible in an electric furnace at 1000 °C for 6 h.

The substitution of Bi³⁺ and Ce⁴⁺ with Y³⁺ and Tb⁴⁺ in Bi₂Ce₂O₇ changes the color from yellow to red. In the series of Bi₂Ce₂O₇ pigments synthesized by Raj et al. [73], the lightness (*L*^{*}) of all the samples is almost similar, even if it slightly decreases with Bi³⁺ content. As shown in the **Table 2. 1** the *b*^{*} value depends on Bi³⁺ doping: an increasing amount of Bi corresponds to an increase in *b*^{*} (i.e., an increase in yellow intensity). The red hue of the pigment (*a*^{*}) shows an increase up to Bi_{0.50}Y_{1.50}Ce₂O₇ and then it decreases. The highest yellow hue (*b*^{*}=51.36) was obtained for Bi_{1.75}Y_{0.25}Ce₂O₇ pigment. The color palette confirms that doping with Y leads to brilliant yellow pigments. In the Bi₂Ce_{2-x}Tb_xO₇ pigments, the lightness (*L*^{*}) of the samples decreases with an increase in terbium concentration. Doping with Tb increases the red component (*a*^{*}) from 5.44 to 10.37 while the yellow component (*b*^{*})

decreases from 48.76 to 15.83. A clear consequence is the color change to dark brown. Considering the color palette, the tuning of color from yellow to red can be obtained by the introducing of Tb into the $\text{Bi}_2\text{Ce}_2\text{O}_7$. The best result in terms of NIR reflectance (93.60 %) is obtained by pigment $\text{Bi}_{0.50}\text{Y}_{1.50}\text{Ce}_2\text{O}_7$. For this pigment L^* and NIR reflectance increase with Y amount. For Tb doped $\text{Bi}_2\text{Ce}_2\text{O}_7$ the NIR reflectance decreases, increasing Tb, from $\text{Tb}=0.50$.

Schildhammer et al.[72] and Raj et al. [73] focused on one of the most explored fields of research for what concerns NIR reflective pigments: the use of rare earth oxides, that recognized to be able to enhance NIR reflectance, as observed for the $\text{Bi}_2\text{Ce}_2\text{O}_7$ pigments doped with Y, synthesized by Raj et al. [73] (**Table 2. 1**). Both authors confirm the relevant role of Bi to increase the yellow hue intensity and NIR reflectance, as confirmed by Wang et al.[77] in sol-gel section. Even if the solid-state route needs a lot of energy and time, it employs rare earth compounds that are not harmful for the environment and human health.

2.5.1.3 Hydrothermal and precipitation route

The precipitation method allows employing many precursors. Infact, it implies no production of solid waste, resulting in the possibility of employing reagents that effectively participate in the reaction. Briefly, this method, also starting from a solution, involves the dissolution of the starting materials in a common solvent followed by the addition of a precipitating agent to form a homogeneous and single phase inorganic solid. Shi et al.[74] realized yellow pigments with the precipitation method. They synthesized the pigments,

with the general formula $\text{Al}_{1-x}\text{Fe}_x\text{PO}_4$ ($x= 0.00, 0.03, 0.05, 0.08$), from the following precursors: aluminum chloride (AlCl_3), potassium phosphate (KH_2PO_4) and ferric chloride (FeCl_3). All the reagents were dissolved in pure water, and each solution was heated at $60\text{ }^\circ\text{C}$ under vigorous stirring. Subsequently, the mixture was filtered, dried at $110\text{ }^\circ\text{C}$ for 4 h, and calcinated at $700\text{ }^\circ\text{C}$ for 2 h. The powder was ball milled for 3 h, with a revolving speed of 300 rpm. In this research, the authors exploited the high near-infrared reflectance (about 95 %) of the phosphates, which is higher than that of titanium dioxide (87 %) [78]. In addition, different colors can be obtained by doping different ions into the phosphate. Thanks to this method, the authors obtained different shades of the same color. In the work of Shi et al.[74], the L^* value decreases from 75.76 to 62.99 with the addition of Fe^{3+} , suggesting that the samples obtain a darker color. In addition, with more Fe^{3+} added, the red hue a^* coordinate increases from 12.46 to 16.54 and the yellow hue b^* rises from 23.7 to 30.11. Finally, the color changes to orange-yellow ($x=0.03\text{--}0.08$). The chromaticity change might be related to the different content of doping Fe^{3+} ions into the crystal structure. From NIR reflectance data extrapolated by NIR reflectance curves the effect of phosphates in the increase of NIR reflectance is evident. The effect of phosphates anion on the NIR reflectance was observed also by Elakkiya and Sumathi [75]. The cited study shows a comparison of yellow shades and NIR reflectance of the same pigment (a nickel and manganese phosphate) obtained through the precipitation method and hydrothermal route.

In the precipitation method, a relevant role is played by the liquid phases (solvents and precipitating agents) [75], while in the hydrothermal method, pressure and temperature

have a crucial role in defining the size and the shape of the final product [90] as reagent are sealed in autoclave

Elakkiya and Sumathi [75] synthesized yellow pigments with the general formula $\text{Ni}_x\text{Mn}_{2-x}\text{P}_2\text{O}_7$ ($x = 0, 0.5, 1.0, 1.5, 2.0$) through both methods using the following reagents: nickel chloride ($\text{NiCl}_2 \cdot 6\text{H}_2\text{O}$), manganese chloride ($\text{MnCl}_2 \cdot 7\text{H}_2\text{O}$), tetra-sodium-pyrophosphate ($\text{Na}_4\text{P}_2\text{O}_7 \cdot 9\text{H}_2\text{O}$) and anhydrous citric acid ($\text{C}_6\text{H}_8\text{O}_7$). In the precipitation method, an appropriate amount of metal chloride (Mn, Ni) was dissolved in 40 mL of distilled water. An aqueous solution of $\text{Na}_4\text{P}_2\text{O}_7$ was added dropwise to the metal chloride solutions with constant stirring. The obtained precipitate was filtered and washed several times with distilled water. In the hydrothermal method, 0.5 g of citric acid and 1 g of polyethyleneglycol-6000 mixture were added to the mixture prepared for the precipitation method, stirred for 2 h in a magnetic stirrer, and transferred into a PTFE-lined stainless steel autoclave. The hydrothermal autoclave was sealed and kept at 150 °C for 16 h, then cooled to room temperature. The obtained products were calcined for 6 h at 250–700 °C in an oxygen atmosphere for both methods. Elakkiya and Sumathi [75] compared the results of two different routes. The b^* values are elevated for all the Ni substituted $\text{Mn}_2\text{P}_2\text{O}_7$. Comparing the b^* values of pigments prepared by hydrothermal and precipitation, there are some differences. The L^* values of all the compositions obtained by the precipitation method are lower when compared to the hydrothermal method. $\text{Mn}_{0.5}\text{Ni}_{1.5}\text{P}_2\text{O}_7$ prepared by the precipitation method has the $L^* = 78.52$, $a^* = 2.15$, and $b^* = 41.91$, while in $\text{Ni}_2\text{P}_2\text{O}_7$ prepared through the precipitation method, b^* value is 66.80. Brighter colors are obtained

in the case of Ni₂ doped Mn₂P₂O₇ prepared by precipitation method, as confirmed by the *L** trend.

It is interesting to note that Elakkiya and Sumathi [75] obtained the Mn₂P₂O₇ pigment at lower temperatures, compared to the previous literature devoted to hydrothermal methods for the production of Mn₂P₂O₇ based pigments [79,80]. However, the equipment (autoclave and furnace are not used) and energy demand (temperatures close to room temperature) are very limited for the precipitation method. In this case, the precipitation method is also suitable for containing the release of nickel compounds. By means of the precipitation methods, the dispersion of toxic nickel compounds was avoided, as the precipitation method does not produce solid wastes (the release of Nickel(II) chloride hexahydrate in water is toxic for the aquatic organisms). During the processing, particular care has to be taken when handling Nickel(II) chloride hexahydrate, which must be used under a chemical fume hood due to the demonstrated carcinogenic effect upon chronic exposure [81].

2.5.1.4 Advantageous aspects of the synthesis processes

For the rare-earth based compounds yellow pigments, the sol-gel method seems to be the best solution considering the possibility to obtain pigments with intense hue (thanks to the doping with rare earths as Ce, Pr, Nd) and high NIR reflectance [82].





The Sol-gel was applied as it is a convenient balance between low temperatures (300 °C - 900 °C) and relatively short thermal treatments (frequently a maximum of 10 h), compared to other processes. One drawback relies on the use of toxic solvents as N.N-













dimethylformamide [61]. However, the literature reports demonstrated the use of less toxic and inexpensive solvents [77]. Yellow rare earths based pigments made by sol-gel were revealed a good alternative in terms of chromophore properties [49].

Other methods, such as solid-state, employ high temperature and long time, compared to sol-gel and hydrothermal routes. Using of a solid-state method to synthesize yellow pigments from rare earths is expensive, as by Schildhammer et al.[72] demonstrated, due to the long times and high temperatures involved. Fe³⁺ doped AlPO₄ pigments by Shi et al. [74] represent an interesting case for the low temperatures and times and also for the use of water as the only solvent and define the sol-gel as a potential strategy to synthesize pigments with low energy expenditure.

2.5.2 Overview on red pigments

Table 2. 2. Color coordinates, NIR reflectance of the powdered red pigments and the synthesis method employed.

Chemical compound	Synthesis method	Color coordinates			Color from color coordinates [®]	NIR reflectance (R%)	Reference
		<i>L</i> *	<i>a</i> *	<i>b</i> *			
BiFeO ₃	Sol-Gel	49.82	15.62	22.26		≈50.00 ^{@@}	[83]
Bi _{0.9} La _{0.1} FeO ₃	Sol-Gel	51.09	14.98	22.74		≈50.00 ^{@@}	[83]
Bi _{0.8} La _{0.2} FeO ₃	Sol-Gel	53.11	18.06	22.12		≈55.00 ^{@@}	[83]
Bi _{0.7} La _{0.3} FeO ₃	Sol-Gel	55.22	21.6	21.96		≈56.00 ^{@@}	[83]

$\text{Bi}_{0.6}\text{La}_{0.4}\text{FeO}_3$	Sol-Gel	61.92	23.52	21.04		$\approx 75.00^{\text{®}}$	[83]
$\text{Y}_2\text{Ce}_2\text{O}_7$	Solid-state	89.69	-2.60	12.96		86.90	[64]
$\text{Y}_2\text{Ce}_{1.8}\text{Tb}_{0.2}\text{O}_7$	Solid-state	49.57	26.01	33.40		80.00	[64]
$\text{Y}_2\text{Ce}_{1.6}\text{Tb}_{0.4}\text{O}_7$	Solid-state	43.08	25.58	27.04		72.30	[64]
$\text{Y}_2\text{Ce}_{1.4}\text{Tb}_{0.6}\text{O}_7$	Solid-state	39.49	24.10	22.84		67.10	[64]
$\text{Y}_2\text{Ce}_{1.2}\text{Tb}_{0.8}\text{O}_7$	Solid-state	35.87	22.27	20.26		60.00	[64]
Y_2CeTbO_7	Solid-state	35.70	19.60	18.24		55.10	[64]
Sep	Commercial product	64.10	3.99	12.89		/	[84]
HNTs	Commercial product	73.55	4.26	11.95		/	[84]
Fe_2O_3	Commercial product	34.21	1.23	13.55		/	[84]
Sep/ Fe_2O_3	Hydrothermal	39.20	25.10	17.50		$\approx 40.00^{\text{®®}}$	[84]
HNTs/ Fe_2O_3	Hydrothermal	33.60	34.40	24.90		$\approx 40.00^{\text{®®}}$	[84]

Legend:

- ® : The color represented is obtained matching color coordinates
- ® : Extrapolated from fig.4 of [85]
- ®® : Extrapolated from fig.10 (a) of [83]
- ®®® : Extrapolated from fig.6 (a) and fig.6 (b) of [84]
- /: Data not showed in the paper

A huge variety of different raw materials use of raw materials was employed in synthesis of red pigments, from on rare earths to clay minerals [86]. In addition, many different production processes, such calcination, solid-state route [64], hydrothermal

method [84] and sol-gel [83] were proposed. Unfortunately, mainly traditional industrial processes characterized by high energy demand (as calcination process) are still employed for the synthesis of red pigments.

2.5.2.1 Sol-Gel route

In the field of the red pigments synthesized via sol-gel, the rare earth compounds showed interesting properties. Rare earth oxides have proven to be good chromophores [85,87,88] capable of increasing the near-infrared reflectance [88]. Šulcová et al. [88] used rare earths as a dopants in the sol-gel technique to obtain many different red hues. The doping with rare earths cations promotes mixed oxide pigments formation [87]. The cations have two different main functions: chromophores action (as Pr, Ce, Nd), structure of stable host oxides and influence particle size [88].

The contribution of the reduction in crystallite size, due to the presence of iron in ceria lattice, is responsible for a higher number of reflectance points, thus improving the scattering of the incident radiation.

Yuan et al. [83] prepared pigments with uniform spherical-like morphology of the particles. These pigments are interesting, showing once again the high possibility offered by the sol-gel route to modify the base structure through doping elements (In this case Yuan et al. compare the effect of La, Fe, and Bi as doping elements). Pigments based on $\text{Bi}_{1-x}\text{La}_x\text{FeO}_3$ ($x = 0, 0.1, 0.2, 0.3, 0.4$) were obtained by the following precursors: bismuth (III) nitrate pentahydrate ($\text{Bi}(\text{NO}_3)_3 \cdot 5\text{H}_2\text{O}$), iron(III)nitrate nonahydrate, ($\text{Fe}(\text{NO}_3)_3 \cdot 9\text{H}_2\text{O}$), lanthanum(III)nitrate hexahydrate ($\text{La}(\text{NO}_3)_3 \cdot 6\text{H}_2\text{O}$), citric acid, acrylamide and glucose.

Stoichiometric amounts of $\text{Bi}(\text{NO}_3)_3 \cdot 5\text{H}_2\text{O}$, $\text{Fe}(\text{NO}_3)_3 \cdot 9\text{H}_2\text{O}$, $\text{La}(\text{NO}_3)_3 \cdot 6\text{H}_2\text{O}$ were dissolved in dilute HNO_3 solution. A stoichiometric amount of citric acid was added as a chelating agent to complex cations in the mole ratio 3:1 with respect to cations (Bi^{3+} , Fe^{3+} , La^{3+}). Afterward acrylamide was added to the solution in the mole ratio 4:1 with respect to the cations (Bi^{3+} , Fe^{3+} and La^{3+}) to control the powders particle size. Finally, a small amount of glucose was added and dissolved. The resultant solution was then heated at $80\text{ }^\circ\text{C}$ in water and stirred continuously until the formation of a homogeneous gel. The gel was dried at $100\text{ }^\circ\text{C}$, obtaining a xerogel. This gel was then calcined at $600\text{ }^\circ\text{C}$ for 4 h producing the final powder samples.

The NIR reflectance increases with La^{3+} content and the final powder samples change color gradually from brown to red, as confirmed by CIEL^{*}*a*^{*}*b*^{*} coordinates (**Table 2. 2**). The substitution of Bi^{3+} with La^{3+} in BiFeO_3 leads to an increase in the L^* value from 49.82 to 61.92, suggesting that pigment becomes brighter. Moreover, La doping increases a^* value from 15.62 to 23.52, indicating that the pigments redness has been enhanced. Simply BiFeO_3 exhibits a NIR reflectance of around 50.00 %. The NIR reflectance increases near up to 75.00 %, when La^{3+} is incorporated in the structure. La acts a chromophore agent, increasing the a^* value (red hues).

Red pigments synthesized by the sol-gel route, as those synthesized Yuan et al. [83], demonstrate that Fe doping increases red color intensity (increase in a^* value) and NIR reflectance [85]. La confers deeper red shades to pigment (higher a^* value) and higher reflectance in the NIR range. The work published by Yuan et al. [83] is a compact

synthesis of features of red pigments synthesis of red pigments by sol-gel: colorimetric coordinates and NIR reflectance modulated by doping elements, with short times and low temperatures during production. The characteristics listed before are in fact present in other papers about red pigments synthesized through sol gel [85,87,88].

2.5.2.2 Solid state route

Similarly, to the sol-gel method, rare earths have been extensively employed in the solid-state synthesis route. Raj et al. [64] synthesized yttrium ceriate-based pigments with a general formula. The precursors were synthesized employing the following raw materials: Y_2O_3 , CeO_2 , and Tb_4O_7 . The compounds were mixed with acetone and ground in an agate mortar. The obtained slurry was dried in an oven at 100 °C. The mixing and drying were repeated thrice to obtain a homogenous mixture. The mixture was treated at 1500 °C for 12 h. The obtained pigments can be described by the formula: $Y_2Ce_{2-x}Tb_xO_7$ ($x = 0.2, 0.4, 0.6, 0.8, 1.0$).

The data reported in **Table 2. 2** confirm the influence of Tb as a doping element. The $Y_2Ce_2O_7$ exhibits the highest values of red component (a^*) at 0.2 mol% of Tb ions substituted Ce^{4+} . In addition, with increasing Tb content, the lightness of the powdered samples decreases. Anyway, Tb doped CeO_2 based pigments give high-quality red hues, as confirmed by the studies of Šulcová et al. [88]. In the case of rare-earth-based red pigments, the solid-state process is a good synthesis method for the possibility of regulating reaction rate, aiming to control the crystalline size and so obtaining a large

range of different red hues. Furthermore, as Raj et al. [64] pointed out, CeO₂ and ceria-based solid solutions also show high thermal stability.

Raj et al. [64] obtained red hues similar to the color “brick red” by exploiting rare earths doping, in accordance with the findings of Yuan et al.[83]. The lightness of those pigments decreases with increasing Tb concentration. The doping with terbium (x=0.2) promotes an increase in the red component ($a^*=26.01$) and yellow component ($b^*=33.40$). From Y₂Ce_{1.6}Tb_{0.4}O₇ pigment, a progressive decrease in the red and yellow hues is observed (as denoted by the chromatic coordinates a^* and b^*), and in the lightness of the pigment (as underlined by L^* decreasing trend from 89.69 to 35.70). Accordingly, the color changes from a creamy white to dark-brown. The Y₂Ce₂O₇ exhibits the highest NIR reflectance (86.90 %). Simultaneously, with Tb replacement of Ce⁴⁺ ions, the NIR reflectance of the pigments progressively decreases from 86.90 % (Tb=0) to 55.10% (Tb=1.0). In this case, the pigments doped with Tb show a decrease in L^* and in NIR reflectance. Compared to sol-gel method the solid state route employs high temperature (higher than 1000 °C) and long times (more than 10 h). Hydrothermal synthesis route in the synthesis of red pigments involves to employ low temperatures and short times respect to the solid state route underlined above, and with the employment of easily available raw material (clays or iron oxide) [84].

2.5.2.3 Hydrothermal and precipitation route

The hydrothermal method has been employed for enhanced efficiency and lower energy consumption [84], rather than for the possibility of using novel precursors to

control the hues. Tian et al. [84] synthesized a series of clay/Fe₂O₃ red hybrid pigments through a hydrothermal route with a one-step reaction process. The starting raw materials consisted of natural sepiolite (Sep), halloysite nanotubes (HNTs) and FeCl₃·6H₂O. Sep or HNTs powder (4 g) was dispersed in 60 mL of an aqueous solution containing 12.0 g FeCl₃·6H₂O forming a homogeneous suspension under stirring and ultrasonication at room temperature. Then, the suspension was introduced in an autoclave at 180 °C for 24 h. The solid product was separated and fully washed with deionized water after cooling. The solid product was dried, ground, and sifted through a 200-mesh sieve. Simply Fe₂O₃ control sample was prepared according to the same experimental procedure. The hybrid pigments derived from Sep and HNTs were marked as Sep/Fe₂O₃ and HNTs/Fe₂O₃, respectively. The presence of Sep or HNTs resulted to be essential to induce the formation of red clay/Fe₂O₃ pigments and to affect the crystal phase formation and microscopic morphologies. The authors also reported an increase in the color parameter a^* for the Sep/Fe₂O₃ and HNTs/Fe₂O₃ hybrid pigments compared to previous reports listed in the paper. The data on red pigments developed by Tian et al. [84] are listed in **Table 2. 2**. As shown in **Table 2. 2**, the a^* coordinate values of the Sep/Fe₂O₃ and HNTs/Fe₂O₃ hybrid pigments are 25.10 and 34.40, respectively. Meanwhile, the b^* coordinate values of the Sep/ Fe₂O₃ and HNTs/Fe₂O₃ hybrid pigments are 17.50 and 24.90, respectively. Both the hybrid pigments exhibit more positive a^* values but less positive values of the b^* coordinate. The positive values of a^* coordinate imply a redshift of the color. However, the b^* coordinate of HNTs/Fe₂O₃ is more positive than that of Sep/Fe₂O₃, suggesting a more yellow tone for the HNTs/Fe₂O₃ hybrid

pigments. Furthermore, the a^* coordinate for Sep and HNTs based pigments is very low, indicating the absence of red hues. The NIR reflectance of the hybrid pigments was lower than those synthesized by Raj et al. or Yuan et al. [64,83]. It has to be considered that reflectance values in **Table 2. 2** are obtained by extrapolation at 750 nm, so at the beginning of NIR reflectance range.

Hydrothermal and precipitation routes represent a cheap alternative to the other synthesis methods due to the processing temperature (higher than sol-gel, but lower than solid-state route) and the reduced cost of the precursors (e.g., clay minerals and metal oxides such as iron and zinc oxides). Unfortunately, there is a lack of data about the NIR reflective properties of red pigments obtained by this technique. Considering the hybrid pigments synthesized by Tian et al. [84], good stability to sunlight was obtained together with a potential NIR reflectance. In fact, clay/Fe₂O₃ hybrids pigments contain Al (in halloysite), which is recognized to increase the NIR reflectance, as demonstrated in the case of yellow pigments synthesized by Shi et al.[74]. For this reason, we believe that the clay/Fe₂O₃ hybrid pigments would show a significant NIR reflectance, even if it was not measured (the reflectance spectra reported in the paper are in the visible range).






2.5.2.4 Advantageous aspects of the synthesis processes





















Traditional industrial processes (as calcination process) for the synthesis of red pigments are still employed. Precipitation and hydrothermal methods are more competitive in terms of cost/benefit ratio than yellow pigments. Also for red pigments,





















a significant decrease in cost was obtained adding clay minerals, as shown by Tian et al [84]. In this case, the hydrothermal method shows advantages due to the raw materials (clay minerals are cheaper and more available than rare earths oxides) and the reduction in temperatures (the temperature used was below 200 °C). Referring to the hydrothermal process developed by Tian et al [84] the process shows long times for calcination and obtain the final product (24 h). In the sol-gel procedure for the synthesis of red pigments were not detected implementation in techniques respect to the yellow pigments but are well underlined the main features that identify sol-gel as smart technique to synthesize pigments: low temperatures, short times and use of different doping elements.

2.5.3 Overview on blue pigments

Table 2. 3. Color coordinates, NIR reflectance of the powdered blue pigments, and the synthesis method employed.

Chemical compound	Synthesis method	Color coordinates			Color from color coordinates [®]	NIR Reflectance (R%)	Reference
		<i>L</i> *	<i>a</i> *	<i>b</i> *			
CoCr ₂ O ₄	Sol-Gel	53.20	-21.70	-9.40		43.00	[56]
Co _{0.75} Zn _{0.25} Cr ₂ O ₄	Sol-Gel	54.60	-22.10	-9.00		44.50	[56]
Co _{0.5} Zn _{0.5} Cr ₂ O ₄	Sol-Gel	57.90	-24.10	-8.30		47.20	[56]
Co _{0.25} Zn _{0.75} Cr ₂ O ₄	Sol-Gel	60.20	-24.20	-4.60		52.10	[56]
ZnCr ₂ O ₄	Sol-Gel	71.20	-6.10	6.40		59.50	[56]

$\text{CoCr}_{1.5}\text{Al}_{0.5}\text{O}_4$	Sol-Gel	51.60	-20.3	-11.40		43.50	[56]
CoCrAlO_4	Sol-Gel	51.10	-15.4	-15.60		43.70	[56]
$\text{CoCr}_{0.5}\text{Al}_{1.5}\text{O}_4$	Sol-Gel	48.60	-9.60	-20.30		43.90	[56]
CoAl_2O_4	Sol-Gel	52.00	-1.20	-35.20		43.60	[56]
$\text{YIn}_{0.9}\text{Mn}_{0.1}\text{O}$	Sol-Gel	39.71	-5.78	-22.28		63.00	[51]
$\text{YIn}_{0.9}\text{Mn}_{0.1}\text{O}_3\text{-ZnO}$	Sol-Gel	49.94	-0.88	-40.55		79.00	[51]
$\text{SrCuSi}_4\text{O}_{10}$	Solid-state	71.20	-5.70	-23.90		$\approx 45.00^\#$	[67]
$\text{Sr}_{0.9}\text{La}_{0.1}\text{Cu}_{0.9}\text{Li}_{0.1}\text{Si}_4\text{O}_{10}$	Solid-state	55.70	5.70	-47.80		$\approx 74.00^\#$	[67]
$\text{Sr}_{0.8}\text{La}_{0.2}\text{Cu}_{0.8}\text{Li}_{0.2}\text{Si}_4\text{O}_{10}$	Solid-state	50.60	9.00	-51.50		$\approx 76.00^\#$	[67]
$\text{Sr}_{0.7}\text{La}_{0.3}\text{Cu}_{0.7}\text{Li}_{0.3}\text{Si}_4\text{O}_{10}$	Solid-state	49.60	10.40	-51.70		$\approx 70.00^\#$	[67]
$\text{Sr}_{0.6}\text{La}_{0.4}\text{Cu}_{0.6}\text{Li}_{0.4}\text{Si}_4\text{O}_{10}$	Solid-state	53.0	4.10	-45.10		$\approx 65.00^\#$	[67]
$\text{Sr}_{0.5}\text{La}_{0.5}\text{Cu}_{0.5}\text{Li}_{0.5}\text{Si}_4\text{O}_{10}$	Solid-state	55.60	1.50	-39.40		$\approx 62.00^\#$	[67]
$\text{Ca}_{0.5}\text{Ce}_{0.5}\text{Al}_{11.5}\text{Ni}_{0.5}\text{O}_{19}$	Solid-state	57.35	-12.37	-27.43		$\approx 66.00^\#\#$	[89]
$\text{Ca}_{0.5}\text{Pr}_{0.5}\text{Al}_{11.5}\text{Ni}_{0.5}\text{O}_{19}$	Solid-state	58.59	-13.03	-22.70		$\approx 80.00^\#\#$	[89]
$\text{Ca}_{0.5}\text{Nd}_{0.5}\text{Al}_{11.5}\text{Ni}_{0.5}\text{O}_{19}$	Solid-state	59.87	-12.15	-24.46		$\approx 85.00^\#\#$	[89]
$\text{CaAl}_{11}\text{Sn}_{0.5}\text{Ni}_{0.5}\text{O}_{19}$	Solid-state	67.51	-9.68	-20.26		/	[89]
$\text{CaAl}_{11}\text{Ge}_{0.5}\text{Ni}_{0.5}\text{O}_{19}$	Solid-state	55.19	-13.77	-22.54		/	[89]
$\text{CaAl}_{11.4}\text{Nb}_{0.2}\text{Ni}_{0.4}\text{O}_{19}$	Solid-state	57.59	-13.63	-26.83		/	[89]
$\text{CaAl}_{11.4}\text{Sb}_{0.2}\text{Ni}_{0.4}\text{O}_{19}$	Solid-state	67.23	-10.49	-18.72		/	[89]
$\text{CaAl}_{11.4}\text{Ta}_{0.2}\text{Ni}_{0.4}\text{O}_{19}$	Solid-state	64.83	-12.02	-19.27		/	[89]

$\text{Ca}_{0.5}\text{La}_{0.5}\text{Al}_{11}\text{Ga}_{0.5}\text{Ni}_{0.5}\text{O}_{19}$	Solid-state	66.28	-10.46	-18.73		/	[89]
$\text{Ca}_{0.5}\text{La}_{0.5}\text{Al}_{11}\text{In}_{0.5}\text{Ni}_{0.5}\text{O}_{19}$	Solid-state	58.81	-11.73	-26.96		/	[89]
$\text{CaAl}_{10}\text{TiNi}_{0.5}\text{Zn}_{0.5}\text{O}_{19}$	Solid-state	54.46	-13.40	-16.78		$\approx 84.00^{\#}$	[89]
$\text{Ca}_{0.5}\text{Na}_{0.5}\text{Al}_{0.5}\text{TiNi}_{0.5}\text{O}_{19}$	Solid-state	54.85	-15.91	-24.97		/	[89]
$\text{Ca}_{0.4}\text{Sr}_{0.6}\text{Al}_{0.8}\text{Ti}_{0.6}\text{Ni}_{0.6}\text{O}_{19}$	Solid-state	66.42	-10.89	-19.85		/	[89]
$\text{Ca}_{0.5}\text{Sr}_{0.5}\text{Al}_{10}\text{TiNiO}_{19}$	Solid-state	50.73	-14.17	-25.93		/	[89]
$\text{Ca}_{0.75}\text{La}_{0.25}\text{Al}_{11.25}\text{Ti}_{0.25}\text{Ni}_{0.5}\text{O}_{19}$	Solid-state	66.69	-11.12	-19.72		/	[89]
$\text{Ca}_{0.5}\text{La}_{0.5}\text{Al}_{11}\text{Ti}_{0.25}\text{Ni}_{0.75}\text{O}_{19}$	Solid-state	56.22	-10.66	-26.83		/	[89]
$\text{CaAl}_{11.8}\text{Co}_{0.2}\text{O}_{19}$	Solid-state	64.17	-4.66	-20.22		/	[89]
$\text{Ca}_{0.5}\text{La}_{0.5}\text{Al}_{11.5}\text{Ni}_{0.5}\text{O}_{19}$	Solid-state	57.00	-6.50	-30.38		$\approx 90.00^{\#}$	[89]
$\text{CaAl}_{11}\text{Ti}_{0.5}\text{Ni}_{0.5}\text{O}_{19}$	Solid-state	65.47	-11.10	-22.76		$\approx 85.00^{\#}$	[89]
$\text{CaAl}_{10}\text{TiNiO}_{19}$	Solid-state	49.59	-14.72	-28.44		$\approx 72.00^{\#}$	[89]
CoAl_2O_4 Commercial cobalt blue	Commercial product	43.51	-4.46	-44.39		$\approx 58.00^{\#}$	[89]
$\text{SrAl}_{11}\text{Ti}_{0.5}\text{N}_{0.5}\text{O}_{19}$	Solid-state	66.07	-10.39	-21.17		/	[89]
$\text{SrAl}_{10}\text{TiNiO}_{19}$	Solid-state	65.12	-11.46	-18.53		/	[89]
$\text{SrAl}_{9.6}\text{Ti}_{1.2}\text{Ni}_{1.2}\text{O}_{19}$	Solid-state	62.94	-12.12	-17.86		/	[89]
$\text{SrAl}_8\text{Ti}_2\text{Ni}_2\text{O}_{19}$	Solid-state	52.31	-17.99	-10.34		/	[89]
Kaolin/ $\text{Co}_2(\text{OH})_2\text{CO}_3$ calcined at 800 °C	Precipitation	34.62	1.16	1.95		19.80	[53]
Kaolin/ $\text{Co}_2(\text{OH})_2\text{CO}_3$ calcined at 900 °C	Precipitation	37.32	-8.50	-9.27		22.10	[53]
Kaolin/ $\text{Co}_2(\text{OH})_2\text{CO}_3$ calcined at 1000 °C	Precipitation	40.88	-9.53	-24.43		55.51	[53]

Kaolin/Co ₂ (OH) ₂ CO ₃ calcined at 1100 °C	Precipitation	38.29	-9.21	-38.90		60.18	[53]
Kaolin/CoAl ₂ O ₄ calcined at 1100 °C for 1h	Precipitation	40.72	-11.76	-23.18		55.72	[53]
Kaolin/CoAl ₂ O ₄ calcined at 1100 °C for 2h	Precipitation	39.29	-10.26	-29.50		58.95	[53]
Kaolin/CoAl ₂ O ₄ calcined at 1100°C for 3h	Precipitation	38.29	-9.21	-38.90		60.18	[53]
Kaolin/CoAl ₂ O ₄ calcined at 1100 °C for 6h	Precipitation	38.02	-8.98	-39.06		60.49	[53]

Legend:

- ® : The color represented is obtained matching color coordinates
- #: extrapolated from fig.9 of [64]
- ##: extrapolated from fig.14 of [89]
- /: Data not showed in the papers

In addition, considering of cool pigments having blue shades, rare earth based pigments have been recently developed. The synthesis of the new blue pigments by Smith et al. [90], based on a YMnO₃ formulation, boosted the development of yttrium oxide-based pigment doped with many different cations [51] to increase the NIR reflectance and modify the blue shade [51,69]. Y and Mn-based blue pigments were synthesized by different sol-gel and solid-state routes [69], to reduce the energy consumption (compared to traditional pigments as cobalt blue [50]), and to use environmentally friendly precursors. Sol-gel is the most used synthesis route for blue pigments in recent literature developments.

2.5.3.1 Sol-Gel route

Hedayati et al [56] improved this technique by using the Pechini sol-gel method [91], synthesizing chromium and cobalt-based pigments from CoCr_2O_4 , by adding Zn^{2+} and Al^{3+} . Hedayati et al [56] synthesized pigments with the general formula $\text{Co}_{1-x}\text{ZnCr}_{2-y}\text{Al}_y\text{O}_4$ employing the Pechini sol-gel route method, where an organic complexing agent was used (citric acid or ethylenediamine tetra acetic acid, EDTA) to complex the metal cations. The resulting polymeric organic network reduces any segregation of metal cations. After the citric acid dissolution in distilled water, the following cationic salts were added to the solution in the stoichiometric ratio: $\text{Co}(\text{NO}_3)_2 \cdot 6\text{H}_2\text{O}$, $\text{Cr}(\text{NO}_3)_3 \cdot 9\text{H}_2\text{O}$, $\text{Zn}(\text{NO}_3)_2 \cdot 6\text{H}_2\text{O}$, $\text{Al}(\text{NO}_3)_3 \cdot 9\text{H}_2\text{O}$. Upon completion of the dissolution, a 60/40 ethylene glycol/citric acid molar ratio was added. The solution was treated in an oven at 120 °C to obtain a viscous gel and then at 300 °C for 1 h in an air atmosphere. Gas liberation after the heat treatment leads to the partial degradation of the organic structure and its expansion. The powder precursor was formed and ground. The obtained powder was calcined at 1200 °C in air. Compared to traditional cool blue pigments, this way results cheaper and with lower toxicity.

Considering the data reported in **Table 2. 3**, it is possible to observe that NIR reflectance value increases with the Zn^{2+} ion concentration. In the paper of Hedayati et al.[56] the amount of cobalt in the pigments was decreased making this process not entirely environmentally friendly and cheap, also considering the calcination temperature higher than 1000 °C. The most interesting finding of the cited paper consists in investigating the role of Al^{3+} in the structure of the pigments, which seems to increase the NIR reflectance in agreement with the findings on yellow pigments [74]. The effect of aluminum on the NIR reflectance is showed in **Table 2. 3**.

The progressive doping with of Zn^{2+} ions in $CoCr_2O_4$ produces an increase in the lightness, L^* , that suggests the formation of lighter pigments. With increasing Zn^{2+} content, b^* value increases and thus, the blueness of the samples weakens. The maximum amount of Zn^{2+} (0.75 mol %) promotes a green hue on the pigment, evident from the negative values of the color coordinate a^* that becomes increasingly negative. In $ZrCr_2O_4$, the a^* value increases to -6.10 and the b^* value reaches 6.40, resulting is a grey pigment. For what concerns the Al^{3+} substituted doped $CoCr_2O_4$ pigments, the progressive substitution of Cr^{3+} with Al^{3+} ions in the $CoCr_2O_4$ structure increases the a^* and decreases the b^* , which means that the green component (b^*) of the pigment decreases (b^* tends to more positive values) and the pigments become blue. Al^{3+} does not change L^* values (almost stable around 50.00).

With increasing Zn^{2+} amount, a higher NIR reflectance is observed. The NIR reflectance is 43.00 % in the $CoCr_2O_4$ pigment and increases up to 59.50 % in $ZnCr_2O_4$. The increase in NIR reflectance with Al^{3+} is observed but less pronounced than the Zn^{2+} doping. (from 43.00 % in $CoCr_2O_4$ to 46.70 % in $CoAl_2O_4$). Jose et al.[51] improved the citrate based sol-gel synthesis employing only environmentally friendly precursors calcined at low temperatures to produce pigments based on Smith et al. [90] formulation. With respect to Li and Subramanian [69], the calcination times and temperatures were reduced. The obtained pigment, with the general formula $YIn_{0.9}Mn_{0.1}O_3-ZnO$, was synthesized by the sol-gel technique. Stoichiometric amounts of yttrium oxide (1.66 mmol), manganese (III) acetate (0.33 mmol), indium (1.49 mmol) and zinc oxide (3.33 mmol) were dissolved in 4.0 M nitric acid (100 mL) and a stoichiometric amount of citric acid respect to metal, under constant stirring and heating on a hot plate. Upon evaporation, a dried gel was obtained. The gel was

then heated at 250 °C for 2 h for the decomposition of the nitrates. The typical $\text{YIn}_{0.9}\text{Mn}_{0.1}\text{O}_3$ -ZnO pigment was ascertained by calcining the dried gel at various temperatures ranging from 600 °C to 900 °C for 2 h in air atmosphere. The typical blue color of the sample was observed only when the dried gel was calcined at 850 °C for 2 h. The presence of ZnO in $\text{YIn}_{0.9}\text{Mn}_{0.1}\text{O}_3$ structure decreases the magnitude of the b^* value from -22.28 to -40.55 compared to $\text{YIn}_{0.9}\text{Mn}_{0.1}\text{O}_3$ pigment (**Table 2. 3**), suggesting a remarkable enhancement in the blueness of the pigment. In addition, the lightness of the pigment has also been improved significantly (from $L^*=39.71$ to 49.94). The observed high NIR reflectance (79.00 %) of $\text{YIn}_{0.9}\text{Mn}_{0.1}\text{O}_3$ -ZnO may be due to the presence of ZnO nanoparticles, in agreement with the findings of Hedayati et al.[56]. In comparison to Hedayati et al. [56], in the paper of Jose et al. [51] the obtained blue shades have higher saturation as confirmed by colorimetric coordinates reported in **Table 2. 3** : L^* is smaller and b^* is more negative compared to Hedayati et al. [56].

Although sol-gel is an energy-saving process, implying the use of lower temperatures than other synthesis methods, high calcination temperatures are needed for the annealing process to produce a more regular morphology of the powdered pigments [92].

As observed for red and yellow pigments, the solid-state route is the most traditional method to synthesize NIR reflective inorganic pigments with high efficiency in NIR reflectance.

2.5.3.2 Solid state route

In Jose and Reddy [67] the substitution of Sr^{2+} with La^{3+} and Cu^{2+} with Li^+ in $\text{SrCuSi}_4\text{O}_{10}$ (0.0-5.0 mol %) produces a decrease of the b^* value from -23.90 to -51.70 (Table 2. 3), increasing blue hue. This effect is observed with Li amount equal to 0.3 mol %. An increasing amount of doping cations in the host matrix changes red hue (a^* from 10.40 to 1.50) and decreases moderately the blue one (b^* from -51.70 to -39.40). Progressive doping of $\text{SrCuSi}_4\text{O}_{10}$ with La^{3+} decreases moderately the NIR solar reflectance of the pigment from 74.00 % to 62.00 %.

Berdahl et al. [93] developed Egyptian blue pigments modified with barium ($\text{BaCuSi}_4\text{O}_{10}$) and strontium ($\text{SrCuSi}_4\text{O}_{10}$) for application in luminescent solar concentrator (LSC). The effective solar reflectance (ESR) measurement confirmed the potential application of Blue Egyptian as NIR reflective pigment. Unfortunately, it is not clear what pigment between strontium and barium compounds shows the best performances. Jose and Reddy [64] synthesized the Egyptian blue pigments considering the effect of lanthanum and lithium. For this purpose, high purity La_2O_3 , SrCO_3 , CuO , Li_2CO_3 and SiO_2 were milled in the agate mortar with acetone for 1 h and dried in an air oven. The precursors were mixed and dried three times to obtain a homogeneous solution. The excess acetone was removed by evaporating in the air. The obtained mixture was calcined at 950 °C for 16 h. The pigment was ground in an agate mortar obtaining uniform particle size. The pigment had the general formula of $\text{Sr}_{1-x}\text{La}_x\text{Cu}_{1-y}\text{Li}_y\text{Si}_4\text{O}_{10}$ ($x = y$ and ranges from 0 to 0.5).

Li et al.[89] obtained blue pigments of various shades through hibonite doping. The structure of hibonite is such that it accommodates ions of various sizes, coordination and

valences. The obtained pigments have the general formula of $\text{CaAl}_{12-x}\text{Ni}_x\text{M}_y\text{O}_{19}$ ($\text{M} = \text{Zn, Ga, In, Si, Ti, Zr, Sn, Ge, Nb, Ta, Sb, Te}$) and $\text{A}_{1-x}\text{A}_x\text{Al}_{12-x}\text{Ni}_x\text{O}_{19}$ ($\text{A} = \text{La, Ce, Pr, Nd, Gd, Y}$) and $\text{Ca}_{1-x}\text{A}_x(\text{Al/Ni/Ti})_{12}\text{O}_{19}$ ($\text{A} = \text{Sr, Na}$). The colored oxides were obtained by the following precursors: ACO_3 ($\text{A} = \text{Ca, Sr, Ba}$), A_2CO_3 ($\text{A} = \text{Na}$), rare earths RE_2O_3 ($\text{RE} = \text{La, Nd, Sm, Eu, Gd, Dy, Ho, Er, Tm, Yb, Lu, Y}$), CeO_2 , Pr_6O_{11} , Tb_4O_7 , MO ($\text{M} = \text{Ni, Cu, Zn}$), M_2O_3 ($\text{M} = \text{Mn, Fe, In, Ga, Cr, Zn}$), MO_2 ($\text{M} = \text{Si, Ti, Sn, Ge, Te}$), M_2O_5 ($\text{M} = \text{Sb, V, Nb, Ta}$) and Co_3O_4 . These compounds were mixed, ground and pelletized. The pellets were heated at 1300/1550 °C for 12 h with intermediate grinding with a heating rate of 300 °C/h. For pure $\text{CaAl}_{12-2x}\text{Ni}_x\text{Ti}_x\text{O}_{19}$ ($x=0-1$) with high Ni content ($x \geq 0.4$) it was necessary to set a temperature within the range of 1300–1350 °C. On the contrary in case of low Ni content ($x < 0.4$) it was necessary to heat the raw material at the temperature of 1400–1450 °C, and 1500–1550 °C for $\text{CaAl}_{12}\text{O}_{19}$. All solid solutions $\text{A}_{1-x}\text{RE}_x\text{Al}_{12-x}\text{Ni}_x\text{O}_{19}$ ($\text{A} = \text{Ca, Sr, RE} = \text{La, Ce, Pr, Nd, } x = 0-1$) were prepared similarly at 1400–1550 °C compared commercial cobalt blue (CoAl_2O_4) and the blue pigments having the general formula: $\text{AAl}_{12-x}\text{M}_x\text{O}_{19}$ (where $\text{A} = \text{Ca, Sr, Rare Earths, M} = \text{Ni}$ or Ni coupled with one of the following: $\text{Ti, Sn, Ge, Nb, Ta, Sb}$). Ni-containing hibonite pigments have higher NIR reflectance than Co-based pigment. However, the authors employed cobalt (III) oxide and nickel(II) oxide: both compounds have a harmful effect on human and aquatic life. On the other hand, the advantages are the lower cost and the higher NIR reflectance with respect to conventional CoAl_2O_4 . The coordinates of two solid solutions $\text{CaAl}_{12-2x}\text{Ni}_x\text{Ti}_x\text{O}_{19}$ ($x = 0-2$) and $\text{Ca}_{1-x}\text{La}_x\text{Al}_{12-x}\text{Ni}_x\text{O}_{19}$ ($x = 0-1$) are represented in **Table 2. 3**. The blue color of all samples shows negative values of b^* from -16.78 (in $\text{CaAl}_{10}\text{TiN}_{10.5}\text{Zn}_{0.5}\text{O}_{19}$) to -30.38 (in $\text{Ca}_{0.5}\text{La}_{0.5}\text{Al}_{11.5}\text{Ni}_{0.5}\text{O}_{19}$). The increasing amount of

impurities is accompanied by a color change from royal blue to dark turquoise. All colorimetric coordinates (L^* , a^* and b^*) decrease up to $x = 1$. The reverse trend is observed for b^* coordinate of $\text{Ca}_{1-x}\text{La}_x\text{Al}_{12-2x}\text{Ni}_x\text{O}_{19}$. The most negative value for b^* is observed for $x = 0.5$ ($b^* = -30.38$). In the case of $\text{CaAl}_{12-2x}\text{Ni}_x\text{Ti}_x\text{O}_{19}$, all the three coordinates decline to $x = 1$, after both L^* and a^* start to flatten and b^* moves towards the positive direction (blue becomes a dark turquoise). The best blue color is given by $x = 1$ in the Ti-containing samples ($b^* = -28.44$). NIR reflectance is inversely proportional to Ni content incorporated in the host material. In $\text{Ca}_{0.5}\text{La}_{0.5}\text{Al}_{11}\text{M}_{0.5}\text{Ni}_{0.5}\text{O}_{19}$, better blue coloration is achieved when the trivalent M was In^{3+} instead of Ga^{3+} . The values of b^* coordinate of the Ni-containing hibonite pigments are not as negative as those exhibited by commercial Co-blue ($b^* = -44.39$). Al, instead, resulted as the doping element able to increase the intensity of the blue shades (as confirmed by $b^* = -30.38$). $\text{Ca}_{0.5}\text{La}_{0.5}\text{Al}_{11.5}\text{Ni}_{0.5}\text{O}_{19}$ is the pigment with higher NIR reflectance ($\approx 90.00\%$). Doping with Ce seems to decrease NIR reflectance as confirmed by $\text{Ca}_{0.5}\text{Ce}_{0.5}\text{Al}_{11.5}\text{Ni}_{0.5}\text{O}_{19}$ pigment, having 66.00 % of NIR reflectance.

As described above, the most used blue pigments are based on cobalt-doped structures and they are produced by solid-state ceramic routes, but innovative approach come from cobalt based pigments synthesized by less energy consuming hydrothermal method.

2.5.3.3 Hydrothermal and precipitation route

Considering the hydrothermal method, Yurdakul and Gomez [94] reached further development on cobalt blue pigments using the hydrothermal process. Authors focused on

the production of blue-colored sintered zirconia cobalt aluminate spinel ($\text{ZrO}_2\text{-CoAl}_2\text{O}_4$) doped with Y_2O_3 . Although these authors did not consider the NIR reflective properties, previous literature reports confirmed the increase of NIR reflectance of Y_2O_3 [51,95]. The present state of the art of the hydrothermal and precipitation method indicates that there is a growing interest on NIR reflective pigments based on Co-based spinel [53,96,97].

Considering Co based pigments Liu et al [53] synthesized of kaolin/ CoAl_2O_4 pigments, demonstrating that the addition of kaolin leads to an increase in near-infrared reflectance together with a decrease in processing costs. In addition to the cost reduction, the avoidance of aggregation and the increase in CoAl_2O_4 nanoparticles formation efficiency are observed. Industrial purity kaolin was employed by Liu et al. [53] to produce the pigments. The material was dried at 120 °C for 5 h to remove water. The pigment was obtained by dispersing kaolin in deionized water and re-dispersing $\text{CoCl}_2\cdot 6\text{H}_2\text{O}$ in the obtained dispersion, with different mass ratio with respect to kaolin (0.6), (0.8) and (1.0). After 30 min of stirring, Na_2CO_3 0.5 M was added, thus reaching a pH value of 9. The precursors were washed several times with deionized water after 2 h long stirring until a neutral solution wash was reached. Finally, the compounds were dried under vacuum for 24 h at 80 °C. The obtained product consists of a precipitate of $\text{Co}_2(\text{OH})_2\text{CO}_3$ surface decorated kaolin. The calcination (from 800 °C to 1100 °C) promotes the decomposition of kaolin and $\text{Co}_2(\text{OH})_2\text{CO}_3$ in Co_3O_4 , CO_2 , H_2O , Al_2O_3 and SiO_2 . We can consider this method as a precipitation route helped by solid state reactions. In the last step, the final products were calcined at different temperatures between 800 °C and 1100 °C, for a time in the range of 1–6 h. Both NIR reflectance and colorimetric coordinates were expressed in function of

different times and calcination temperatures. Temperature close to 1000 °C promoted the decomposition of Co_3O_4 into Co, while SiO_2 and kaolin became metastable. Moreover, increasing the temperature and time of calcination, an increase in the dimension of CoAl_2O_4 nanoparticles [94] inducing melting. For kaolin/ CoAl_2O_4 pigments [94], a^* and b^* values decrease with the increasing calcination temperature from 800 °C to 1000 °C, while L^* has an opposite trend (Table 2. 3). Increasing the calcination temperature to 1100 °C, L^* decreases to 38.29, a^* increases (-9.21), and b^* decreases (-38.90). For the pigments calcined at 1100 °C, an increase in the blue component up to 39.06 (at 6 h) from -23.18 is observed. Increasing the calcination time, also L^* decreases progressively, producing a deeper blue. Using different calcination temperatures, NIR reflectance showed a relevant increase from 19.80 % (800 °C) to 60.18 % (at 1100 °C). The rise in calcination times affects the NIR reflectance value. After 6 h of calcination at 1100 °C the NIR reflectance changes from 55.72 % to 60.49 %. Increasing the temperature from 800 °C to 1000 °C the NIR reflectance value of the final product is increased from 19.80 % to 55.51 %; on the other hand, the colorimetric coordinates a^* and b^* decrease towards the most saturated hues. The same trend of NIR reflectance and colorimetric coordinates is observed for the increased time of calcination. After 6 h of calcination, the NIR reflectance reaches a maximum. Authors underlined that prolonging calcination times to 6 h does not change spinel particle dimensions. Consequently, the best NIR reflectivity properties are obtained without a higher cost in energy and time. As pointed out by Liu et al. [53], one of the synthesis route to produce CoAl_2O_4 blue is the solid-state method which implies the use of cobalt chloride hexahydrate ($\text{CoCl}_2 \cdot 6\text{H}_2\text{O}$) and gibbsite ($\text{Al}(\text{OH})_3$) as precursors. The pigment obtained by the authors

resulted agglomerated. The authors demonstrated that employing natural available kaolinite ($\text{Al}_4(\text{OH})_8\text{Si}_4\text{O}_{10}$) as aluminum source (cheap and a rich in aluminum (45 %)) [53], agglomeration problems are avoided. Yurdakul and Gocmez [94] further developed cobalt blue pigments using the hydrothermal process. Authors focused on producing of blue-colored sintered zirconia cobalt aluminate spinel ($\text{ZrO}_2\text{-CoAl}_2\text{O}_4$) doped with Y_2O_3 . Although these authors did not consider the NIR reflective properties, previous literature reports confirmed the increase of NIR reflectance of Y_2O_3 [51,95]. The pigment was obtained preparing a 2 M solution of zirconium acetate in acetic acid. 3 mol % yttrium chloride hexahydrate ($\text{YCl}_3\cdot 6\text{H}_2\text{O}$) and 1.75 M urea ($\text{CH}_4\text{N}_2\text{O}$) were added dropwise into the prepared solution. For the production of the blue color, 0.15 g metal chloride ($\text{CoCl}_2\cdot 6\text{H}_2\text{O}$) was incorporated into the homogeneous mixture. When cobalt oxide-containing powder is heat-treated at high temperatures, volatilization of CoAl_2O_4 occurs. 0.23 g aluminum chloride (AlCl_3) was used to form the stable CoAl_2O_4 spinel structure. The hydrothermal reaction was performed in PTFE reactor after homogenization of the solution. Powders were obtained after 12–24 h at 20 bars pressure. Heat treatment was then applied at 150 °C. The synthesized powder was washed several times in water and ethanol until the detection of Cl^- ions by silver nitrate. In this case, the addition of ethanol reduces the capillary forces and the agglomeration of powder is reduced. The two procedures described, developed respectively by Liu et al. [53] and Yurdakul and Gocmez [94], decrease the production costs of the pigments thanks to: (i) the use of lower temperatures compared to the solid state route and (ii) the use of relatively cheap raw materials. However, cobalt is still present in these compounds [98].

2.5.3.4 Advantageous aspects of the synthesis processes

The blue pigments produced by the sol-gel route starting from rare earth's precursors seem to show interesting advantages in terms of used raw materials and employed energies.

Although the literature on blue pigments is not so comprehensive, few of the literature reports recalled in this manuscript show promising results. The procedure developed by Jose et al. [51] involves low amount (≈ 0.4 g) of rare earth precursors (Y_2O_3 , In_2O_3). The citrate sol-gel route applied by Jose et al. [51] is interesting for the favorable compromise between the temperature and time of the two thermal treatments (dry and calcination) and for the quality and homogeneity of the particles produced. The first heat treatment, which aims to decompose nitrates, has been set at 250 °C for 2 h, and the final calcination required 2 h at 850 °C.

For blue pigments, significant results are obtained using solid-state routes. This is mainly because this route is involved in the realization of pigments requiring low amounts of reagents, shorter processing time, and lower calcination temperatures, than yellow and red pigments [67]. Egyptian blue obtained by Jose and Reddy [67] implies the use of relatively low temperature (950 °C for 16 h) in a single calcination step. Other optimization of the solid-state route is characterized by using a single calcination step, as shown by Schildhammer et al. [72] and Raj et al. [73]. In the last two studies a single step of calcination was used, at 1350 °C for 20 h and 1500 °C for 12 h respectively. Similarly, the hydrothermal method seems promising in terms an employment of low energy. Considering the case of Liu et al. [53], a cost decrease in raw materials was achieved using kaolin. The use of

transition metals for hydrothermal route did not produce significant improvement for the use of temperature higher than 1000 °C and also for the use of Co-based precursors [94]. The synthesis of rare earth based pigments by precipitation or hydrothermal route is not employed, according to our literature survey. Clay minerals could be a cost-effective source of chromophore elements (Al) but this kind of precursors is not used in sol-gel, probably due to the possible production of by-products and the difficulties of obtaining a fixed stoichiometry. Solid-state seems not a cost-effective process due to the high temperatures involved. For this reason, the application of clay minerals in solid-state route is limited.

2.5.4 An evaluation of the best synthesis techniques

For each discussed color, rare earths based compounds are demonstrated to be extremely important to developing effective NIR reflective pigments. However, it was suggested by many different literature references that also Al, Bi, PO_4^{3-} , and Fe play a significant role. The first three elements are able to increase NIR reflectance. Bi is also a good chromophore for yellow hues. Fe seems to decrease NIR reflectance but is a confirmed red chromophore. In addition, Al is confirmed as a good chromophore, giving intense blue shades. Clay minerals are a widespread class of starting materials to synthesize pigments with good processing properties. This group of minerals is rich in Al and PO_4^{3-} , which resulted able to improve color appearance and NIR reflectance.

Because of the analyzed literature, the industrial and academic research trends on NIR reflective pigments synthesis are focused on finding environmentally friendly

processes using no toxic reagents. However, many synthesis routes aiming to reduce toxic reagents, such as Cr and Co based compounds, are still unable to avoid using such materials.

2.5.5 Environmentally friendly syntheses route of Near Infrared (NIR) Reflective pigments

As pointed out by literature reviews of pigments listed in tables, there is a lack of an in-depth study concerning the state of the art of the progress in the specific field of environmentally friendly NIR reflective pigments.

Based on the overall evaluation of the up-to-date literature, promising results in optimization of synthesis route come from the hydrothermal method [75,84] and the sol-gel as synthesis route [61,70,99]. As confirmed by Rosati et al.[100] and Jose et al.[63] both method imply low temperatures, short times, and starting materials are non-toxic precursors.

2.5.5.1 Hydrothermal synthesis

The term, hydrothermal, originated from geology, beginning during the mid-19th century when geologists simulated hydrothermal conditions to study the formation of certain minerals and rocks. On this basis, hydrothermal methods started to be applied to single crystal growth; powder preparation has been developed for nearly 200 years [101]. The hydrothermal method refers to the use of an aqueous solution as a reaction system in a special closed reaction vessel (**Figure 2. 1**) to create a high-temperature, high-pressure

reaction environment by heating the reaction system and pressurizing it (or the vapor pressure generated by itself). The process dissolves and recrystallizes a substance that is poorly soluble or insoluble under normal conditions [102]. The general preparation steps of the hydrothermal method [103] are described below and shown in **Figure 2. 1**.



Figure 2. 1. General steps for hydrothermal preparation.

1. In the first step the reactants are dissolved in the hydrothermal medium and enter the solution in the form of ions or molecular groups;
2. Second, the ions or molecules are separated by the temperature difference between the upper and lower portions of the kettle. The ions or molecular groups are transported to the low-temperature region, where the seed crystal is grown to form a supersaturated solution;
3. Third, the ions or molecular groups are adsorbed, decomposed, and desorbed at the growth interface;

4. Fourth, the adsorbed material moves at the interface. Finally, the dissolved matter crystallizes. The crystal morphology of crystals under hydrothermal conditions is closely related to the growth conditions [104,105].

Powder of oxides with high purity, narrow particle size distribution, phase homogeneity and a high degree of crystallinity can be produced through a hydrothermal process. Hydrothermal synthesis of powder oxides offers many advantages over other powder preparation methods.

First, it provides a means for preparing anhydrous oxides in a single step. Second, the combined effect of pressure and temperature can reduce free energies for various equilibrium stabilizing phases that may be stable under atmospheric conditions. However, hydrothermal processes can be utilized with expensive apparatus. The hydrothermal method has great scope for the preparation of multiple oxide phases, i.e. containing two or more metals, where the rapid mixing of the constituent elements would provide a great synthetic advantage, as well as potentially leading to the discovery of new materials [106]. For example, nano-crystalline praseodymium-doped ceria powders were prepared for the first time by a microwave-assisted hydrothermal route [107]. Hydrothermal method, which involves low temperatures and a wet chemical technique, offers the possibility for synthesizing high-purity, homogeneous, and ultrafine powders. In particular, the use of microwaves as the heating source may offers benefits in terms of cost savings through the reduction in processing time and energy. It may results in an improved yield of the obtained compounds [108].

Together with the high cost of autoclave a limit of hydrothermal route is related to the difficulty related of controlling the crystal growth [73,109].

Unlike the hydrothermal method, the sol-gel process is a wet chemical process, having some peculiarities that demonstrate its efficiency. Its efficiency is in the intimate mixing of components, which ensures homogeneity of the final product. In terms of energy cost temperatures and times of sol-gel route are lower than hydrothermal method [100].

During the last 30 years, sol-gel processes have been widely used for the preparation of glasses and ceramics. Usually, starting with molecular precursors like alkoxides/acetates/nitrates, the sol-gel process takes place in solution [92]. This provides definitive homogeneity for multi-component systems. In the particular case of doping, the sol-gel process offers an ideal way to control the level and the homogeneity of doping. As the name implies, the sol-gel process involves the evolution of inorganic networks through the formation of a colloidal suspension (sol) and gelation of the sol to form a network in a continuous liquid phase (gel).

2.5.5.2 Sol-Gel Synthesis

For the preparation of mixed oxide nano-pigment particles, the sol-gel method offers great advantages compared to the conventional solid-state method and hydrothermal route. Aside from precursor preparation, the picture below shows the schematic diagram of the sol-gel method (**Figure 2. 2**).

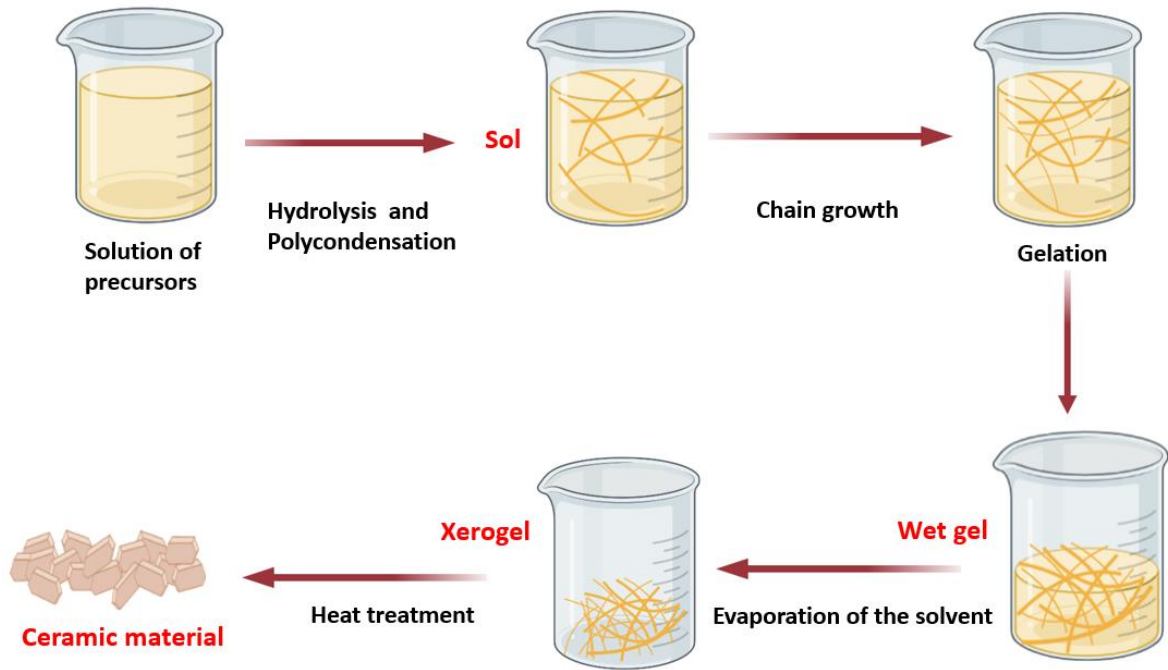


Figure 2. 2. Schematic representation of sol-gel process.

1. Preparation of the solution of precursors;
2. Hydrolysis and partial condensation of alkoxides to form a sol;
3. Formation of the gel via polycondensation of hydrolyzed precursors;
4. Drying. The gel forms a dense “xerogel” (solid formed from a gel by drying, which is accompanied by shrinkage) via the collapse of the porous network caused by the evaporation of the solvent (or an aerogel for example through supercritical drying);
5. Calcination to obtain mechanically stable materials.

The parameters that could be controlled in the sol-gel method includes (1) concentration and type of precursor, (2) nature of solvent, (3) pH of the solution, (4) type and concentration of additives (catalysts, surfactants, structure directing agents), (5) pre- and post-heat treatment of the materials, and (6) aging time.

Most of the examples of alkoxide-based sol-gel chemistry involve early transition group metals (M= Ti, Zr) or p block metals (M= Al, Si) however there are many other examples of elemental alkoxides (as rare earths as Y, In, La) [51,110]. The sol-gel chemistry of metal is typically driven by either acid or base catalysts as the neutral reaction is very slow. The structure of the resulting gel is significantly different depending on the catalyst which affects the relative rates of the hydrolysis and condensation reactions. Hydrolysis results in the replacement of an alkoxy group with a hydroxyl with a pentacoordinate transition state in both the acid and base catalyzed systems. Depending on the conditions and the metal/H₂O ratio, more than one alkoxy group may be hydrolysed. The rate of each hydrolysis step depends on the stability of the transition state which in turn depends on the relative electron withdrawing or donating power of -OH versus -OR groups.

Condensation follows a similar pattern, being catalyzed by either acid and resulting in the formation of siloxane bonds (or metaloxane bonds for other metals). The condensation reaction occurs in parallel with the hydrolysis reaction: the partially hydrolyzed alkoxide

molecules may either react with another OH⁻ bearing species by removing water or react with alkoxy group producing an alcohol molecule.

The hydrolysis and polycondensation reactions lead to the formation of clusters that bind to each other to form a single three-dimensional polymeric network called gel, at which the viscosity is observed to increase abruptly [111]. Due to the high electronegativity of oxygen respect to the metal, the M-O-C are highly polarized and hydrolysis rates are high. Instead, in case of non-metal alkoxides, the rates of hydrolysis rate are slower. In multicomponent systems (mixed oxide preparation), the different hydrolysis rates of the precursors can cause the gelation to occur at different times.

This problem can be overcome by modification of the hydrolysis rate of the most reactive precursors with the use of reaction inhibiting agents (chelating agents) and by enhancing the hydrolysis rate of the most reactive precursors through catalyzed (acidic or basic) pre hydrolysis [92].

The wet gel obtained from hydrolysis and the polycondensation of the alkoxide undergoes a drying process and an appropriate heat treatment to obtain the material with the required final properties. In the drying process, the wet gel is heated at the temperature of about 100 °C allowing the desorption of water and alcohol physically bounded. The transformation of wet gel into a dry gel by a simple evaporation leads to a deformation of its primitive porous backbone and it is often accompanied by the formation of cracks [90][112]. The driving forces for shrinkage include chemical effects, such as condensation reaction, and physical effects, such as capillary pressure. If the pressure in the liquid were

uniform, the lattice would be uniformly compressed and there would be no tendency to fracture. The low permeability of the gel, on the other hand, generates a pressure gradient, the difference in the contraction speed between inside and outside the gel is responsible for the formation of fractures [112]. The product of this uncontrolled drying is called xerogel and, in the absence of structure-directing agent, it is characterized by disordered porosity. Warping and cracking phenomena can be cushioned by aging the gel. The chemical reactions that lead to gelation are shown to continue long after the formation of the wet gel, causing changes in the physico-chemical properties of the gel. The formation of new crosslinks produces shrinkage (syneresis) and increases also the viscosity of the gel, so that aging reduces the subsequent shrinkage during drying [111]. Aerogel is obtained from gels in which the pore liquid is replaced by air with moderate shrinkage of the matrix. This is commonly obtained at the supercritical drying (SCD) condition, leading to minimal impact on the porous structure. The subsequent heat treatment depends on the type of product desired. Generally, the dry gel is heated to temperatures in the range of 300–500 °C to remove residual organics. Calcination often results in more mechanically stable materials, but sintering can cause the density of the materials to increase and the pore volume and surface area to decrease [113,114].

Compared with the conventional ceramic route, as solid state route, the sol-gel exhibits many advantages: the low process temperature, the high control of purity, composition, microstructure and textural properties of the final material [115,116]. A homogeneous gel can be obtained from a solution of the appropriate precursors, usually alkoxides. The homogeneousness of the gel guarantees a significant reduction in the

synthesis temperature of the mixed oxide phases. Solid state diffusion during calcination is not needed and the aggregation of particles is limited. The major disadvantages of using the metal alkoxide-based sol-gel processes are their moisture sensitivity and the unavailability of suitable commercial precursors, especially for mixed-metal oxides. The sol-gel synthesis of mixed oxides from alkoxide mixture usually suffers from different hydrolysis susceptibilities of the individual components and the benefits of improved homogeneity can be lost during the hydrolysis of the alkoxides, which may ultimately lead to component segregation and mixed phases in the final materials. Recently developed non alkoxide sol-gel route involving the use of an epoxide as a gelation agent requires relatively few steps to obtain metal oxides and is low temperature and low-cost [109]. This simple and effective route for preparing agglomerate-free, homogeneous nanopigments through a non alkoxide sol-gel synthesis, demonstrates the versatility of the epoxide addition method, which can be used for the preparation of a variety of mixed metal oxides of transition, rare-earth, and main group elements.

However, based on up to date literature, the sol-gel route is confirmed as the best synthesis route being environmentally friendly, cheap and leads to the formation of pure and homogeneous products.

As specified before, during the mixed oxide preparation the different rates of hydrolysis of the precursors can cause the gelation to take place at different times, in mixed oxide preparation. To overcome this problem a chelating agent as the citric acid represents

a common strategy. This approach is called the “citrate sol-gel method”. Citrate sol-gel route reduces the particle size and promotes more uniform distribution of ions in oxides [117].

Citric acid is a weak triprotic acid, which means it has three acidic hydrogen atoms in its structure, as you can see below (**Figure 2. 3**). Citric acid has three carboxylic acid moieties that can dissociate according to the following step manner:

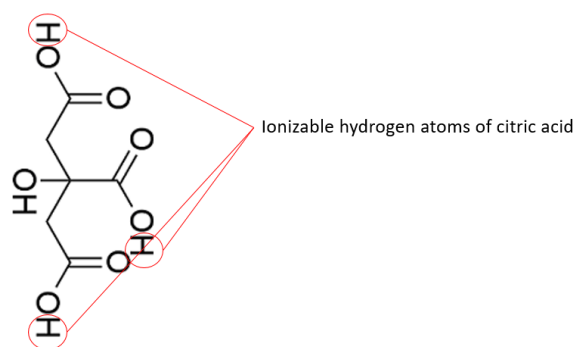
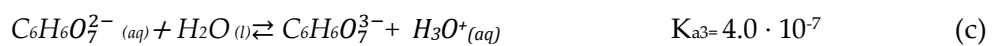
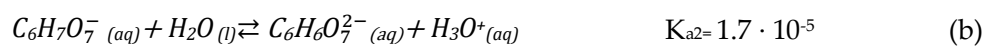
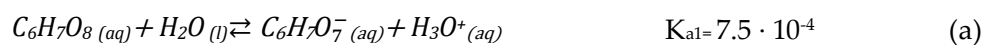


Figure 2. 3. Citric acid structural chemical formula.

Citric acid has three carboxylic acid moieties that are able to dissociate according to the following step manner:



Each of these three steps has a different value for the acid's dissociation constant, K_a .

Notably all three dissociation constants are smaller than 1, which is characteristic of a weak

acid. Another interesting observation is that the dissociation constant for step (c) is very small, meaning that the number of acid molecules that undergo ionization in this stage is, for all intended purposes, zero. In a typical synthesis, aqueous metal salts (e.g. nitrates) are mixed with citric acid and the resulting solution is heated to form a viscous solution or gel. Some reports describe the addition of bases such as ammonia or ethylene diamine to modify the pH and enhance cation binding to the citrate. The homogeneity and stability of metal citrate solutions can thus depend strongly on pH. Therefore, the addition of acidic or basic solutions is important to prevent the precipitation of individual hydroxides. Conversion of the gel to a metal oxide is simply achieved by pyrolysis in air, with the maximum temperature depending on the specific system. The method has been used to synthesize binary, ternary, and quaternary metal oxides in both crystalline and amorphous forms. The citric acid is responsible for increased homogeneity of the obtained dried gel precursor with respect to the othersol-gel routes [118,119]. During the formation of metal-oxo networks the citric acid avoids segregation of cationic species and/or preferential hydrolysis kinetics of individual metal precursors. As the metal–citrate ‘gels’ are heated, the organic component undergoes combustion at ~300–400 °C, depending on the metal counter ion and presence of additives. The role of citric acid is also to ensure that when nucleation occurs in its first stage, the metals are evenly dispersed and numerous, ensuring a small crystallite size. When ternary or quaternary systems are synthesized the citric acid ensures also that different metals remain mixed on atomic scale [92]. A lot of crystalline phases, having a complex stoichiometry, corresponding to ternary or quaternary systems, are synthesized by citrate sol-gel route, as pyrochlore-type structure [120,121] (having general formula $A_2B_2O_7$, where

the A cations are often rare-earth elements, while B cations can be transition metals elements in group IVB, VB, VIB, VIIB and VIII or non-transition elements in group IVA). Also garnet based pigments structures [122,123], in particular Yttrium Iron Garnet (YIG), [124] having the chemical composition $Y_3Fe_5O_{12}$ or Yttrium Aluminum Garnet (YAG, $Y_3Al_5O_{12}$) [125] were synthesized by citrate sol-gel. Of course citrate sol gel route has made possible synthesis of compounds with more complex stoichiometry than ternary or quaternary systems, as cobalt chromite pigments doped with Zn or Al. An example of pigment having complex stoichiometry is made by pigment synthesized by Hedayati et al. [56] having the following formulation: $Co_{1-x}Zn_xCr_{2-y}Al_yO_4$. In the optic of an environmentally friendly synthesis of near infrared reflective pigments the citrate sol-gel route is revealed to be a smart solution in terms of times, temperatures and starting reagents for $YInO_3$ based pigments, which are revealed to be highly performing NIR reflective pigments [69,90].

2.5.5.3 Pigments based on $YInO_3$

Pigments based on $YInO_3$ formulation were developed by Smith et al.[90]. They obtained the chemical compound by heating manganese trioxide (Mn_2O_3) with the oxides of yttrium (Y_2O_3) and indium (In_2O_3) to about 1100 °C. The initial idea was to synthesize a new class of oxides for applications in electronics as magnetic capacitors. The obtained product ($YIn_{1-x}Mn_xO_3$) did not have the required ferromagnetic properties, but Subramanian, noticed that the compound, of a bright blue color, showed high infrared radiation reflection [69]. Commercial inorganic blue pigments, such as cobalt blue ($CoAl_2O_4$), ultramarine ($Na_7Al_6Si_6O_{24}S_3$), Prussian blue ($Fe_4[Fe(CN)_6]_3$) and azurite

[Cu₃(CO₃)₂(OH)₂] suffer from environmental and/or durability issues [90]. Cobalt exerts documented toxic effects discussed above [56]. Ultramarine and azurite are thermally unstable and decompose under acidic conditions. Prussian blue liberates HCN in diluted acids. Furthermore, manufacturing some of these pigments causes environmental pollution [90]. The intense blue color was obtained introducing Mn³⁺ into the trigonal bipyramidal (TBP) sites of hexagonal YInO₃, although YInO₃ and YMnO₃ end members are white and black.

YInO₃ and YMnO₃ can crystalize in an acentric hexagonal structure (*P6₃cm*) consisting of alternating layers of edge-shared YO₆ octahedra and corner-shared MO₅ (M = In, Mn) trigonal bipyramids (**Figure 2. 4**).

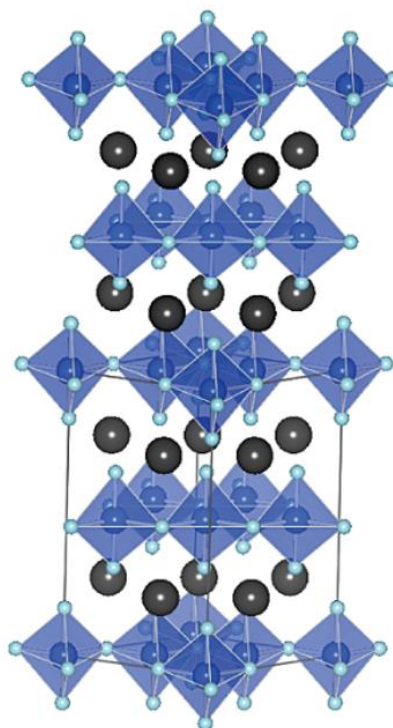


Figure 2. 4. Hexagonal structure of Y(In,Mn)O₃ obtained by Smith et al. [90] (Adapted from Figure 1 of reference [90]).

Hexagonal structure differs strongly from the ideal cubic and distorted orthorhombic perovskite and is generally stabilized for small enough R cation in $RMnO_3$ (where R is lanthanides smaller than Tb^{3+} , Sc^{3+} and Y^{3+}). The Mn cations adopt a fivefold trigonal bipyramidal coordination contrasting with its octahedral coordination in the classical perovskite structure [126,127]. Accordingly, the framework of the hexagonal phase (space group $P6_3cm$) is built from the stacking along the c -axis of layers built of corner sharing (MnO_3) trigonal bipyramids. This coordination of Mn leads to a crystal field splitting, different from the octahedral one, with an unoccupied dz^2 orbital hybridized with the p_z orbital of oxygen along the c -direction. Only few reports describing substitutions at the Mn-site in $YMnO_3$, which preserve the hexagonal structure.

As for the substitution of cobalt for manganese in $YMnO_3$, the solubility range is important, the structure transforms to an orthorhombic when Co is equal to 0.15 in $YMn_{1-x}Co_xO_3$ [128]. This is related to the ionic radius as underlined by Moure et al. [128]. The incorporation of large cations such as Ca^{2+} , can cause a transition to an orthorhombic structure. The transition from orthorhombic to hexagonal in the case of Ca^{2+} is also related also to the cation dimension [128]. Is in general valid that a pigment made by an oxide of manganese and rare earth, having the general structure $REMnO_3$ (where RE consists in rare earths) crystallizes in orthorhombic structure, perovskite-like structure (space group $Pnma$), if the rare earth ionic radius is large enough. Thus, $REMnO_3$ oxides with $R = La, Pr, Nd$, are orthorhombic, whereas the $RMnO_3$ manganites for R equal to Y, Tm, Yb, Lu, Er with an ionic radius smaller than that of Dy usually crystallize in a hexagonal structure (space group $P6_3cm$) [69]. Replacing Y^{3+} with other rare earth cations resulted in complete solid solutions

of $\text{REIn}_{1-x}\text{Mn}_x\text{O}_3$ (where RE consists in Dy, Ho, Er) with similar blue color. Substitutions at the Y^{3+} site with small amount of Ca^{2+} or rare earth elements have little impact on the color. Inspired by the success of intense $\text{Y}(\text{In},\text{Mn})\text{O}_3$ blue, Tamilarasan et al. [129] reported a series of metastable purple oxides $\text{YGa}_{1-x}\text{Mn}_x\text{O}_3$ that were prepared by a modified Pechini or sol-gel method as the procedure described by Rusakov et al.[130]. Hexagonal solid solutions of $\text{InMn}_{1-x}\text{Ga}_x\text{O}_3$ prepared using a high-pressure technique show blue colors for compositions with low Mn content [130].

Mn content substitution with Al maintains the hexagonal structure [131] (the obtained pigment has the following formulation, $\text{YAlO}_3\text{-YMnO}_3$) but the color is not a brilliant blue navy as $\text{Y}(\text{In},\text{Mn})\text{O}_3$ blue [131]. The $\text{YAlO}_3\text{-YMnO}_3$ system was explored in consideration of replacing indium with cheaper aluminum for making Mn-containing blue pigments. However, by solid state route was produced a pigment with only poor Al amount ($\text{YAl}_{1-x}\text{Mn}_x\text{O}_3$, where $x \geq 0.9$). By sol-gel route was obtained a complete solution of $\text{YAl}_{1-x}\text{Mn}_x\text{O}_3$ ($x = 0\text{--}1$).

The blue color obtained by Li et al. [131] was not the only attempt to obtain different shades modifying a doping element. Introducing Fe^{3+} into the hexagonal YInO_3 system Jiang et al. [132] discovered new solid solutions of $\text{YIn}_{1-x}\text{Fe}_x\text{O}_3$. The color of these phases varies from yellow, orange to dark red with increasing Fe content. New solid solutions of $\text{YIn}_{1-x}\text{Fe}_x\text{O}_3$ were prepared, starting from metal nitrate solutions using citric acid as a chelating agent, and by solid state route [132]. In this case, sol-gel route is demonstrated to be a promising route synthesis to obtain YFeO_3 hexagonal phase for its low temperature of the

final calcination (700 °C) process [133], respect to the solid state method [132] (1500 °C). A significant development in $Y(\text{In,Mn})\text{O}_3$ was achieved by a double substitution of $\text{Cu}^{2+}/\text{Ti}^{4+}$ into the TBP sites of hexagonal TBP resulting in solid solutions of the type $\text{YM}_{1-x}(\text{Cu}_{0.5}\text{Ti}_{0.5})_x\text{O}_3$ with green colors [134]. The green color of $\text{YCu}_{0.5}\text{Ti}_{0.5}\text{O}_3$, obtained by Smith et al. [134], was found to be enhanced by minor substitutions of In, Al, and Ga. The structure of $\text{YCu}_{0.5}\text{Ti}_{0.5}\text{O}_3$ is the same as that of hexagonal YMnO_3 . Even if Cu^{2+} and Ti^{4+} occupy the TBP sites in a disordered manner, the d^9 electronic configuration of Cu^{2+} favors the TBP position through crystal field stabilization. A main difference in $\text{YCu}_{0.5}\text{Ti}_{0.5}\text{O}_3$ respect to the YMnO_3 structure is related to the difference in apical distance between Cu^{2+} and O^{2-} and Ti^{4+} and O^{2-} . Unlike the situation in YMnO_3 , the two apical distances are different. One is reported to be about 1.85 Å and the other about 1.96 Å, based on the atomic coordinates given. These alternating short and long distances along the c axis might be attributed to the known tendency of Ti^{4+} for such behavior. This difference in apical distance produces a distortion that is absent in YMnO_3 pigments.

YInO_3 and YMnO_3 can also have other two polymorphic structures: cubic and orthorhombic polymorphs. The metastable orthorhombic phase is obtained under high-pressure conditions or with special synthesis techniques as glycine–nitrate process [135] which implies temperatures higher than 1000 °C [135]. The cubic polymorph is also obtained with energy consuming synthesis routes such as pyrolysis of aerosols, in terms of employed temperatures [136].

Hexagonal phase synthesized by Smith et al.[90] reveal to be suitable for NIR reflective pigments, having high values of near infrared reflectance [137,138], and more exploitable as a colourful pigment. Hexagonal phase of YInO_3 aimed to be doped with elements that can act as chromophore agents or change NIR reflectance, obtaining different pigments starting from the same base formulation, as demonstrated by works discussed above [128,130–133]. Doping elements show complete miscibility in YInO_3 hexagonal phase for the similar distance between In–O and doping elements (as Mn, Cu, Ti, Ga) –O in the basal plane [69]. The large ionic radius difference between In^{3+} and Mn^{3+} affects only in the apical distances. So even if Mn^{3+} , or others doping elements, have large size differences with respect to the In^{3+} , can be hosted in trigonal bipyramidal coordination. The trigonal bipyramidal structure allows for metal specific apical bond distances of doping element and In which results in a systematic progression of color upon increasing Mn^{3+} concentration [90,139].

With the extremely wide range of doping elements, influencing colors and NIR reflectance, the sol-gel route has pushed to further development on the development on the synthesis of YInO_3 class of pigments.

2.6 Review on colorimetry fundamentals

Premise: The author considered appropriate to anticipate the section dedicated to materials and methods through a review on colorimetry, since the instrumental apparatus was used not only to measure parameters such as color coordinates but also for a spectral analysis.

Several systems for expressing color numerically were developed by an international organization concerned with issues of lighting and color, the International Commission on Illumination (CIE). One of the best known of these systems is the $L^*a^*b^*$ color space (also referred to as CIE $L^*a^*b^*$) devised in 1976 [68], represented in **Figure 2. 5**. According to this space, L^* is the lightness axis (black (0) white (100)), a^* is the green (-) to red (+) axis, and b^* is the blue (-) to yellow (+) axis. The center is achromatic, as the a^* and b^* values increase and the point moves out from the center, the saturation of the color increases.

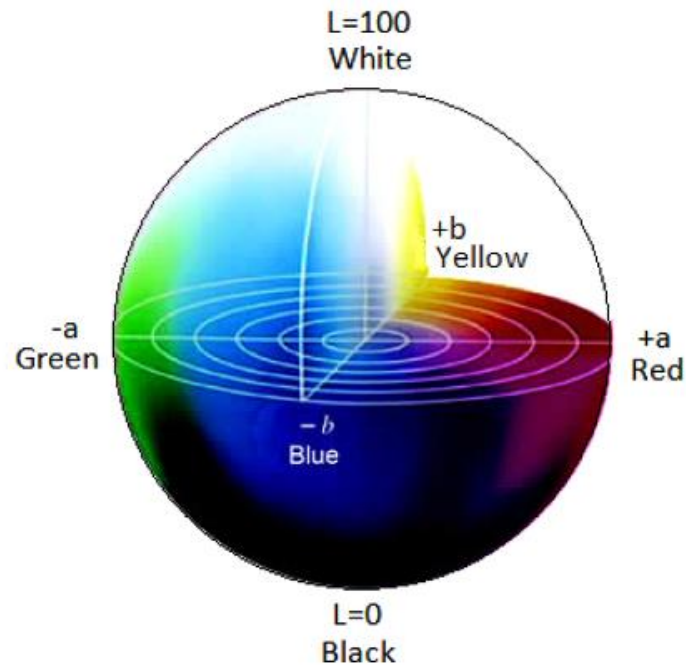


Figure 2. 5. CIE-1976 $L^*a^*b^*$ 3d Color Space [140].

The color is represented by a point in this space, which allows high precision in the definition of this one. The values of L^* , a^* , and b^* are proportional to the tristimulus values XYZ [141] and to X_n , Y_n and Z_n , which are the tristimulus values XYZ of a perfect reflecting diffuser, set by the CIE in 1931, as seen in the transfer Eq (3.1-3):

$$L^* = 116 x \left(\frac{Y}{Y_n}\right)^{1/3} - 16 \quad (3. 1)$$

$$a^* = 500 \left[\left(\frac{X}{X_n}\right)^{1/3} - \left(\frac{Y}{Y_n}\right)^{1/3} \right] \quad (3. 2)$$

$$b^*=200\left[\left(\frac{Y}{Y_n}\right)^{1/3}-\left(\frac{Z}{Z_n}\right)^{1/3}\right] \quad (3.3)$$

2.6.1 Principle of colorimetry and spectrophotometry

The principle of colorimetry is based on the tristimulus method [142]. Each color is the combination in different proportions of red, green and blue. A colorimeter provides numerical data representing the measured sample and a color difference in comparison to a standard sample [143].

For one color, the colorimeter gives the percentages of the three primary colors. A set of three sensors filtered to have nearly the same color sensitivity as the human eye, receive light from the object and transmit the information to the data process or that determines the tristimulus values XYZ by the standards of the CIE. In a colorimeter, the light source typically illuminates the sample at an incidence angle of 45°. The reflected light from the sample is collected and passed to a detector, which consists of the three colored filters.

Multiple spectral sensors receive light from the object and transmit the information to the microprocessor. For each wavelength in the visible light range, the spectral reflectance is measured. Spectral reflectance is measured for each wavelength in the visible light range. From the spectral data, the tristimulus values XYZ are calculated by integration, in microprocessor and then can be converted to other color space. **Figure 2. 6** illustrates a colorimeter's essential components, including, which include an illuminant, colored filters.

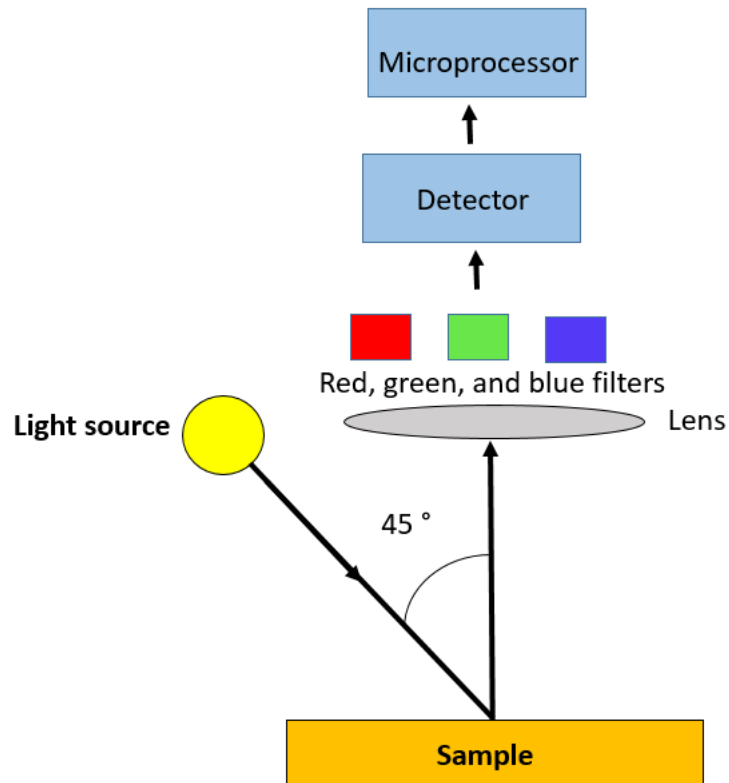


Figure 2. 6. Operating principle of colorimeter.

As it can be seen from **Figure 2. 6** the sample absorbs the wavelengths and reflects the light. The reflected light that is captured by the colorimeter is filtered through the trichromatic filter of red, green, and blue chroma.

Colorimeters are usually easy to operate, inexpensive, and fast [144]. However, they are limited to a single illuminant observer combination. Hence, it is impossible to determine features as metamerism (two colors appear to correspond with a lighting condition and instead appear different when the light changes).

In addition to displaying numerical color data, a spectrophotometer represents data of a spectral reflectance graph numerical color data, a spectrophotometer represents data of

a graph of the spectral reflectance to provide more detailed information about the nature of the color.

The spectrophotometer is similar to a colorimeter. In addition to extrapolating the tristimulus values of a sample, the spectrophotometer measures the complete spectral composition of light between 360 and 700 nm. Spectrophotometers are equipped with the spectral power distributions of a wide range of illuminants and thus can display color differences not noticeable to the naked eye using one of the standard illuminants. Differently from colorimeter when the spectrophotometer performs the measurement the reflected light is captured by the device, and wavelengths between 360-700 nm are processed by the monochromator which measures the light in different wavelengths, obtaining the color of the sample (**Figure 2. 7**). A colorimeter, instead uses the colored filters, working at fixed wavelength.

All spectrophotometers have been designed with the same basic parts: a light source, a method to separate the light spectrum, a detection system, and a microprocessor for analysis of data and calculations. The layout of the parts and how it is operated determines the optical geometry of the instrument [144]. **Figure 2. 7** shows the typical parts of a dual beam spectrophotometer.

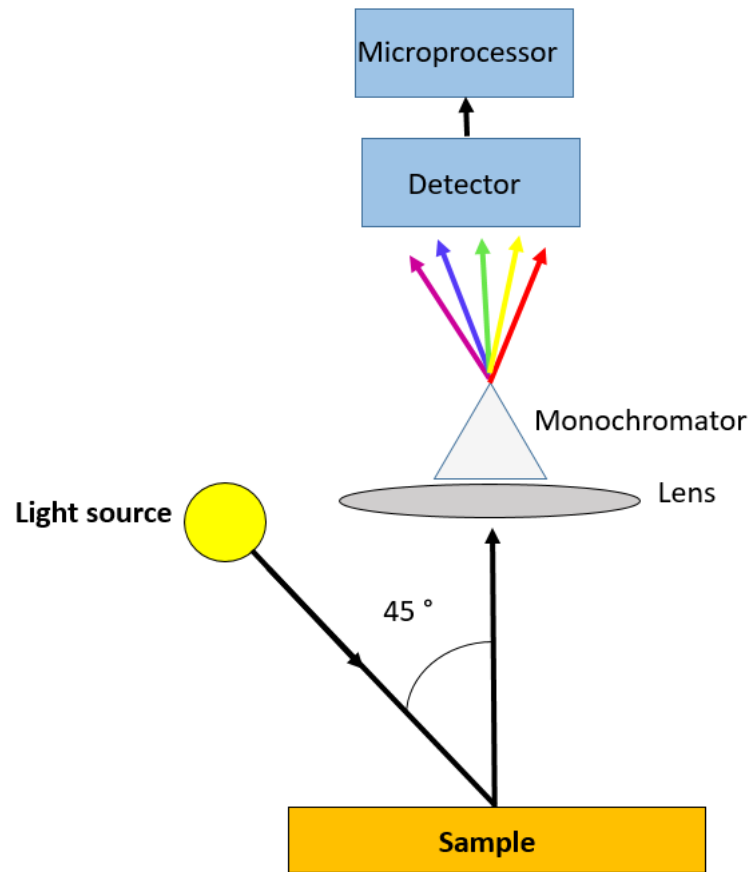


Figure 2. 7. Operating principle of spectrophotometer.

3 Materials and methods

3.1 Materials

3.1.1 Pigments precursors

Pigments were synthesized with the following reagents: Y_2O_3 (Sigma-Aldrich, 99.99 %), In_2O_3 (Sigma-Aldrich 99.99 %), ZnO <100 nm nanopowders (~ 80 % Zn, Sigma-Aldrich), and citric acid (99 %). The reagents described above were employed to synthesize the “base structure of pigments”, described in the introduction section of the thesis: $YIn_{1-x}M_xO_3$. M was the doping element that allowed to obtain different pigments. Doping elements were Mn, Fe, and Cu. The obtained pigments can be defined as coupled compounds, as was ZnO nanopowders were added to the base structure. Three different group of pigments were obtained based on the following formula: $YIn_{1-x}Mn_xO_3-ZnO$, $YIn_{1-x}Fe_xO_3-ZnO$, and $YIn_{1-x}Cu_xO_3-ZnO$.

The precursors of the three doping elements were manganese (III) acetate, $Mn(O_2CCH_3)_3$, iron chloride tetrahydrate, $FeCl_2 \cdot 4H_2O$, and copper(II) nitrate trihydrate, $Cu(NO_3)_2 \cdot 3H_2O$.

3.1.2 Coatings precursors

The obtained pigments (synthesis routes are described in the section below) were dispersed in different acrylic binders: polymethylmethacrylate (PMMA, Sigma-Aldrich), labelled as PMMA, and an industrial clear acrylic water-based paint (ALPINA, DAW Italia GmbH, Italy), labelled as Acrylic WB. The PMMA was involved in the first part of the

experiment for the dispersion of pigments, as PMMA can represent a model of acrylic paint with high transparency and resistance to solar radiation [145]. The use of a commercial industrial acrylic paint aims to test a possible application of pigments in market-ready polymeric binder.

3.2 Methods

3.2.1 Synthesis of $\text{YIn}_{0.9}\text{M}(\text{Mn, Fe, Cu})_{0.1}\text{O}_3\text{-ZnO}$ pigments

The $\text{YIn}_{0.9}\text{M}(\text{Mn, Fe, Cu})_{0.1}\text{O}_3\text{-ZnO}$ pigments were synthesized by a sol-gel method. Stoichiometric amounts of yttrium oxide (1.66 mmol), indium oxide (1.49 mmol), and zinc oxide (3.33 mmol) were dissolved in 4.0 M nitric acid (100 mL) with constant stirring at 800 rpm at 50 °C. Manganese (III) acetate (0.33 mmol) was added to obtain pigments based on the following formulation: $\text{YIn}_{0.9}\text{Mn}_{0.1}\text{O}_3\text{-ZnO}$. The copper nitrate trihydrate was used in the synthesis of the $\text{YIn}_{0.9}\text{Cu}_{0.1}\text{O}_3\text{-ZnO}$ pigments, while iron (II) chloride tetrahydrate (0.33 mmol) was put in Sol-Gel bath to obtain the $\text{YIn}_{0.9}\text{Fe}_{0.1}\text{O}_3\text{-ZnO}$ pigments. Manganese (III) acetate was used as chromophore agent by Jose et al.[51] in the synthesis of $\text{YIn}_{0.9}\text{Mn}_{0.1}\text{O}_3\text{-ZnO}$ blue pigment, and resulting a promising precursor in the optic of an environmentally friendly precursor without waste production and toxic by-products.

After 1 h, a uniform solution was obtained. A stoichiometric amount of citric acid was added with the molar ratio of 3.5:1 with respect to metals. A yellowish solution was obtained after 6 h. This resultant solution was dried at 80 °C, obtaining a dried gel. The gel was heated at 250 °C to decompose nitrates.

Finally, the dried gel was heated at different temperatures according to the decomposition temperatures and crystallization peaks shown on TGA and DSC curves, respectively. $\text{YIn}_{0.9}\text{Mn}_{0.1}\text{O}_3\text{-ZnO}$ pigments were obtained heating the dried gel at 550 °C, 800 °C and 850 °C, obtaining three different colors: ochre, cyan blue, and deep blue (**Figure 3. 1**).

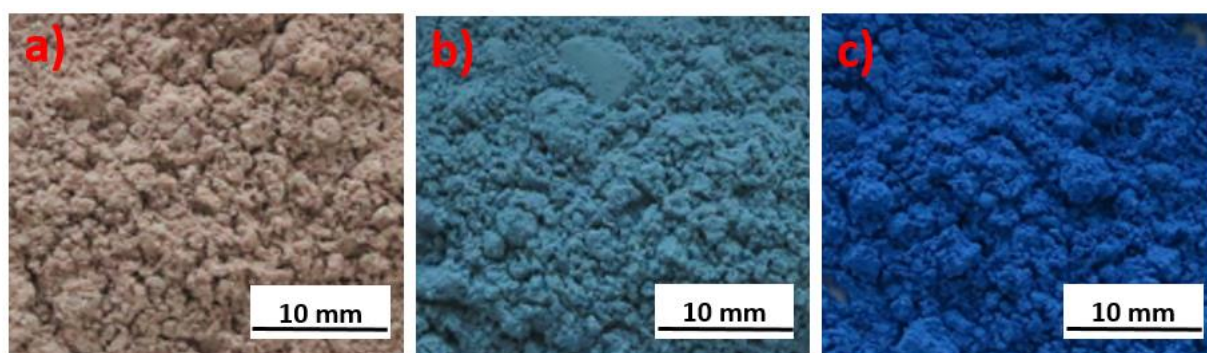


Figure 3. 1. The three different pigments (optical micrographs) having the stoichiometry $\text{YIn}_{0.9}\text{Mn}_{0.1}\text{O}_3\text{-ZnO}$ obtained calcining the dried gel at different temperatures: 550 °C (a), 800 °C (b) and 850 °C (c).

Copper nitrate trihydrate resulted of interest as possible catalyst, besides being used as a chromophore. In fact, nitrate precursors, like other oxidants, participate in the spread self-combustion of dried gel [146]. As the combustion rapidly propagates faster, the samples are burnt out completely and formed an aggregate of lightweight powders with a large number of microscopic pores [147]. The dried gel obtained was calcined at 650 °C and 850 °C. The resulting colors are two shades of pale green (**Figure 3. 2**).

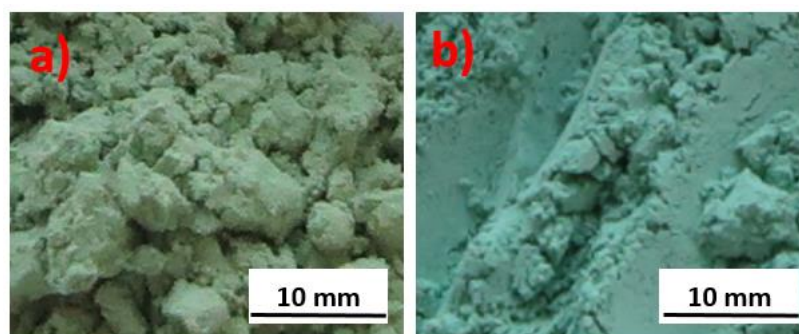


Figure 3. 2. The two different pigments (optical micrographs) having the stoichiometry $\text{YIn}_{0.9}\text{Cu}_{0.1}\text{O}_3\text{-ZnO}$ obtained calcining the dried gel at different temperatures: 650 °C (a) and 850 °C (b).

Iron(II) chloride tetrahydrate was employed as chromophore agent in $\text{YIn}_{0.9}\text{Fe}_{0.1}\text{O}_3\text{-ZnO}$ pigments as it can be considered a prototype of a low-cost and easily available material prototype. In fact, when iron metals are exposed to hydrochloric acid, crystals of $\text{FeCl}_2 \cdot 4\text{H}_2\text{O}$ are firstly formed [148,149]. The as obtained dried gel was calcined at three different temperatures: 650 °C, 750 °C, and 850 °C obtaining three different pigments (**Figure 3. 3**).

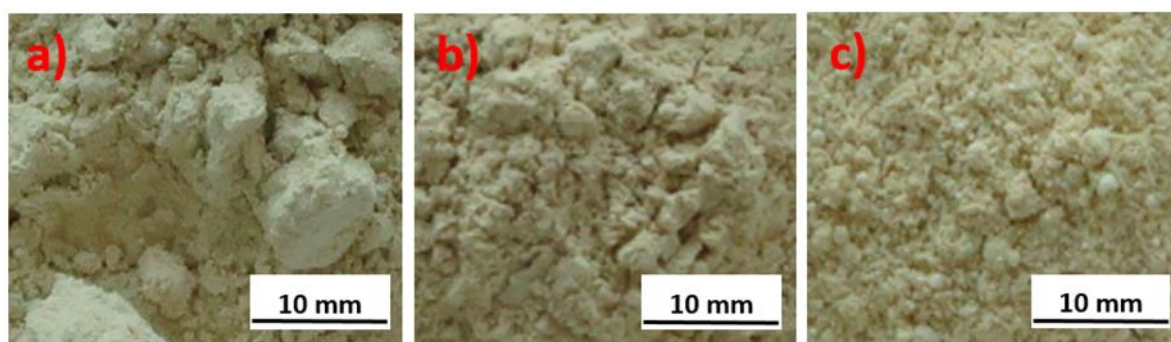


Figure 3. 3. The three different pigments (optical micrographs) having the stoichiometry $\text{YIn}_{0.9}\text{Fe}_{0.1}\text{O}_3\text{-ZnO}$ obtained calcining the dried gel at different temperatures: 650 °C (a), 750 °C (b) and 850 °C (c).

Each calcination temperature was maintained for 2 h. The dried gel's calcination was carried out in a high-temperature electrical furnace (Forno MAB, Rozzano, Mi, Italy) by heating the samples in a ceramic crucible.

Each pigment was labelled according to the name listed in the following table (**Table 3. 1**). Each pigment image was obtained by taking a photo from the same working distance, simultaneously with all pigments. All images were obtained with the same light source.

Table 3. 1. Pigments synthesized according to the different doping elements with relative labels.

Doping element	Pigments labels
Mn	YInMnO-ZnO/ 550 °C
	YInMnO-ZnO/ 800 °C
	YInMnO-ZnO/ 850 °C
Cu	YInCuO-ZnO/ 650 °C
	YInCuO-ZnO/850 °C
Fe	YInFeO-ZnO/ 650 °C
	YInFeO-ZnO/ 750 °C
	YInFeO-ZnO/ 850 °C

3.2.2 Deposition of obtained coatings from pigments

A 2 wt.% of each pigment was added to PMMA, previously dissolved in acetone, or to Acrylic WB. The polymeric paste containing the pigments was ultra-sonicated (Hielscher ultrasound technology UP400S, Teltow, Germany) for 10 min.

Aluminum alloy panels (AA5005- 0.7% Fe, 0.3% Si, 0.5% Mg, 0.2% Mn, 0.2% Cu, 0.25% Zn, 0.1% Cr, bal. Al) were used as substrates (90 mm × 150 mm × 3 mm) were used as substrate (90 mm × 150 mm × 3 mm). The substrate has been pre-treated as follows: (1) cleaning with ethanol under ultrasounds during 6 min; (2) alkaline etching in a 5 wt.%

NaOH solution at room temperature for 120 s; (3) dissolution of the sodium aluminate (formed during alkaline etching) in 34 V/V% of HNO₃ at room temperature during 60 s. After each step, the panels have been thoroughly rinsed with demineralized water. The paint was applied onto the AA5005 plates using an Elcometer 4340 Motorised Film Applicator (Elcometer, . Manchester, UK). The applied paints (PMMA and Acrylic WB) are left to dry in the air, obtaining about 100 µm dry film coating thickness.

Three coatings with the different YIn_{0.9}Mn_{0.1}O₃ZnO pigments were firstly prepared. The other set of coatings was created making a dispersion of the two pigments having Cu as doping agent. These first two sets of coatings were produced making a dispersion of pigments in PMMA.

The last set of coatings was obtained with the mix of the three pigments having Fe in the base structure in the Acrylic WB.

In addition to the coatings described above, a white reflective coating containing titanium (IV) oxide (Sigma-Aldrich 99.7 %), and a black absorber coating containing graphite (Sigma-Aldrich 99.0 % carbon basis) were prepared and employed as the positive and the negative control respectively, for the characterization of the coatings. Titanium (IV) oxide, TiO₂, and graphite were added in the same concentration of pigments (2 wt.%). The titanium (IV) oxide, in the form of anatase, was used for comparison due to its well-known advantages for outdoor architectural applications (self-cleaning, high solar reflectance, and photo catalysis) [150–152] along with large scale commercial availability [150]. On the other hand, the negative control, graphite, is widely employed for producing components with

high heat adsorption [153] and coatings for solar energy concentration [154]. A bare AA5005 aluminum sheet was also subjected to the experimental tests for comparison purposes. For the reference samples containing powdery material (TiO_2 and graphite) the binders were the PMMA (for coatings having pigments with Mn and Cu in the base structure) and Acrylic WB (for coatings having pigments with Fe in the base structure).

All the obtained coatings made with $\text{YIn}_{0.9}\text{Mn}_{0.1}\text{O}_3\text{-ZnO}$ pigments and $\text{YIn}_{0.9}\text{Cu}_{0.1}\text{O}_3\text{-ZnO}$ pigments dispersed in PMMA are shown in **Figure 3. 4** and **Figure 3. 5**. Coatings made with $\text{YIn}_{0.9}\text{Fe}_{0.1}\text{O}_3\text{-ZnO}$ pigments dispersed in Acrylic WB are reported in **Figure 3. 6**. The coatings acting as reference samples are shown in **Figure 3. 7**. As was claimed for pigments, all the coatings pictures were obtained with the same camera on the same day, exposing the samples to the same light source.

Table 3. 2. Labels to identify all the coatings covered by the study.

Coatings s labels	Description
YInMnO–ZnO/550 °C + PMMA	YInMnO–ZnO pigments embedded in PMMA
YInMnO–ZnO/800 °C + PMMA	
YInMnO–ZnO/850 °C + PMMA	
YInCuO–ZnO/ 650 °C + PMMA	YInCuO–ZnO pigments embedded in PMMA
YInCuO–ZnO/ 650 °C + PMMA	
YInFeO–ZnO/ 650 °C + Acrylic WB	YInFeO–ZnO pigments embedded in ALPINA acrylic binder
YInFeO–ZnO/ 750 °C+ Acrylic WB	
YInFeO–ZnO/ 850 °C + Acrylic WB	
TiO ₂ + PMMA	TiO ₂ embedded in the PMMA
Graphite + PMMA	Graphite embedded in the PMMA
Substrate	Bare substrate (AA5005)

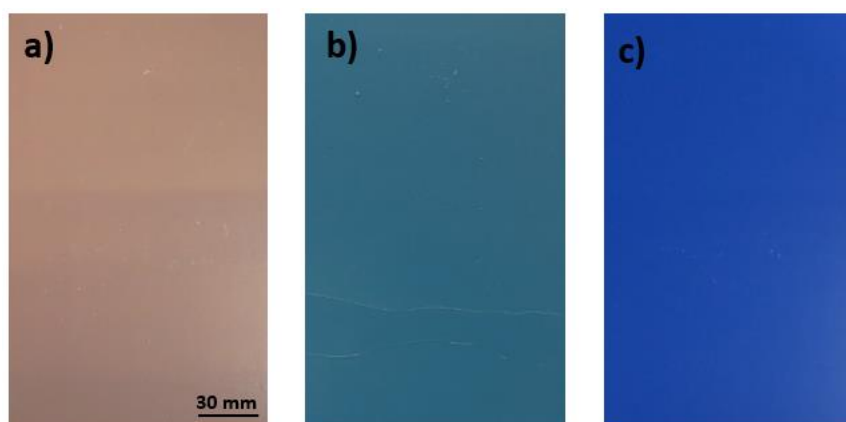


Figure 3. 4. Samples coated with the different pigments having following stoichiometry YIn_{0.9}Mn_{0.1}O₃–ZnO: YInMnO–ZnO/ 550 °C + PMMA (a), YInMnO–ZnO/ 800 °C + PMMA (b), YInMnO–ZnO/ 850 °C + PMMA (c).

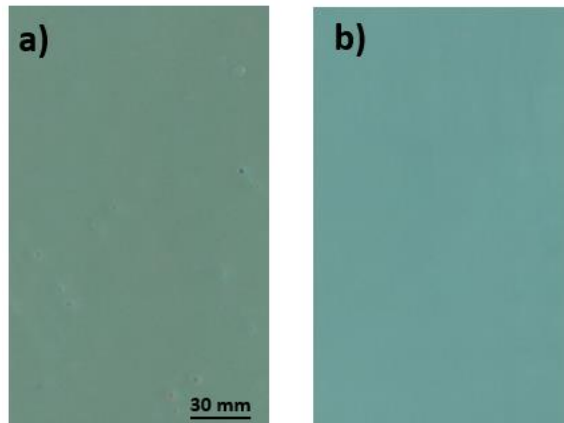


Figure 3. 5. Samples coated with the different pigments having following stoichiometry $\text{YIn}_{0.9}\text{Cu}_{0.1}\text{O}_3\text{-ZnO}$: $\text{YInCuO-ZnO}/ 650\text{ }^\circ\text{C} + \text{PMMA}$ (a), $\text{YInCuO-ZnO}/ 850\text{ }^\circ\text{C} + \text{PMMA}$ (b).

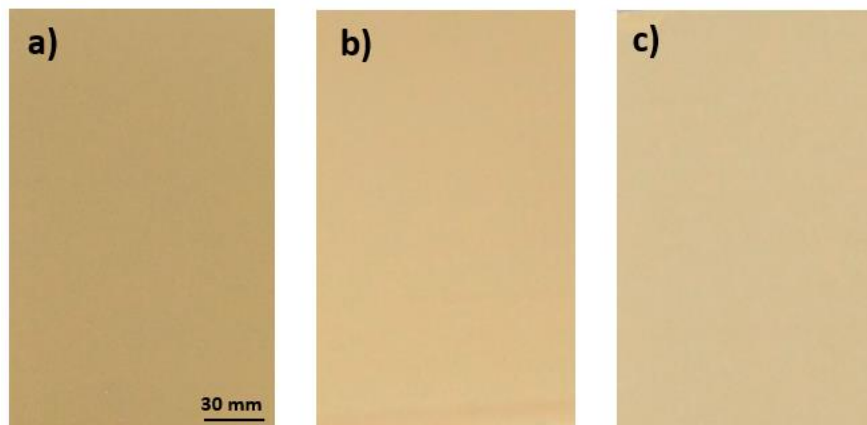


Figure 3. 6. Samples coated with the different pigments having following stoichiometry $\text{YIn}_{0.9}\text{Fe}_{0.1}\text{O}_3\text{-ZnO}$: $\text{YInFeO-ZnO}/ 650\text{ }^\circ\text{C} + \text{Acrylic WB}$ (a), $\text{YInFeO-ZnO}/ 750\text{ }^\circ\text{C} + \text{Acrylic WB}$ (b) and $\text{YInFeO-ZnO}/ 850\text{ }^\circ\text{C} + \text{Acrylic WB}$ (c).

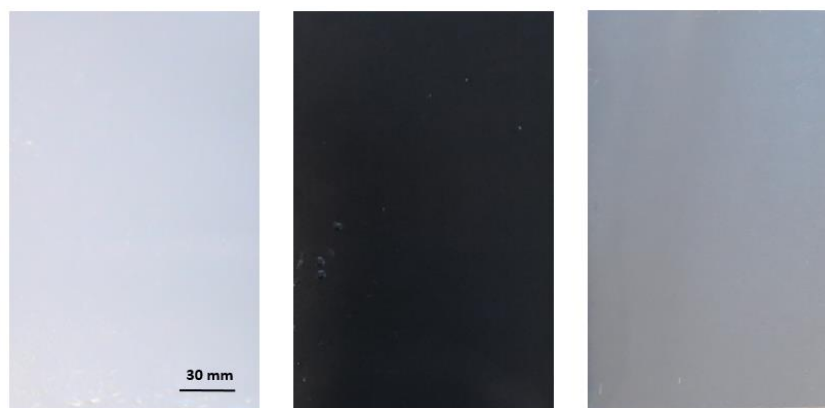


Figure 3. 7. Three of the samples used as reference material: (from left to right) TiO₂ + PMMA, Graphite + PMMA and bare substrate.

3.2.3 Characterization techniques of pigments

3.2.3.1 Thermogravimetric (TGA) and differential scanning calorimetry (DSC)

In this work thermogravimetry (TGA) and differential scanning calorimetry (DSC) analysis were carried out in air atmosphere using a differential thermal analyzer TG/DSC NETZSCH STA 409 PC Luxx (NETZSCH-Gerätebau, Germany).

The Thermogravimetry (TGA) and differential scanning calorimetry (DSC) analysis were carried out in air atmosphere (50 mL·min⁻¹ flow rate) in the temperature range of 50–1000 °C The heating rate was of 20 °C·min⁻¹. TGA and DSC measurements were carried out on the dried gel and the obtained pigments. In particular, the dried gel's thermal analyses aim to assess the temperature range without thermal decomposition or phase transitions and, therefore, identify the minimum temperature required to obtain a pigment. On the other hand, the thermal characterization performed on the calcinated pigments aimed to evaluate the thermal stability.

3.2.3.2 Fourier transform infrared (FT-IR) spectroscopy

Fourier transform infrared (FT-IR) spectra were collected using a Varian 4100 FT-IR Excalibur Series instrument (Varian, Palo Alto, U.S.A). In the characterization of pigments was exploited the Diffuse reflectance infrared Fourier transform spectroscopy (DRIFTS) sampling technique. The powder was diluted with non-absorbing KBr particles and pressed into tablets. The FT-IR spectra provide a clear evolution of the pigments' composition, showing peaks related to compounds and phases formed at different calcination temperatures. The acquisition conditions were as follows:

- 4000-400 cm^{-1} ;
- 32 scans for each acquisition;
- 2 cm^{-1} resolution.

3.2.3.3 Powder X-ray diffraction analysis

The pigments' crystal structure was examined at room temperature by an Italstructures IPD3000 diffractometer (Ital Structures Sas, Riva del Garda, TN, Italy) equipped with a Co anode source (line focus) coupled with a multilayer monochromator suppressing k-beta radiation and fixed 100 μm slits. Reflection geometry with a fixed omega angle with respect to the incident beam (5°) was considered; diffraction patterns were collected employing an Inel CPS120 detector over $5-120^\circ$ 2-theta range (0.03 degrees per channel) with an acquisition time of 30 minutes. The Rietveld refinement of the X-ray

diffraction data has been done using the JAVA based software, namely Materials Analysis Using Diffraction (MAUD) [155,156].

The high-temperature X-ray diffraction (HTXRD) was used for the dried gel's XRD sampling. This technique presents the advantage of in situ analysis of the sample, at the desired temperature, eliminating errors that may appear due to factors like cooling effects, the time between different analyses, and atmosphere impurities (HTXRD equipment is a closed system). Apart from being an in situ analysis system, in our case, the high-temperature chamber proved to perform the synthesis of the desired material, simultaneously giving real-time information about its evolution with time and temperature. The used equipment is HTK 16 N high temperature chamber. The analysis temperature ranges from 25 °C to 1600 °C. The samples were heated with platinum heating filament. The measurements were performed in controlled air atmosphere.

To perform the measurements the samples were heated from 25 to 250 °C with an heating rate of 5 °C ·min⁻¹. The temperature was maintained for 2 h. From 250 °C the temperature was increased at the following temperatures: 550 °C, 650 °C, 750 °C, 800 °C, 850 °C, 900 °C, 950 °C, 1000 °C; the heating rate was maintained of 5 °C·min⁻¹ maintaining each temperature for 2 h, before passing to the next.

3.2.3.4 Colorimetric measurements

The L^* , a^* , b^* color coordinates of heat-treated pigments at each temperature, as well as the visible reflectance spectra, were determined by coupling the analytical software Spectra Magic NX to the CM-2600d Spectrophotometer (Konica Minolta, Tokyo, Japan),

after calibration with the white standard, at 10 nm intervals in the range of 360–740 nm. The colorimetric coordinates were determined following the CIE-1976 $L^*a^*b^*$ colorimetric method [68].

The CM-2600d Spectrophotometer incorporate sphere optics and pulsed xenon lamps, covering the entire visible spectrum. The spectral reflectance of the samples is measured between 360 and 740 nm with a resolution of 10 nm. The signals from the detector array are processed by a data processor to yield the appropriate color scale values. The instrument is controlled by the computer with the SpectraMagic NX proprietary software for the CM-2600d. The area of measurement is 20 mm for the Konica spectrophotometer

3.2.3.5 Near-infrared reflectance (700-2500 nm)

The reflectance spectra of pigments were acquired using a UV/Vis/NIR double-beam double monochromator spectrophotometer (Perkin Elmer, model Lambda 1050, Perkin Elmer, Waltham, U.S.A), equipped with a 60 mm integrating sphere, in the 200-2500 nm range. The integrating sphere is covered with a 99% reflectance Spectralon® surface and has a high sensitivity photomultiplier (PMT) and a Peltier-controlled lead sulfide (PbS) detectors for the 200-860 nm and 861-2500 nm ranges, respectively. The adopted geometrical configuration (0°/d) made it possible to work in diffuse reflectance by collecting the diffusely scattered light, thus avoiding specularly reflected radiation. The powdered pigments' optical properties were measured using ZnO (99.0 % assay) as a reference. The same amount of pigment (3 g) was used and the powders were placed in quartz cuvettes of

the same dimensions (5 mm x 20 mm x 30 mm) to avoid extrinsic effects (as particle distribution and material thickness) on the measurement. To measure the reflectance of coatings of this experience was used Spectralon® Diffuse Reflectance Standard (99 % reflectance over the wavelength range from 700 to 2500 nm) as a reference.

In order to quantify the solar reflectance, this parameter is used: the *Total Solar Reflectance* (TSR) expressed in percentage.

The NIR solar reflectance (R^*) was calculated employing the equation (2. 2), which was shown before in the Introduction section of the thesis. Where $r(\lambda)$ is the experimentally obtained spectral reflectance ($W\ m^{-2}$) and $i(\lambda)$ is the solar spectral irradiance ($W\ m^{-2}\ nm^{-1}$), obtained following ASTM standards G173-03 [157].

Furthermore, by multiplying the spectral irradiance, of G173-03, with the spectrally corresponding paint reflectance, $r(\lambda)i(\lambda)$, yields the the solar irradiance reflective spectra [158], that is the reflected power for every wavelength.

3.2.3.6 SEM observation and analysis

The morphology and particle size of the synthesized pigments were investigated employing low-vacuum SEM (JEOL JSM-IT300, JEOL, Peabody, U.S.A) equipped with an energy dispersive spectrometer (EDS) obtaining semi-quantitative information about the chemical composition of the samples.

3.2.4 Characterization techniques of coatings

3.2.4.1 Near-infrared reflectance (700-2500 nm)

The NIR reflectance of each coating was measured with the same Spectrophotometer used for pigments (Perkin Elmer Lambda 1050 UV/VIS/NIR). The NIR solar reflectance (R^*) of the coatings was calculated as underlined for pigments.

3.2.4.2 Thermal behavior

In cool roof field, the monitoring of thermal performances in real dynamic environmental conditions is a preliminary focus to set up the research, collecting data to obtain a trend of how vary solar reflectance and heat adsorption during the course of a day and/or a year [159] or focusing on particular thermal scenarios [160]. In the last case, we are referring to some studies performed in buildings [161] or entire cities [160,162].

3.2.4.3 Exposure to sun radiation

In order to assess the thermal behavior of the investigated sample under real solar exposure, coatings with the three pigments with formulation $YIn_{0.9}Mn_{0.1}O_3$ -ZnO (having 550 °C, 800 °C and 850 °C of calcination temperature) dispersed in PMMA were evaluated by exposing the coated panels to solar radiation during summer 2020. In particular, the tests were performed on sunny days on July 18th–20th, 2020 in an unsheltered area located on the rooftop of the university building in Trento (Italy, coordinates: 46.067870° N, 11.121080° E). The average temperatures in the site of measurements were 26.2 °C, on July 18th, and 25.9 °C on July 20th. The meteorological data of Global Solar Radiation ($W \cdot m^{-2}$) and low relative humidity (%) for the tests in real conditions were collected by Weather station “Gardolo

Nord Trento" (Italy, coordinates: 46.1069336° N, 11.1120652° E) and plotted (Figure 3. 8). The performance of the coatings was evaluated in real dynamic conditions to find the best simulating artificial radiation source. The selected period is the one that presents the most suitable weather conditions to test coatings as cool coatings (no clouds and constant temperatures). The samples were exposed at 12.00 p.m. to obtain perpendicular solar radiation on the samples and maximum values of Global Solar Radiation ($W \cdot m^{-2}$) and low relative humidity (%). The samples were exposed to solar radiation employing the experimental set-up shown in Figure 3. 9. The as-prepared coated aluminum sheets were placed as the ceiling on a roofless box (size: 150 mm \times 270 mm \times 200 mm) made of polyurethane foam sheets (Figure 3. 9).

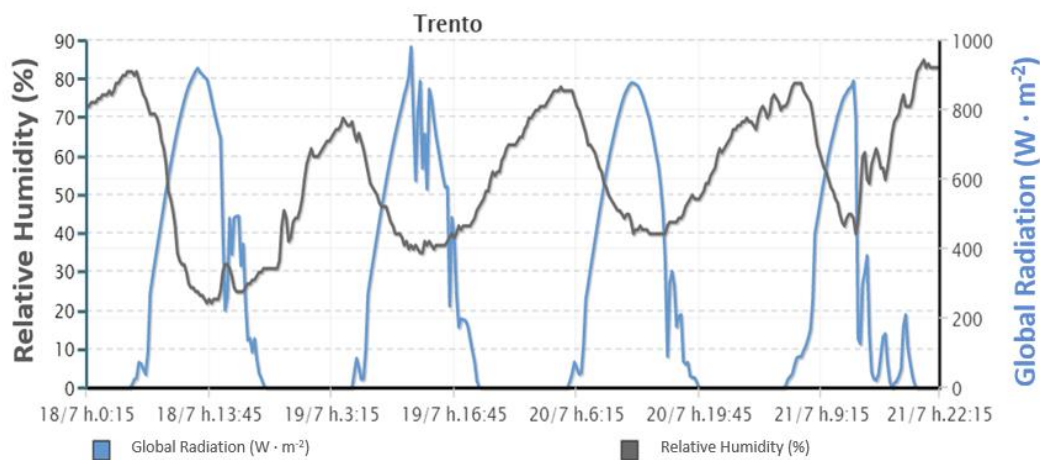


Figure 3. 8. Relative humidity (%) and global radiation values ($W \cdot m^{-2}$) registered by the weather station in Trento on July 18th - 20th, 2020.

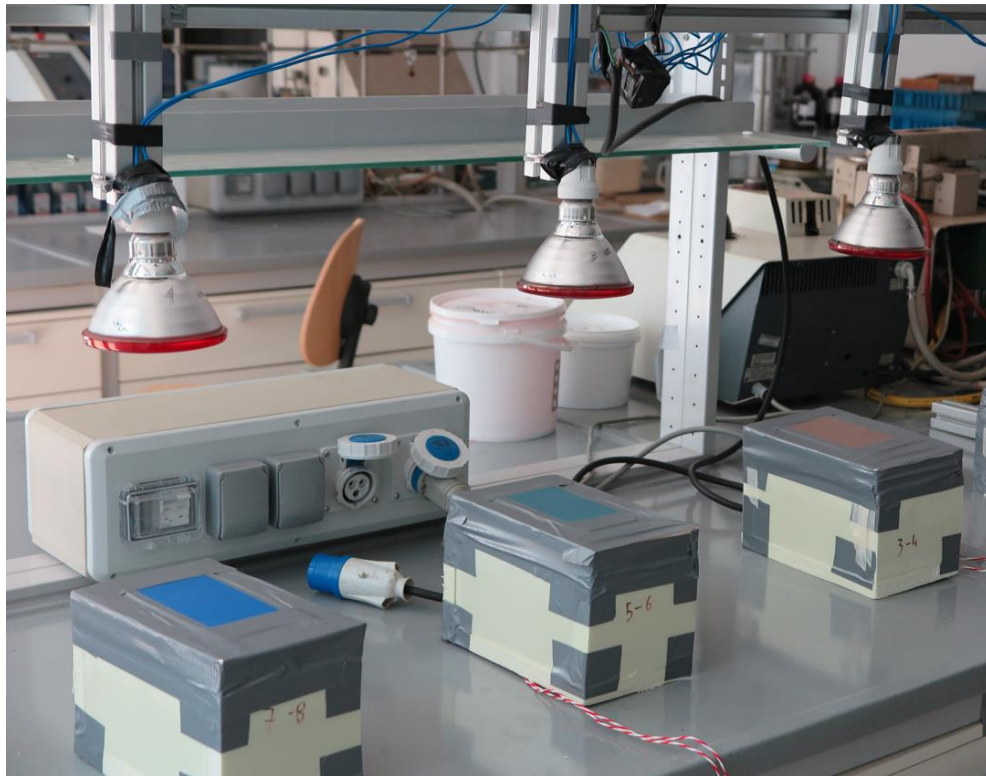


Figure 3. 9. From right to left YInMnO–ZnO/850 °C + PMMA, YInMnO–ZnO/850 °C + PMMA, YInMnO–ZnO/850 °C+ PMMA placed on roofless boxes used to simulate buildings indoor environments indoor.

Thus, the employed geometry aims at testing the thermal performances by simulating a flat roof. Two different thermocouples were employed for collecting the temperatures. One thermocouple, located on the rear part of the coating panel, was used to obtain the temperature of the panel. Another thermocouple, in the middle of box, at 100 mm from the coated panel recorded the temperature inside the box. The thermocouples were connected to a Delta OHM HD 32.7 RTD data logging instrument (Delta OHM Srl, Selvazzano Dentro PD, Italy), for temperature data recorder every 60 s, as shown in **Figure 3. 10.** DeltaLog 9 software was employed to control the instrument.

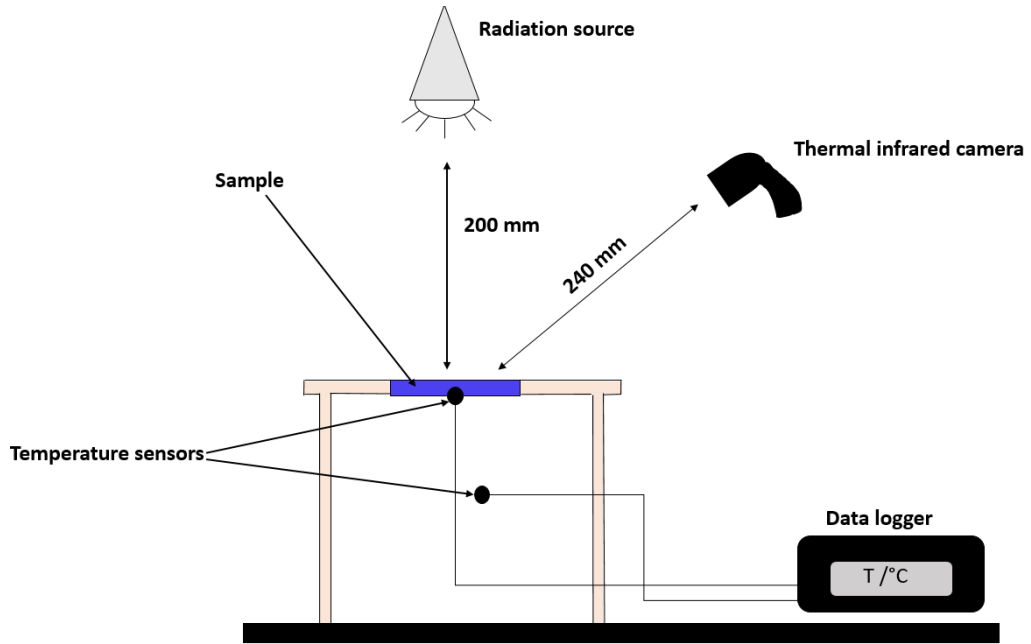


Figure 3. 10. Experimental set-up of the foam boxes used as support for the roof panels for measurements performed with the IR emitting lamp, tungsten halogen lamp, and xenon arc lamp.

The temperature values measured by the thermocouples have been recorded until a plateau was reached. The plateau temperatures values were used to calculate the arithmetic mean temperature and the standard deviation of the temperature at plateau. The plateau temperature values recorded by the thermocouple located on the rear part of the coated panel (T_{panel}) and in the middle of the box (T_{box}) were recorded. The values of T_{panel} and T_{box} were employed to calculate the heat flux ($q_{1,2}$) between panel and box area according to the formula 3. 1:

$$q_{1,2} = \frac{A\sigma(T_{panel}^4 - T_{box}^4)}{(1/\varepsilon_1) + (1/\varepsilon_2) - 1} \quad (3. 1)$$

where σ is Stephan-Boltzmann constant, $\sigma = 5.66 \times 10^{-8} \text{ W}/(\text{m}^2 \cdot \text{K}^4)$, $\varepsilon_1 = \varepsilon_2 = 0.9$ is the emissivity for roof surfaces [163,164]. A is referred to the area of the coated panel and of the area of the internal bottom of the box. Having areas with the same dimension the value A is equal to 1. So $A=1$ [165,166]. The surface temperature (T_{surface}) of the panels was measured using an IR-camera (FLIR model T62101, FLIR, Wilsonville, U.S.A). The IR-images were obtained at 240 mm in front of the house model set-up, in correspondence of the thermocouple location on the rear part of the panel (**Figure 3. 10**). Several IR-images for each sample were collected at the end of each thermal measurement and the result was represented as a mean value obtained from the recorded images. The emittance of each coating sample was assumed to be 0.9. Most common building materials, including glass and paints of all colors, have high emissivities near 0.9 [167,168].

3.2.4.4 Exposure to artificial radiation sources

Three different radiation sources were tested to assess the capability to provide reliable results, which can be considered representative of the real outdoor exposure: **1.** 150 W (Philips IR 100R PAR38 E27 230V, Philips, Eindhoven, Netherlands) incandescent infrared emitting lamp, with 121 mm of diameter; **2.** 140 W (Philips 140 W E27 230V A55) tungsten halogen lamp, equipped with an AA8021 aluminum alloy reflector, which gives a diameter of the focused beam of 100 mm; **3.** 1000 W xenon arc lamp (Wissen, Offenbach, Germany).

As the literature dealing with cool coatings reports data collected with many different radiation sources, we have obtained temperature data (T_{panel} , T_{box}) and related parameter

*q*_{1,2} using a Infrared lamp (Philips IR 100R PAR38 E27 230V), a halogen lamp (Philips 140 W E27 230V A55) and a xenon arc lamp (Wissen).

The use of infrared lamps to test cool coatings is widespread in the literature [169–172]. PAR 38 thermal infrared lamps are employed to test a cool roof making an overheating of samples [173]. The acronym PAR stands for Parabolic Aluminum Reflector, while 38 indicates the diameter of the lamp: 38 × 1/8 inches. It is a gas-filled lamp made of moulded glass with a thickness of approximately 3 mm, which ensures the high quality of its mechanical and thermal properties

PAR 38 thermal infrared lamp features are shown in **Figure 3. 11**. They have a peculiar design to overheat a surface. 90 % of energy is in fact transmitted as infrared heat. PAR 38 lamps are designed with a 100 % aluminized internal reflector, which means that 100 % of the heat leaves via the front, perpendicular to the surface to irradiate. However, because the infrared light's spectral emission does not match the sunlight [174,175]. Even if thermal infrared lamps are diffused in literature as radiation source in cool roof and NIR reflective material applications, nowadays their application is limited because the approach is oriented to radiation sources fitting solar spectrum radiation as halogen lamps [176] and xenon arc lamps [177].



Figure 3. 11. Infrared lamps used in literature to test cool coatings [169–172].

Tungsten halogen lamps were revealed to be another frequently used radiation source for testing cool roof surfaces [176]. However these lamps radiate weaker in the ultraviolet and stronger in the infrared regions compared to the solar spectrum with its color temperature of 5800 K [178]. A Tungsten halogen lamp is a type of incandescent lamp, which contains a halogen in the form of bromine or iodine surrounding a tungsten filament heated by an electric current as shown in **Figure 3. 12**.

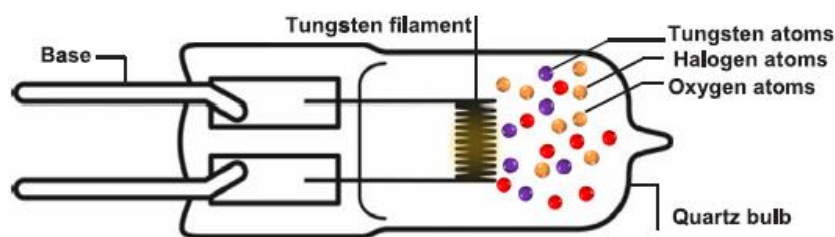


Figure 3. 12. Tungsten halogen lamp structure [179].

A xenon arc lamp consists of a point-shaped cathode and a rounded-shaped anode contained in a spherical quartz bulb (**Figure 3. 13**) [177]. In the research this kind of lamp is

suggested to act as a solar simulator [177,180] for its close match to the spectral distribution of natural solar radiation. Moreover, they are preferred for the stable spectrum in the UV and the visible bands. This kind of lamps has the possibility to filters the strong IR emission. Furthermore, a collimated high-intensity light beam can be obtained [181].

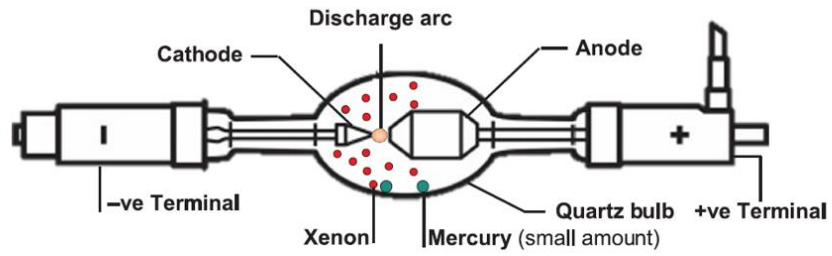


Figure 3. 13. Xenon arc lamp scheme [212].

4 Results & Discussion

4.1 Analysis performed on obtained pigments

4.1.1 Thermogravimetry (TGA) and Differential scanning calorimetry (DSC)

Preliminarily, two different thermal analyses were performed on the dried gel: a thermogravimetric analysis (TGA) and a differential scanning calorimetry (DSC). Both thermal analyses of dried gel precursors were carried out in the 50–1000 °C range.

4.1.1.1 YInMnO–ZnO pigments

Both the integral and derived curves of TGA are shown in the thermogram of the citrate dried gel (**Figure 4. 1a**). The weight loss can be observed on the integral curve, where the curve begins to decrease. The maximum rate of weight loss of the sample, shown by a downward peak, is assumed as the decomposition temperature on the derived curve. The marked slope between 80 and 135 °C of the TGA curve indicates the removal of adsorbed moisture. Considering DTGA, the peak at 250 °C is related to the decomposition of nitrates [182]; while peak at 400 °C corresponds to the citric acid decomposition [182,183]. The corresponding part on the integral curve shows that the decomposition of citric acid occurs at about 600 °C. The exothermic peaks in the DSC curve (**Figure 4. 1.b**), at 250 °C and 400 °C, confirm the nitrate and citrate's decomposition processes, respectively. The two adjacent exothermic peaks at 420 °C and 450 °C are related to the citrate's combustion [184]. The slight increase of heat flow from 600 °C to 850 °C is related to the oxidation of residual carbon

[184], which came from the incomplete combustion of citrate. The small exothermic peak at about 900 °C is attributed to the combustion of carbon [184].

Considering the TGA and DSC curves (**Figure 4. 1.a** and **Figure 4. 1.b**), in the range from ~550/650 °C to 1000 °C, no significant mass changes connected with products formation are observed. Furthermore, almost all the organic fraction, related to the citrate composition, is degraded, and the temperature of 550 °C can be assumed as the minimum temperature of calcination for the production of pigments without phase transitions connected with thermal degradation of citrate and nitrate. Based on this output of thermal analyses, three calcination temperatures of the dried gel were selected: 550 °C, 800 °C, and 850 °C. In the DSC curve **Figure 4. 1.b**, it is possible to see a small exothermic peak at about 900°C, attributed to the combustion of carbon

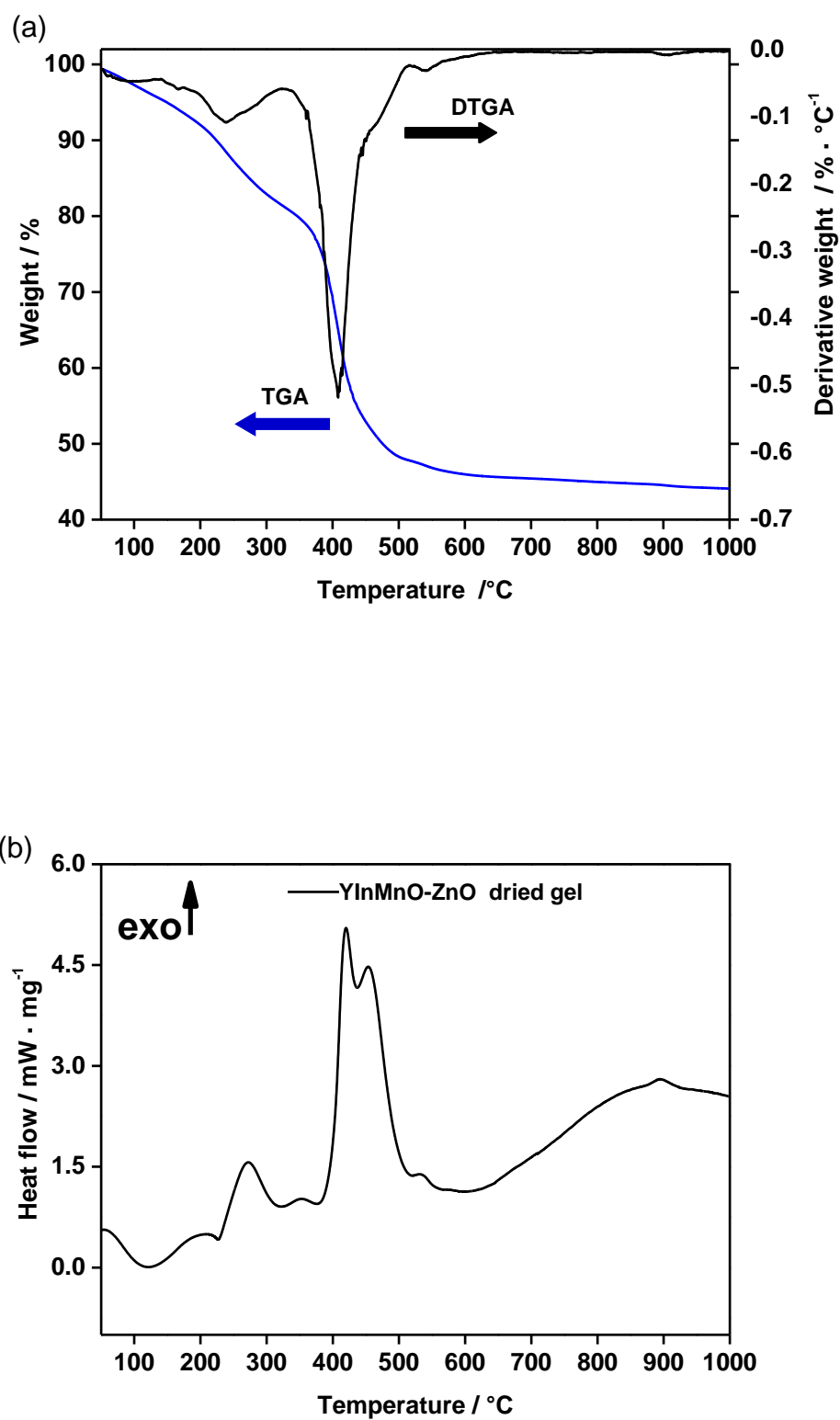


Figure 4. 1. TGA-DTGA (a) and DSC curves (b) of YInMnO-ZnO citrate dried gel.

4.1.1.2 YInCuO–ZnO pigments

In **Figure 4. 2** are represented TGA-DTGA (a) and DSC curves (b) of $\text{YIn}_{0.9}\text{Cu}_{0.1}\text{O}_3\text{-ZnO}$ citrate dried gel.

The exothermic peaks in the DSC curve (**Figure 4. 2.b**), at 250 °C and 400 °C, confirm nitrate and citrate's decomposition process, respectively. Differently from YInMnO-ZnO dried gel, the YInCuO-ZnO dried gel sample shows a slight, and not well define exothermic peak. Comparing DSC with TGA the mass decrease at 250 °C confirms the nitrate degradation. In the 100 °C–300 °C temperature range, a broadened exothermic peak occurs caused by the dehydration of citrate precursor [185].

The double peak ranging from 300 °C to 600 °C is related to the citrate's combustion [184] and corresponds to the carbon-burning temperature range of the citrate group [186]. Peaks are broadened and overlapped respect to sample investigated before, as sometimes citrate burns in a wider temperature range and the resulting exothermic peaks are more broadened [187,188]. Considering DSC curve, the increase of heat flow, up to 1000 °C is related to the degradation of residual carbon, as in fact is not related to any mass change in TGA thermogram. A degradation of residual carbon is a common final by-product during a TGA experiment in citrate gel derived products [186]. To make considerations towards $\text{YInCuO}_3\text{-ZnO}$ pigment having organic composition and pigment without residual organic compounds, two different calcination temperatures were selected: 650 °C and 850 °C.

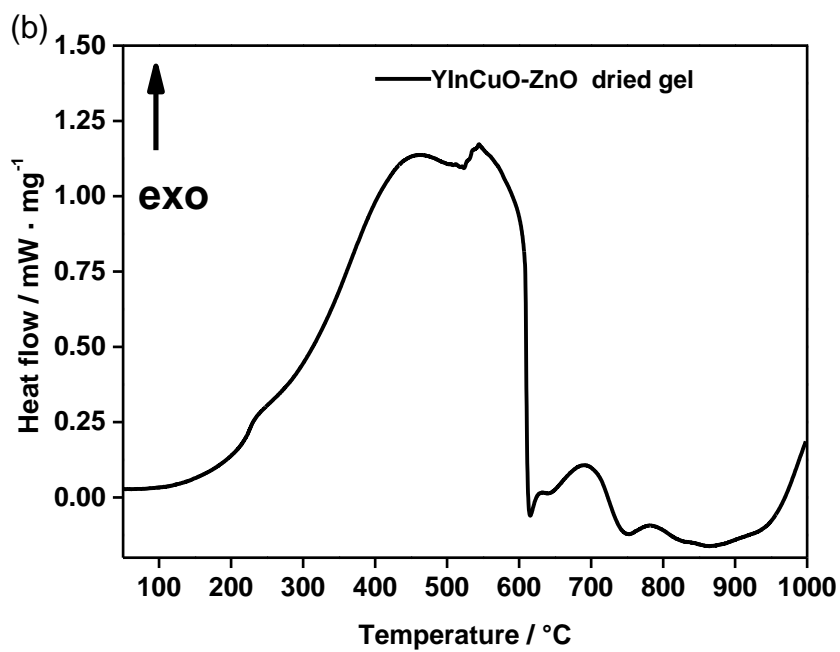
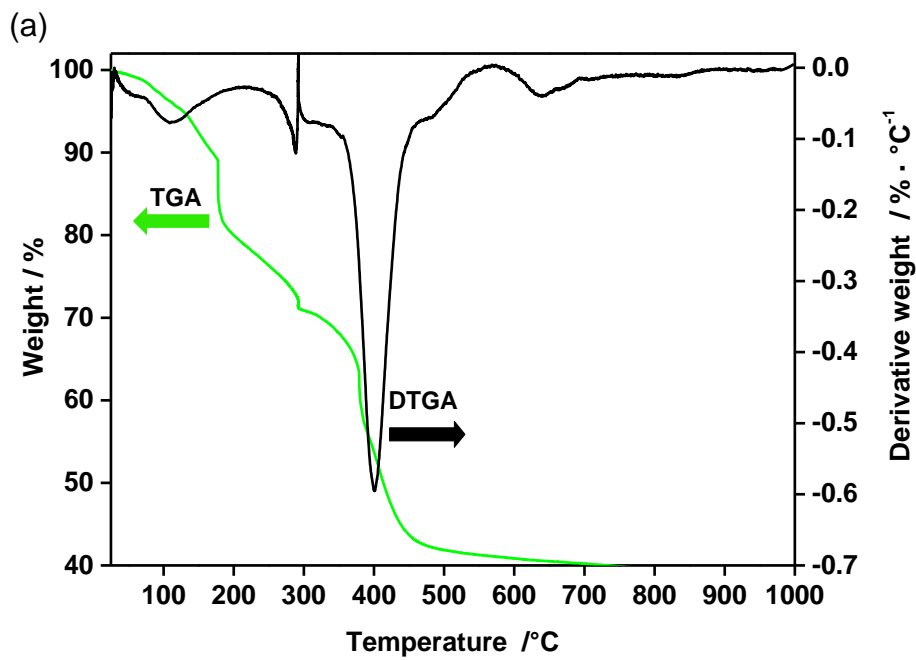


Figure 4. 2. TGA-DTGA (a) and DSC curves (b) of YInCuO–ZnO citrate dried gel.

4.1.1.3 YInFeO–ZnO pigments

The thermogram of the citrate dried gel having YInFeO–ZnO composition is shown in **Figure 4. 3.a**. The weight loss can be observed on the integral curve, where the curve begins to decrease. The slight slope between 80 and 135 °C of the TGA, observed for other samples, related to the removal of adsorbed moisture, is observed in **Figure 4. 3.a**. Considering DTGA, the peak at 250 °C is related to the decomposition of nitrates [182]; and the peak at 400 °C corresponds to the citric acid decomposition [182,183]. The corresponding part on the integral curve shows that the decomposition of citric acid occurs at about 600 °C. The exothermic peaks in the DSC curve (**Figure 4. 3.b**), at 250 °C and 400 °C, confirm nitrate and citrate decomposition process. The two exothermic peaks at 420 °C and 450 °C are related to the citrate combustion [184]. The slight increase of heat flow between 600 °C and 850 °C is related to the-residual carbon oxides release [184]. Considering the DSC curve (**Figure 4. 3.b**), in the range from 700 °C to 900 °C an exothermic peak is present, connected to the formation of yttrium iron oxide crystalline phase [147]. Furthermore, almost all the organic fraction related to the citrate composition is degraded at the temperature of 650 °C. Therefore, a first temperature of dried gel calcination was 650 °C, to obtain pigments without large amount of residual organic fraction.

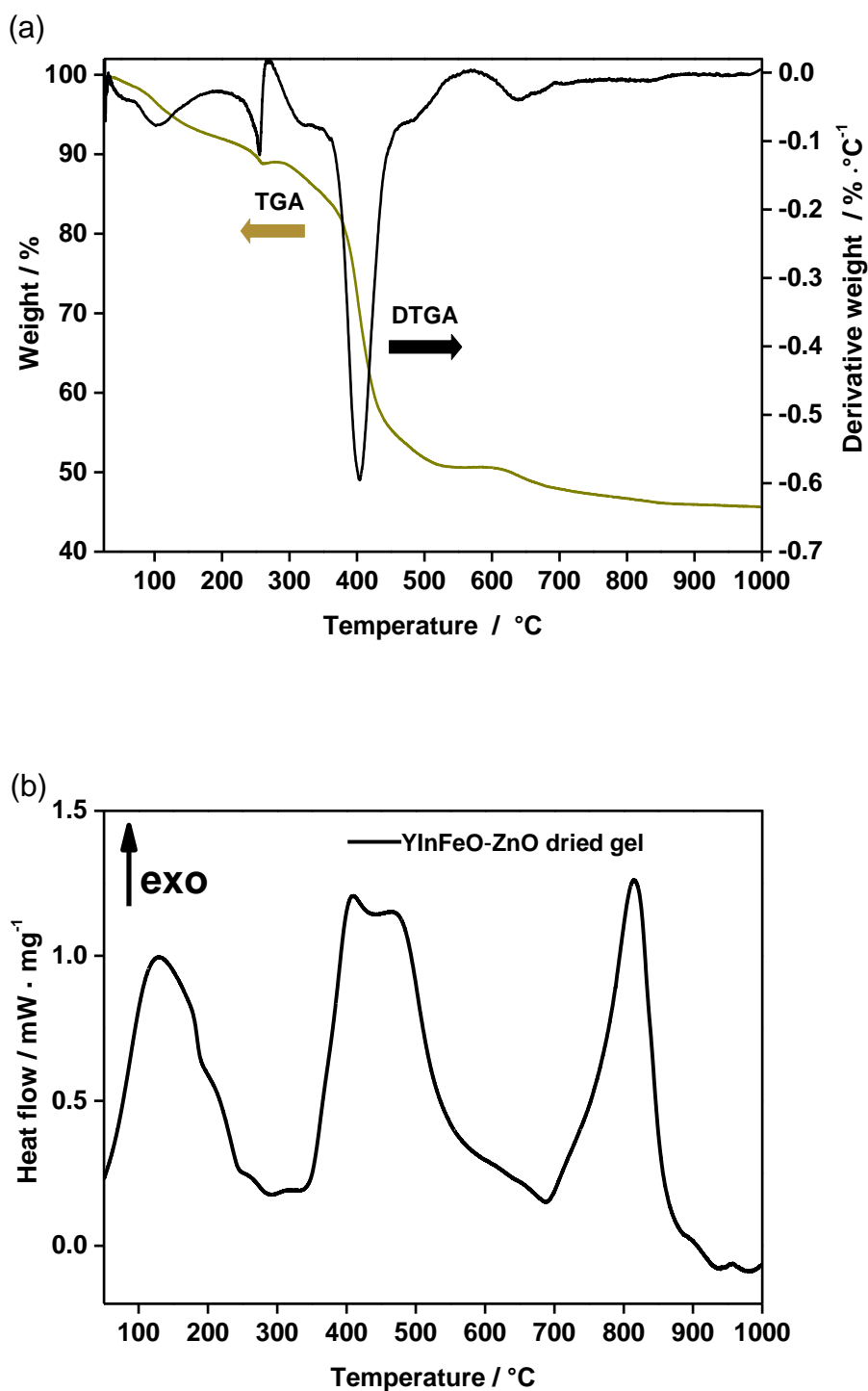


Figure 4. 3. TGA-DTGA (a) and DSC curves (b) of YIn_{0.9}Fe_{0.1}O₃-ZnO citrate dried gel.

For all synthesized pigments, according to TGA measurements, the temperature of 850 °C is the minimum temperature required to obtain pigments without organic fraction due to residual carbon of citrate. As demonstrated by thermogram of pigments calcined at

850 °C (Figure 4. 4), the resulted flat curve demonstrates the negligible weight loss of pigments up to 1000 °C and involves their use for high temperature exposure.

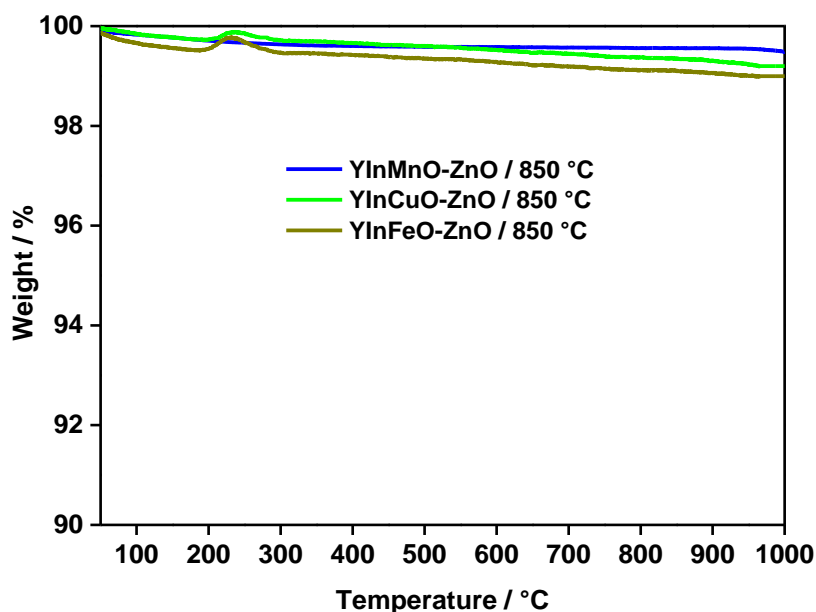


Figure 4. 4. TGA of pigments calcined at 850 °C.

4.1.2 Fourier transform infrared spectroscopy (FT-IR)

4.1.2.1 YInMnO-ZnO pigments

Figure 4. 5 shows the FT-IR spectra of the synthesized citrate gel as well as calcined powders at different temperatures (550 °C, 800 °C, and 850 °C).

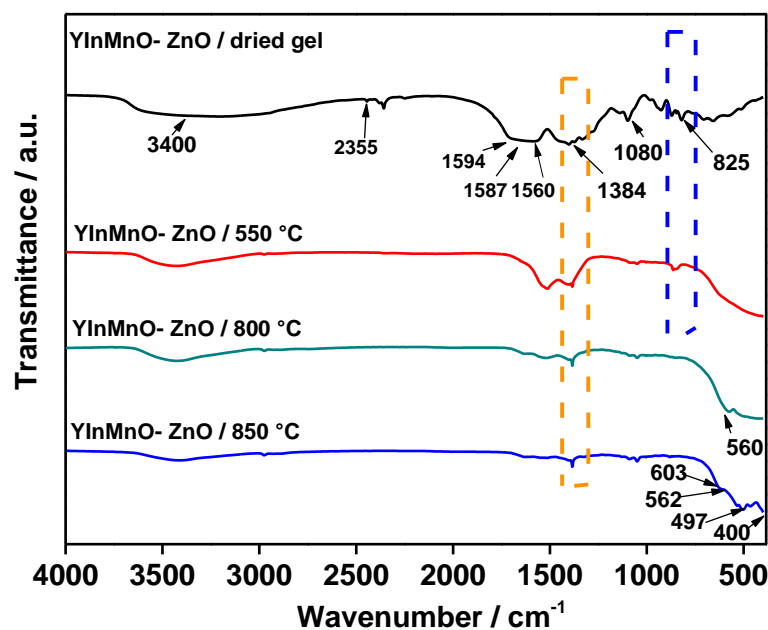


Figure 4. 5. FT-IR spectra of YInMnO–ZnO citrate dried gel and pigments obtained at the different calcination temperatures (550, 800, and 850 °C).

With the increase of calcination temperature, peaks due to the organic fraction disappear or decrease in intensity. The broad band observed in the citrate gel spectrum at 3400 cm^{-1} can be assigned to O–H stretching frequencies of the intermolecular hydrogen-bonded water [183,189]. The absorption peak at 2355 cm^{-1} is related to the absorption of CO_2 from the atmosphere [190]. The peaks at 1080 cm^{-1} and 825 cm^{-1} can be attributed to the vibration of the carboxylic group [191]. The peak at 825 cm^{-1} is also attributed to the bending of nitrate [192]. Further, the FT-IR spectrum of the citrate-dried gel shows intense absorption bands characteristic of the carboxylate groups at 1560 and 1380 cm^{-1} [189]. The IR spectrum of the gel shows two bands in $1594\text{--}1587\text{ cm}^{-1}$ and $1400\text{--}1398\text{ cm}^{-1}$ attributed to asymmetric and symmetric vibrations of the COO^- ion (ν_a and ν_s), respectively [189,193]. According to Rama Rao et al. [189] the separation $\Delta\nu$, between ν_a and ν_s , is an indication of the type of carboxylate group bonding in metal carboxylates. In this case, the value between 105 and

200 cm^{-1} indicates the presence of bridging and/ or chelating coordination of the carboxylate [189]. The band at 1384 cm^{-1} corresponds to nitrate stretching vibrations [192]. Non-degraded nitrates remain in pigments calcined at 850 °C. Non-degraded nitrates residues were observed in previous studies by Olivares [194] at temperatures higher than 250 °C and 400 °C. In this research, a later stage of decomposition of nitrates was observed up to 900 °C.

The spectra of pigments calcined at 800 °C and 850 °C show the adsorption bands of the indium-oxygen bond (603 cm^{-1}) [192] overlapped with the band of stretching mode (ν_s) of the manganese-oxygen bond (600 cm^{-1}) [195]. Around 562 cm^{-1} and 497 cm^{-1} , two bands of Y-O stretching vibration [196–198] are partially overlapped with the indium-oxygen bond peak. For the pigment calcined at 850 °C, the peak attributed to ZnO (wurtzite) is located at 464 cm^{-1} [199]. At around 400 cm^{-1} it is possible to observe part of the peak related to the bending (ν_b) of the Mn-O bond, related to the MnO_5 trigonal bipyramid. The intensity reduction indicates by the peaks at 1384 cm^{-1} (underlined by orange dotted area) and 825 cm^{-1} (highlighted by blue dashed area), a decrease of carbon nitrates and oxides is observed [192].

4.1.2.2 YInCuO–ZnO pigments

Figure 4. 6 shows the FT-IR spectra of the synthesized citrate gel as well as calcined powders at different temperatures (650 °C, and 850 °C).

All the peaks observed in the spectrum of the YInMnO–ZnO /dried gel are observed also in the YInCuO–ZnO /dried gel. Non-degraded nitrates residues were observed in YInCuO–ZnO calcined at 650 °C and 850 °C. As marked by orange dotted area residual nitrates remain up to the calcination at 850 °C. Blue and pink dotted areas underline the evolution of peaks related to carboxylate and nitrate group respectively. In FT-IR spectra of pigments are well marked the peaks related to indium-oxygen bond (603 cm⁻¹) [192], ZnO (wurtzite) (464 cm⁻¹) [199] and typical bands of Y₂O₃ (420 cm⁻¹) [198].

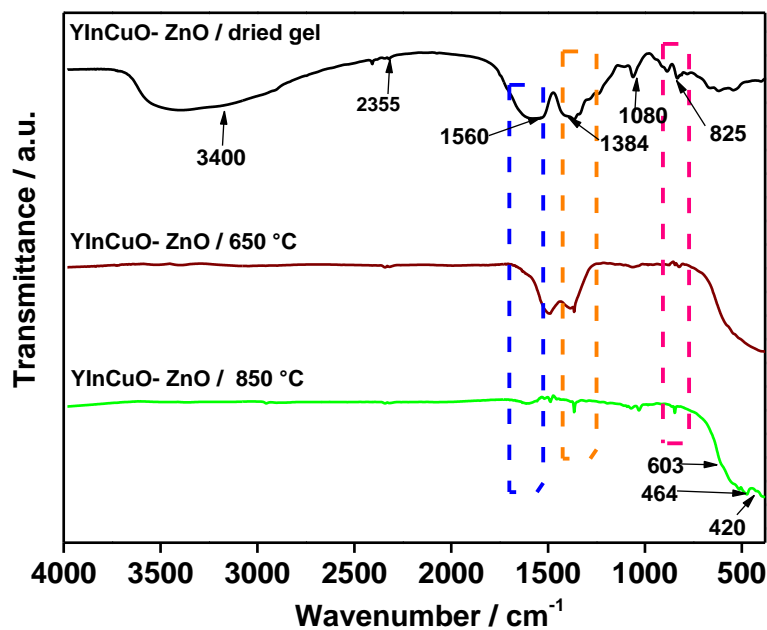


Figure 4. 6. FT-IR spectra of YInCuO–ZnO citrate dried gel and pigments obtained at the different calcination temperatures (650 °C and 850 °C).

4.1.2.3 YInFeO–ZnO pigments

Figure 4. 7 shows the FT-IR spectra of the different powders and pigments having iron as doping element (YInFeO–ZnO/650 °C YInFeO–ZnO/750 °C YInFeO–ZnO/850 °C) and dried gel precursor YInFeO–ZnO/dried gel. As observed for YInMnO–ZnO and YInCuO–ZnO dried gel precursors, the same peaks related to the organic composition of the dried gel are present. This result demonstrates one of the most important advantages of sol-gel route: chemical homogeneity of the final dried gel product [90]. The spectra of synthesized pigments show the adsorption bands of the indium-oxygen bond (603 cm^{-1}) [192]. Around 568 cm^{-1} and 497 cm^{-1} , two bands of Y–O stretching vibration [196–198] are partially overlapped with the In–O bond peak (603 cm^{-1}). On the basis of available literature peaks at 568 cm^{-1} and 436 cm^{-1} are due to the formation of Fe–O (asymmetric stretching vibration of Fe–O) [200–202]. The peak attributed to ZnO (wurtzite) is located at 464 cm^{-1} [199]. Typical bands of Y_2O_3 are at the wavelength of ~ 460 and $\sim 420\text{ cm}^{-1}$ [198]. The fact that peaks due to the Fe–O are at the same wavelength in all pigments (568 cm^{-1} and 436 cm^{-1}), and do not change position along the wavelength range, underline that citrate sol-gel route realizes uniform distribution of ions in oxides [115].

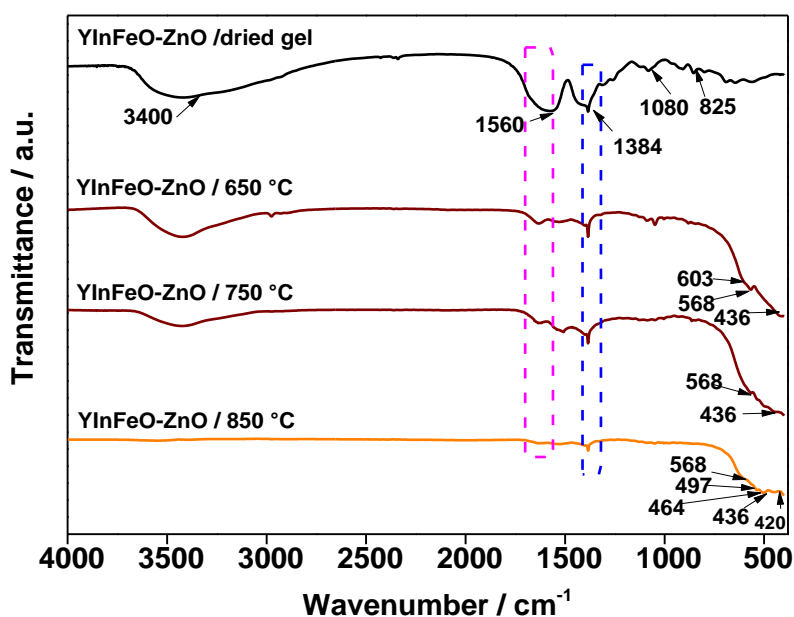


Figure 4. 7. FT-IR spectra of YInFeO–ZnO citrate dried gel and pigments obtained at the different calcination temperatures (650 °C, 750 °C and 850 °C).

4.1.3 Powder X-ray diffraction analysis

4.1.3.1 X-ray diffraction as function of temperature

Figure 4. 8 shows the XRD patterns of the dried gel of YInMnO–ZnO pigments group recorded at the different temperatures. The crystalline phases peaks of the pigments calcined at different temperatures are present starting from 750 °C. The pigments calcined until 750 °C show a semi-crystalline phase. From 850 °C to 1000 °C XRD patterns maintain the same shapes of peaks and the same phases. The small peak at 2 theta values of about 25° is related to YIn_{0.9}Mn_{0.1}O₃ cubic phase (**Figure 4. 9**) and disappears at a temperature of 950 °C. YIn_{0.9}Mn_{0.1}O₃ in cubic phase can be therefore considered a metastable phase. From 850

°C the crystalline phases are $\text{YIn}_{0.9}\text{Mn}_{0.1}\text{O}_3$ in hexagonal phase and ZnO in hexagonal phase (Figure 4. 9). These two phases are stable up to 1000 °C.

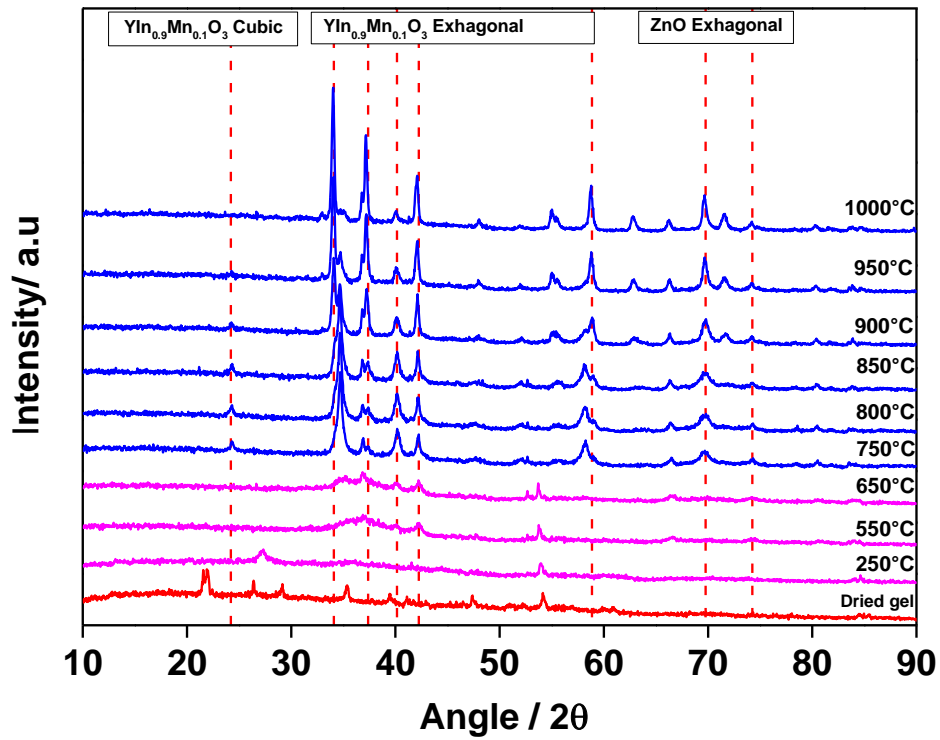


Figure 4. 8. XRD diffraction pattern of YInMnO-ZnO dried gel at different temperatures, underlining phase modifications.

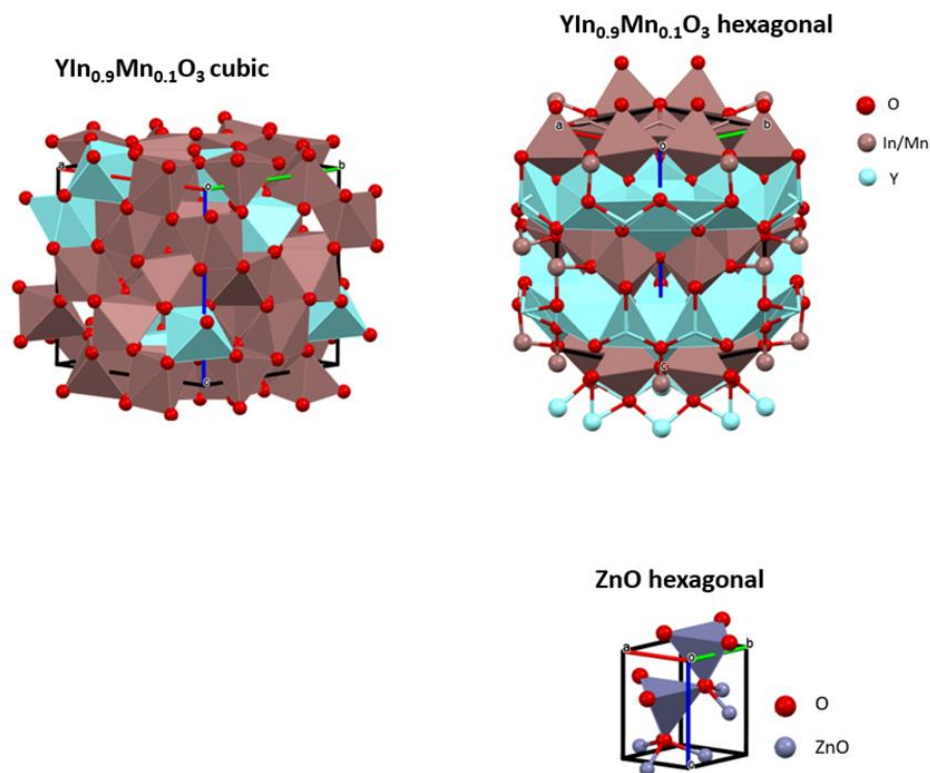


Figure 4. 9. Cubic and hexagonal crystal structures of YInMnO_3 in pigment calcined at $800\text{ }^\circ\text{C}$ and hexagonal crystal structure of YInMnO_3 in pigment calcined at $850\text{ }^\circ\text{C}$. ZnO in two pigments is present as a hexagonal wurtzite structure.

The $\text{YIn}_{0.9}\text{Cu}_{0.1}\text{O}-\text{ZnO}$ dried gel shows a crystalline phases starting from $800\text{ }^\circ\text{C}$ (**Figure 4. 10**). The XRD pattern of dried gel discussed before ($\text{YInMnO}-\text{ZnO}$) shows the formation of crystalline phases starting from $750\text{ }^\circ\text{C}$. Differently from $\text{YInMnO}-\text{ZnO}$ pigments, the cubic phase with composition $\text{YInCuO}-\text{ZnO}$ is maintained at all the investigated calcination temperatures. The temperature of crystalline phase formation and the temperature at which a phase prevails to another are not exactly determinable. The literature confirms this on YInO_3 based pigments [136,203]. A temperature range stability of cubic phase respect to hexagonal can vary in different published works. The yttrium carbide ($\text{YC}_{0.4}$) as observed as a new phase [204] (**Figure 4. 11**). This new phase formation is due to a low fraction of yttrium, sputtered from YInO_3 structure, free to react with the residual

carbon. The cubic yttrium carbide is stable above about 900 °C [204,205] as confirmed by peaks underlined in **Figure 4. 10**. All the crystalline phases maintain the same structure observed before, even with copper as doping element. (**Figure 4. 11**).

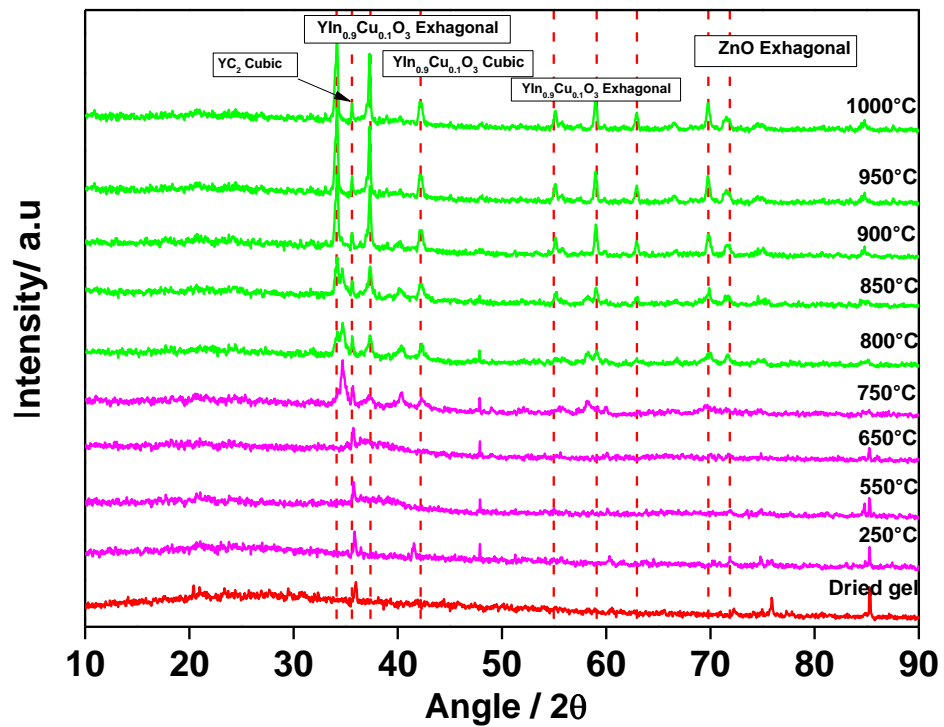


Figure 4. 10. XRD diffraction pattern of YInCuO-ZnO dried gel at different temperatures, underlining phase modifications.

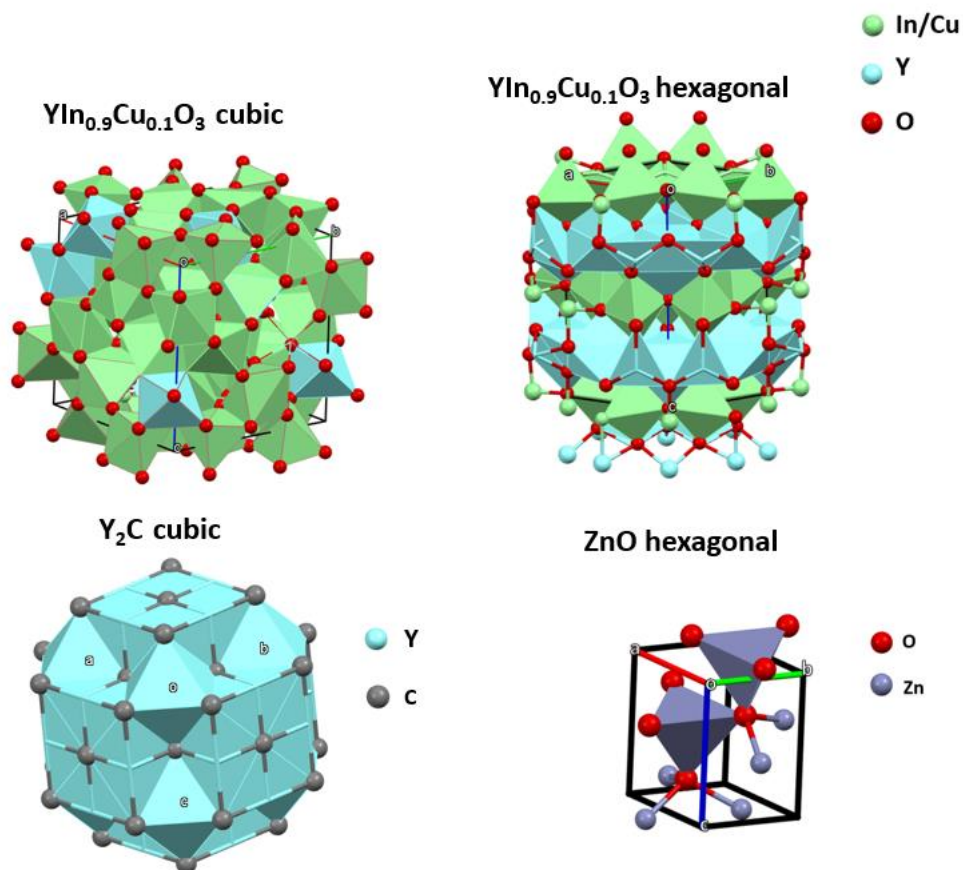


Figure 4. 11. Cubic and hexagonal crystal structures of YInCuO₃ in pigment calcined at at 850 °C. ZnO in the pigment is present as hexagonal wurtzite structure.

Considering the dried gel having YIn_{0.9}Fe_{0.1}O₃–ZnO composition, from 750 °C no formation of new phases is highlighted and all crystalline phases identified at 750 °C are stable up to 1000 °C (**Figure 4. 12**). It is interesting to note that YInFe_{0.1}O₃ cubic phase (**Figure 4. 13**) results stable up to 1000 °C, as in YInCuO–ZnO pigments. The new phase not observed before is Y₂Fe₂O₇. This phase is stable from 800 °C up to 1000 °C, like the other phases. The crystalline phases of the pigments calcined at temperatures higher than 750 °C are highlighted in **Figure 4. 13**.

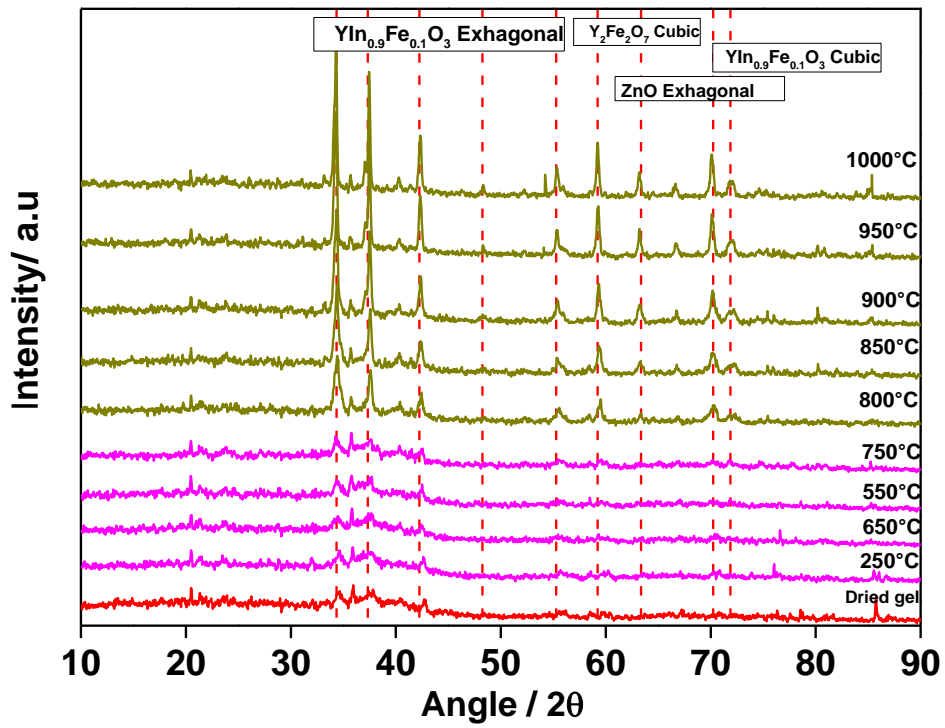


Figure 4. 12. XRD diffraction pattern of YInFeO–ZnO dried gel at different temperatures, underlining phase modifications.

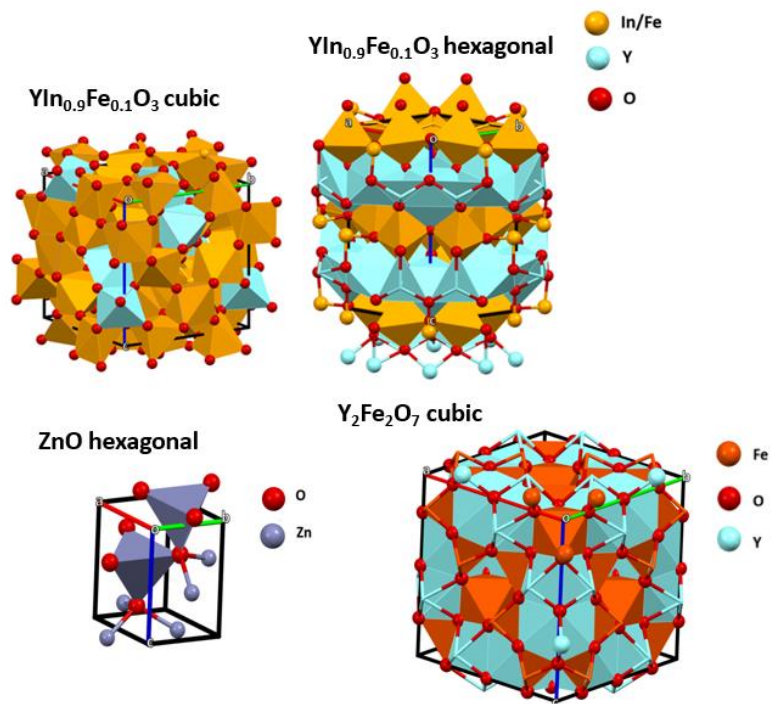


Figure 4. 13. Cubic and hexagonal crystal structures of YInFeO_3 in pigment calcined at at $750\text{ }^\circ\text{C}$ and $850\text{ }^\circ\text{C}$. ZnO in the pigment is present as hexagonal wurtzite structure.

For a detailed analysis of the XRD pattern of each calcined dried gel, used as pigment, and of each formed crystalline phase the section below give detailed information.

4.1.4 X-ray diffraction of calcined dried gels used as pigments

4.1.4.1 YInMnO-ZnO pigments

Figure 4. 14 shows the diffraction pattern of the calcined dried gel. The crystalline structures of the pigments calcined at temperatures higher than $750\text{ }^\circ\text{C}$ are shown in **Figure 4. 9** mentioned before. Considering the spectrum of pigment calcined at $800\text{ }^\circ\text{C}$, the $\text{YIn}_{0.9}\text{Mn}_{0.1}\text{O}_3$ shows a cubic phase and hexagonal one. The cubic-hexagonal transformation of $\text{YIn}_{0.9}\text{Mn}_{0.1}\text{O}_3$ starts at $800\text{ }^\circ\text{C}$ and finishes at $850\text{ }^\circ\text{C}$. Other authors found that cubic-hexagonal transformation begins at $900\text{ }^\circ\text{C}$ and ends at $1100\text{ }^\circ\text{C}$ [136], or starts at $1000\text{ }^\circ\text{C}$

and then finishes at 1250 °C [203] or at higher temperatures [90]. In this case, the pure hexagonal phase was obtained by employing lower calcination temperatures than other synthesis routes such as solid-state [136,206] or sol-gel [203]. The XRD pattern of YInMnO–ZnO pigment calcined at 850 °C exhibits a mixture of hexagonal YInO₃ phase and ZnO hexagonal wurtzite (space group P6₃mc) structure [207,208] (**Figure 4. 13**).

By Rietveld refinement performed by MAUD software [155,156] YInMnO–ZnO calcined at 800 °C results formed by a mixture of a 25.18 % of ZnO (space group P6₃mc) [209,210], 22.27 % hexagonal YInMnO₃, with a space group P6₃cm [51,136], and 52.55 % of cubic phase (space group Ia-3) [136] (**Figure 4. 9**). By increasing the calcination temperature up to 850 °C, the pigment turns into a mixture of two constituents, YIn_{0.9}Mn_{0.1}O₃ (74.31 %) and ZnO (25.68 %) with YIn_{0.9}Mn_{0.1}O₃ in hexagonal phase (space group P6₃cm) (**Table 4. 1**). The obtained weighted profile R factor (R_{wp}) and the best possible R_{wp} , called the expected R factor (R_{exp}), were considered as the parameters of refining quality (**Table 4. 1**). The background was fitted with third order polynomial. Cell values parameters of the hexagonal and cubic phase of YIn_{0.9}Mn_{0.1}O₃ were refined to improve the fit. The unit cell volumes, R_{wp} and R_{exp} , are very close to the values published in the literature [51,52]. Rietveld refinement underlines that the ratio between YIn_{0.9}Mn_{0.1}O₃ and ZnO is not 1:1, and, thus, differs from the nominal stoichiometry; probably this fact is correlated to the part of the pigments which remains amorphous or nanocrystalline, after the calcination process, thus resulting not detected. As shown in the pigments calcined at 800 °C and 850 °C In/Mn ions are trigonal bipyramidally coordinated by oxide ions, in accordance with Jose et al. [51]. All the shown crystalline structures have already been described in the literature.

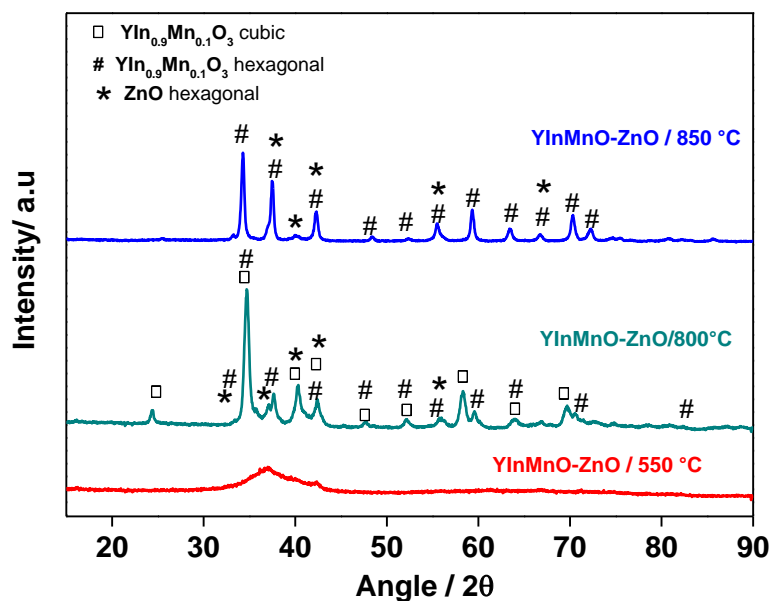


Figure 4. 14. XRD patterns of YInMnO-ZnO pigments with peaks marked according to different crystalline phases.

Table 4. 1. Crystallographic data for YInMnO-ZnO pigments calcined at 800 and 850 °C, obtained by Rietveld refinement using Maud software.

Reliability factors (%)		YIn _{0.9} Mn _{0.1} O ₃ Phases					ZnO Phases			
R _{wp}	R _{exp}	Cubic (Space group Ia-3)		Hexagonal (Space group P6 ₃ cm)			Hexagonal (Space group P6 ₃ mc)			
		Cell parameters (Å)	Amount (%)	Cell Parameters (Å)		Amount (%)	Cell parameters (Å)		Amount (%)	
		a		a	c		a	c		
YInMnO-ZnO/800 °C	11.37	4.55	10.5673 ± 0.0009	52.55 ± 1.12	6.3454 ± 0.0019	12.2777 ± 0.0043	22.27 ± 1.34	3.3158 ± 0.0007	5.2927 ± 0.0022	25.18 ± 0.01
YInMnO-ZnO/850 °C	10.85	7.30	--	--	6.2636 ± 0.0002	12.1708 ± 0.0007	74.31 ± 1.24	3.2568 ± 0.0004	5.2099 ± 0.0009	25.68 ± 0.00

4.1.4.2 YInCuO-ZnO pigments

Figure 4. 15 shows the diffraction pattern of calcined dried gel YInCuO-ZnO used as pigments. The pigments calcined at temperature of 650 °C has a semi-crystalline state.

Considering the spectrum of pigment calcined at 850 °C, the $\text{YIn}_{0.9}\text{Cu}_{0.1}\text{O}_3$ shows two cubic and hexagonal phases (**Figure 4. 11**). The cubic-hexagonal transformation of YInMnO-ZnO pigments is not present in YInCuO-ZnO pigments: at $\text{YInCuO-ZnO} / 850$ °C shows in fact cubic and hexagonal phase of $\text{YIn}_{0.9}\text{Cu}_{0.1}\text{O}_3$. In the case of YInCuO-ZnO pigments, the $\text{YIn}_{0.9}\text{Cu}_{0.1}\text{O}_3$ cubic phase is stable up to 1000 °C. Compared to manganese, copper seems to have an effect on promoting the transition of $\text{YIn}_{0.9}\text{Cu}_{0.1}\text{O}_3$ cubic phase to hexagonal at higher temperatures. As confirmed by the literature in similar compounds as $(\text{Cu}_{0.5}\text{Ti}_{0.5})_{1-x}\text{M}_x\text{O}_3$ pure hexagonal phases are ascertained at calcination temperatures of calcination higher than 1000 °C [69,134]. The formation of $\text{YIn}_{0.9}\text{Cu}_{0.1}\text{O}_3$ hexagonal phase at higher temperature than $\text{YIn}_{0.9}\text{Mn}_{0.1}\text{O}_3$ can also be dependent on the synthesis route parameters listed above in the case of YInMnO-ZnO pigments. The XRD pattern of YInCuO-ZnO pigment calcined at 850 °C exhibits a mixture of hexagonal and cubic YInCuO_3 phase and ZnO hexagonal wurtzite structure with cubic $\text{YC}_{0.4}$ phase (space group $Fm\bar{3}m$).

By Rietveld refinement performed by MAUD software [155,156] YInCuO-ZnO calcined at 850 °C results formed by a mixture of a 26.90 % of ZnO (space group $P6_3mc$) [209,210], 60.22 % hexagonal YInCuO_3 , with a space group $P6_3cm$ [51,136], and 10.16 % of cubic phase (space group $Ia-3$) [136]. The obtained weighted profile R factor (R_{wp}) and the expected R factor (R_{exp}), were considered as the parameters of refining quality (**Table 4. 2**). The background was fitted with third order polynomial, as sample YInMnO-ZnO . Cell values parameters were refined to improve the fit. It was verified that the lattice parameters and unit cell volumes are close to the existing literature about YInO_3 based pigments [52] and similar to the R_{wp} and R_{exp} for the pigments YInMnO-ZnO shown before.

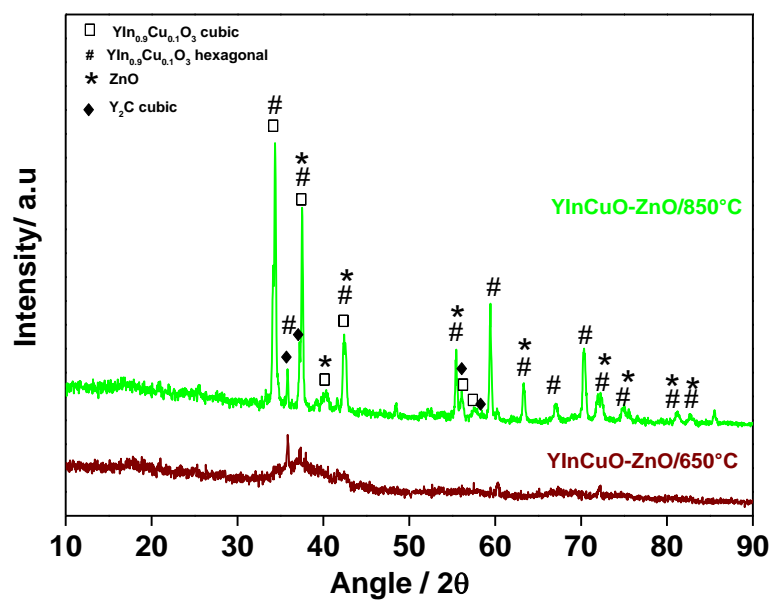


Figure 4. 15. XRD patterns of YInCuO-ZnO pigments with peaks marked according to different crystalline phases.

Table 4. 2. Crystallographic data for YInCuO–ZnO pigment calcined at 850 °C, obtained by Rietveld refinement using Maud software.

Reliability factors (%)		YIn _{0.9} Cu _{0.1} O ₃ Phases						ZnO Phases			YCo ₄ Phases	
R _{wp}	R _{exp}	Cubic (Space group Ia-3)		Hexagonal (Space group P6 ₃ cm)				Hexagonal (Space group P6 ₃ mc)			Cubic (Space group F m ⁻³ m)	
		Cell parameters (Å)	Amount (%)	Cell parameters (Å)		Amount (%)	Cell parameters (Å)		Amount (%)	Cell parameters (Å)	Amount (%)	
		a		a	c		a	c		a		
YInCuO–ZnO/850 °C	16.79	10.94	10.53 ± 0.0031	10.16 ± 0.26	6.2750 ± 0.0006	12.2490 ± 0.0040	60.22 ± 0.00	3.2626 ± 0.0005	5.2171 ± 0.0015	26.90 ± 0.35	5.0511 ± 0.0064	2.69 ± 0.09

4.1.4.3 YInFeO-ZnO pigments

Figure 4. 16 shows the XRD patterns of the investigated pigments. The pigment calcined at 650 °C have a semi-crystalline state, while pigments calcined at temperatures higher than 650 °C show crystalline phases. The crystalline phases of pigments are shown in the previously discussed section (**Figure 4. 13**).

Considering the spectrum of pigment calcined at 750 °C and 850 °C, the YIn_{0.9}Fe_{0.1}O₃ shows a cubic phase and a hexagonal one (**Figure 4. 13**). In the work of Rosati et al [211] cubic-hexagonal transformation in YIn_{0.9}Mn_{0.1}O₃ begins at 750 °C and ends at 850 °C. YIn_{0.9}Fe_{0.1}O₃ pigments show a coexistence of cubic and hexagonal phase up to 850 °C. Biphasic presence of YIn_{0.9}Fe_{0.1}O₃ (cubic and hexagonal) is not unusual [212]. Shukla et al.[212] observed a biphasic compound in YIn_{1-x}Fe_xO₃ (0.3 ≤ x ≤ 0.9) systems. A two phases compound is due to the presence of the transition from unstable cubic phase to hexagonal phase of YInO₃. Increasing the temperature decreases the cubic metastable phase and increases the

hexagonal phase. The stability of cubic phase up to 850 °C is likely to be related to the size difference between the A-site (Y^{3+}) and B-site ($In_{1-x}Fe_x$). Literature reports that the cubic-hexagonal transformation of $YInO_3$ shows the cubic-hexagonal transformation starts at 900 °C and ends at 1100 °C [136], or start at 1000 °C and finishes at 1250 °C [203] (or at higher temperatures [90]). In the work of Rosati et al [211] both cubic, and hexagonal phases of $YIn_{0.9}Fe_{0.1}O_3$, up to 850°C, are present. Both phases were obtained by employing lower calcination temperatures than other synthesis routes as solid-state [136,206] or sol-gel [203,211] as observed for $YInMnO-ZnO$ pigments.

The other crystalline phase present in pigments calcined at 750 °C and at 850°C is the $Y_2Fe_2O_7$ with pyrochlore structure. A third phase formation was observed in the study of Shukla et al. [212], which is the orthorhombic $YFeO_3$ garnet. In the present study, the cubic $Y_2Fe_2O_7$ pyrochlore structure is present instead of $YFeO_3$. Probably this is because different precursors are used respect to Shukla et al. [212] thus leading to a modification of the atomic recombination. Yttrium iron garnet $Y_3Fe_5O_{12}$ via-citrate sol-gel could be obtained combining Y and Fe with the molar ratio 3:5 [147].

As it can be observed by comparing data of **Table 4. 3**, with those in **Table 4. 1** and **Table 4. 2**, the lattice parameters of $YIn_{0.9}M_{0.1}(Mn, Cu, Fe)O_3-ZnO$ pigments remain unchanged. This can be explained by the fact that Mn, Cu, and Fe do not modify identified crystalline structures. When Fe or Mn are in the $YIn_{0.9}M_{0.1}O_3$ structure, hexagonal and cubic structures are maintained with unchanged lattice parameters, probably for the similar ionic radii of Mn^{3+} (0.066–0.067 nm) and Fe^{3+} (0.064 nm) [213]. Even if Cu^{3+} ionic radius is of 0.054 nm [214]

the lattice parameters remain the same for pigments having Mn^{3+} and Fe^{3+} , confirming $\text{YIn}_{0.9}\text{M}_{0.1}\text{O}_3$ as a suitable compound for different doping elements [69].

By Rietveld refinement performed by MAUD software $\text{YInFeO-ZnO}/750\text{ }^\circ\text{C}$ results formed by a mixture of a 20.76 % of hexagonal ZnO (space group $\text{P6}_3\text{mc}$) [209,210] (**Table 4. 3**), 36.77 % hexagonal YInO_3 , with a space group $\text{P6}_3\text{cm}$ [51,139] [136], and 42.13 % of cubic phase of YInO_3 (space group Ia-3) [136]. We can claim that $\text{Y}_2\text{Fe}_2\text{O}_7$ is an impurity as it was detected the 0.32 %. By increasing the calcination temperature up to $850\text{ }^\circ\text{C}$, the pigment turns into a mixture of the three constituents in the different percentages; YInO_3 cubic is the 16.41 %, ZnO is 26.75 %, while YInO_3 in hexagonal phase is the 56.21 %. A small fraction of $\text{Y}_2\text{Fe}_2\text{O}_7$ (0.60 %) is another identified phase. The obtained weighted profile R factor (R_{wp}) and the R factor (R_{exp}), were considered refining quality parameters, as for the other two pigments discussed before. The background was fitted with third order polynomial.

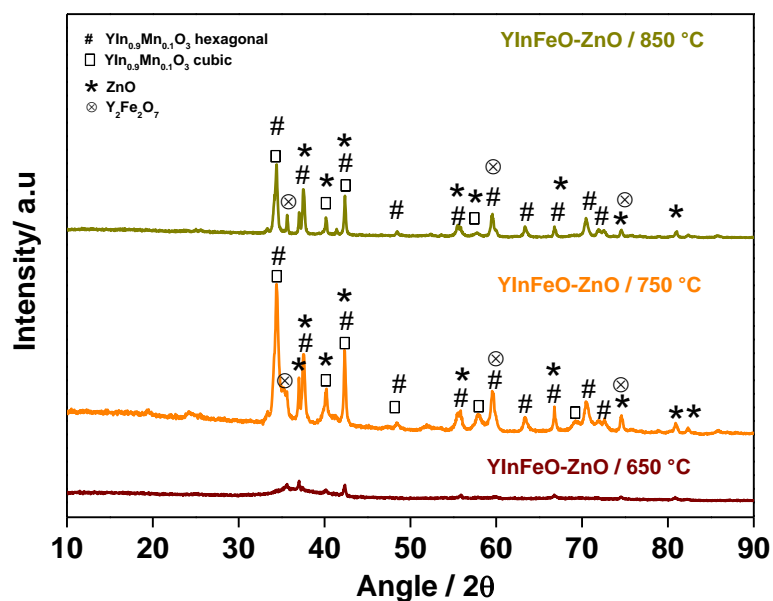


Figure 4. 16. XRD patterns of YInFeO-ZnO pigments with peaks marked according to different crystalline phases.

Table 4. 3. Crystallographic data for YInFeO-ZnO pigment calcined at 750 °C and 850 °C, obtained by Rietveld refinement using Maud software.

		Reliability factors (%)		YIn _{0.9} Fe _{0.1} O ₃ Phases				ZnO Phases			Y ₂ Fe ₂ O ₇ Phases	
	<i>R</i> _{wp}	<i>R</i> _{exp}	Cubic (Space group Ia-3)		Hexagonal (Space group P6 ₃ cm)		Hexagonal (Space group P6 ₃ mc)		Cubic (Space group F23)			
			Cell parameters (Å)	Amount (%)	Cell parameters (Å)	Amount (%)	Cell parameters (Å)	Amount (%)	Cell parameters (Å)	Amount (%)		
			<i>a</i>		<i>a</i>	<i>c</i>	<i>a</i>	<i>c</i>	<i>a</i>			
YInFeO-ZnO/750 °C	17.92	4.43	10.50 ± 0.0023	42.13 ± 1.68	6.2658 ± 0.0008	12.2406 ± 0.0030	36.77 ± 1.45	3.2626 ± 0.0005	5.2171 ± 0.0015	20.76 ± 0.00	10.1737 ± 0.0023	0.32 ± 0.02
YInFeO-ZnO/850 °C	29.21	7.47	10.6318 ± 0.0004	16.42 ± 1.64	6.2776 ± 0.0008	12.2519 ± 0.0003	56.21 ± 3.34	3.2665 ± 0.0007	5.2295 ± 0.0020	26.75 ± 0.01	10.1810 ± 0.0027	0.60 ± 0.06

4.1.5 Colorimetric analysis on pigments

4.1.5.1 YInMnO–ZnO pigments

The color is measured according to CIE-1976 $L^*a^*b^*$ colorimetric method [68]. **Table 4. 4** shows the colorimetric coordinates of pigments calcined at different temperatures. The highest value of L^* is showed by the light ochre pigment calcined at 550 °C (**Figure 4. 17**). It is interesting to note that the color coordinates of the ochre pigment show comparable color coordinates with traditional tiles and brick made with clays [215,216]. The other two colors are two shades of blue: a cyan blue (pigment calcined at 800 °C) and a deep blue (pigment calcined at 850 °C); showing lower value of L^* and a shift for a^* and b^* coordinates towards negative values. **Figure 4. 18** reports the visible reflectance spectra of the YInMnO–ZnO pigment powders. Visible reflectance spectra of ochre pigments show that pigment calcined at 550 °C is the most reflective in the red region (63 %), so it is the reddest pigment, as confirmed by colorimetric coordinate a^* (7.96). As the temperature increases, L^* value tends to decrease, and the blue component increases (b^* changing to more negative values). Color change is characterized by a negative shift of $L^*a^*b^*$ coordinates (**Table 4. 4**), with a progressive darkening of the pigments, as shown in L^* plot in **Figure 4. 17**.

Visible reflectance spectra of YInMnO–ZnO pigments (**Figure 4. 18**) show that pigment calcined at 550 °C is the most reflective in the red region (63 %), so it is the reddest pigment, as confirmed by colorimetric coordinate a^* (7.96). As the temperature increases, L^*

value tends to decrease, and the blue component increases (b^* changing to more negative values).

Table 4. 4. Colorimetric coordinates values for YInMnO–ZnO pigments calcined at different temperatures.

YInMnO–ZnO pigments calcined temperatures	COLOR COORDINATES		
	L^*	a^*	b^*
550 °C	62.55	5.88	13.67
800 °C	59.13	-9.41	-8.34
850 °C	54.92	-2.84	-40.88

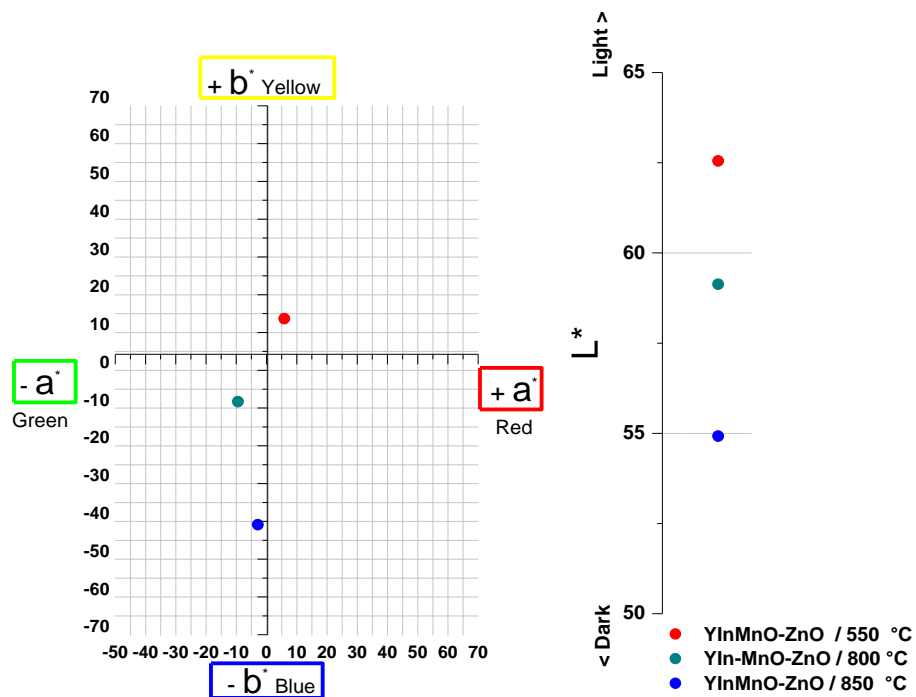


Figure 4. 17. Colorimetric coordinates values for YInMnO–ZnO pigments calcined at different temperatures.

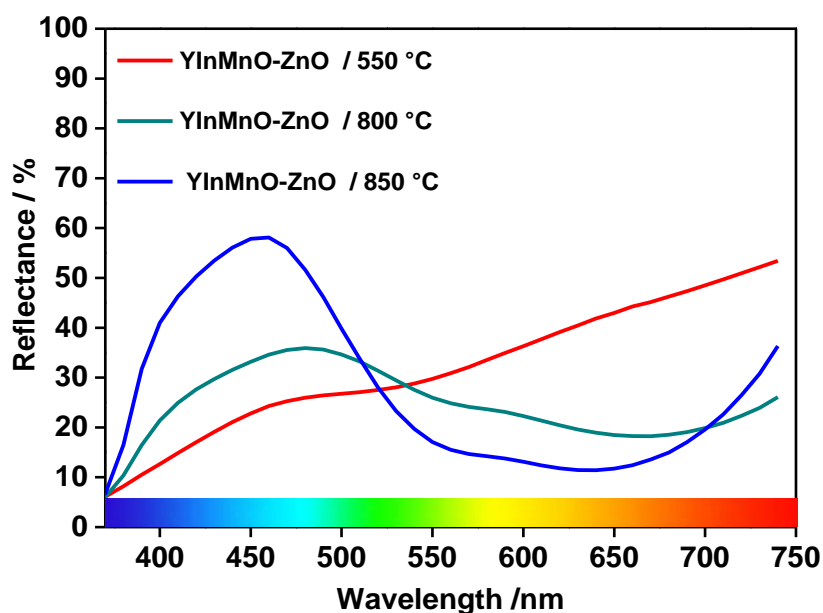


Figure 4. 18. Visible light diffuse reflectance spectra for YInMnO–ZnO pigments.

4.1.5.2 YInCuO–ZnO pigments

Table 4. 5 shows the colorimetric coordinates of YInCuO–ZnO pigments calcined at different temperatures. The highest value of L^* is showed by the pigment calcined at 850 °C (Figure 4. 19). In the case of copper based pigments color coordinates of the YInCuO–ZnO /650 °C match color coordinates of Verona Green earth pigment (pigments derived from minerals calcedonite and glauconite) [217]. YInCuO–ZnO /850 °C has color coordinates comparable with malachite pigment ($\text{Cu}_2(\text{OH})_2\text{CO}_3$) [217]. From YInCuO–ZnO /650 °C to YInCuO–ZnO /850 °C L^* value is slightly increased (Figure 4. 19), showing a modification from a deep green to a lighter color (pigment calcined at 850 °C). Increasing calcination temperature a^* shift to more negative values (toward green) and the blue component decreases (b^* changing to more negative values).

Visible reflectance spectra of YInCuO–ZnO pigments (**Figure 4. 20**) show that pigment calcined at 850 °C is the most reflective in the green region (57%), so it is the greenest pigment, as confirmed by colorimetric coordinate a^* (-16.74). As the temperature increases, L^* value tends to increase, and the blue component decreases (b^* changing to more negative values). Color change is characterized by a negative shift of $L^*a^*b^*$ coordinates with a clearing of the pigment, as shown in L^* plot in **Figure 4. 19**.

Table 4. 5. Colorimetric coordinates values for YInCuO–ZnO pigments calcined at different temperatures.

YInCuO–ZnO pigments	COLOR COORDINATES		
	L^*	a^*	b^*
650 °C	74.75	-7.54	14.70
850 °C	75.93	-16.74	10.19

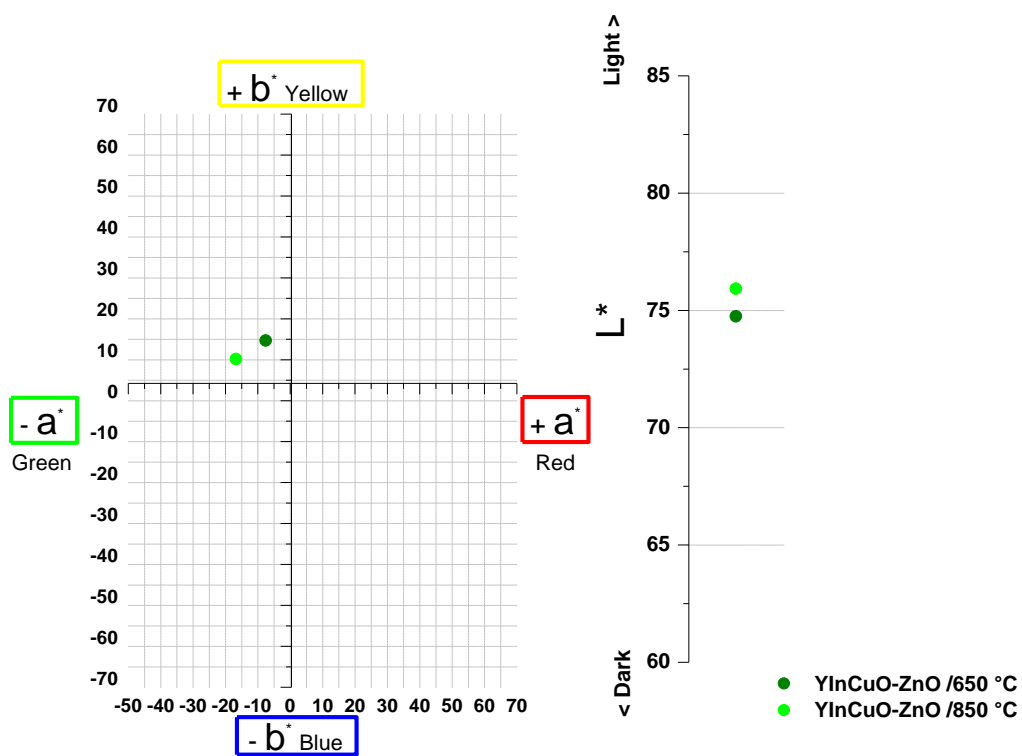


Figure 4. 19. Colorimetric coordinates values for YInCuO–ZnO pigments calcined at different temperatures.

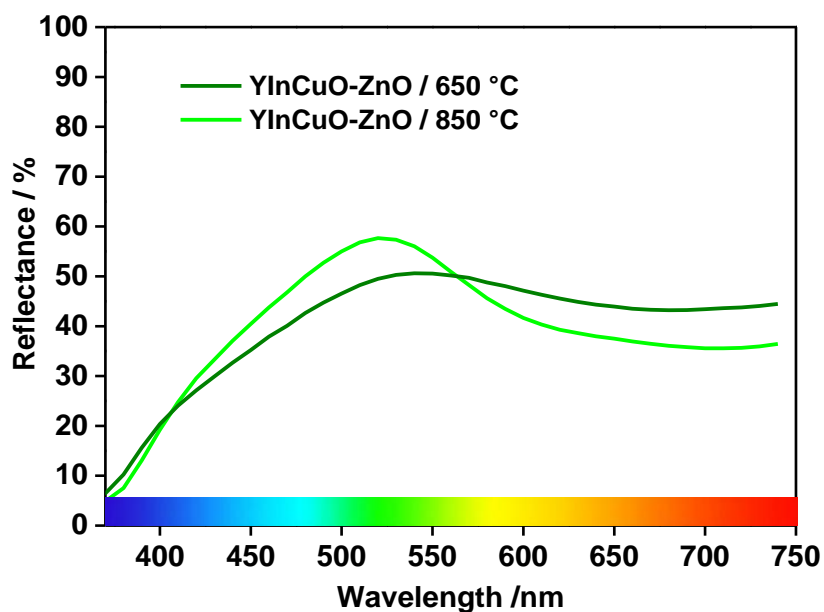


Figure 4. 20. Visible light diffuse reflectance spectra for YInCuO–ZnO pigments.

4.1.5.3 YInFeO–ZnO pigments

Colorimetric coordinates are listed in **Table 4. 6**. **Figure 4. 21** represents values of colorimetric coordinates of pigments in CIE-1976 $L^*a^*b^*$ color space. The highest value of L^* is showed by the YInFeO–ZnO calcined at 850 °C. It is evident that the most saturated color is the pigment YInFeO–ZnO /650 °C. The a^* and b^* values increase increasing temperature of calcination. The increase in calcination temperature involves also an increase in the visible reflectance towards yellow region of visible spectrum (**Figure 4. 22**).

Table 4. 6. Colorimetric coordinates values for YInFeO–ZnO pigments calcined at different temperatures.

YInFeO–ZnO pigments	COLOR COORDINATES		
	L^*	a^*	b^*
650 °C	85.14	0.1	18.57
750 °C	85.73	3.43	21.00
850 °C	87.05	4.18	23.53

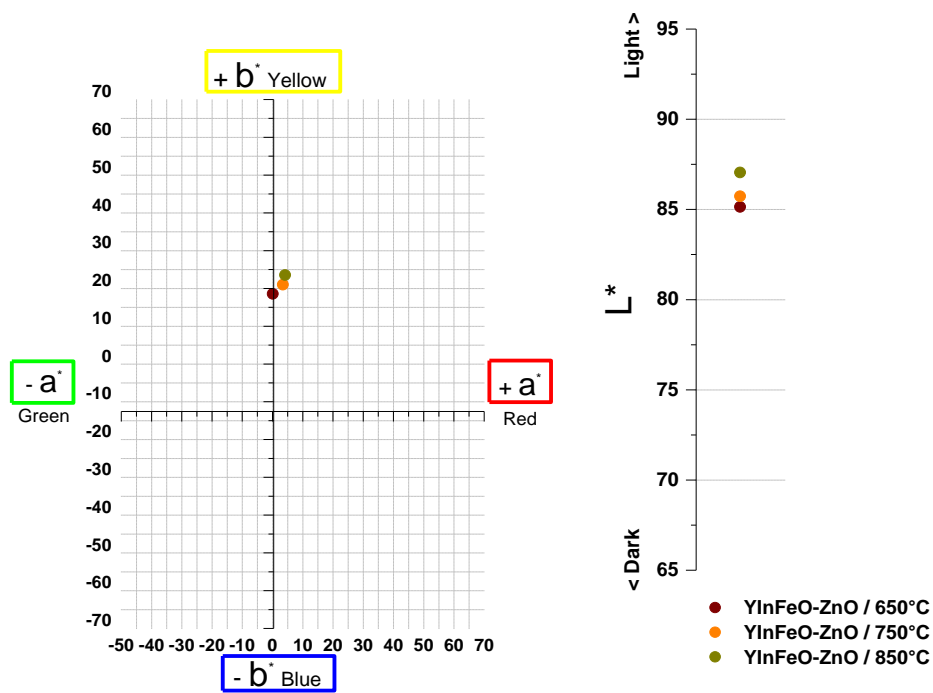


Figure 4. 21. Colorimetric coordinates values for YInFeO–ZnO pigments calcined at different temperatures.

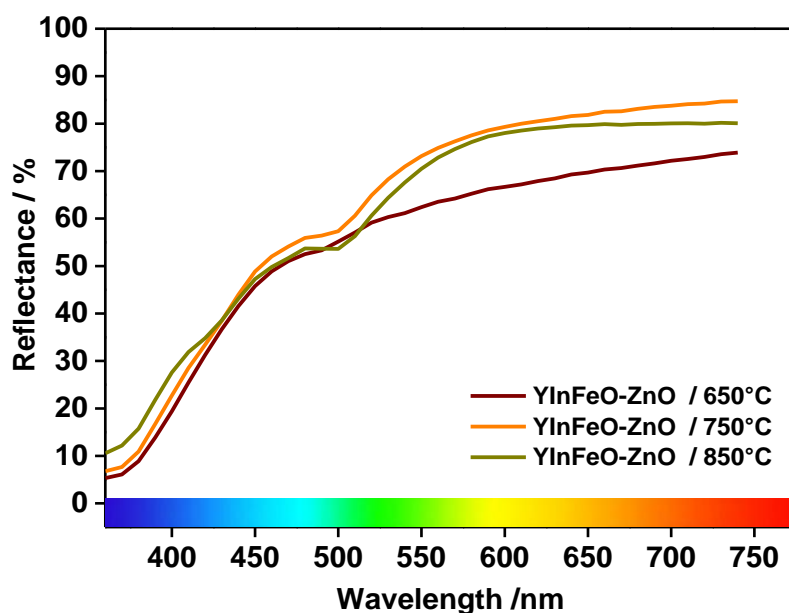


Figure 4. 22. Visible light diffuse reflectance spectra for YInFeO–ZnO pigments.

4.1.6 SEM Observation and analysis

The pictures below represent SEM images of synthesized pigments with the corresponding EDS pictures.

4.1.6.1 YInMnO–ZnO pigments

Looking at the picture of YInMnO–ZnO /550 °C pigment at the lowest magnification (**Figure 4. 23.a**) are still recognizable the pores and voids of dried -gel typical sponge like structure. In SEM pictures of other pigments, YInMnO–ZnO /800 °C and YInMnO–ZnO /850 °C, (**Figure 4. 25** and **Figure 4. 27**) porous particles of dried gel are not present. So that means that highest amount of the organic fraction was decomposed. The mapping results in **Figure 4. 24**, **Figure 4. 26** and **Figure 4. 28** show uniform distribution of Y, In, Mn and ZnO. In all

YInMnO–ZnO pigments there is no a uniform morphology and shape, probably due to the grinding with mortar.

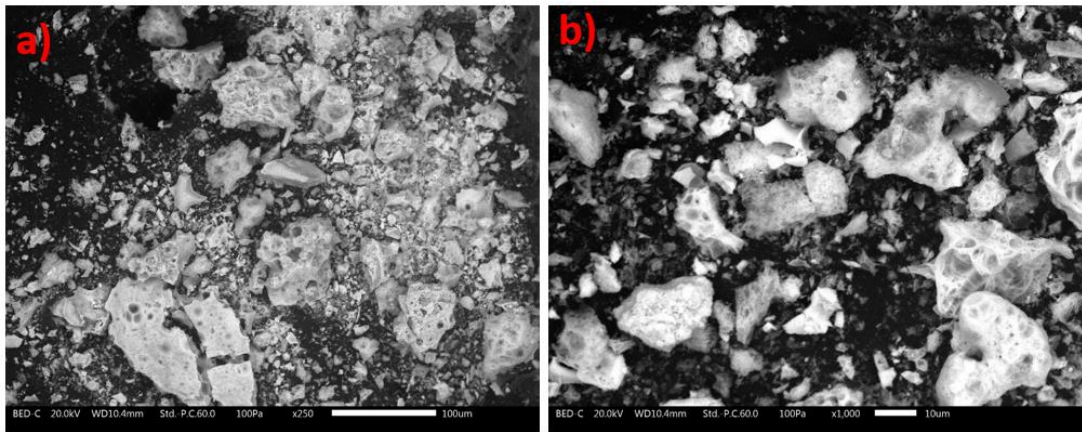


Figure 4. 23. SEM pictures of YInMnO – ZnO /550 °C pigment at two different magnifications.

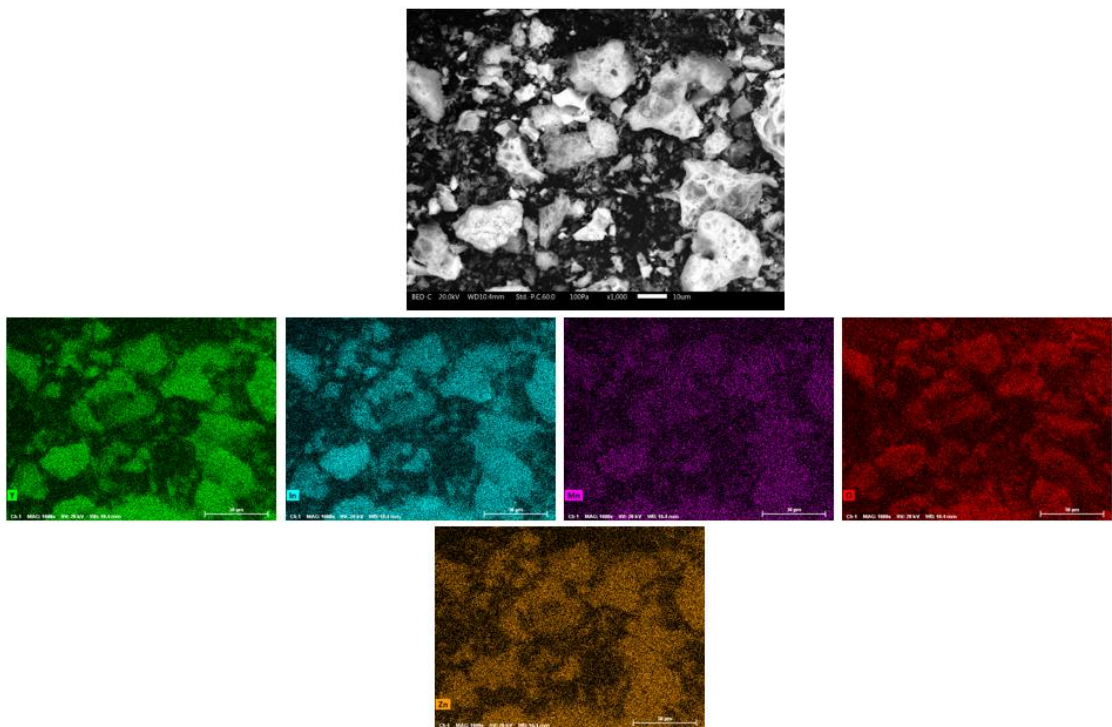


Figure 4. 24. SEM pictures of YInMnO–ZnO /550 °C pigment at the highest magnification with the corresponding EDS elements distribution map.

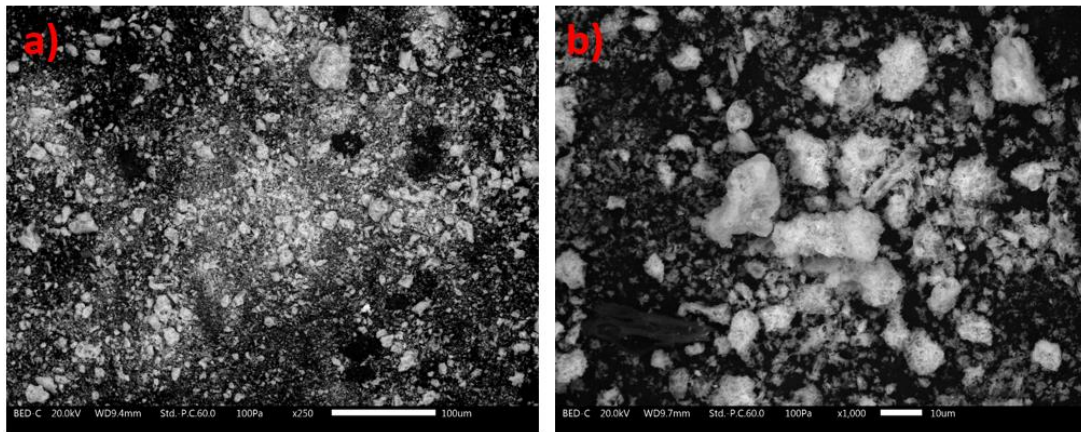


Figure 4. 25. SEM pictures of YInMnO–ZnO /800 °C pigment at the highest magnification with the corresponding EDS elements distribution map.

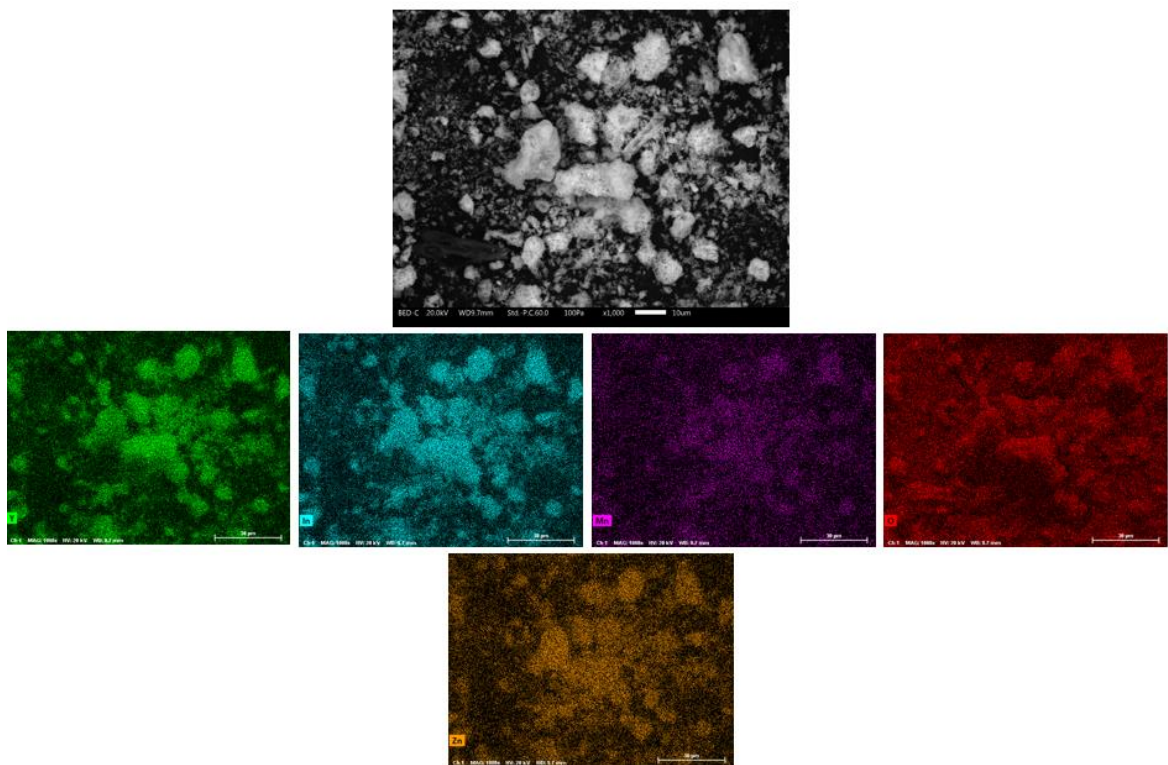


Figure 4. 26. SEM pictures of YInMnO–ZnO /800 °C pigment at the highest magnification with the corresponding EDS elements distribution map.

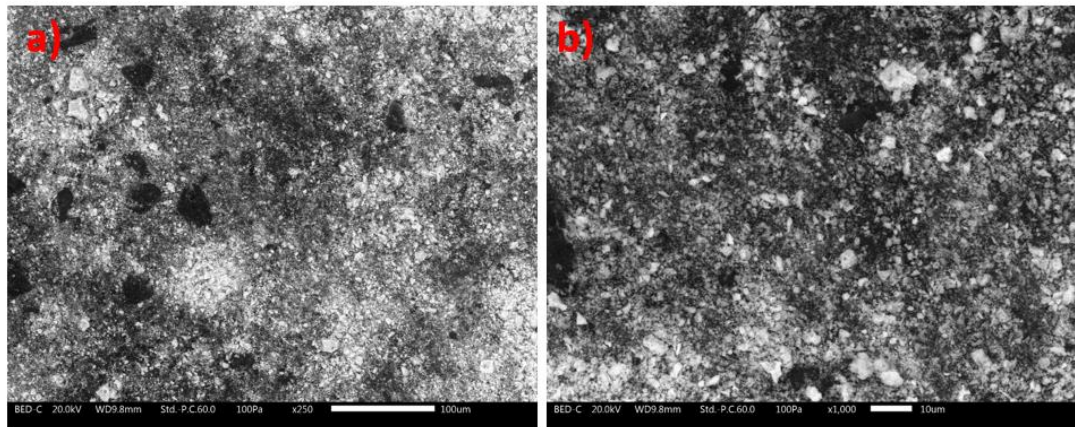


Figure 4. 27. SEM pictures of YInMnO-ZnO /850 °C pigment at higher (a) and lower (b) magnifications.

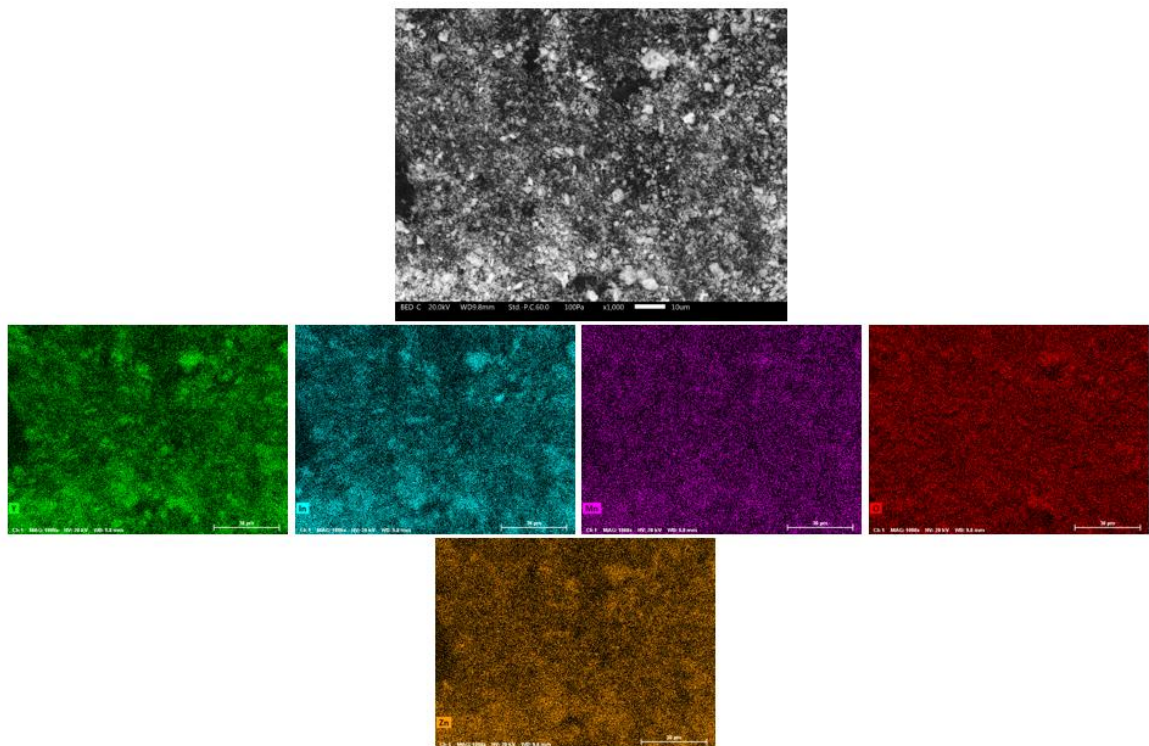


Figure 4. 28. SEM pictures of YInMnO-ZnO /850 °C pigment at the highest magnification with the corresponding EDS elements distribution map.

4.1.6.2 YInCuO-ZnO pigments

The shapes and dimensions of YInCuO-ZnO pigments are visible in **Figure 4. 29** (YInCuO-ZnO /650 °C) and **Figure 4. 31** (YInCuO-ZnO /850 °C). As for pigments shown

before there are more pores in particles of YInCuO–ZnO /650 °C pigment, while YInCuO–ZnO /850 °C shows small flakes shape particles. From EDS mapping (Figure 4. 30 and Figure 4. 32) it is clear that all elements are equally distributed in the pigments.

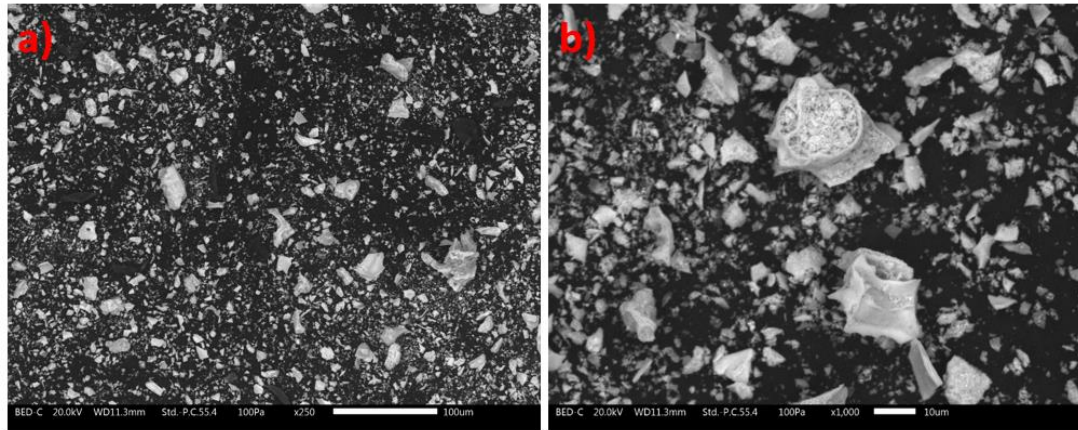


Figure 4. 29. SEM pictures of YInCuO–ZnO /650 °C pigment at higher (a) and lower (b) magnifications.

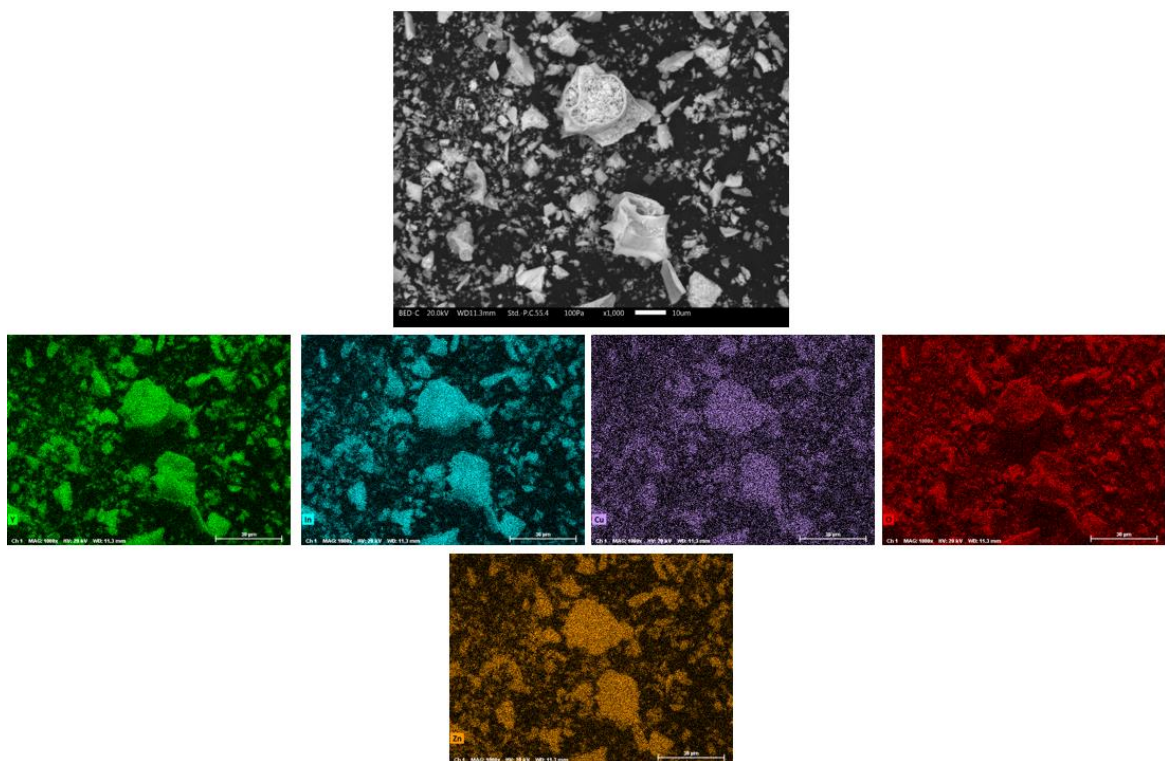


Figure 4. 30. SEM pictures of YInCuO–ZnO /650 °C pigment at the highest magnification with the corresponding EDS elemental mapping.

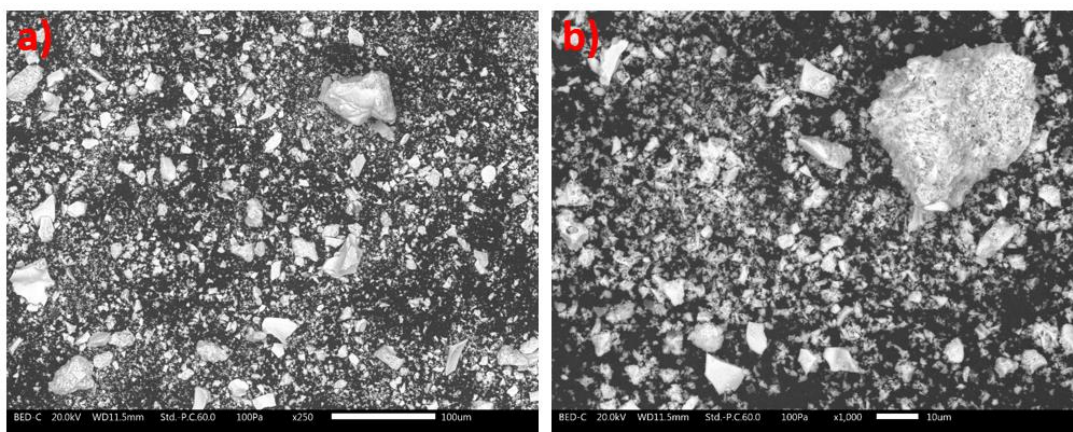


Figure 4. 31. SEM pictures of YInCuO–ZnO /850 °C pigment at higher (a) and lower (b) magnifications.

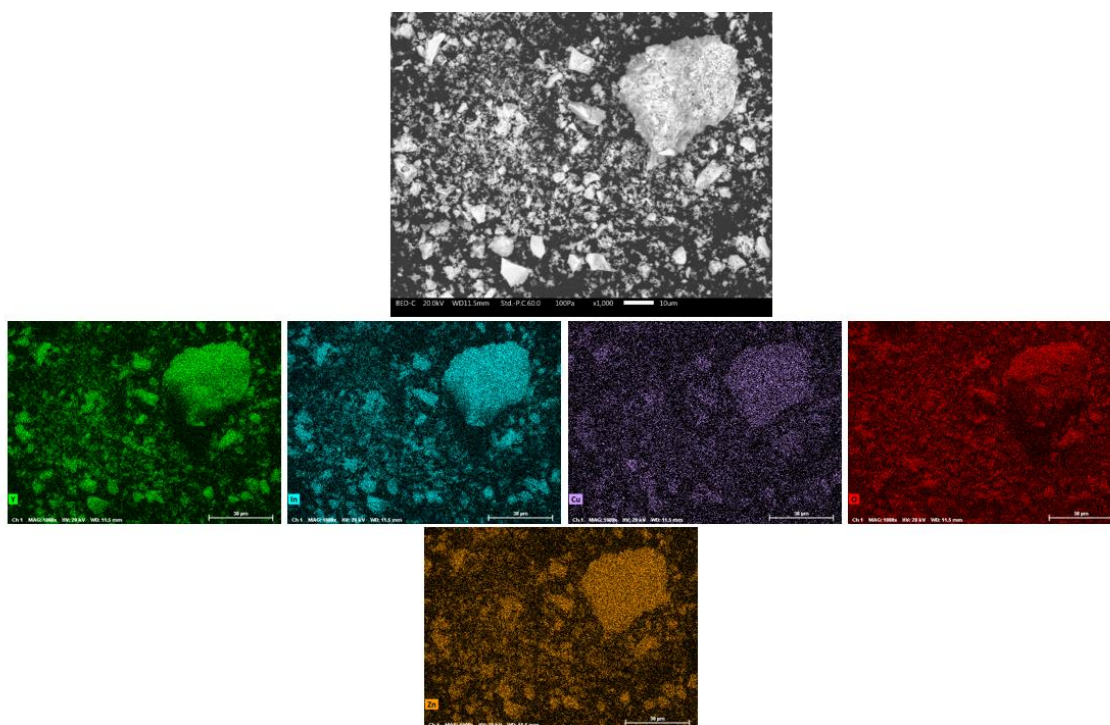


Figure 4. 32. SEM pictures of YInCuO–ZnO /850 °C pigment at the highest magnification with the corresponding EDS elemental mapping.

4.1.6.3 YInFeO–ZnO pigments

SEM pictures (**Figure 4. 33**, **Figure 4. 35** and **Figure 4. 37**) show typical rounded dried gel particles together with well-calcined particles with flakes shape morphology. Small

particle with cavity are also visible in pigment YInFeO-ZnO /850 °C (**Figure 4. 37**). This is probably because some dried gels particles remain unburnt during calcination process in the furnace.

An interesting observation can be done observing EDS mapping. All the elements of the pigments are uniformly distributed but Zn tends to be concentrated in specific areas of YInFeO-ZnO images. ZnO is not uniformly distributed and tends to form clusters. Observing **Figure 4. 38** ZnO areas correspond to large hexagonal particles clearly visible in **Figure 4. 37.b**.

In sol-gel route in fact nitric acid bath tends to dissolve the zinc oxide. After the re-precipitation of ZnO suitable environmental conditions (the evaporation of the acidic solvent) allows the precipitate to grow and larger particles were formed [218]. A reduction in pH, together with NO_3^- ions, is responsible of modification in shapes and increase in size of ZnO. As demonstrated by Amin et al.[219] ZnO growth in nitric acid is governed by precipitation of metallic cation (Zn^{2+}) and further ripening of the corresponding oxide [219].

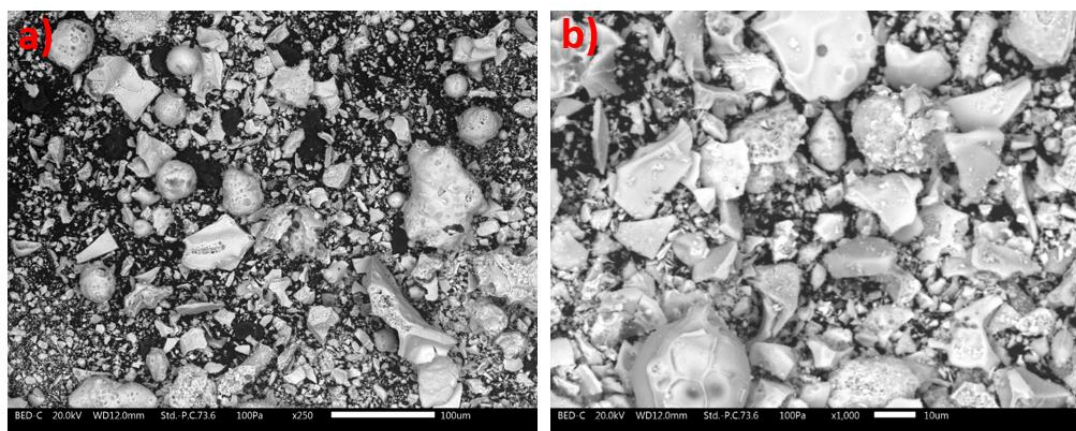


Figure 4. 33. SEM pictures of YInFeO-ZnO /650 °C pigment at higher (a) and lower (b) magnifications.

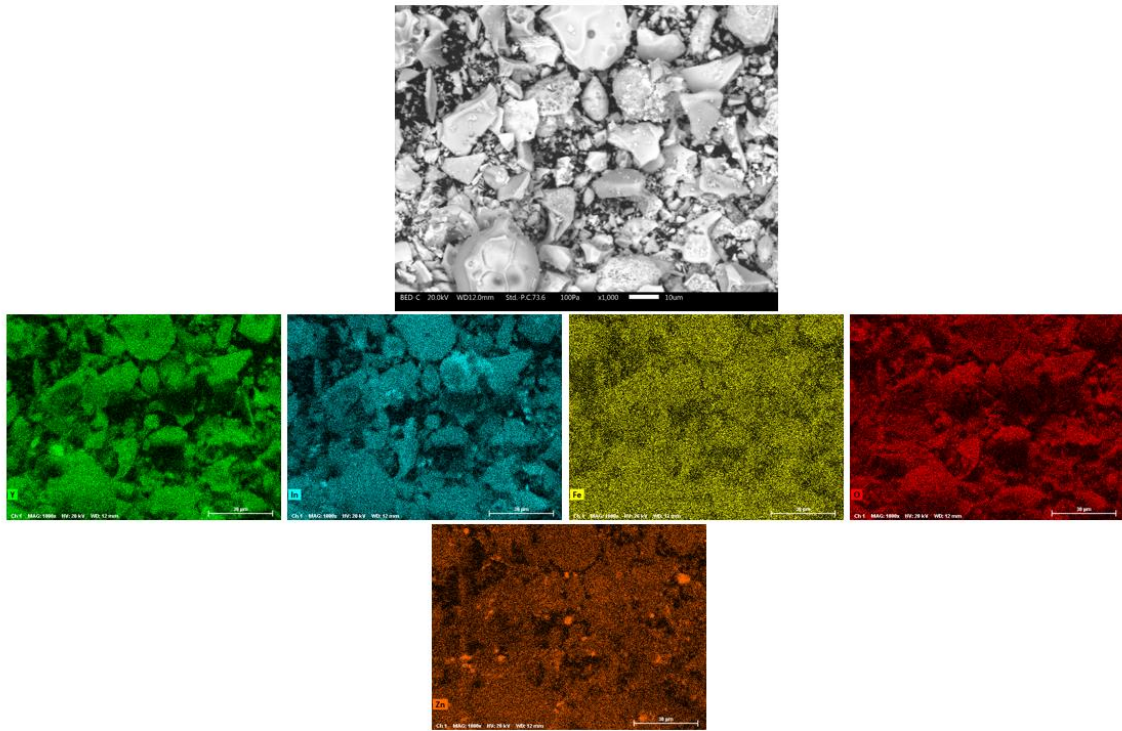


Figure 4. 34. SEM pictures of YInFeO–ZnO /650 °C pigment at the highest magnification with the corresponding EDS elemental mapping.

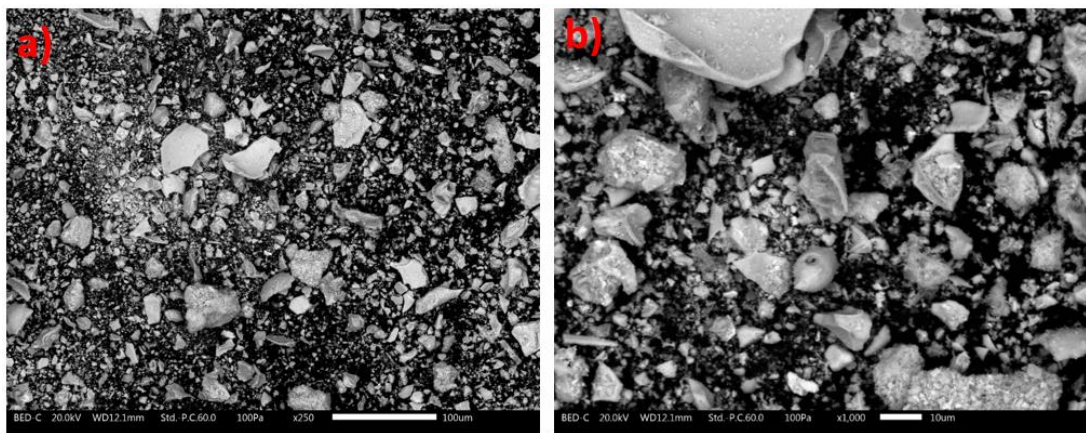


Figure 4. 35. SEM pictures of YInFeO–ZnO /750 °C pigment at higher (a) and lower (b) magnifications.

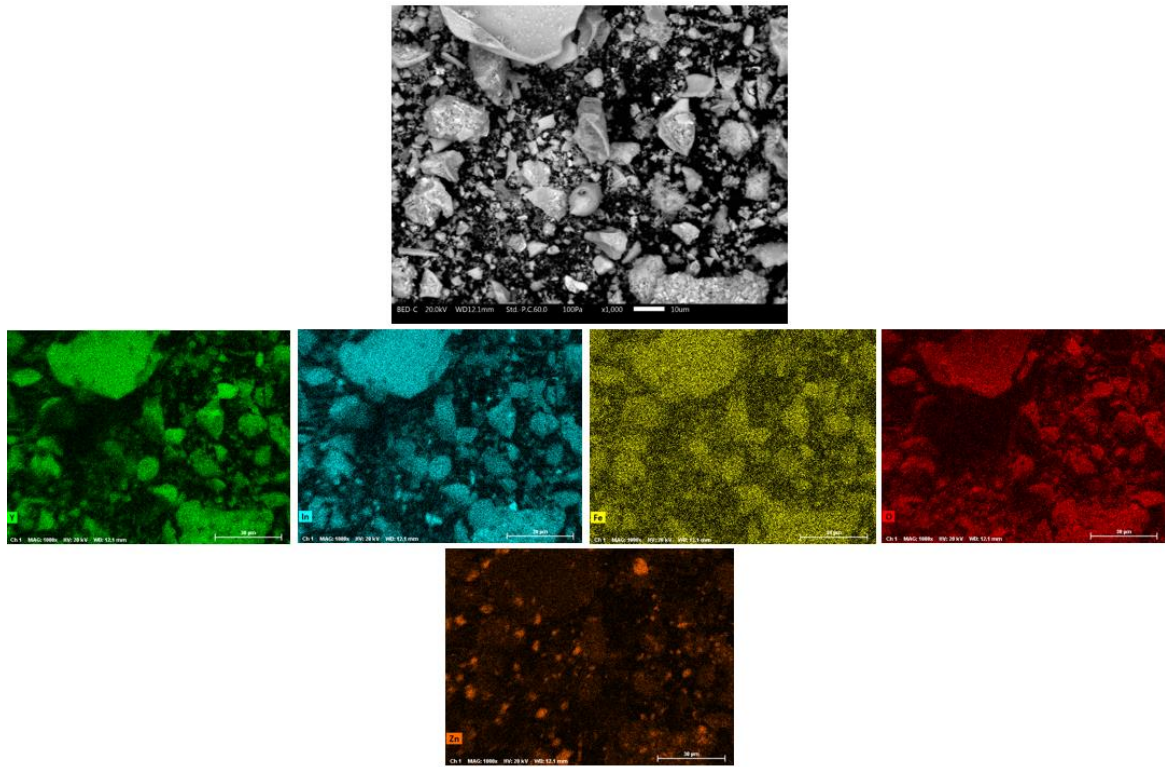


Figure 4. 36. SEM pictures of YInFeO-ZnO /750 °C pigment at the highest magnification with the corresponding EDS elemental mapping.

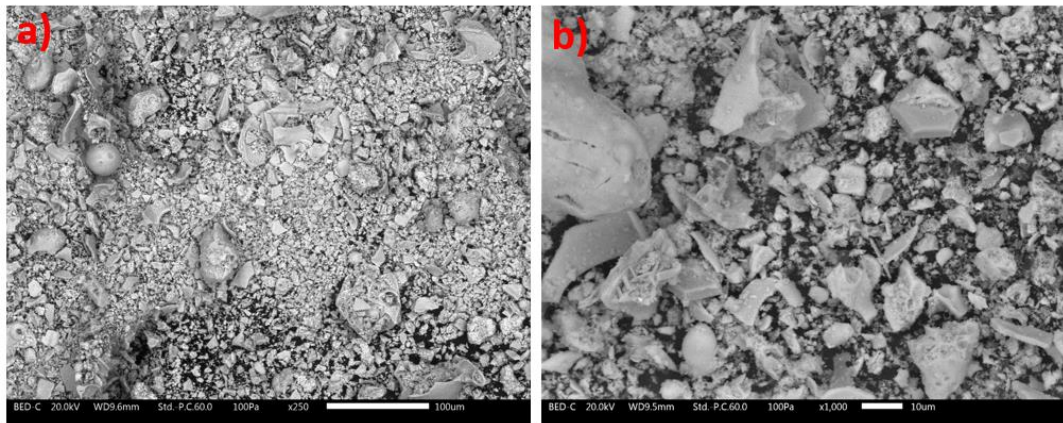


Figure 4. 37. SEM pictures of YInFeO-ZnO /850 °C pigment at higher (a) and lower (b) magnifications.

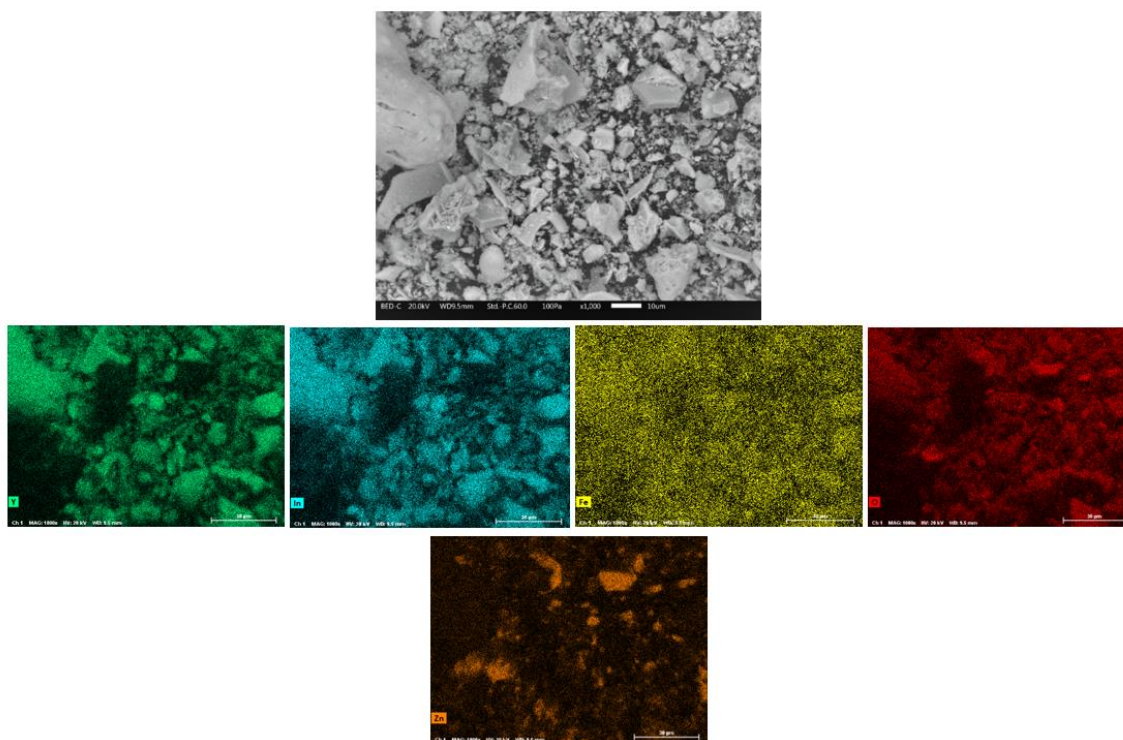


Figure 4. 38. SEM pictures of YInFeO–ZnO /850 °C pigment at the highest magnification with the corresponding EDS elemental mapping.

4.1.7 Near Infrared Reflectance of pigments

4.1.7.1 YInMnO–ZnO pigments

Figure 4. 39 shows the near-infrared (NIR) reflectance (a) and the corresponding NIR solar reflectance obtained according to the ASTM standards G173-03 [157] (b) of YInMnO–ZnO pigments. By increasing the calcination temperature from 550 °C to 850 °C, a relevant increase in the NIR reflectance is observed. The high value of NIR reflectance of each pigment is due to the presence of ZnO, which is recognized to show high NIR reflectance [38]. **Table 4. 7** underlines the value of calculated solar reflectance and NIR reflectance at 1100 nm (in the heat-producing region of the NIR domain). Compared to

spectra in **Figure 4. 39.a**, in solar reflectance spectra of **Figure 4. 39.b** YInMnO–ZnO /550 °C shows higher solar reflectance values in the range of 750-1100 nm. The solar reflectance values tabulated in **Table 4. 7** are of 73.78 % and 62.39 % in YInMnO–ZnO /550 °C and YInMnO–ZnO /800 °C respectively. The values of NIR reflectance at 1100 nm are of 84.48 % for YInMnO–ZnO /550 °C and 76.61 % for YInMnO–ZnO /800 °C confirming that for cool coatings application the pigment calcined at lowest temperature presents a promising use. However, the best pigment in YInMnO–ZnO group is YInMnO–ZnO /850 °C, as confirmed by spectra in **Figure 4. 39** and values in **Table 4. 7**. The increase in NIR reflectance increasing calcination temperature is probably due to the transition from a "dense" semicrystalline structure, with high carriers concentration, in which light is subjected continuous scattering and adsorption, to a crystalline structure where the concentration of the free carrier is reduced for charge transfer, as the $Mn^{3+}-O^2$ due to temperature increase [220]. Nevertheless, the high reflectance values of YInMnO–ZnO /550 °C are due to the fact that light-colored pigments (e.g. white, pale yellow, and pale brown) are recognized to reflect NIR light better than saturated colors pigments [221].

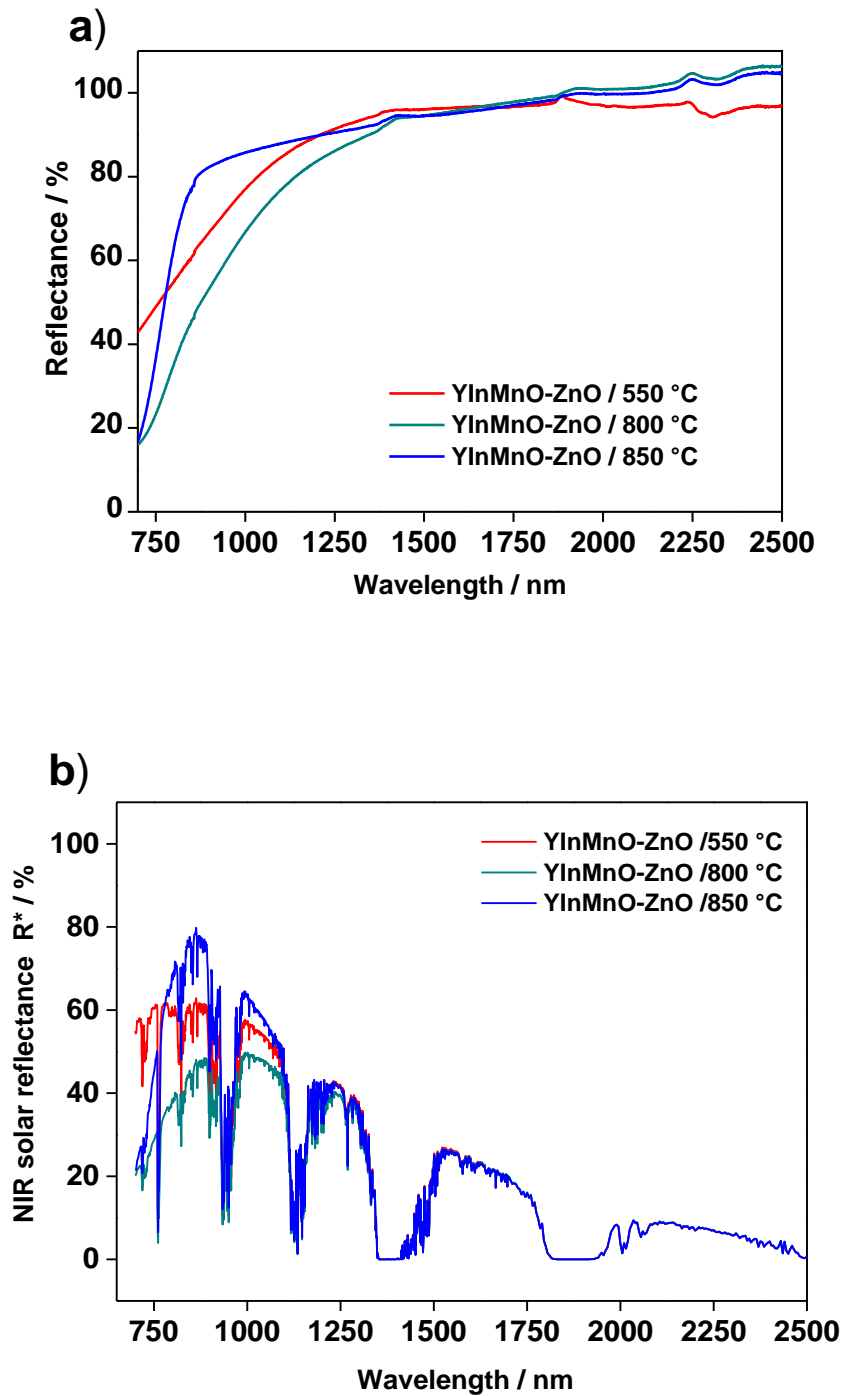


Figure 4. 39. NIR reflectance of the YInMnO–ZnO pigment powders calcined at different temperatures (a) and NIR solar reflectance spectra, obtained in compliance with ASTM G173-03 standard (b).

Table 4. 7. NIR reflectance at 1100 nm and solar reflectance of the YInMnO–ZnO synthesized pigments.

Pigments	NIR reflectance at 1100 nm (%)	Solar reflectance R* (%)
YInMnO–ZnO /550 °C	84.48	73.78
YInMnO–ZnO /800 °C	76.61	62.39
YInMnO–ZnO /850 °C	87.64	76.11

4.1.7.2 YInCuO–ZnO pigments

The NIR spectral reflectance and corresponding NIR solar reflectance of the two pigments YInCuO–ZnO are shown in **Figure 4. 40**. The two pigments show comparable values of NIR reflectance (**Figure 4. 40.a**). Even if a crystalline pigment is associated with an increase in the NIR reflectance, as discussed above in the case of YInMnO–ZnO, an high value of reflectance in amorphous YInCuO–ZnO /650°C can be due to other factors discussed before, as the presence of ZnO and light colors. Looking the values of **Table 4. 8** we can observe that at 1100 nm the YInCuO–ZnO /850 °C has higher reflectance values (75.05 %) with respect to YInCuO–ZnO /650 °C (67.83 %), while solar reflectance values are almost comparable. Comparing values of YInMnO–ZnO and YInCuO–ZnO pigments the increase or decrease in NIR reflectance seem to be related to factors different from crystalline phase and the presence of ZnO. The different reflectance values seem to be related to the presence of Mn or Cu in the $Y_{0.9}In_{0.1}O_3$ structure.

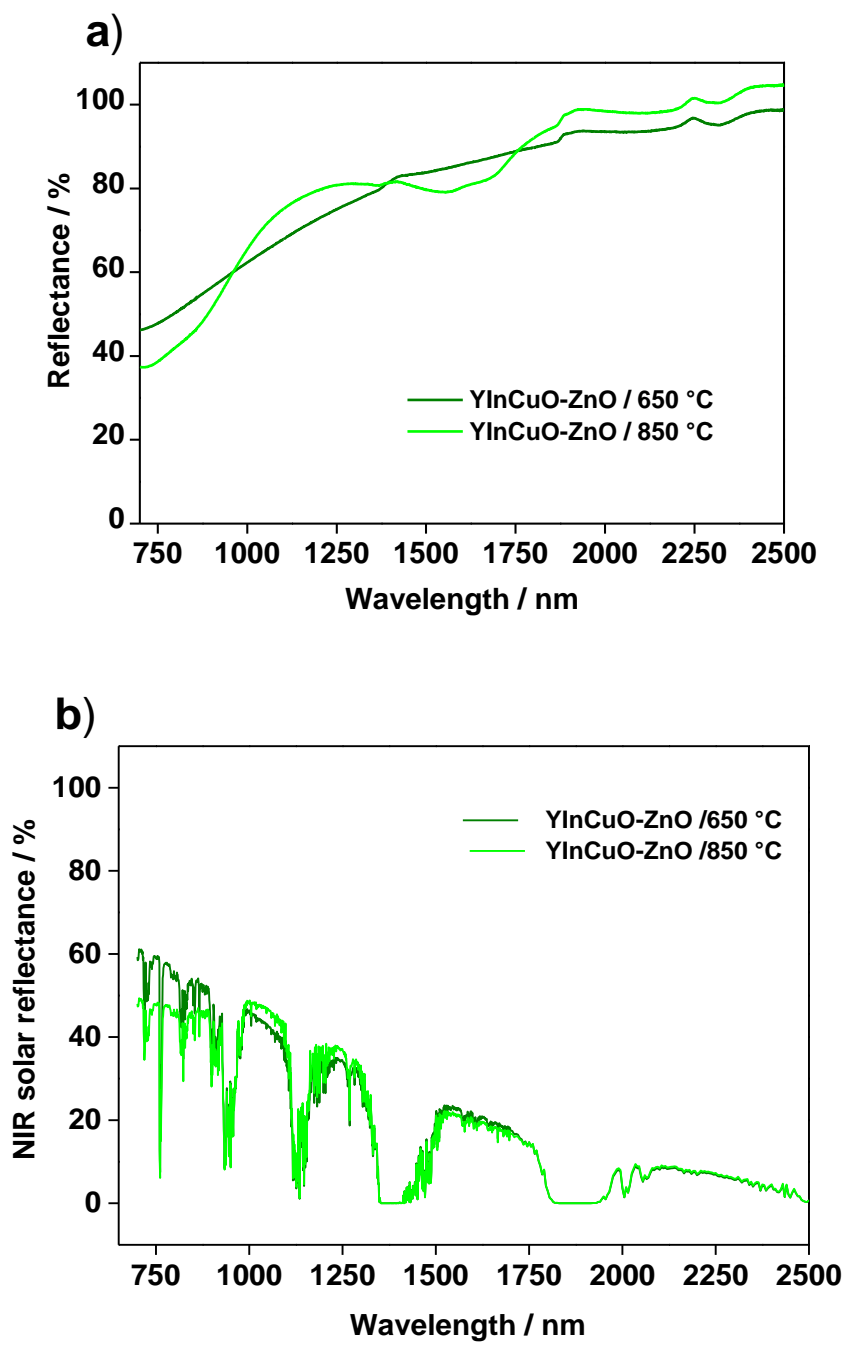


Figure 4. 40. NIR reflectance of the YInCuO–ZnO pigment powders calcined at different temperatures (a) and NIR solar reflectance spectra, obtained in compliance with ASTM G173-03 standard (b).

Table 4. 8. NIR reflectance at 1100 nm and solar reflectance of the YInCuO–ZnO synthesized pigments.

Pigments	NIR reflectance at 1100 nm (%)	Solar reflectance R* (%)
YInCuO–ZnO /650 °C	67.83	65.12
YInCuO–ZnO /850 °C	75.05	63.14

4.1.7.3 YInFeO–ZnO pigments

The YInFeO–ZnO pigments show similar trends in the NIR spectra (**Figure 4. 41**) and the NIR reflectance values (**Table 4. 9**). The YInFeO–ZnO /650°C is the pigment with the lowest NIR reflectance at the highest wavelengths (**Figure 4. 41**). By comparing the values reported in **Table 4. 9** it is possible to observe that all the three pigments show high and comparable values of NIR reflectance and NIR solar reflectance. An increase in reflectance is due to the presence of doping elements (Mn, Cu, Fe) in $Y_{0.9}In_{0.1}O_3$ structure, also with the presence in the pigment of an higher amount of organic fraction. In particular, iron seems to significantly improve the NIR reflectance [49].

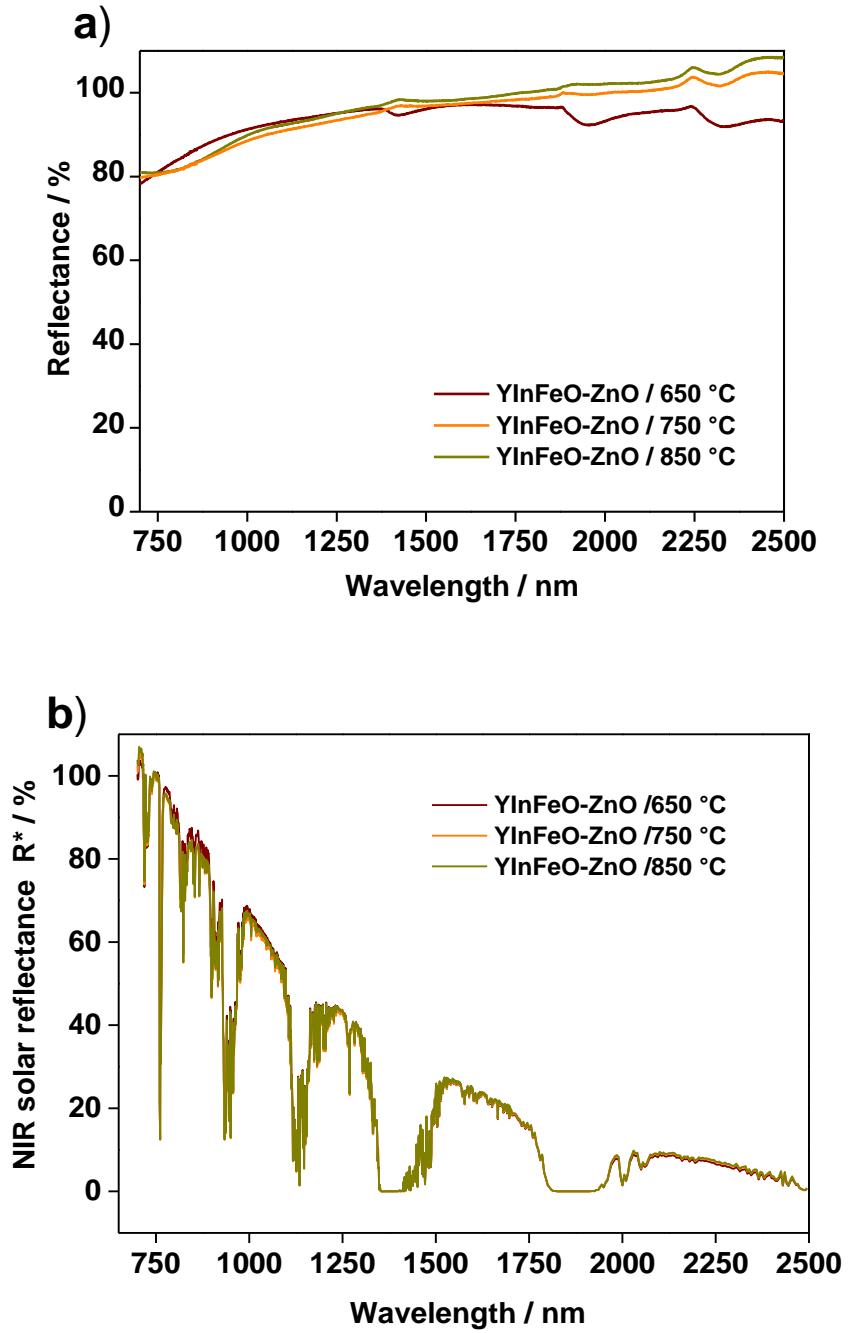


Figure 4. 41. NIR reflectance of the YInFeO–ZnO pigment powders calcined at different temperatures (a) and NIR solar reflectance spectra, obtained in compliance with ASTM G173-03 standard (b).

Table 4. 9. NIR reflectance at 1100 nm and solar reflectance of the YInFeO–ZnO synthesized pigments.

Pigments	NIR reflectance at 1100 nm (%)	Solar reflectance R* (%)
YInFeO–ZnO /650 °C	93.07	90.17
YInFeO–ZnO /750 °C	90.85	89.10
YInFeO–ZnO /850 °C	92.32	90.10

4.1.7.4 YInM(Mn, Cu, Fe)O–ZnO pigments: comparison of different reflective values.

In this section id reported a comparison of all the data related to reflectance of pigments, obtained after calcination of the different dried gels at 850 °C. Pigments obtained after calcination at 850 °C are without a high amount of organic fraction and have high thermal stability, together with high reflectance values. **Figure 4. 42** compares NIR reflectance and NIR solar reflectance spectra of the different pigments obtained after 850 °C calcination. Values of NIR reflectance at 1100 nm and NIR solar reflectance are represented in **Table 4. 10**. Observing reflectance spectra and values in **Table 4. 10** the pigment YInFeO–ZnO/ 850 °C is the most reflective. In the compared pigments, the doping element is the only variable. Therefore, the reflectance values are dependent by the doping elements. This observation is supported by previous studies underlining the relevant effect of doping elements in $Y_{0.9}In_{0.1}O_3$ structure [40] in tuning NIR reflectance. Other factors such as particles dimensions (which in general has a role in the tuning of NIR reflectance) seem to be of secondary importance respect to doping elements. Iron based pigments, as YInFeO₃ based

pigments, attracted much attention in the NIR reflective materials field for their high values of reflectance and the relatively low energetic consumption of the synthesis routes [222]. As shown in **Figure 4. 42** the reflectance spectra show a slight increase above 100 % in reflectance up to about 105 % at the 1750–2500 nm range. This is not unusual in analysis of powdery materials in the high wavelengths region of the NIR spectra [69,89,223]. This phenomenon is due to the fact that at the considered wavelength range the powdery materials show higher reflectance with respect to the used reference. This is not strictly dependent on the chemistry of the analyzed material, but on differences in granulometry of different particles and the packing in cuvettes used to perform measurements.

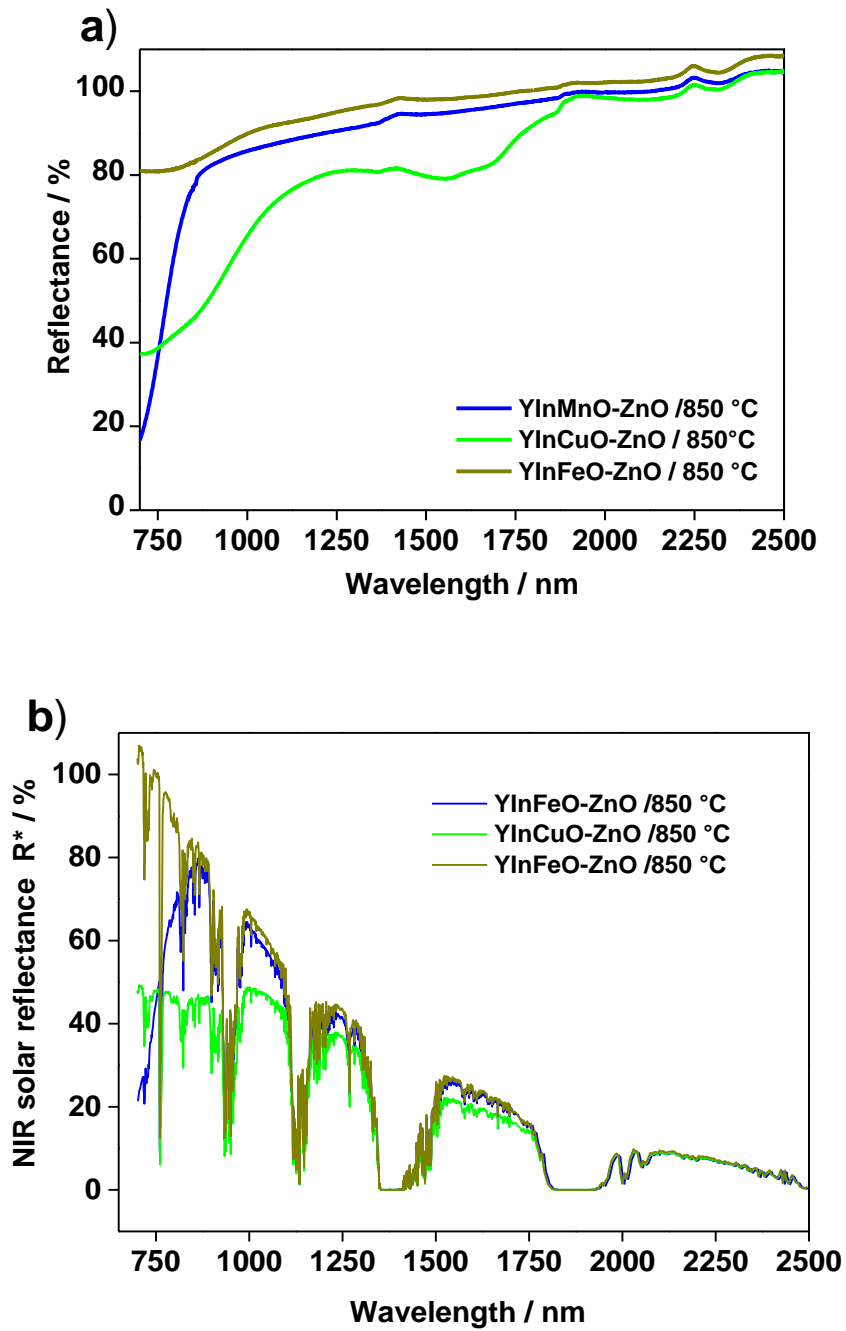


Figure 4. 42. NIR reflectance of the pigments powders after calcination of the dried gel at 850 °C (a) and NIR solar reflectance spectra, obtained in compliance with ASTM G173-03 standard (b).

Table 4. 10. NIR reflectance at 1100 nm and solar reflectance of the pigments powders after calcination of the dried gel at 850 °C.

Pigments	NIR reflectance at 1100 nm (%)	Solar reflectance R* (%)
YInMnO–ZnO /850 °C	87.64	76.11
YInCuO–ZnO /850 °C	75.05	63.14
YInFeO–ZnO /850 °C	92.32	90.10

4.2 Analysis performed on pigmented coatings

4.2.1 NIR reflectance

4.2.1.1 Coatings with YInMnO–ZnO pigments

Figure 4. 43.a shows the NIR reflectance spectra of YInMnO–ZnO + PMMA coatings compared to the reference samples (Graphite + PMMA, TiO₂ + PMMA, and Substrate). The binder partially smooths the difference in reflectance among the YInMnO–ZnO pigments, in particular considering the NIR reflectance values. This is in accordance with the NIR reflectance at 1100 nm (%) and the solar reflectance (R*) values of the pigments and the coatings (**Table 4. 11**). The NIR solar reflectance power spectra of the investigated coatings, obtained in compliance with ASTM G173-03 standard (**Figure 4. 43.b**), confirm the trend observed for the NIR reflectance. The obtained results can be explained considering that the NIR reflectance relies mainly on the presence of ZnO, which is present in all pigments. Light-colored pigments (e.g. white, pale yellow, and pale brown) are recognized to reflect

NIR light better than saturated colors pigments [221]. The hypothesis to explain the experimental results is that the presence of ZnO, together with a pale ochre color, and the influence of Mn, as a doping element, gives high values of IR reflectance at 1100 nm (%) and solar reflectance, R^* (%). Bare substrate shows values of 40% of NIR reflectance in the entire NIR spectrum. Aluminum is known to reflect in the IR wavelengths (also in thermal infrared) and the peak at 800 nm is a characteristic of pure aluminum [221]. TiO₂ + PMMA and Graphite + PMMA confirm their suitability as reference samples. The TiO₂ + PMMA is the most reflective sample, while Graphite + PMMA is the sample with NIR reflectance near to zero.

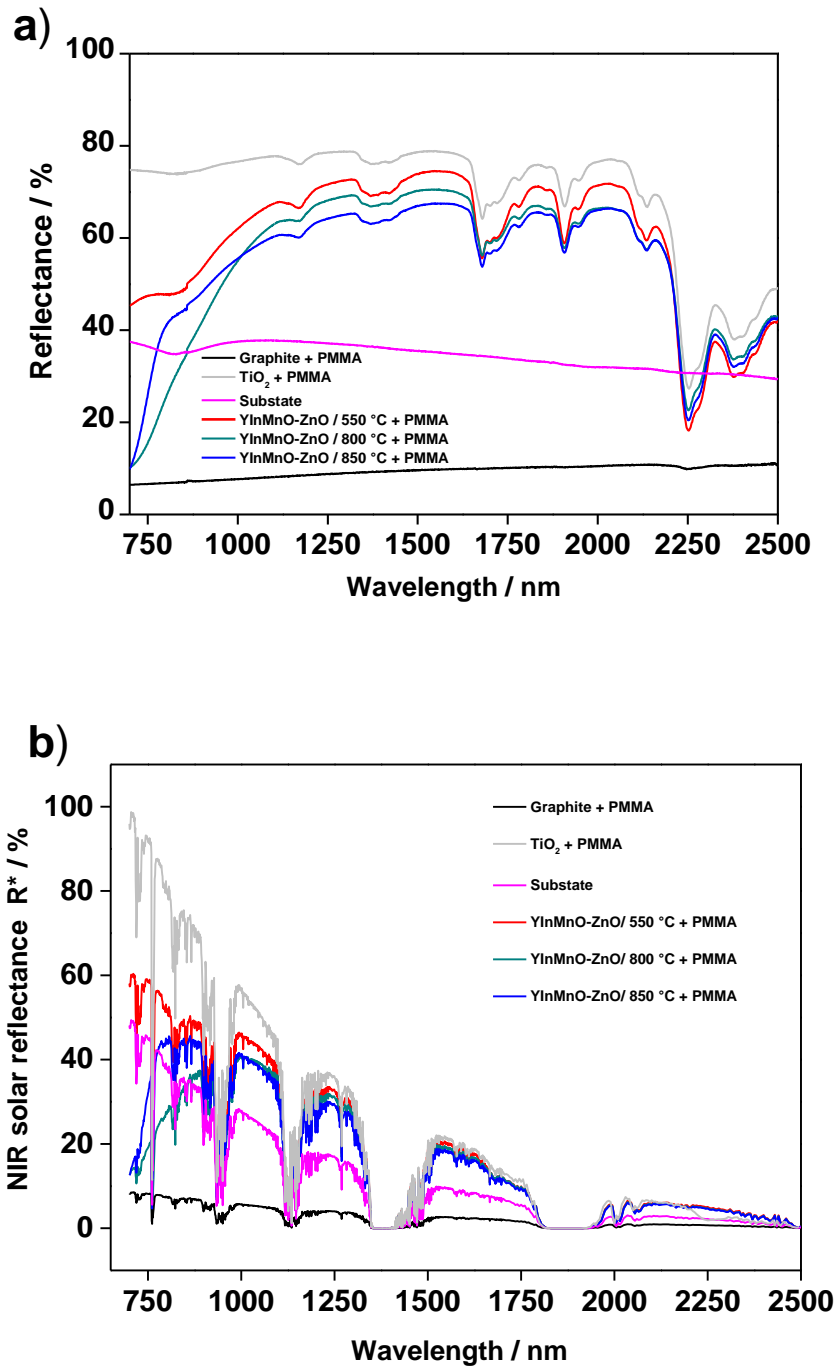


Figure 4. 43. NIR reflectance spectra of the coatings under investigation (a) and NIR solar reflectance spectra (b).

Table 4. 11. NIR reflectance at 1100 nm and solar reflectance of the obtained coatings.

Sample	NIR reflectance at 1100 nm (%)	Solar reflectance, R* (%)
Graphite + PMMA	8.50	7.93
TiO ₂ + PMMA	77.72	76.82
Substrate	37.76	35.90
YInMnO–ZnO /550 °C + PMMA	67.64	59.02
YInMnO–ZnO /800 °C + PMMA	62.97	46.48
YInMnO–ZnO /850 °C + PMMA	60.38	49.58

4.2.1.2 Coatings with YInCuO–ZnO pigments

As underlined before in NIR reflectance data of pigments also in the corresponding coatings, the difference in the reflectance values is less marked. Spectra of NIR reflectance (**Figure 4. 44.a**) and NIR solar reflectance (**Figure 4. 44.b**) of YInCuO–ZnO /650 °C + PMMA and YInCuO–ZnO /850 °C + PMMA show difference in values at 750 nm and 1100 nm. **Table 4. 12** presents comparable values of solar reflectance, R* for YInCuO–ZnO /650 °C + PMMA and YInCuO–ZnO /850 °C + PMMA. It is evident from experimental spectra and the results reported in **Table 4. 12** that the IR reflectance at 1100 nm of YInCuO–ZnO /850 °C + PMMA is higher than YInCuO–ZnO /650 °C + PMMA. Even if the two coatings under investigation show similar reflectance values, is evident the influence of pigments obtained after calcination of the dried gel at higher temperature increases the reflectance of corresponding coatings.

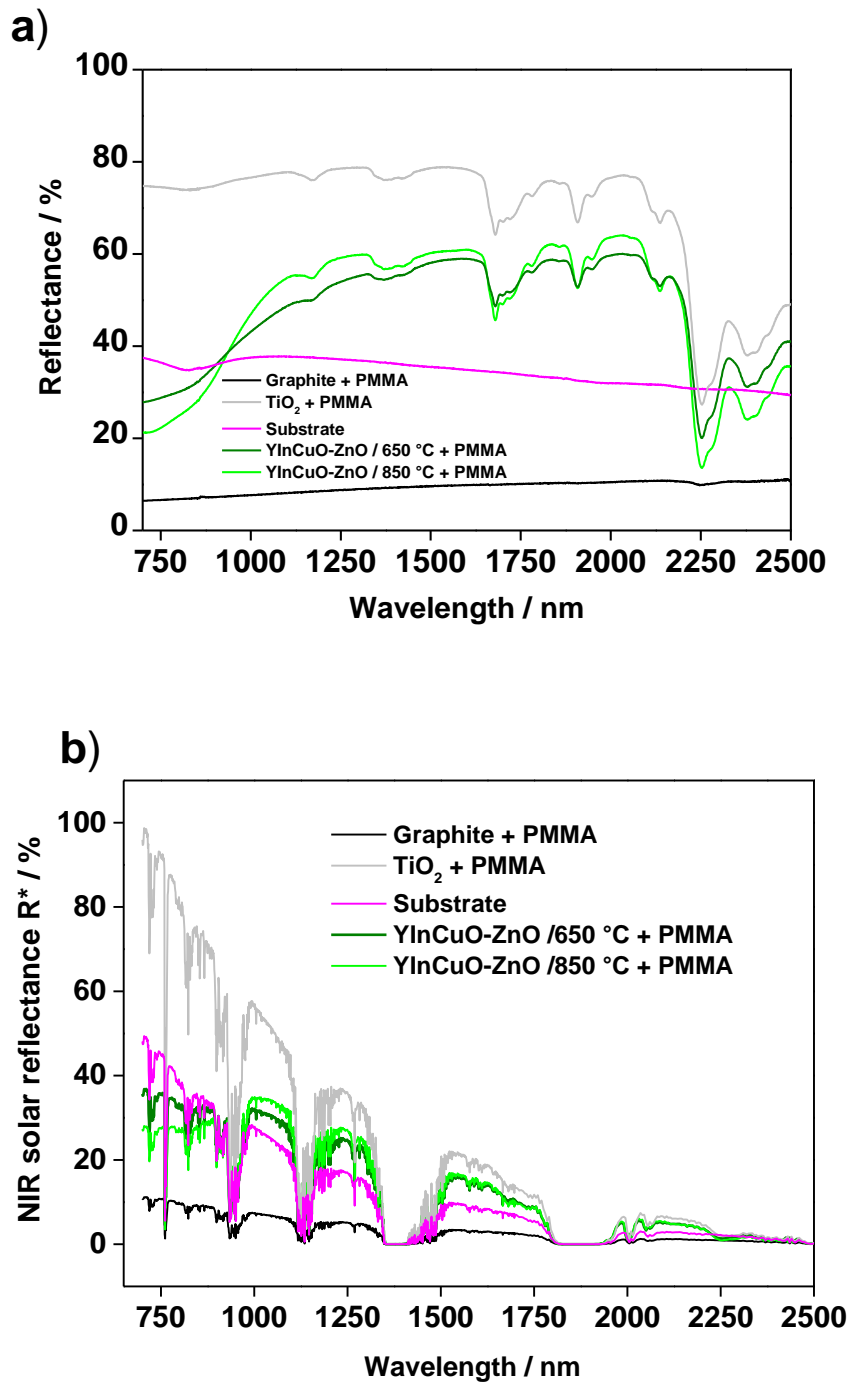


Figure 4. 44. NIR reflectance spectra of the coatings under investigation (a) and NIR solar reflectance spectra (b).

Table 4. 12. NIR reflectance at 1100 nm and solar reflectance of the investigated coatings.

Sample	NIR reflectance at 1100 nm (%)	Solar reflectance, R* (%)
Graphite + PMMA	8.50	7.93
TiO ₂ + PMMA	77.72	76.82
Substrate	37.76	35.90
YInCuO–ZnO /650 °C + PMMA	48.66	41.53
YInCuO–ZnO /850 °C + PMMA	54.72	41.04

4.2.1.3 Coatings with YInFeO–ZnO pigments

Respect to the coatings discussed before, coatings based on YInFeO–ZnO pigments show similar values in reflectance. **Figure 4. 45.a** underlines how the NIR reflectance of TiO₂ + Acrylic WB (the ALPINA acrylic binder) is comparable with YInFeO–ZnO/ 750 °C + Acrylic WB at long wavelength, in particular at 1500 nm and 200 nm. **Figure 4. 45.b** underlines better the minimal difference in reflectance for the YInFeO–ZnO + Acrylic WB coatings and **Table 4. 13** confirms that all the three different coatings present comparable values of reflectance.

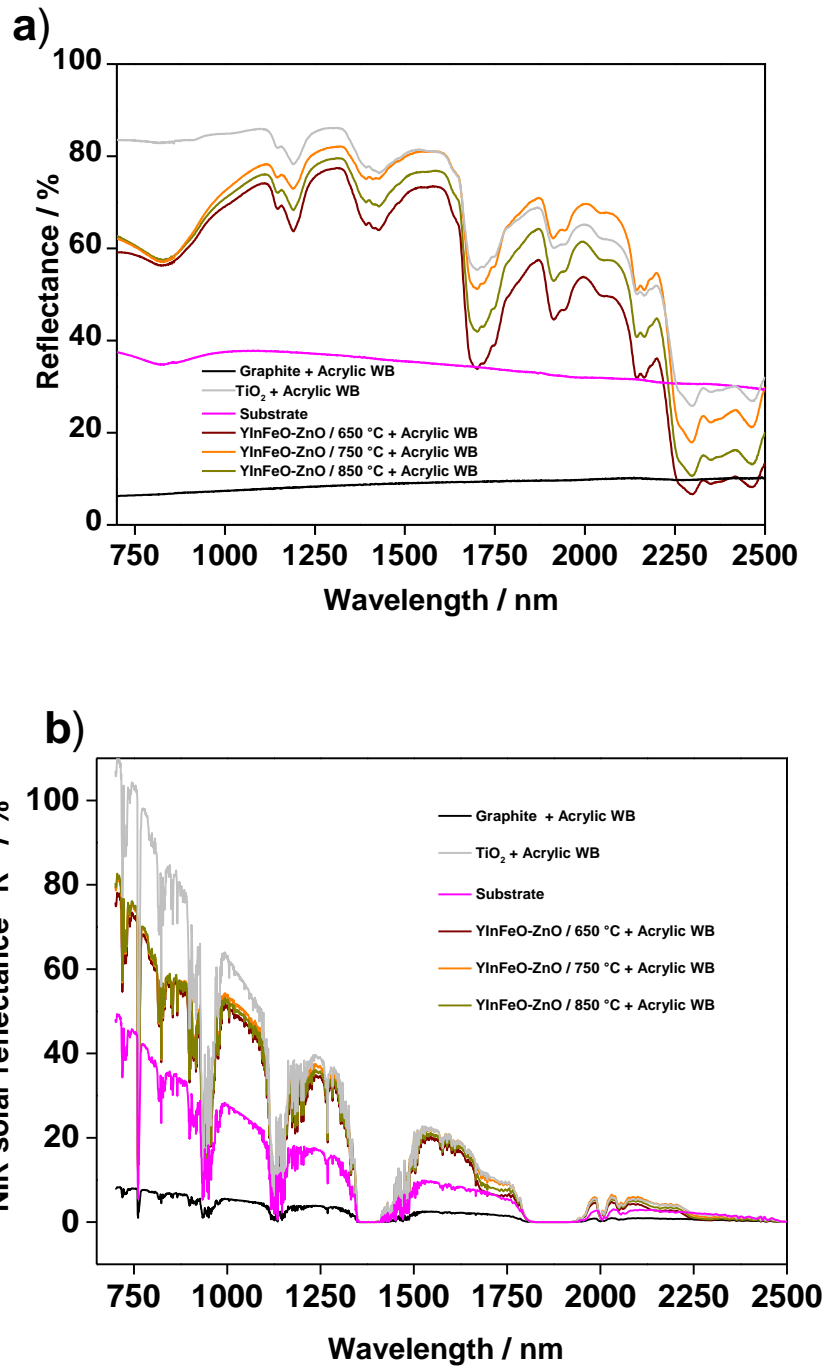


Figure 4. 45. NIR reflectance spectra of the coatings under investigation (a) and NIR solar reflectance spectra (b).

Table 4. 13. NIR reflectance at 1100 nm and solar reflectance of the investigated coatings.

Sample	NIR reflectance at 1100 nm (%)	Solar reflectance, R* (%)
Graphite + Acrylic WB	8.11	7.76
TiO ₂ + Acrylic WB	85.89	82.32
Substate	37.76	36.30
YInFeO–ZnO /650 °C+ Acrylic WB	74.02	63.70
YInFeO–ZnO /750 °C + Acrylic WB	77.98	67.69
YInFeO–ZnO /850 °C+ Acrylic WB	75.93	66.07

The reflectance spectra reported below (**Figure 4. 46**) allow us to confirm that NIR reflectance in each coating is effectively connected with the different pigments as the two binders, deposited on substrate surface, have comparable values of reflectance along the considered spectral range. Focusing on the two coatings used as positive references, TiO₂ + Acrylic WB shows a higher SR (82.32 %) and NIR reflectance at 1100 nm (85.89 %) with respect to TiO₂ + PMMA, (76.82 % and 77.72 % respectively). This is because industrial clear acrylic water-based paint is more prone to disperse pigments with respect to standard PMMA. This results in higher reflective properties of the obtained coatings with industrial binder respect to the coating with PMMA.

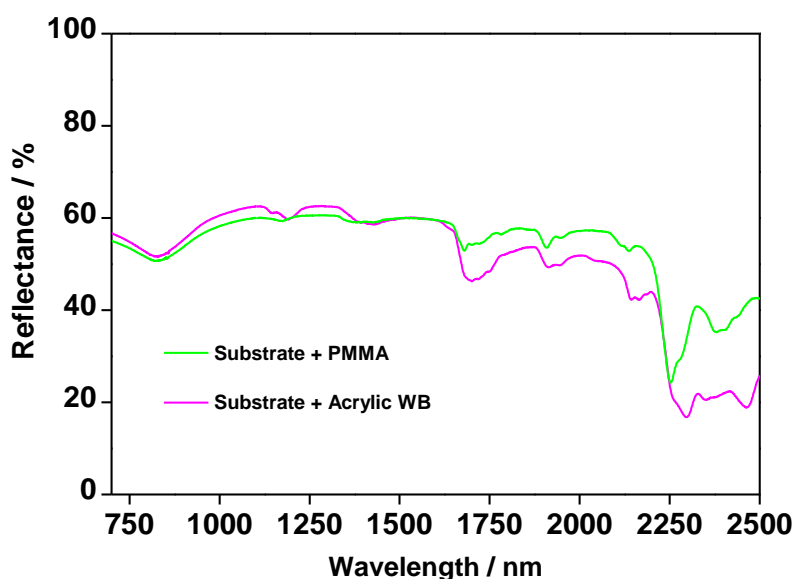


Figure 4. 46. Compared NIR reflectance spectra of Substrate with the two different binders deposited on the substrate surface.

4.2.1.4 Discussion of compared values of reflectance

As observed for pigments, the highest reflectance values are shown for the coatings having pigments calcinated at 850 °C. **Figure 4. 47** and **Table 4. 14** shows that the same hierarchy of reflectance data observed for pigments is maintained; the coating YInFeO–ZnO/ 850 °C + Acrylic WB is the most reflective. These comparative observations can be done considering the negligible influence of the two binders in tuning reflectance, as underlined in **Figure 4. 47**. As underlined above a contribution of the binder is on the distribution of pigment particles inside it. A factor influencing the high NIR reflectance of YInFeO–ZnO/ 850 °C + Acrylic WB is made by a better dispersion of pigment in the binder.

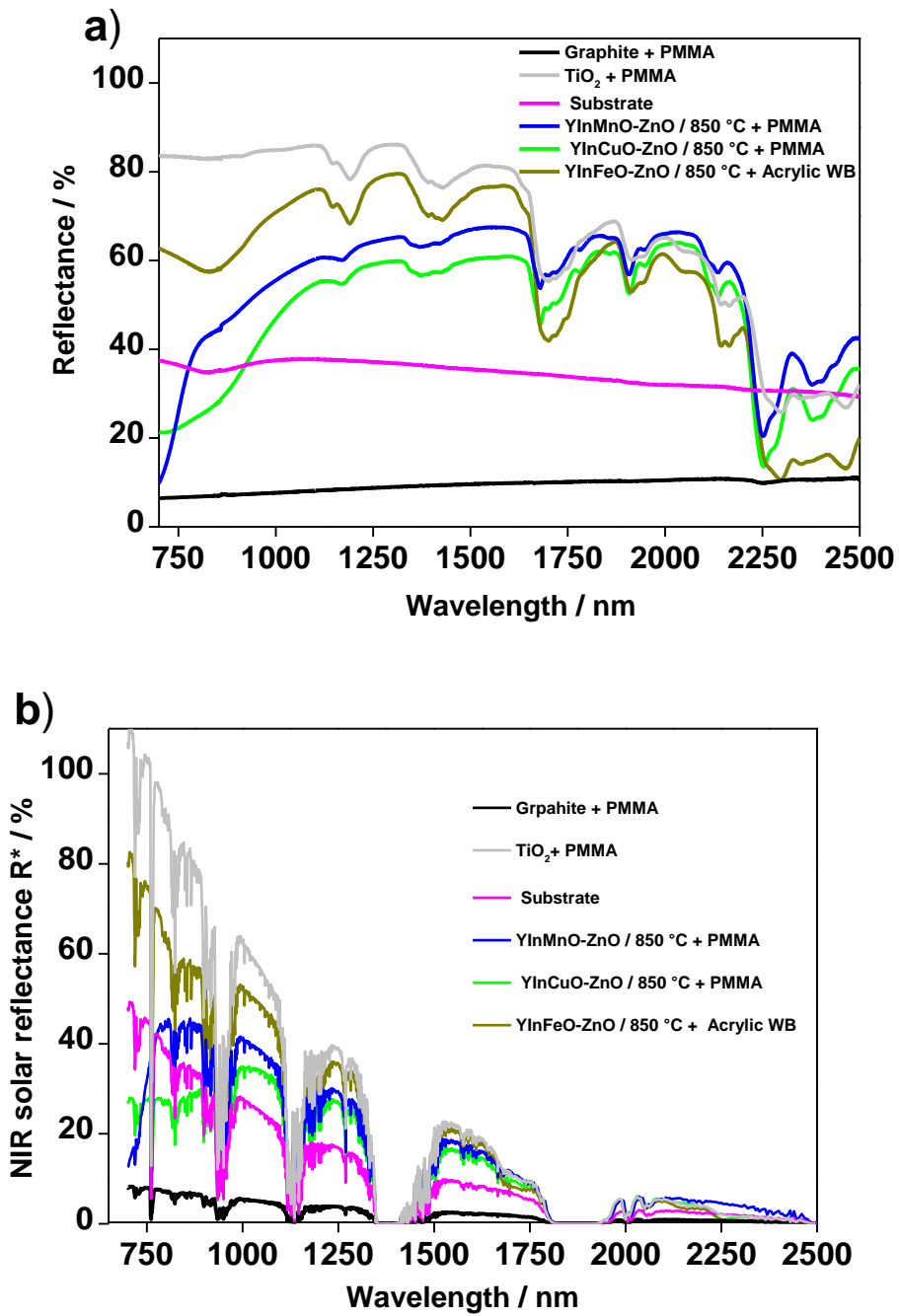


Figure 4. 47. Compared NIR reflectance of the coatings with pigments obtained after calcination of the dried gel at 850 °C (a) and NIR solar reflectance spectra, obtained in compliance with ASTM G173-03 standard (b).

Table 4. 14. NIR reflectance at 1100 nm and solar reflectance of the investigated coatings with pigments obtained after calcination of the dried gel at 850 °C.

Sample	NIR reflectance at 1100 nm (%)	Solar reflectance, R* (%)
Graphite + PMMA	8.50	7.93
TiO ₂ + PMMA	77.72	76.82
Substate	37.76	35.90
YInMnO-ZnO /850 °C + PMMA	60.38	49.58
YInCuO-ZnO /850 °C + PMMA	54.72	41.04
YInFeO-ZnO /850 °C + Acrylic WB	75.93	66.07

4.2.2 Thermal performances analysis

4.2.2.1 Preliminary analysis on coatings having YInMnO–ZnO based pigments

The **Figure 4. 48** represents the thermal trend of the samples YInMnO–ZnO/550 °C +PMMA, YInMnO–ZnO/750 °C + PMMA and YInMnO–ZnO/850 °C + PMMA under solar exposure. The thermal performances of the coatings corresponding to the pigments were evaluated placing the samples on the rooftop of the university building in the city of Trento in the condition underlined before in Materials and Method section. The plot of the average outer temperature of the coatings (T_{surface}) (**Figure 4. 48.a**), recorded by the thermal camera, underlines that, considering the NIR pigmented samples, the highest value is for the coating YInMnO–ZnO/550 °C + PMMA and the lowest is for coating YInMnO–ZnO/850 °C +PMMA. This is attributed to the higher organic fraction phase of the ochre pigment compared to the deep blue pigment, as observed in [211]. The highest organic fraction, related to residual unburned carbon of citric acid used in pigments synthesis is likely to be responsible for an increase in temperature of the coated surface. Interestingly, YInMnO–ZnO/550 °C + PMMA shows T_{panel} and T_{surface} near to T_{panel} and T_{surface} values of Graphite + PMMA (70 °C). The temperature data obtained for YInMnO–ZnO/550 °C + PMMA sample exposed to sunlight mismatch with the NIR reflectance data. **Table 4. 12** and **Figure 4. 43** show that YInMnO–ZnO/550 °C + PMMA is the most reflective coating. NIR reflectance spectra show that the high reflection values for YInMnO–ZnO/550 °C + PMMA are observed up to about

2000 nm. These observations lead to hypothesize that a reflectance spectrum in the range between 700 and 2500 nm does not perfectly model the interaction between NIR reflective material and solar radiation. In **Figure 4. 48.b** the average rear temperature (T_{panel}) shows a trend of temperature similar to that represented in **Figure 4. 48.a**, except for the bare aluminum (Substrate). The value of Substrate T_{panel} shows a similar temperature with respect to $\text{TiO}_2 + \text{PMMA } T_{\text{panel}}$. The outer temperature of the substrate remains cooler, compared to that measured on the rear part of the panel due to its high reflectivity of solar radiation. The coating seems to cool down the inner and outer temperature of coated surface with respect to the other two ($\text{YInMnO-ZnO}/550 \text{ }^\circ\text{C} + \text{PMMA}$ and $\text{YInMnO-ZnO}/850 \text{ }^\circ\text{C} + \text{PMMA}$). To better understand the thermal properties of the coatings, the efficiency in terms of heat flux retention inside the foam box has been calculated (**Table 4. 15**). $\text{YInMnO-ZnO}/800 \text{ }^\circ\text{C} + \text{PMMA}$ and $\text{YInMnO-ZnO}/850 \text{ }^\circ\text{C} + \text{PMMA}$ samples seem to be promising to reduce the heat flux inside the device when exposed to sunlight. The q_{12} values reflect the trend for T_{panel} values. The values in **Table 4. 15** demonstrate the active role of white and a black coating (containing Graphite) to act as the positive and the negative control respectively, also in the heat control. The q_{12} values of $\text{YInMnO-ZnO}/800 \text{ }^\circ\text{C} + \text{PMMA}$ and $\text{YInMnO-ZnO}/850 \text{ }^\circ\text{C} + \text{PMMA}$ demonstrate that the two coatings have the same effect on the heat retention inside the box, while $\text{YInMnO-ZnO}/550 \text{ }^\circ\text{C} + \text{PMMA}$ increases the heat transfer inside the box.

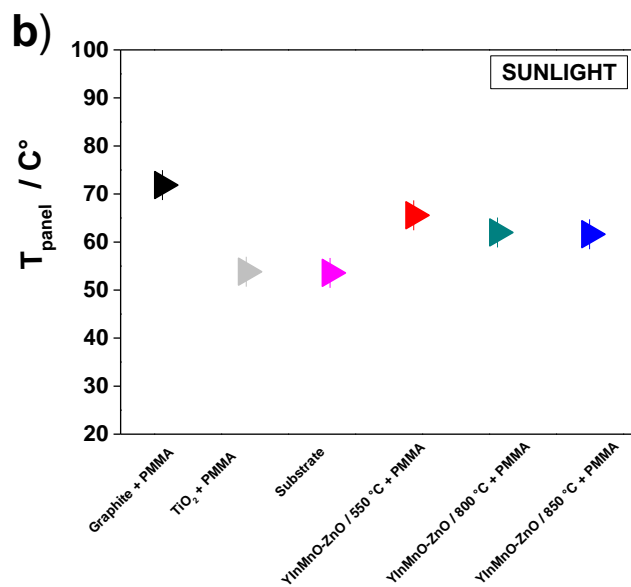
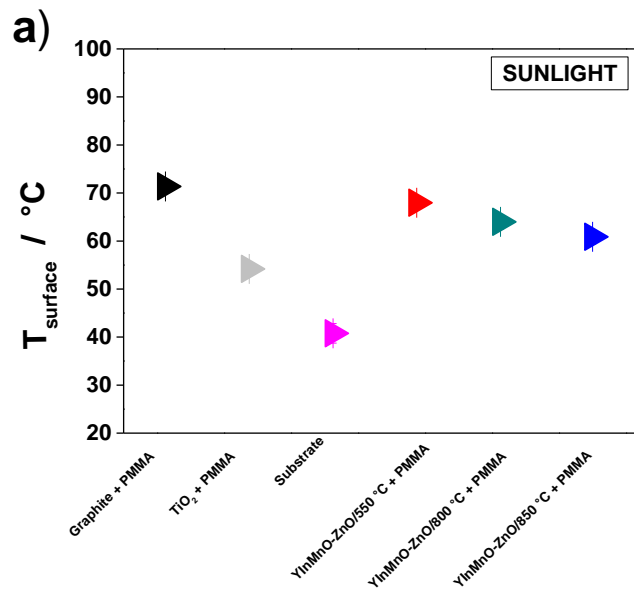


Figure 4. 48. Recorded average temperatures produced by exposure to sunlight: the average temperature recorded on the outer surface of the panel, $T_{\text{surface}} / ^\circ\text{C}$ (a), and the average temperature recorded on the rear part of the panel, $T_{\text{panel}} / ^\circ\text{C}$ (b).

Table 4. 15. Average temperature recorded on the rear part of the panel ($T_{\text{panel}} / ^\circ\text{C}$) and the average temperature recorded in the area inside foam box ($T_{\text{box}} / ^\circ\text{C}$) with resulting heat flux q_{12} ($\text{W}\cdot\text{m}^{-2}$), after exposure to sunlight.

Sample	$T_{\text{panel}} (^\circ\text{C})$	$T_{\text{box}} (^\circ\text{C})$	$\Delta T (^\circ\text{C})$	$q_{12} (\text{W}\cdot\text{m}^{-2})$
Graphite + PMMA	71.9 ± 0.5	47.8 ± 0.6	24.1	164.6
TiO ₂ + PMMA	53.8 ± 0.5	42.7 ± 0.3	11.1	68.6
Substrate	58.6 ± 0.8	44.7 ± 0.3	13.9	88.0
YInMnO–ZnO/550 °C+ PMMA	65.6 ± 0.4	43.2 ± 0.4	22.4	145.8
YInMnO–ZnO/800 °C+ PMMA	62.0 ± 0.7	43.4 ± 0.5	18.6	119.5
YInMnO–ZnO/850 °C+ PMMA	61.6 ± 0.6	42.4 ± 0.3	19.2	122.7

4.2.2.2 Thermal performances analysis with artificial radiation source

Analysis with infrared lamp

Figure 4. 49 represents the T_{surface} and T_{panel} of samples after exposure to the incandescent infrared emitting lamp. Cool roofs are usually tested with infrared lamps [165]. The coating YInMnO–ZnO/550 °C + PMMA shows significantly lower temperature values of about 50 °C (**Figure 4. 49.a** and **Figure 4. 49.b**), compared to the coatings with the blue pigments (YInMnO–ZnO/800 °C + PMMA and YInMnO–ZnO/850 °C + PMMA) with values of about 65 °C. Measurements performed with infrared lamp show an opposite trend compared to the measurements obtained after solar exposure, for T_{surface} and T_{panel} measurements. Coating YInMnO–ZnO/550 °C + PMMA shows average temperatures values, which are comparable with TiO₂ + PMMA (the positive control). Lighting with IR

LAMP the sample Graphite + PMMA (negative control), the coating surface is overheated and reaches temperature of 90 °C, instead, the temperature of the inner back of the panel (T_{panel}) is significantly lower and reaches 75 °C. With infrared lamp, YInMnO–ZnO/800 °C + PMMA and YInMnO–ZnO/850 °C + PMMA maintain similar temperatures, showed under sunlight exposure.

Values of q_{12} are represented in **Table 4. 16**. For samples with pigments the heat flux (q_{12}) increases, passing from YInMnO–ZnO/550 °C + PMMA to YInMnO–ZnO/800 °C + PMMA and YInMnO–ZnO/850 °C + PMMA. The aluminum substrate shows the lowest values of q_{12} , due to its ability cool down after irradiation with infrared radiations. For the measurements performed with infrared lamp, the highest value of q_{12} of Graphite + PMMA is well marked with respect to the other samples. The q_{12} values confirm that YInMnO–ZnO/550 °C + PMMA is more efficient in reducing heat flux than YInMnO–ZnO/800 °C + PMMA and YInMnO–ZnO/850 °C + PMMA when exposed to infrared lamp.

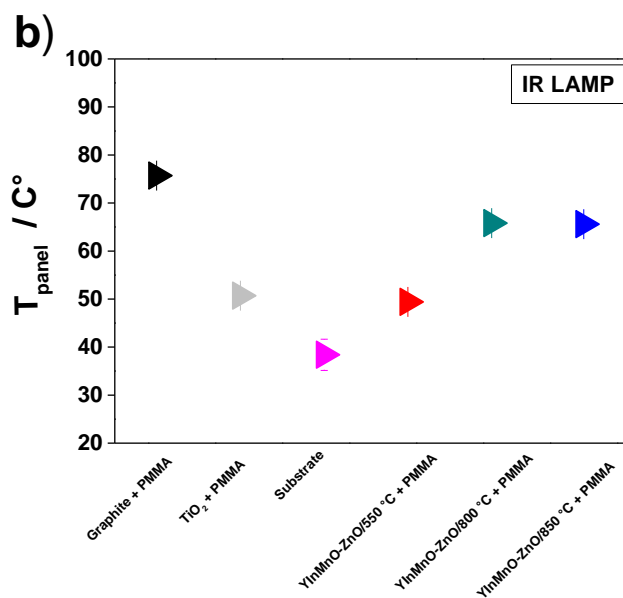
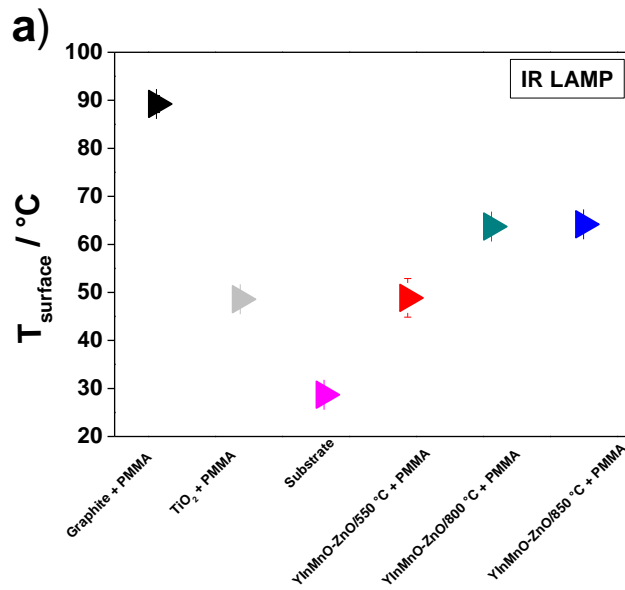


Figure 4. 49. Recorded average temperatures after exposure to infrared lamp : the average temperature recorded on the outer surface of the panel, $T_{\text{surface}} / ^\circ\text{C}$ (a), and the average temperature recorded on the rear part of the panel, $T_{\text{panel}} / ^\circ\text{C}$ (b).

Table 4. 16. Average temperature recorded on the rear part of the panel (T_{panel} / °C) and the average temperature recorded in the area inside foam box (T_{box} / °C) with resulting heat flux q_{12} ($\text{W}\cdot\text{m}^{-2}$), after exposure to IR LAMP.

Sample	T_{panel} (°C)	T_{box} (°C)	ΔT (°C)	q_{12} ($\text{W}\cdot\text{m}^{-2}$)
Graphite + PMMA	75.7 ± 1.2	30.5 ± 1.2	45.2	292.1
TiO ₂ + PMMA	50.7 ± 0.8	27.1 ± 0.4	23.6	133.2
Substrate	38.4 ± 3.3	26.9 ± 0.4	11.5	60.7
YInMnO–ZnO/550 °C + PMMA	49.4 ± 1.1	28.1 ± 0.7	21.3	119.7
YInMnO–ZnO/800 °C + PMMA	65.8 ± 0.3	29.4 ± 0.5	36.4	223.1
YInMnO–ZnO/850 °C + PMMA	65.6 ± 0.7	29.7 ± 0.6	35.9	219.9

Analysis with halogen lamp

T_{surface} and T_{panel} trends of samples exposed to tungsten halogen lamp are shown in **Figure 4. 50**. Together with infrared lamps, halogen lamps are employed in cool roof tests [224]. Considering **Figure 4. 50.a** the T_{surface} of the blue coatings are almost comparable (around 42 °C) and slightly below the temperature measured for the PMMA coating with ochre pigments (about 47 °C). Similar results were obtained for the T_{panel} (**Figure 4. 50.b**). Comparing the T_{surface} and T_{panel} of Graphite + PMMA, the T_{surface} is higher than T_{panel} of about 20 °C, as for samples exposed to infrared lamp. Substrate shows a temperature, lower of about 10 °C respect to TiO₂ + Binder 1 (considering T_{surface}) or comparable to TiO₂ + PMMA (considering T_{panel}). In terms of cooling effect, it seems that under the halogen lamp irradiation, the coatings YInMnO–ZnO/800 °C + PMMA and YInMnO–ZnO/850 °C + PMMA perform similarly to the sample TiO₂ + Binder 1. Accordingly, the heat flux (q_{12}) values (**Table 4. 17**) confirm the behavior observed for T_{surface} and T_{panel} .

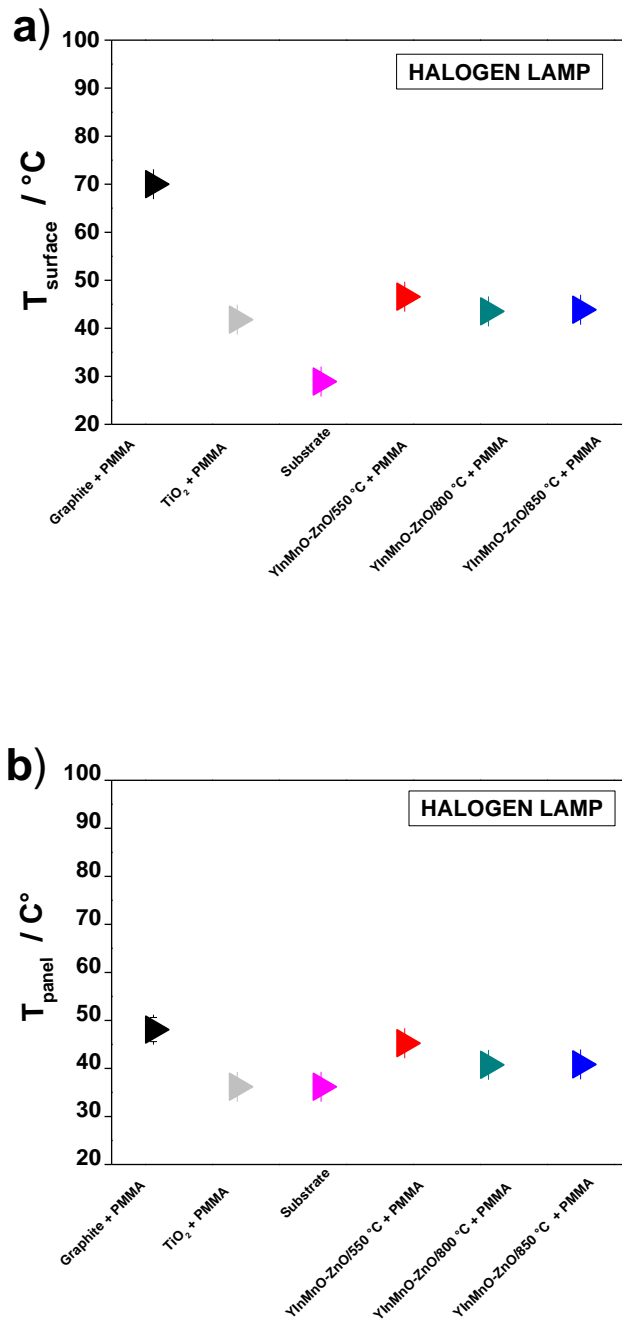


Figure 4. 50. Average temperature recorded on the rear part of the panel ($T_{\text{panel}}/ \text{ }^{\circ}\text{C}$) and the average temperature recorded in the area inside foam box ($T_{\text{box}}/ \text{ }^{\circ}\text{C}$) with resulting heat flux q_{12} ($\text{W}\cdot\text{m}^{-2}$), after exposure to halogen lamp.

Table 4. 17. Average temperature recorded on the rear part of the panel ($T_{\text{panel}}/ ^\circ\text{C}$) and the average temperature recorded in the area inside foam box ($T_{\text{box}}/ ^\circ\text{C}$) with resulting heat flux q_{12} ($\text{W}\cdot\text{m}^{-2}$), after exposure to halogen lamp.

Sample	$T_{\text{panel}} (^\circ\text{C})$	$T_{\text{box}} (^\circ\text{C})$	$\Delta T (^\circ\text{C})$	$q_{12} (\text{W}\cdot\text{m}^{-2})$
Graphite + PMMA	48.1 ± 2.5	31.0 ± 0.7	17.1	97.2
TiO ₂ + PMMA	38.8 ± 0.4	27.9 ± 0.3	10.9	58.2
Substrate	36.2 ± 0.1	27.3 ± 0.4	8.9	46.5
YInMnO–ZnO/550 °C + PMMA	45.2 ± 1.1	28.7 ± 0.4	16.5	91.4
YInMnO–ZnO/800 °C + PMMA	40.8 ± 0.2	28.3 ± 0.2	12.5	67.1
YInMnO–ZnO/850 °C + PMMA	40.8 ± 0.3	28.6 ± 0.3	12.2	66.5

Analysis with xenon arc lamp

Other authors have already employed xenon arc lamp for the ageing and characterization of cool roof coatings [225]. T_{surface} and T_{panel} for the different coatings exposed to xenon arc lamp are reported in **Figure 4. 51**. The surface temperature is of $64.8 ^\circ\text{C}$ for the YInMnO–ZnO/550 °C + PMMA sample. In comparison, it progressively decrease passing from YInMnO–ZnO/800 °C + PMMA ($61.8 ^\circ\text{C}$) to YInMnO–ZnO/850 °C + PMMA coatings ($58.4 ^\circ\text{C}$), as shown in **Figure 4. 51.a**. Comparable results were obtained for the T_{panel} (**Figure 4. 51.b**); and a reduction of the measured temperatures for YInMnO–ZnO/800 °C + PMMA and YInMnO–ZnO/850 °C + PMMA compared to the YInMnO–ZnO/550 °C + PMMA is well marked. According to the trend reported in **Figure 4. 51**, YInMnO–ZnO/850 °C + PMMA shows a significantly lower T_{surface} and T_{panel} temperature than other samples. Also for this light source, the heat exchange values q_{12} were measured (**Table 4. 18**). Heat exchange values

give further evidence about the cooling effect of YInMnO-ZnO/850 °C + PMMA with respect to other pigmented coatings. With respect to other light sources, samples exposed to xenon arc lamp show much more marked differences in heat flux values.

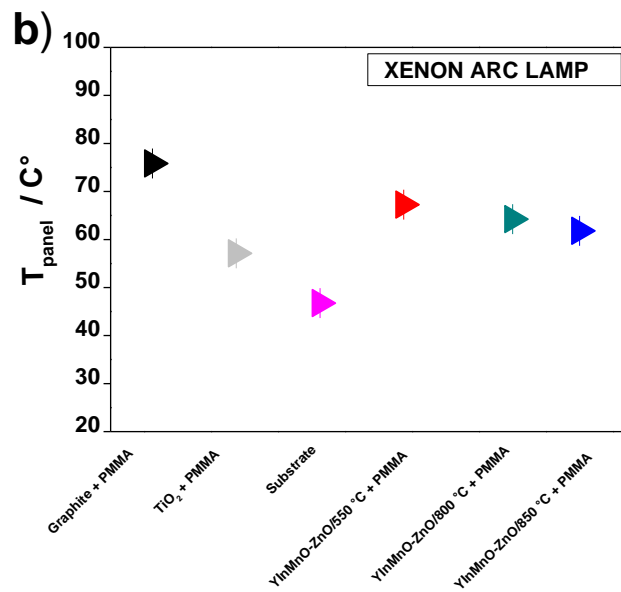
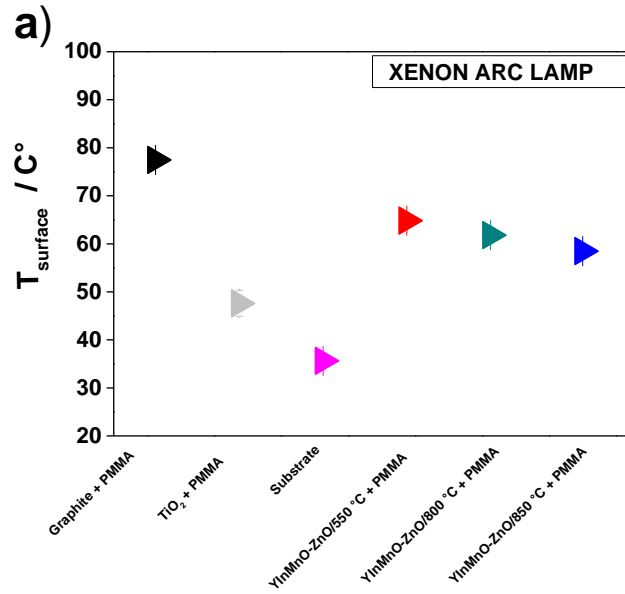


Figure 4. 51. Recorded average temperatures after test with xenon arc lamp: the average temperature recorded on the outer surface of the panel, $T_{\text{surface}} / ^\circ\text{C}$ (a), and the average temperature recorded on the rear part of the panel, $T_{\text{panel}} / ^\circ\text{C}$ (b).

Table 4. 18. Average temperature recorded on the rear part of the panel ($T_{\text{panel}}/ ^\circ\text{C}$) and the average temperature recorded in the area inside foam box ($T_{\text{box}}/ ^\circ\text{C}$) with resulting heat flux q_{12} ($\text{W}\cdot\text{m}^{-2}$), after exposure to xenon arc lamp.

Sample	$T_{\text{panel}} (^\circ\text{C})$	$T_{\text{box}} (^\circ\text{C})$	$\Delta T (^\circ\text{C})$	$q_{12} (\text{W}\cdot\text{m}^{-2})$
Graphite + PMMA	75.8 ± 0.4	37.4 ± 0.3	38.4	255.7
TiO ₂ + PMMA	57.1 ± 0.3	33.6 ± 0.2	23.2	140.7
Substrate	46.7 ± 0.9	31.4 ± 0.3	15.3	86.7
YInMnO–ZnO/550 °C+ PMMA	67.2 ± 0.5	34.6 ± 0.1	32.6	206.1
YInMnO–ZnO/800 °C+ PMMA	64.2 ± 0.5	35.3 ± 0.2	28,9	180.9
YInMnO–ZnO/850 °C+ PMMA	61.8 ± 0.7	33.9 ± 0.4	27.9	171.4

Comparing the different T_{surface} and T_{panel} values of the investigated coatings, the halogen and xenon arc lamps seem to provide a ranking consistent with that obtained upon natural exposure during sunny days of July 2020. In particular, the measured temperature values obtained using xenon arc lamp match quite well those obtained with natural exposure to sunlight. The last observation is further supported by multispectral analysis performed on different used lamps and compared with a standard solar illuminator SUN 2000 [226] (**Figure 4. 52**). As results, observing the figure below the xenon arc lamp spectrum match the spectrum of the standard sun simulator and xenon arc lamp can be used as a model to simulate solar radiation.

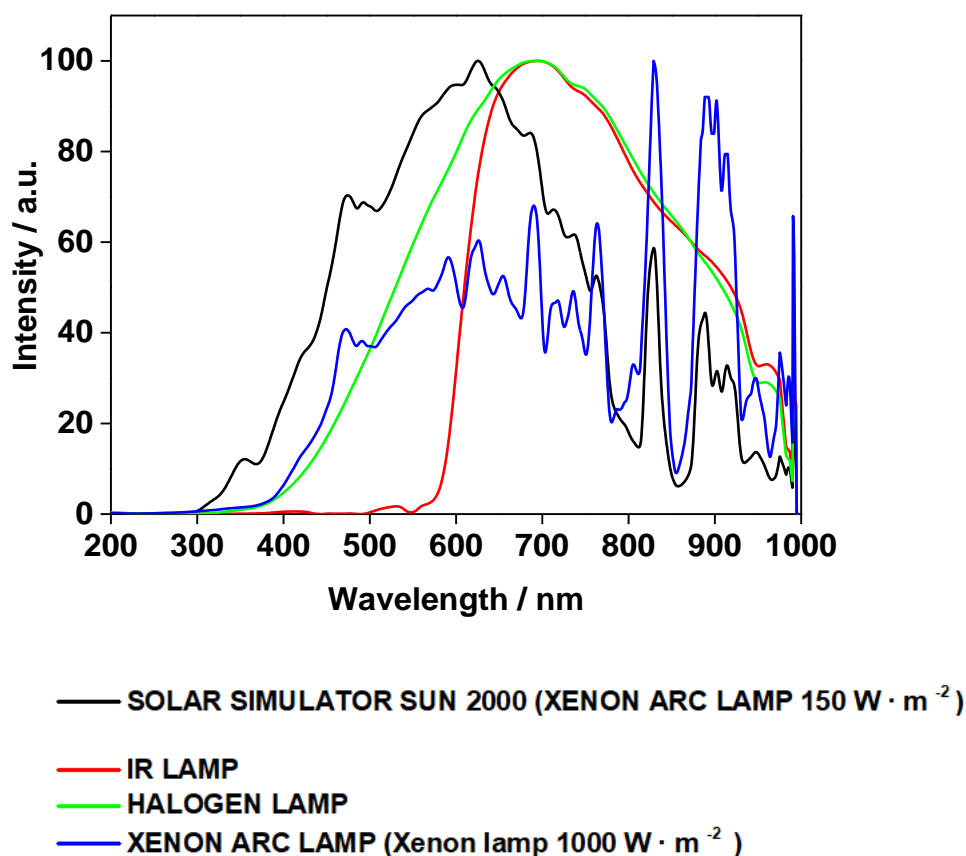


Figure 4. 52. Light sources spectra versus solar simulator SUN 2000 spectrum.

4.2.2.3 Analysis on coatings having YInCuO–ZnO pigments

The plot below reported in **Figure 4. 53** represents the T_{panel} and T_{box} of YInCuO–ZnO/650 °C + PMMA and YInCuO–ZnO/850 °C + PMMA samples (**Figure 4. 53**). As can be observed in the plots no relevant difference can be observed between the two-synthesized coatings. Respect to TiO_2 + PMMA the YInCuO–ZnO/650 °C + PMMA and YInCuO–ZnO/850 °C + PMMA show a relevant increase in T_{panel} and T_{box} temperature (**Table 4. 19**). Even if no relevant difference is observed between the two different coatings, in T_{surface} and T_{panel} (**Figure 4. 53.a** and **Figure 4. 53.b**), the $\Delta T/^\circ\text{C}$ values (**Table 4. 19**) aim to confirm that YInCuO–ZnO/850 °C + PMMA is the coating able to confer the lowest exchange in

temperature between the outdoor and indoor environment of the foam box. This result is clearer looking at the q_{12} values.

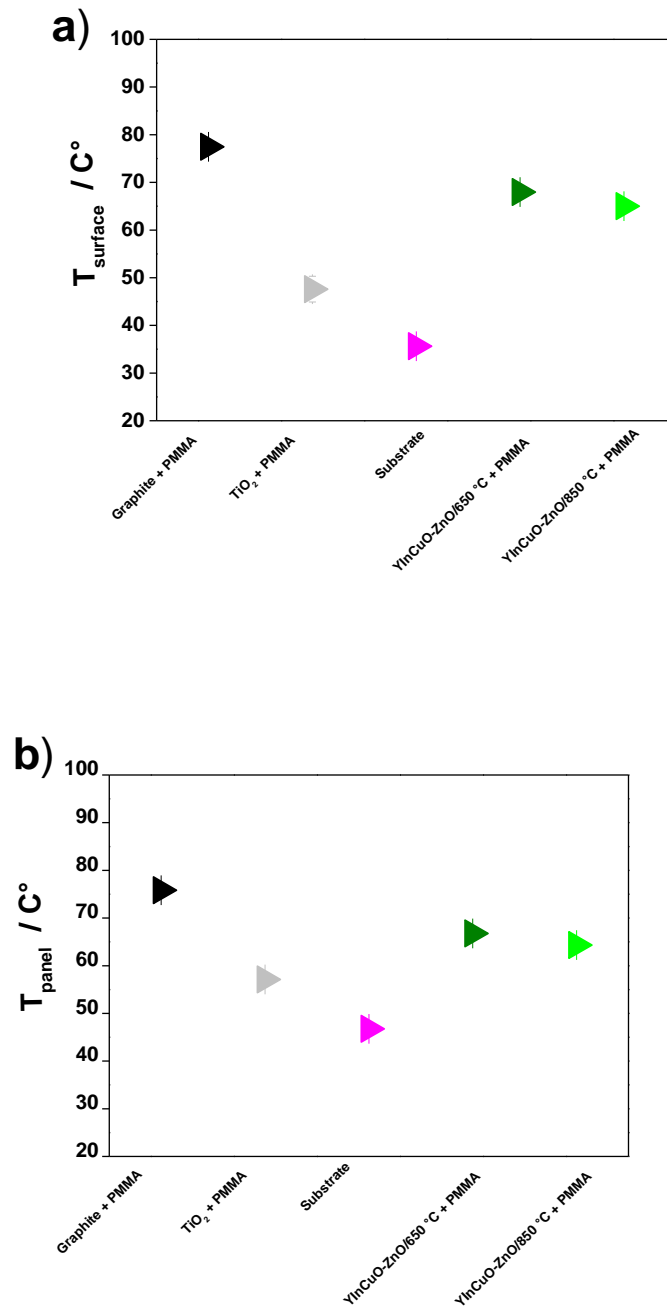


Figure 4. 53. Recorded average temperatures after test with xenon arc lamp: the average temperature recorded on the outer surface of the panel, $T_{\text{surface}} / ^\circ\text{C}$ (a), and the average temperature recorded on the rear part of the panel, $T_{\text{panel}} / ^\circ\text{C}$ (b).

Table 4. 19. Average temperature recorded on the rear part of the panel ($T_{\text{panel}}/^\circ\text{C}$) and the average temperature recorded in the area inside foam box ($T_{\text{box}}/^\circ\text{C}$) with resulting heat flux $q_{12}/(\text{W}\cdot\text{m}^{-2})$, after exposure to xenon arc lamp.

Sample	$T_{\text{panel}} (^\circ\text{C})$	$T_{\text{box}} (^\circ\text{C})$	$\Delta T (^\circ\text{C})$	$q_{12} (\text{W}\cdot\text{m}^{-2})$
Graphite + PMMA	75.8 ± 0.4	37.4 ± 0.3	38.4	255.7
TiO ₂ + PMMA	57.1 ± 0.3	33.6 ± 0.2	23.5	140.7
Substrate	46.7 ± 0.9	31.4 ± 0.3	15.3	86.7
YInCuO–ZnO/650 °C+ PMMA	66.7 ± 0.8	27.4 ± 0.2	39.3	240.1
YInCuO–ZnO/850 °C+ PMMA	64.3 ± 0.9	28.2 ± 0.8	36.1	218.8

4.2.2.4 Analysis on coatings with YInFeO–ZnO pigments

Figure 4. 54 reports T_{surface} of YInFeO–ZnO + Acrylic WB coatings. The plotted temperature trend underlines that the coatings with pigments calcined at higher temperatures show higher T_{surface} . Values of plotted data start in fact from 68.3 °C (YInFeO–ZnO /650 °C + Acrylic WB) to 66.2 °C (YInFeO–ZnO /750 °C + Acrylic WB) and decrease up to 63.2 °C (YInFeO–ZnO /850 °C + Acrylic WB). The difference of temperature values is less marked looking at **Figure 4. 54.b**, which is the plot of recorded inner T_{panel} . Anyway, even if the temperature difference is less marked, YInFeO–ZnO /850 °C + Acrylic WB results the coating showing lower T_{panel} (**Table 4. 20**) and lower heat flux q_{12} .

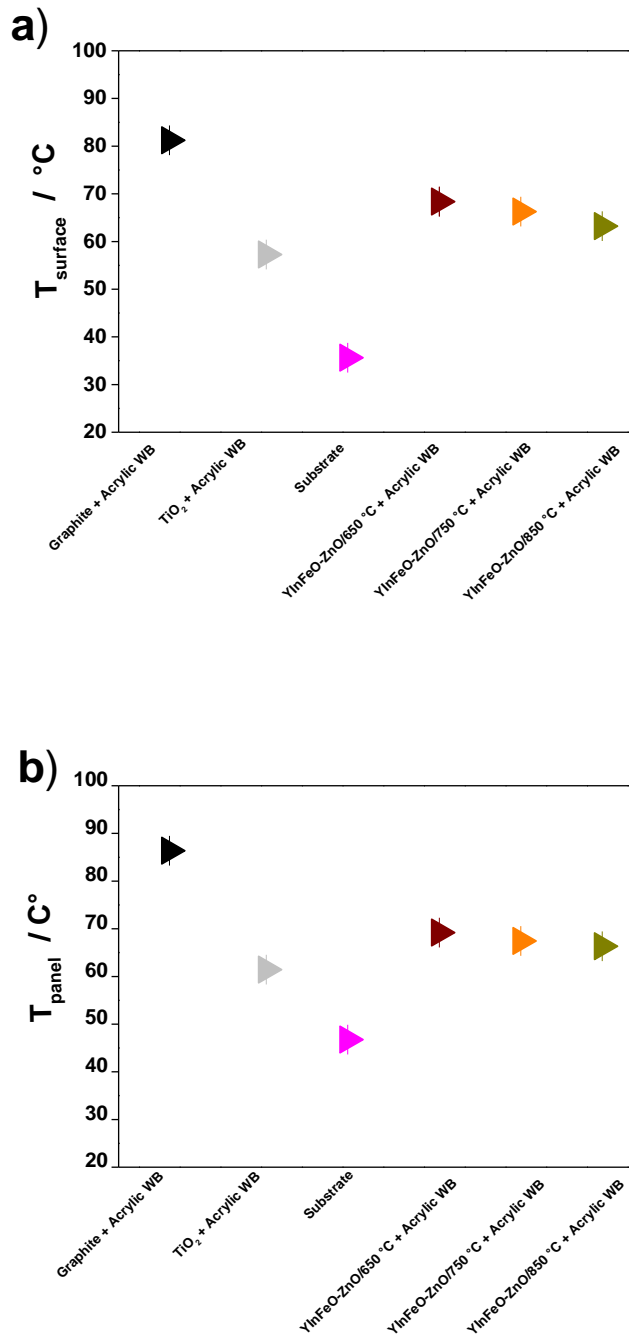


Figure 4. 54. Recorded average temperatures after test with xenon arc lamp: the average temperature recorded on the outer surface of the panel, $T_{\text{surface}}/^\circ\text{C}$ (a), and the average temperature recorded on the rear part of the panel, $T_{\text{panel}}/^\circ\text{C}$ (b).

Table 4. 20. Average temperature recorded on the rear part of the panel ($T_{\text{panel}}/ ^\circ\text{C}$) and the average temperature recorded in the area inside foam box ($T_{\text{box}}/ ^\circ\text{C}$) with resulting heat flux q_{12} ($\text{W}\cdot\text{m}^{-2}$), after exposure to xenon arc lamp.

Sample	$T_{\text{panel}} (^\circ\text{C})$	$T_{\text{box}} (^\circ\text{C})$	$\Delta T (^\circ\text{C})$	$q_{12} (\text{W}\cdot\text{m}^{-2})$
Graphite + Acrylic WB	86.4 ± 1.3	43.0 ± 0.5	43.4	306.1
TiO ₂ + Acrylic WB	61.4 ± 0.2	35.2 ± 0.4	26.2	161.8
Substrate	46.7 ± 0.9	31.4 ± 0.4	15.3	86.7
YInFeO–ZnO/650 $^\circ\text{C}$ + Acrylic WB	72.1 ± 0.5	40.9 ± 0.7	31.2	208.5
YInFeO–ZnO/750 $^\circ\text{C}$ + Acrylic WB	67.4 ± 0.6	35.7 ± 0.5	31.7	201.6
YInFeO–ZnO/850 $^\circ\text{C}$ + Acrylic WB	66.3 ± 0.7	38.4 ± 0.4	27.9	178.4

4.2.3 Comparison among different temperature data

Picture below (**Figure 4. 55**) and **Table 4. 21** let us to discuss in a comparative way the effects of the radiation source chosen to simulate the sun, on the different coatings. As observed for the reflectance data the best performances, in terms of heat reduction are for coatings having pigments obtained after calcination of the dried gel at 850 $^\circ\text{C}$. The lowest T_{surface} is observed for YInMnO–ZnO /850 $^\circ\text{C}$ + PMMA (58.4 $^\circ\text{C}$), while the highest is for YInFeO–ZnO /850 $^\circ\text{C}$ + Acrylic WB (63.23 $^\circ\text{C}$) **Figure 4. 55.a**. The same is valid for T_{panel} and q_{12} values (**Figure 4. 55** and **Table 4. 21**). Anyway YInFeO–ZnO /850 $^\circ\text{C}$ + Acrylic WB seems to be the coating with the highest difference in temperature (ΔT) between the back surface (T_{panel}) and the interior box (T_{box}) but YInFeO–ZnO /850 $^\circ\text{C}$ + Acrylic WB (27.9 $^\circ\text{C}$) shows value of ΔT equal to YInMnO–ZnO /850 $^\circ\text{C}$ + PMMA (27.9 $^\circ\text{C}$). According these compared thermal data we can claim that the two considered coatings have comparable performances

as cooling material, while YInCuO-ZnO /850 °C + PMMA is less performing as it is confirmed by value of q_{12} (218.8 W·m⁻²). As observed for reflectance values, also for thermal characterization were obtained tunable values. Only by changing an element of the host structure of the pigment we obtain different values of surface temperature.

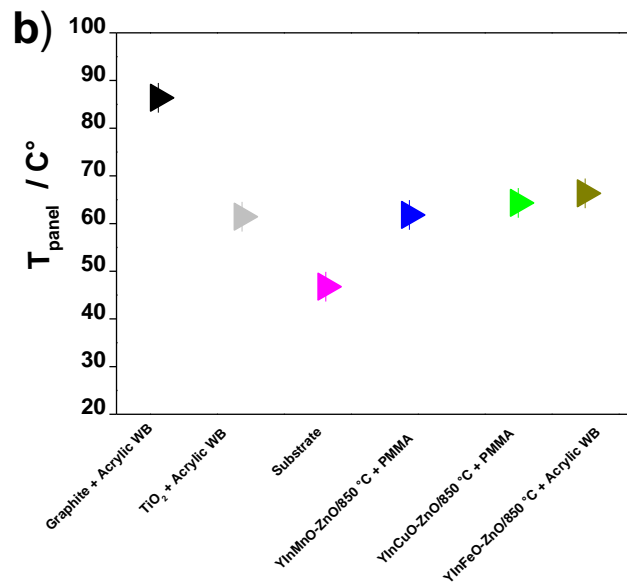
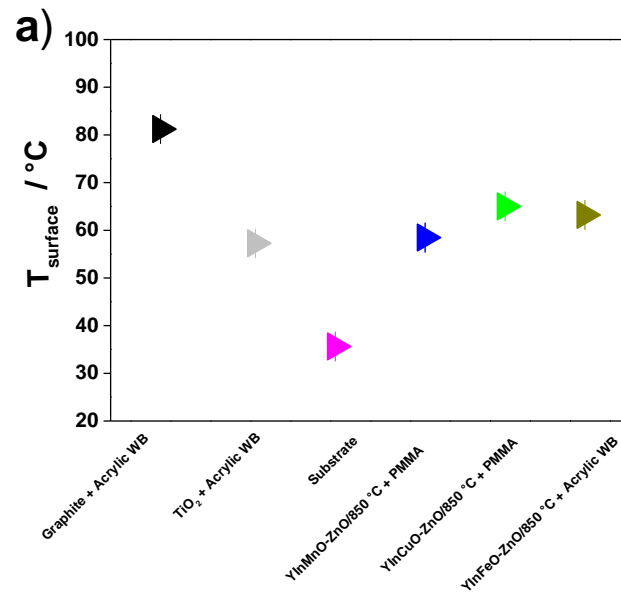


Figure 4. 55. Recorded average temperatures of coatings having pigments obtained after calcination of the dried gel at 850 °C: the average temperature recorded on the outer surface of the panel, $T_{\text{surface}}/^\circ\text{C}$ (a), and the average temperature recorded on the rear part of the panel, $T_{\text{panel}}/^\circ\text{C}$ (b).

Table 4. 21. Average temperature recorded on the rear part of the panel ($T_{\text{panel}}/^\circ\text{C}$) and the average temperature recorded in the area inside foam box ($T_{\text{box}}/^\circ\text{C}$) with resulting heat flux q_{12} ($\text{W}\cdot\text{m}^{-2}$), of coatings having pigments obtained after calcination of the dried gel at 850°C .

Sample	$T_{\text{panel}} (^\circ\text{C})$	$T_{\text{box}} (^\circ\text{C})$	$\Delta T (^\circ\text{C})$	$q_{12} (\text{W}\cdot\text{m}^{-2})$
Graphite + Acrylic WB	86.4 ± 1.3	43.0 ± 0.5	43.4	306.1
TiO ₂ + Acrylic WB	61.4 ± 0.2	35.2 ± 0.4	26.2	161.8
Substrate	46.7 ± 0.9	31.4 ± 0.4	15.3	86.7
YInMnO-ZnO /850 °C + PMMA	61.8 ± 0.7	33.9 ± 0.4	27.9	171.4
YInCuO-ZnO /850 °C + PMMA	64.3 ± 0.9	28.2 ± 0.8	36.1	218.8
YInFeO-ZnO /850 °C + Acrylic WB	66.3 ± 0.7	38.4 ± 0.4	27.9	178.4

5 Investigation of photocatalytic properties of YInFeO–ZnO pigments

5.1 Introduction

In addition to overheating buildings, urban areas experience pollution, generally formed and released during combustion in congested urban environments. Photocatalytic degradation for pollutants removal is an attractive proposition to increase local air quality. Photocatalysis reactions lead to the mineralization of hazardous compounds under mild conditions alone or coupled with other oxidation processes [227]. Since some pigments exhibit photocatalytic properties along with reflective properties, composite compounds can be designed to perform both NIR reflection and photocatalytic air purification simultaneously. As discussed before, the improvement of NIR reflectance ability relies on the combination of different crystalline phases and the same happens in photocatalysis [228–230]. Coupled compounds can be designed to perform in the same time both IR reflection and photocatalytic air purification. ZnO and Fe₂O₃ are used in photocatalytic and cool pigment applications [228], and also TiO₂ and Fe₂O₃ [231]. In case of Fe₂O₃ when is coupled with TiO₂ or ZnO the absorption range of material towards visible light is extended and its photocatalytic activity is enhanced [228,232]. In photocatalytic materials, there are photo generated electron/hole (e⁻/h⁺) pairs due to the oxidation processes. In a one-component system, as α -Fe₂O₃, the high recombination rate of photo generated electrons and holes reduces photocatalytic performance because of the short lifetime of photo

generated charge carriers and small diffusion length of the hole [231,233]. If a wide bandgap semiconductor (such as ZnO or TiO₂) couples with α -Fe₂O₃ the photocatalytic activity of the formed composite will elevate [231,233,234]. Pigments with stoichiometry of YIn_{1-x}Fe_xO₃ reflect NIR radiation efficiently[51,69]. Solid solutions based on YFeO₃ are promising photocatalyst [138,235] but only few papers in literature discuss the NIR reflectance of YFeO₃ based materials [236]. Synthesis of YIn_{1-x}Fe_xO₃ and YFeO₃ based pigments seems to be promising considering environmentally friendly production routes as precipitation method [236] and sol-gel route [202]. YIn_{1-x}Fe_xO₃ based pigments are characterized by yellow, ochre-red hue, so they are a good substitute for toxic traditional yellow pigments. As an example, chrome yellow (PbCrO₄) or solid solutions Pb(Cr,S)O₄, widely used in traffic paints, began to be considered as a source of lead and hexavalent chromium in water and sediments [237]. The pigments based on yttrium, iron, and indium oxides (YIn_{1-x}Fe_xO₃ and YFeO₃) could be labeled as “smart pigments” for building applications considering their photocatalytic activity, sunlight reflection, and environmentally friendly synthesis routes. As discussed before, a two-component system can increase photocatalytic performances and NIR reflectance. Coupling pigments based on yttrium, iron, and indium oxides with zinc oxide (ZnO) can produce an improvement in photocatalytic action and NIR reflectance. Among the pigments previously reviewed, the YInFeO–ZnO based pigments seem to be promising as cool material for their high value of reflectance and the ability of corresponding coatings to retain

heat and having high NIR reflectance. To the ability to have high reflectance is added that of acting as a probable photocatalyst.

5.2 Pigments and materials used for photocatalytic test

To understand if the highest contribute of photocatalytic activity is related to crystalline phases having iron, $\text{YIn}_{0.9}\text{Fe}_{0.1}\text{O}_3$ cubic or hexagonal, or ZnO, were synthesized two pigments. A pigment was obtained by sol-gel route using the same reagents above introduced, excluding ZnO. The times and temperatures of synthesis were maintained the same underlined before. The resulting pigment having the following composition $\text{YIn}_{0.9}\text{Fe}_{0.1}\text{O}_3$ (**Figure 5. 1.a**) was marked as YInFeO. A second pigment was obtained by mixing ZnO nanopowders (**Figure 5. 1.d**) with $\text{YIn}_{0.9}\text{Fe}_{0.1}\text{O}_3$. The two components were mechanically mixed in an agate mortar. The amount of ZnO to add respect to YInFeO₃ was determined according to percentages resulting by XRD analysis on YInMnO–ZnO /850 °C pigment underlined in **Table 4. 3** (27 % of ZnO respect to YInFeO). The resulting pigment was labelled as YInFeO MIX ZnO/ 850°C, (**Figure 5. 1.b**). In **Figure 5. 1.c** is represented the YInMnO–ZnO /850 °C pigment discussed above. Comparing YInMnO–ZnO /850 °C with YInFeO MIX ZnO/ 850 °C there is a clear evidence that ZnO nanoparticles mechanically added modify the shade of yellow toward less light color.

All the powders covered by the study, and the different strategies to obtain them, are summarized in **Table 5. 1** along with the labelling used. **Table 5. 1** shows that the presence of ZnO lightens the shades of yellow of the powder.

The photocatalytic behaviour of pigments was investigated by using 4-Nitrophenol (4-NP) as a model pollutant. Runs were carried out in a cylindrical photoreactor made of Pyrex (V= 20 ml) containing an aqueous suspension of 4-NP with a concentration of 0.3 mM, to which the following quantities of pigments were added: 1 g/L of YInFeO, 0.5 g/L of ZnO, 1.85 g/L of YInFeO – ZnO and of YInFeO MIX ZnO. The suspension, maintained at a temperature of about 27 °C, was kept in the dark under stirring for 30 min to achieve adsorption/desorption equilibrium and then irradiated by six UV actinic fluorescent lamps (Philips, 14 W each, main emission: 365 nm, irradiance: 7 W·m⁻²) placed around the reactor in hexagonal geometry. Samples taken at fixed reaction times were filtered through a 0.2 µm filter (HA, Millipore), acidified with fixed amounts of concentrated H₂SO₄, and analysed by means of a UV–vis spectrophotometer (Shimadzu UV-1900i) by considering the absorbance 316 nm.

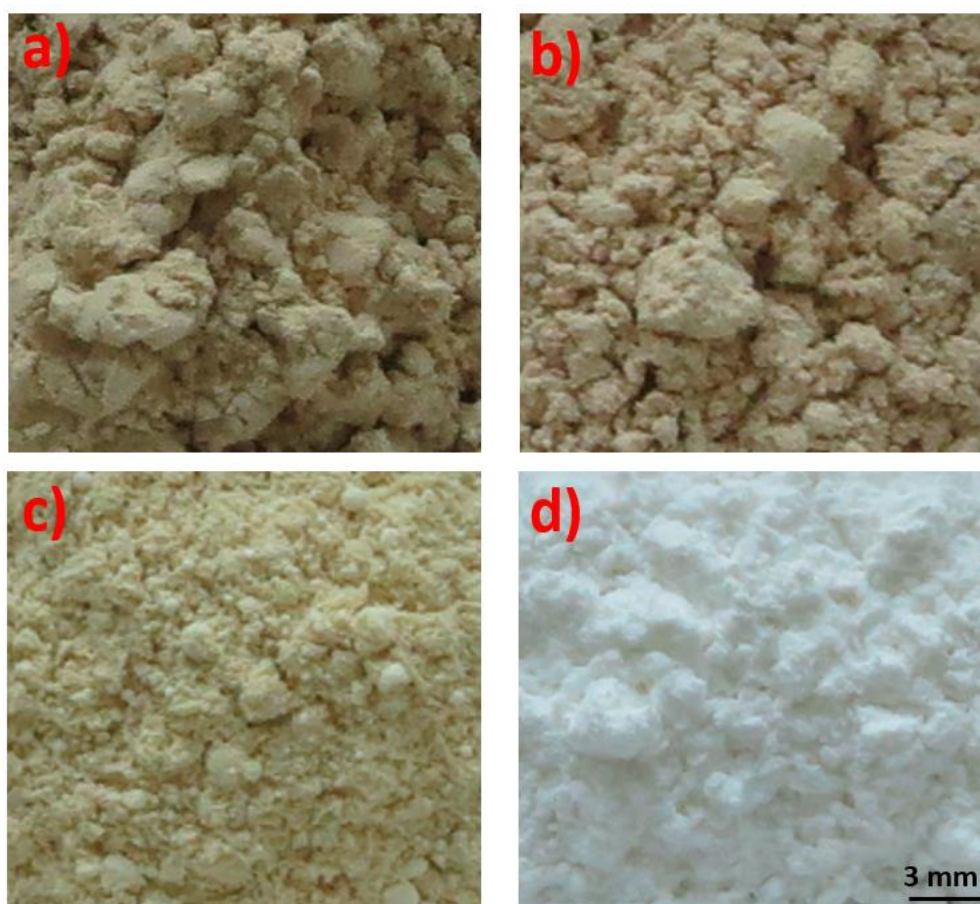


Figure 5. 1. Pictures of the pigments: YInFeO/850 °C (Fig 1.a), YInFeO MIX ZnO/850 °C (Fig 1.b), YInFeO-ZnO/850 °C (Fig 1.c), commercial ZnO (Fig 1.d).

Table 5. 1. Labelling and brief description of the preparation of the pigments.

Pigments label	Description
YInFeO /850 °C	Sol-Gel derived $\text{YIn}_{0.9}\text{Fe}_{0.1}\text{O}_3$ pigments
YInFeO MIX ZnO /850 °C	Sol-Gel derived $\text{YIn}_{0.9}\text{Fe}_{0.1}\text{O}_3$ with ZnO mechanically mixed
YInFeO-ZnO /850 °C	Sol-Gel derived $\text{YIn}_{0.9}\text{Fe}_{0.1}\text{O}_3$ with ZnO added during synthesis
ZnO	ZnO used as supplied

5.3 Deposition and characterization of corresponding coatings

Figure 5. 2 represents the coatings object of this final part of the research. The deposition route followed for the deposition of coatings is the same described in the materials and method section. Acrylic WB, described before, is used to disperse pigments. The obtained coatings were deposited on AA5005 (90 mm × 150 mm × 3 mm) and show comparable dry thickness with the coatings analysed before. As it is evident from the picture the coatings having ZnO show pale yellow color respect to sample without ZnO. Photocatalytic activity of the coated samples have been investigated by using both 4-NP and methylene blue (MB) as the model compounds. The coated samples were cut in low dimensions samples (4 mm²) and were immersed in 20 mL of a 0.06 mM stirred solution of the chosen model compound, irradiated by means of the xenon arc lamp used to evaluate thermal performances, placed at a distance of 30 cm from the solution. Samples taken at fixed intervals of times were analysed by means of UV-vis spectroscopy (Shimadzu UV-1900i, Kyoto, Japan) as above described. The obtained coatings were labelled as described in **Table 5. 2**.

Table 5. 2. Labels to identify all the coatings covered by the study.

Labels	Coating composition
YInFeO / 850 °C+ Acrylic WB	Substrate coated with YIn _{0.9} Fe _{0.1} O ₃ embedded in the binder
YInFeO–ZnO /850 °C+ Acrylic WB	Substrate coated with YIn _{0.9} Fe _{0.1} O ₃ –ZnO embedded in the binder
YInFeO MIX ZnO/ 850 °C + Acrylic WB	Substrate coated with YIn _{0.9} Fe _{0.1} O ₃ MIX ZnO embedded in the binder
ZnO + Acrylic WB	Substrate coated with ZnO embedded in the binder

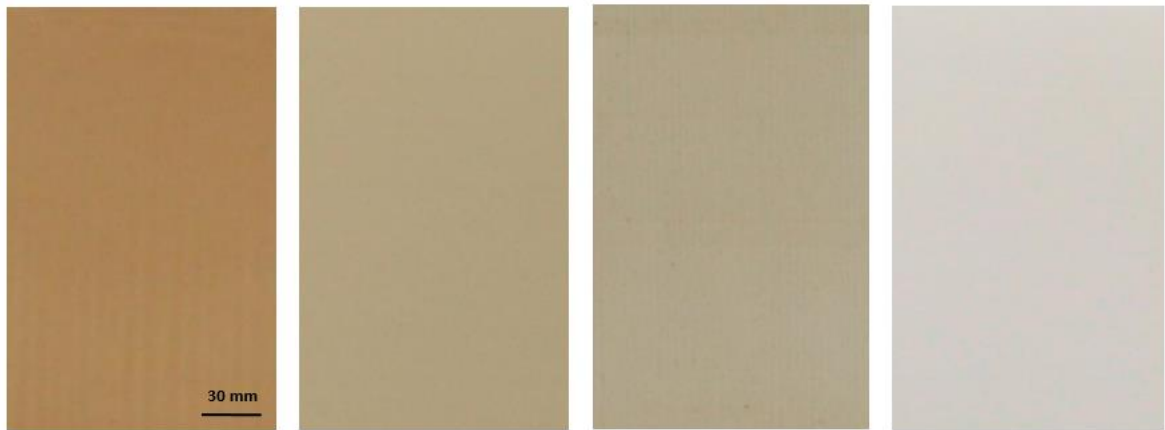


Figure 5. 2. Coated AA5005 samples: (from left to right) YInFeO/ 850 °C + Acrylic WB, YInFeO–ZnO/ 850° C + Acrylic WB, YInFeO MIX ZnO /850 °C + Acrylic WB, ZnO + Acrylic WB.

5.4 Characterization techniques

5.4.1 Structural and morphological analysis

Scanning electron microscopy images of pigments are reported in **Figure 5. 3**. Comparing EDS Zn maps (**Figure 5. 3.b** and **Figure 5. 3.d**) in pigments YInFeO–ZnO/850 °C (**Figure 5. 3.a**), with YInFeO MIX ZnO/850 °C (**Figure 5. 3.c**), it is evident that larger ZnO particles are present in the first case (**Figure 5. 3. a,b**), while ZnO is more homogeneously dispersed in the second case (**Figure 5. 3.c,d**). This can be ascribed to the different preparation methods. In particular by mechanical mixing ZnO nanoparticles result homogeneously dispersed in the powdery mixture. However, concerning the YInFeO–ZnO/ 850 °C, adding ZnO to the nitric acid solution results in the formation of Zn^{2+} ions and further recrystallization and growth of larger ZnO particles through coarsening mechanism, as reported in the literature in similar experimental conditions [238].

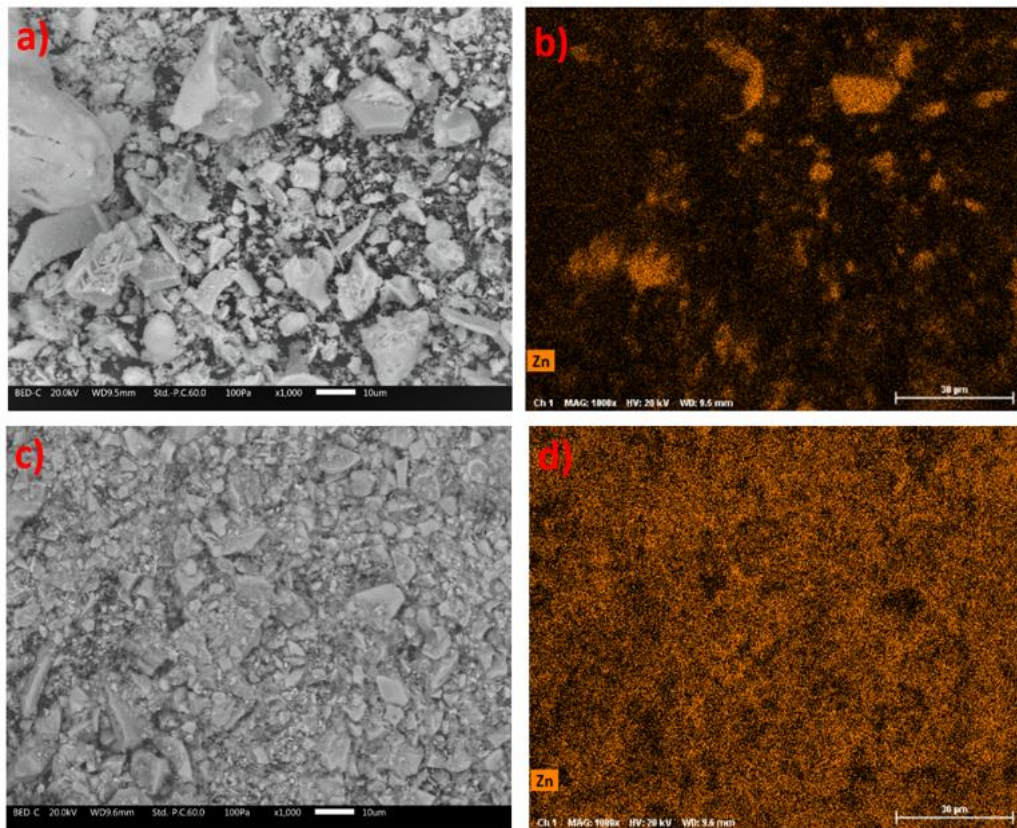


Figure 5. 3. SEM pictures of YInFeO – ZnO/ 850 °C (a) with the corresponding EDS Zn distribution (b), and SEM pictures of YInFeO MIX ZnO/ 850 °C (c) with the corresponding EDS Zn distribution (d).

5.4.2 Color properties

The color is measured according to CIE-1976 $L^*a^*b^*$ colorimetric method. Colorimetric coordinates are listed in **Figure 5. 4**. **Figure 5. 4.a** represents values of colorimetric coordinates of pigments in CIE-1976 $L^*a^*b^*$ color space. The highest value of L^* is showed by the zinc oxide. It is evident that the most saturated color is the pigment $YIn_{0.9}Fe_{0.1}O_3$, without zinc oxide. The a^* and b^* values are similar in all compositions, while the L^* value

depends on the Zn content. Looking at the b^* component it is interesting to note that zinc oxide addition in the sol-gel bath produces the highest value of b^* (24.68), while a physical mixing gives lower value of b^* (17.68). The value of L^* near to 100 (98.86) and a^* and b^* near to 0 are well known for ZnO [239]. All changes in color coordinates due to ZnO are well underlined in **Table 5. 3**. Visible reflectance spectra of pigments and ZnO powder (**Figure 5. 4.b**) confirm that the absence of ZnO produces a deep yellow, and the ZnO contributes to make to shift the color towards blue, making a more pale yellow color.

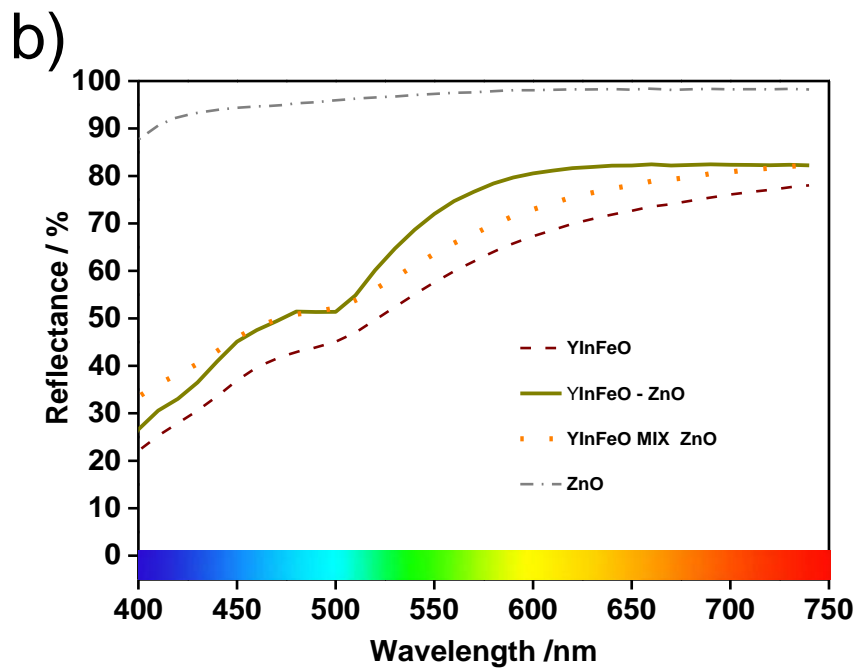
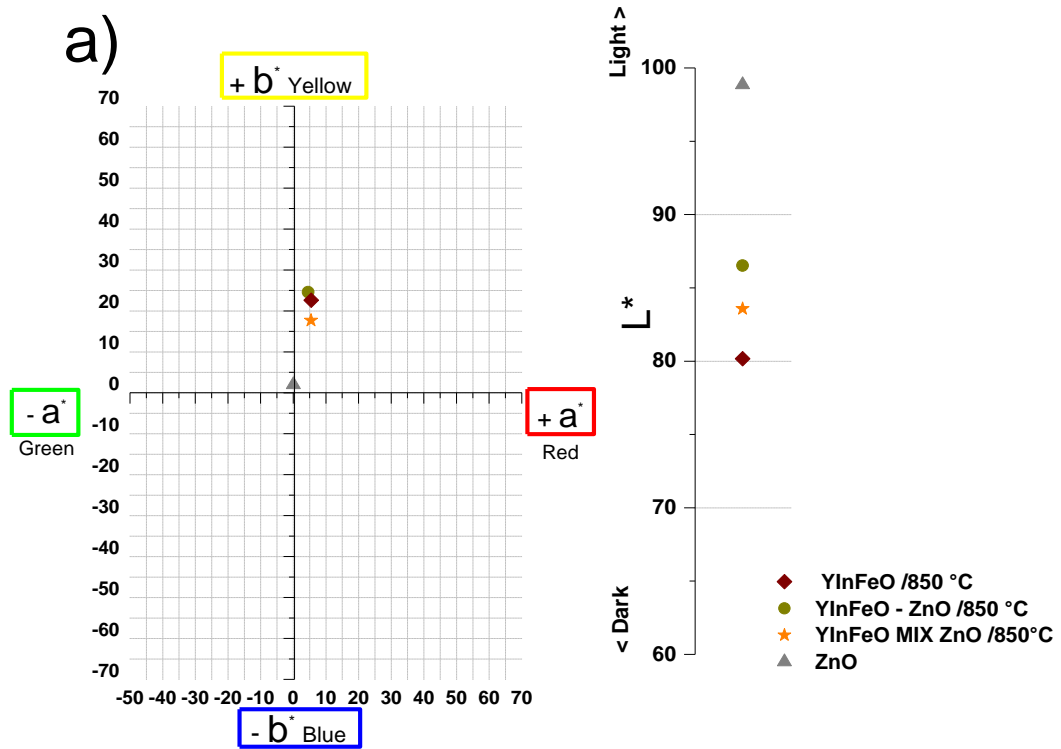


Figure 5. 4. Colorimetric coordinates values for pigments, in CIE-1976 L*a*b* color space (a) and visible light reflectance spectra (b).

Table 5. 3. Colorimetric coordinates values for pigments.

PIGMENTS	COLOR COORDINATES		
	L^*	a^*	b^*
YInFeO ₃	80.17	5.51	22.63
YInMnO-ZnO /850 °C	86.52	4.56	24.58
YInMnO MIX ZnO /850 °C	83.57	5.44	17.68
ZnO	98.86	0.03	2.00

5.4.3 Powder X-ray diffraction analysis

Figure 5. 5 shows the XRD patterns of the investigated pigments employed to test photocatalytic activity. All synthesized pigments having iron (YInFeO, YInFeO-ZnO, YInFeO MIX ZnO) show cubic and hexagonal phases of YIn_{0.9}Fe_{0.1}O₃ while ZnO is present as hexagonal phase. While for similar systems (YIn_{0.9}Mn_{0.1}O₃) the cubic-hexagonal transition was completed above 850 °C [211], cubic and hexagonal phase coexist up to 850 °C for YIn_{0.9}Fe_{0.1}O₃.

Table 5. 4 underlines that the hexagonal phase of YIn_{0.9}Fe_{0.1}O₃ is around 5.65 %. A low percentage of the hexagonal phase of YIn_{0.9}Fe_{0.1}O₃ is also shown in YInFeO MIX ZnO (2.51 %). The hexagonal phase of YIn_{0.9}Fe_{0.1}O₃ is in percentage of 56.21 in YInFeO-ZnO. Probably ZnO also acts as a crystallization seed and favors the growth of a higher amount of YIn_{0.9}Fe_{0.1}O₃ with hexagonal phase. X-ray diffraction studies confirmed the formation of epitaxial hexagonal phases over wurtzite ZnO core particles [240,241]. Therefore, the formation of a higher amount of hexagonal YIn_{0.9}Fe_{0.1}O₃ is not due only to thermal stability

but is likely to be related to the presence of ZnO crystals. Pigments particles nucleate and grow on ZnO surface through a citrate sol-gel method [71].

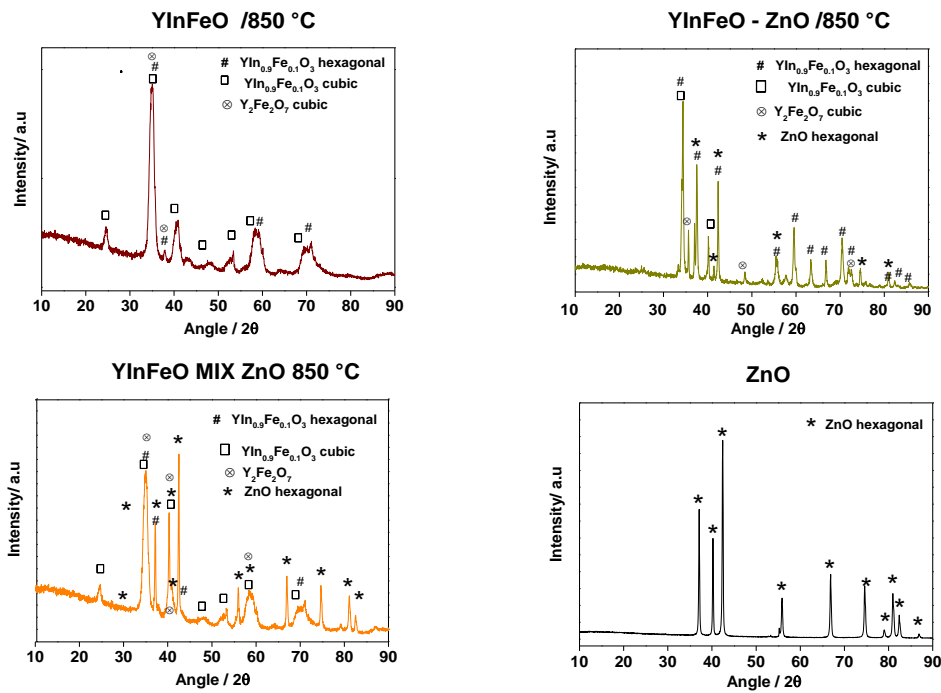


Figure 5. 5. XRD patterns of the investigated pigments.

Table 5. 4. Crystallographic data for pigments used in photocatalytic test, obtained by Rietveld refinement using Maud software.

Reliability factors (%)		$YIn_{0.9}Fe_{0.1}O_3$ Phases						ZnO Phase			$Y_2Fe_2O_7$ Phase	
R_{wp}	R_{exp}	Cubic (Space group Ia-3)		Hexagonal (Space group P6 ₃ cm)		Hexagonal (Space group P6 ₃ mc)		Cubic (Space group F23)		a	Amount (%)	
		Cell parameters (Å)	Amount (%)	Cell parameters (Å)	Amount (%)	Cell parameters (Å)	Amount (%)	Cell parameters (Å)	Amount (%)			
		a		a	c	a	c	a	c			
YInFeO ₃	12.92	4.20	10.4558 ± 0.0020	93.76 ± 14.00	6.2698 ± 0.0003	12.1879 ± 0.0122	5.65 ± 1.72				10.3007 ± 0.0023	0.58 ± 0.09
YInFeO - ZnO	29.21	7.47	10.6318 ± 0.0004	16.42 ± 1.64	6.2776 ± 0.0008	12.2519 ± 0.0003	56.21 ± 3.34	3.2495 ± 0.0006	5.2295 ± 0.0020	26.75 ± 0.01	10.1810 ± 0.0027	0.60 ± 0.06
YInFeO MIX ZnO	16.88	4.39	10.4145 ± 0.0002	75.30 ± 1.93	6.2648 ± 0.0021	2.4454 ± 0.0019	2.51 ± 0.25	3.2665 ± 0.0007	5.2051 ± 0.0001	21.81 ± 0.00	10.2861 ± 0.0020	0.36 ± 0.03
ZnO								3.2492 ± 0.0006	5.2055 ± 0.0001	100 ± 0.00		

5.4.4 Near-infrared reflectance of investigated pigments

Figure 5. 6.a shows the near-infrared reflectance spectra of the studied pigments and in **Figure 5. 6.b** the corresponding NIR solar reflectance. A slight increase in the NIR reflectance is observed in the mixed samples with respect to YInFeO/ 850 °C. A noteworthy behavior is observed in the NIR reflectance spectra up to 1300 nm. Since 700–1100 nm is the most significant heat-producing region in the NIR domain, considerations about these pigments' NIR reflectance ability can be focused in this range. Up to 1100 nm, samples with ZnO have NIR reflectance spectra that are well stacked and the reflectance is slightly higher than the reflectance spectrum of YInFeO/ 850 °C sample. The high value of NIR reflectance of each pigment is due to the presence of ZnO, which is recognized to show high NIR reflectance as can be observed in the obtained spectrum in **Figure 5. 6.a**. The slight increase above 100 % in reflectance is observed in YInFeO MIX ZnO/ 850 °C sample up to about 105 % at the 1750–2500 nm range. This is usual in analysis of powdery materials in the high wavelengths region of the spectra as was observed for previous samples discussed before. **Table 5. 5** shows the NIR reflectance values at the 1100 nm and the NIR solar reflectance values. Comparing data in **Table 5. 5** there is no marked difference in reflectance between YInFeO–ZnO, with large ZnO crystals, and YInFeO MIX ZnO with nanometric ZnO. Values in **Table 5. 5** underline that YInFeO/ 850 °C is able to reflect near infrared radiation similarly to pigments with ZnO. This is clear looking NIR reflectance spectrum of YInFeO/ 850 °C in **Figure 5. 6**, which has reflectance values near to the other spectra, at 1100 nm (see values in

column IR reflectance at 1100 nm (%) of **Table 5.5**). Thus, NIR reflectance is mainly due to intrinsic factors of YInFeO/ 850 °C, as sustained before.

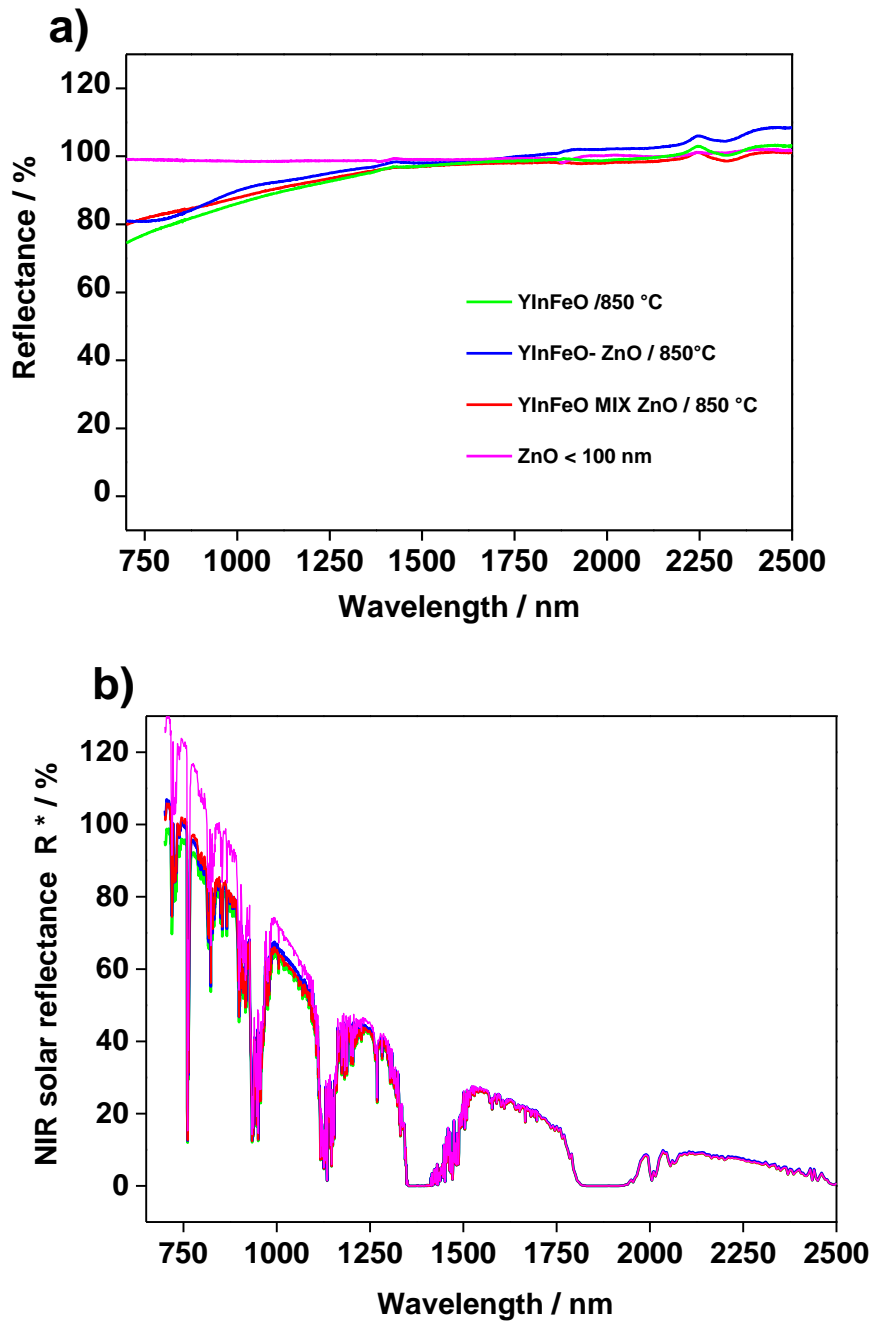


Figure 5.6. NIR reflectance spectra (a) and NIR solar reflectance of the pigments under investigation and NIR solar reflectance obtained in compliance with ASTM G173-03 standard (b).

Table 5. 5. Solar reflectance and NIR reflectance at 1100 nm of the investigated pigments.

Pigments	Solar reflectance, R* (%)	NIR reflectance at 1100 nm (%)
YInFeO ₃	85.53	89.29
YInFeO-ZnO	90.10	92.32
YInFeO MIX ZnO	89.04	90.54
ZnO	100.17	98.90

5.4.5 Photocatalytic test of obtained pigments

The photocatalytic activity of the pigments was evaluated in terms of degradation of 4-Nitrophenol under UV light irradiation. The concentration in **Figure 5. 7** is expressed as a ratio of 4-NP concentration after irradiation (C) respect to 4-NP concentration after irradiation (C₀). The YInFeO/ 850 °C sample does not show any activity. On the contrary, bare ZnO is capable to degrade almost completely 4-NP after ca. 120 minutes, according to the relevant literature [229]. Coupling ZnO and YInFeO/ 850°C improves the degradation efficiency with respect to bare ZnO only when the components were mechanically mixed, while lower activity can be observed for the YInFeO-ZnO/ 850 °C sample. The lower activity of the YInFeO/ 850 °C sample can be justified by considering the characterization results above reported. In fact, the size of the ZnO particles increases during the synthesis (**Figure 5. 3**), thus reducing the exposed surface area. Moreover, XRD results highlight the growth

of YInFeO/ 850 °C particles on the surface of ZnO, further reducing the direct interaction between the active surface of ZnO and the target pollutant. On the other hand, the simply mixing ZnO and YInFeO maintains the size distribution of the ZnO particles, thus resulting in improved photocatalytic efficiency. Notably, the mechanical mixture is slightly more active than bare ZnO, even if the amount of the ZnO as the active phase is 30 % lower in the reacting mixture. This suggests that a synergistic effect between the two components could take place, even if further investigation is required to confirm this hypothesis.

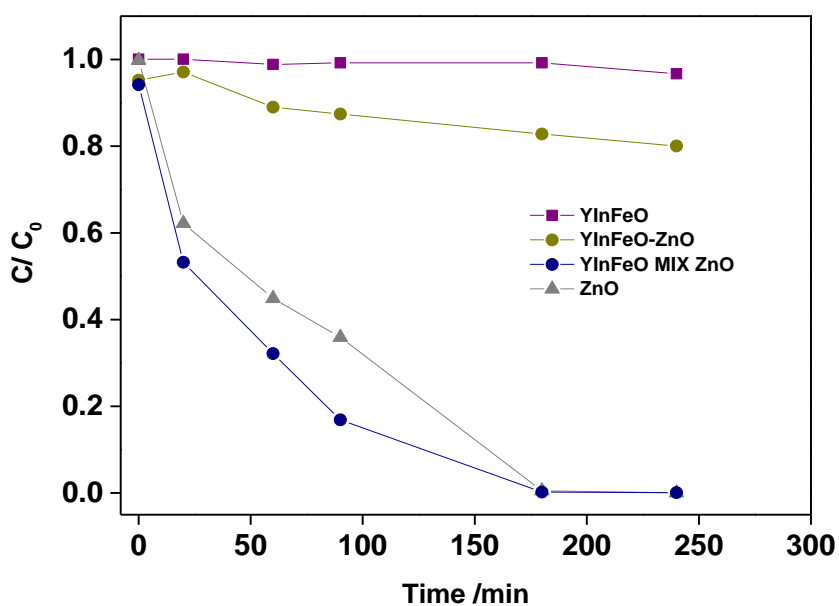


Figure 5. 7. Concentration of 4-Nitrophenol versus UV light irradiation time in the presence of synthesized pigments.

5.4.6 Near-infrared reflectance of coatings

Figure 5. 8.a shows the NIR reflectance spectra of pigmented coatings and the reference samples (Graphite + Acrylic WB, TiO₂ + Acrylic WB, and Substrate). As done for NIR reflectance spectra of pigments, a focus on the analysis of NIR reflectance spectra up to 1100 nm can explain their behavior for application as cool roof. From the comparison of the spectra, it is possible to note that coatings maintain the same behavior as the pigments. Differently from reflectance spectra of pigments, in this case, the difference between coatings having ZnO (YInFeO–ZnO/ 850 °C + Acrylic WB, YInFeO MIX ZnO/ 850 °C + Acrylic WB, ZnO + Acrylic WB) and coatings without it (YInFeO/ 850 °C + Acrylic WB) is more marked. Coating YInFeO/ 850°C + Acrylic WB shows a significant decrease in the NIR reflectance up to 1100 nm. The NIR solar reflectance power spectra of the investigated coatings, obtained in compliance with ASTM G173-03 standard (Figure 5. 8.b), confirm the trend observed for the NIR reflectance. The obtained results can be explained considering that the NIR reflectance relies mainly on the presence of ZnO, which confers the highest values of IR reflectance at 1100 nm (%) and Solar reflectance, R* (%), among the investigated materials.

The difference between coatings with and without ZnO is evident by comparing data shown in Table 5. 6. The calculated solar reflectance R* is, in fact, lower for the coating having YInFeO/ 850 °C (60.65 %) while the R* increases clearly with the addition of ZnO in the binder. For coating YInFeO MIX ZnO/ 850 °C + Acrylic WB R* is the highest (68.95 %), excluding sample TiO₂ + Acrylic WB (82.32 %). Comparing values in Table 5. 6 (R* and IR

reflectance at 1100 nm) there are no marked differences in the values of the YInFeO MIX ZnO /850°C + Acrylic WB and YInFeO–ZnO/ 850 °C + Acrylic WB samples, (YInFeO–ZnO/ 850 °C + Acrylic WB has R^* value of 66.07 %, while with YInFeO MIX ZnO + Acrylic WB is of 68.95 %). ZnO + Acrylic WB has R^* value is of 70.48 %, similar to those for YInFeO–ZnO + Acrylic WB and YInFeO MIX ZnO + Acrylic WB.

Bare AA5005 (Substrate) shows constant values of 40 % of NIR reflectance in the entire NIR spectrum. TiO₂ + Acrylic WB and Graphite + Acrylic WB confirm their suitability as control samples: TiO₂ + Acrylic WB is the most reflective sample (having R^* of 82.32 %) while Graphite + Acrylic WB is the sample with NIR reflectance near zero (R^* is of 8.50 %).

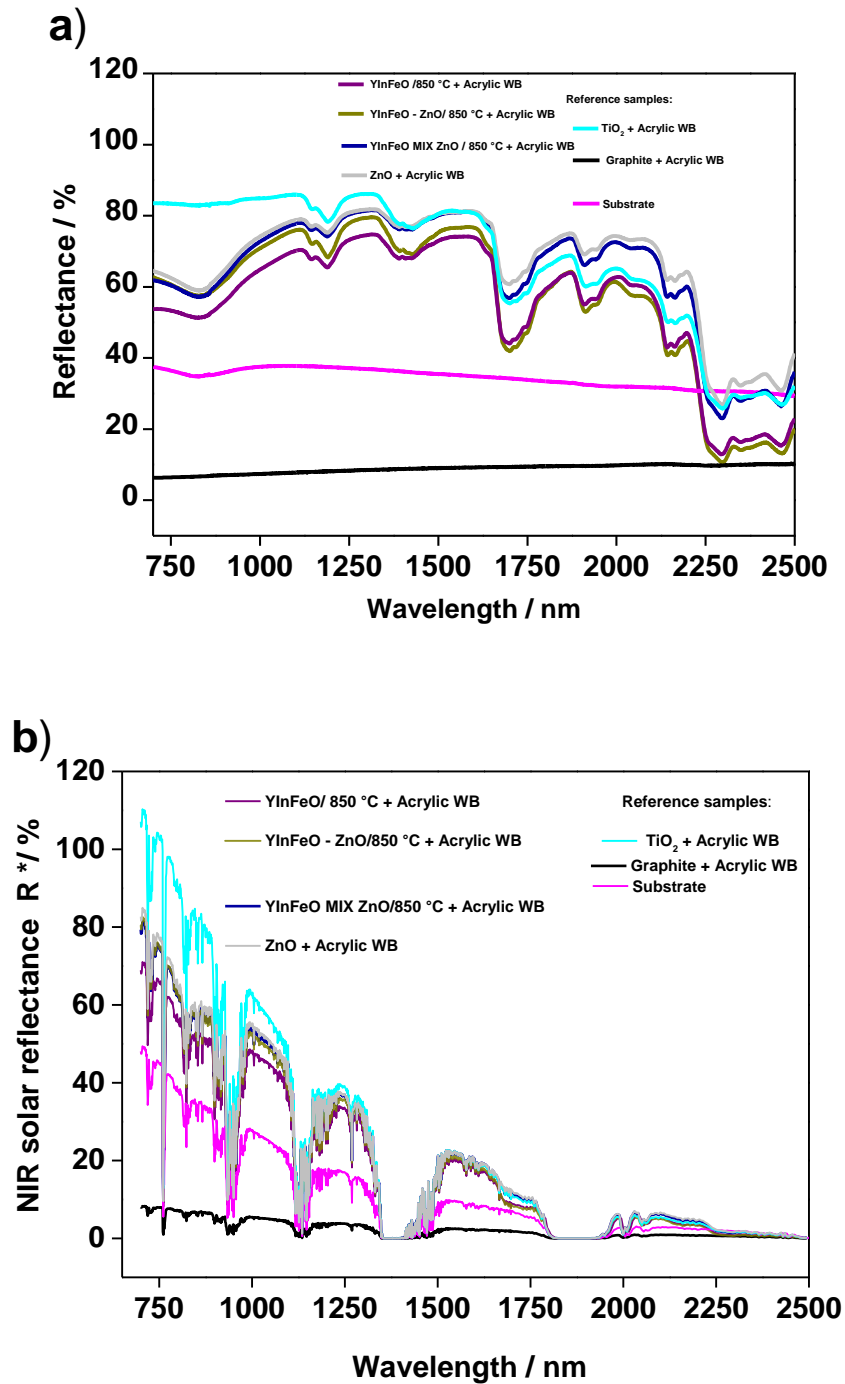


Figure 5. 8. NIR reflectance spectra (a) of the coatings under investigation with corresponding NIR solar reflectance obtained in compliance with ASTM G173-03 standard (b).

Table 5. 6. Solar reflectance and NIR reflectance at 1100 nm of the investigated coatings.

Sample	NIR reflectance at 1100 nm (%)	Solar reflectance, R* (%)
Graphite + Acrylic WB	8.11	7.76
TiO ₂ + Acrylic WB	85.89	82.32
Substate	37.76	36.30
YInFeO /850 °C + Acrylic WB	69.74	60.65
YInFeO–ZnO /850 °C + Acrylic WB	75.93	66.07
YInFeO MIX ZnO /850 °C + Acrylic WB	77.04	68.95
ZnO + Acrylic WB	78.98	70.48

5.4.7 Photocatalytic test of coatings derived from pigments

The photocatalytic activity of the pigments embedded in the acrylic binder was tested by considering both the degradation of 4-NP and of methylene blue (MB). We decided to test also MB in this case because this compound is used as a probe molecule to evaluate the photocatalytic activity [223]. TiO₂ + Acrylic WB was also tested for comparison. All of the samples showed the same behavior in degrading the pollutants. Two representative runs, for 4NP (curve a) and MB (curve b) degradation respectively, are reported in **Figure 5. 9**. The values of decrease in concentration of all samples were used to calculate an average value of C/C_0 at each time. No degradation of 4NP could be observed in the presence of all of the embedded pigments even under longer irradiation time (up to 240 hours). By considering the photocatalytic results obtained in the presence of the pigments (**Figure 5. 7**), this behavior can be ascribed to the presence of the acrylic binder which strongly limits the direct interaction between 4NP and the pigments, suppresses the interfacial electron

transfer and the generation of reactive oxygen species. Therefore, even if the addition of ZnO endows the pigment with both efficient NIR adsorption and photocatalytic activity, a different binder must be chosen to allow displaying the smart properties of the coatings. On the other hand, MB concentration in solution decreased with the same trend in the presence of all of the embedded pigments and the acrylic binder without pigments. These results highlight that, as also reported in several paper [242,243], MB is not a suitable compound to test the activity of coatings because of the complex photochemistry and on the plethora of photoinduced mechanisms which can take place concurrently to the direct photocatalytic one, which is the target to be investigated when testing the activity of photoactive materials.

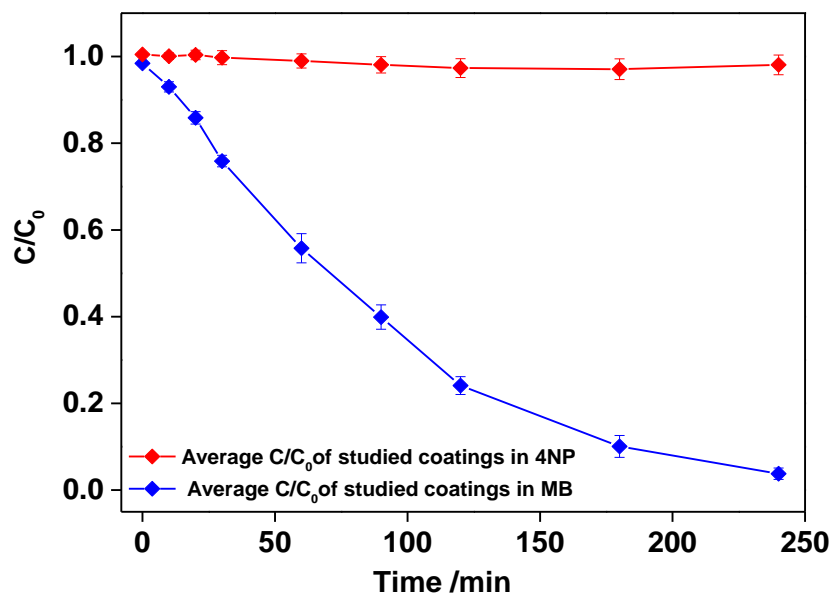


Figure 5. 9. Average concentration of M-B and 4 NP versus xenon arc lamp irradiation time in the presence of synthesized coatings.

5.4.8 Effect of coatings under xenon radiation source

T_{surface} for the different coatings exposed to xenon arc lamp is reported in **Figure 5. 10.a**. The T_{surface} is of 64.8 °C for the sample YInFeO/ 850 °C + Acrylic WB, while it progressively decreases passing from coating YInFeO – ZnO/ 850 °C + Acrylic WB (63.2 °C) to YInFeO MIX ZnO/ 850 °C + Acrylic WB coating (60.2 °C), as shown in **Figure 5. 10**. Coating with nanometric ZnO shows a slight decrease in temperature with respect to pigments with ZnO added during synthesis. It is possible to affirm that the $\text{YIn}_{0.9}\text{Fe}_{0.1}\text{O}_3$ and nanometric ZnO play an important role in decreasing temperature, and then YInFeO MIX ZnO/ 850 °C pigment could be recognized as a cool material. According to the trends reported in T_{panel} plot, the coatings YInFeO – ZnO/ 850 °C + Acrylic WB and YInFeO MIX ZnO/ 850 °C + Acrylic WB seem to show lower T_{panel} temperatures compared to the other samples. Of course the YInFeO MIX ZnO/ 850 °C pigment is able to cool down better the coating with respect to YInFeO-ZnO/ 850 °C, as nanometric particles of ZnO with good distribution in the coatings increase the cool activity for their higher active surface. In **Table 5. 7** there are showed T_{panel} values, which confirm the cooling performance of YInFeO MIX ZnO/ 850 °C + Acrylic WB coating.

Samples YInFeO–ZnO/ 850 °C + Acrylic WB, YInFeO MIX ZnO/ 850 °C + Acrylic WB, and ZnO + Acrylic WB show values of T_{box} that are 38.4 °C, 38.1 °C and 36.3 °C respectively. The coating with $\text{YIn}_{0.9}\text{Fe}_{0.1}\text{O}_3$ pigment shows highest T_{box} value (43.7 °C), that is approximately similar to Graphite + Acrylic WB (43.0 °C). T_{box} value of ZnO + Acrylic WB (36.3 °C) is

coherent to the fact that ZnO can make a cool surface, which makes a cooling in the analyzed inner temperature.

Table 5. 7 represents also the heat exchange values $q_{1,2} / (W m^{-2})$. Heat exchange values give further evidence that all coatings lead to surface cooling. The q_{12} value of YInFeO + Acrylic WB is the lowest of coatings having synthesized pigments ($153.1 W m^{-2}$) and this is an evidence of the intrinsic nature of $YIn_{0.9}Fe_{0.1}O_3$ phases to confer cooling properties to coatings as demonstrated by other authors.

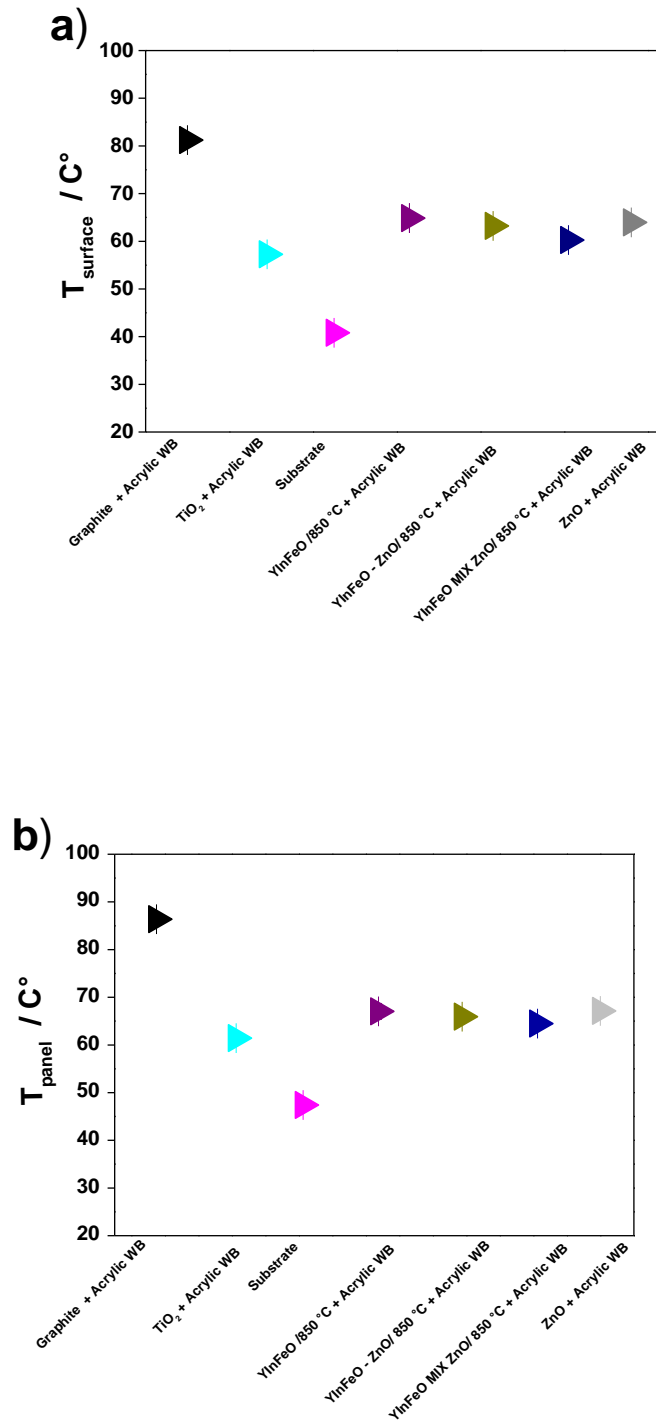


Figure 5. 10. Recorded average temperatures after test with xenon arc lamp: the average temperature recorded on the outer surface of the panel, $T_{\text{surface}} / ^\circ\text{C}$ (a), and the average temperature recorded on the rear part of the panel, $T_{\text{panel}} / ^\circ\text{C}$ (b).

Table 5. 7. Average temperature recorded on the rear part of the panel (T_{panel} / °C) and the average temperature recorded in the area inside foam box (T_{box} / °C) with resulting heat flux $q_{1,2}$ / ($\text{W}\cdot\text{m}^{-2}$), after exposure to Xenon Arc Lamp.

Sample	T_{panel} (°C)	T_{box} (°C)	ΔT (°C)	$q_{1,2}$ ($\text{W}\cdot\text{m}^{-2}$)
Graphite + Acrylic WB	86.4 ± 1.3	43.0 ± 0.5	43.4	306.1
TiO ₂ + Acrylic WB	61.4 ± 0.2	35.2 ± 0.4	26.2	161.8
Substrate	46.7 ± 0.9	31.4 ± 0.4	15.3	86.7
YInFeO / 850 °C+ Acrylic WB	67.0 ± 0.7	43.7 ± 1.3	23.3	153.1
YInFeO–ZnO / 850 °C + Acrylic WB	66.3 ± 0.7	38.4 ± 0.4	27.9	178.4
YInFeO MIX ZnO / 850 °C + Acrylic WB	64.5 ± 1.2	38.1 ± 0.7	26.4	167.3
ZnO + Acrylic WB	65.1 ± 0.4	36.3 ± 0.5	28.8	181.9

5.5 Observations on properties of YInFeO–ZnO pigments and corresponding coatings

A pigments group based on sol-gel synthesis route was investigated, aiming to employ it as a smart material that can cool down coatings surfaces and photocatalytic activity. YInFeO MIX ZnO/ 850°C is a promising pigment that can reflect NIR radiation, cool down the coatings' temperature, and show photocatalytic activity even higher than bare ZnO. It is interesting to note that recorded temperatures and values of reflectances in YInFeO MIX ZnO and ZnO are almost comparable but ZnO in the mechanical mix modifies color shades and increases photocatalysis. Mechanically mixing the two components is a better procedure with respect to the hydrothermal synthesis of the composite, especially as far as the photocatalytic activity is concerned. In fact, even if only slight differences could be observed in the NIR absorption, the nanostructured distribution of the ZnO particles is

preserved in the first case and the photocatalytic activity is significantly higher. NIR reflectance spectra and NIR solar reflectance value of pigment $\text{YIn}_{0.9}\text{Fe}_{0.1}\text{O}_3$, that are comparable with values of pigments having ZnO, underline that NIR reflectance high values are not due only to the ZnO but also to the intrinsic nature of $\text{YIn}_{0.9}\text{Fe}_{0.1}\text{O}_3$, as was demonstrated in the literature [42]. Further evidence of the reliable application of $\text{YIn}_{0.9}\text{Fe}_{0.1}\text{O}_3$ as a material for cool roof is given by heat exchange value q_{12} of coating having $\text{YIn}_{0.9}\text{Fe}_{0.1}\text{O}_3$ ($\text{YInFeO} + \text{Acrylic WB}$), which is the lowest compared to all the samples. Considering all synthesized pigments, when they are added in an acrylic binder, they can confer the features of a cool coating to the layer (high NIR reflectance and low temperature on the coating surface). However, embedding the pigments in the acrylic binder completely suppresses photocatalytic activity probably due to the shielding action of the polymeric binder. It is also highlighted that methylene blue, and possibly of similar dyes, must be avoided when testing the photocatalytic activity of photoactive materials.

6 Comparison among significant results

This part aims to collect the fundamental measures for the characterization of the most promising pigments and of the corresponding coatings with cool coating application.

The **Figure 6. 1** underlines that among pigments obtained through the calcination of the dried gel at 850 °C the pigments having iron are the most reflective, and it can be claimed that YInFeO MIX ZnO/ 850 °C has comparable reflectance values with YInFeO–ZnO/ 850 °C pigment, up to 1100 nm. Looking at the values in **Table 6. 1**, the solar reflectance values of YInFeO MIX ZnO/ 850 °C and YInFeO–ZnO/ 850 °C are almost comparable.

The **Figure 6. 2** represents the T_{surface} of all coatings having pigments synthesized as 850 °C, with also YInFeO MIX ZnO / 850 °C. T_{surface} is a diagnostic, and easy to interpret parameter to understand the thermal behavior of the coatings exposed to lamp. The coatings are subjected to heating due only by direct irradiation. In the plot is evident that T_{surface} of YInFeO MIX ZnO / 850 °C + Acrylic WB is slightly lower than YInFeO–ZnO/ 850 °C + Acrylic WB. Even if YInMnO–ZnO/ 850 °C + PMMA results the coating having the lowest T_{surface} (**Table 6. 2**). The YInFeO MIX ZnO / 850 °C + Acrylic WB gives the lowest q_{12} . The highest value of NIR reflectance at 1100 nm and solar reflectance (**Figure 6. 3** and **Table 6. 3**) obtained for YInFeO MIX ZnO / 850 °C+ Acrylic WB confirm that is the best coating to be used in cool coating application.

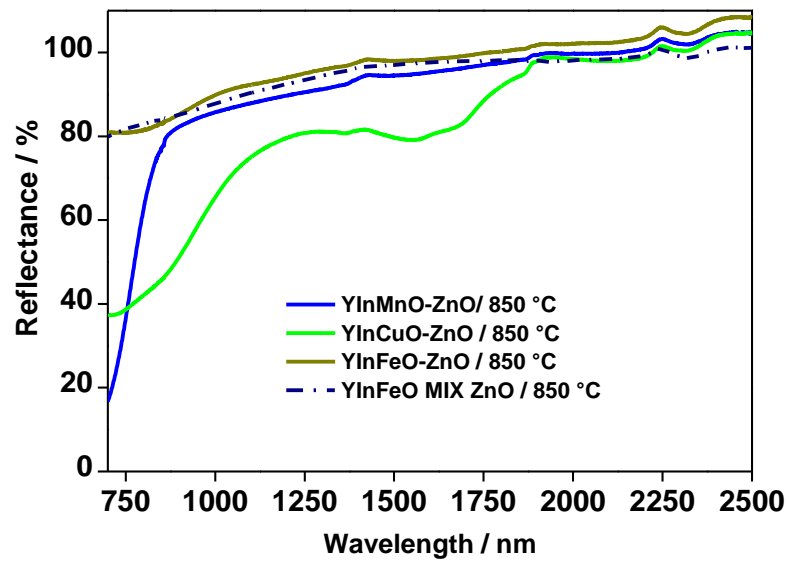


Figure 6. 1. NIR reflectance spectra of all the pigments, covered in the study, obtained after calcination of the dried gel at 850 °C, with the inclusion of YInFeO MIX ZnO / 850 °C pigment.

Table 6. 1. NIR reflectance at 1100 nm and solar reflectance of the investigated coatings with pigments obtained after calcination of the dried gel at 850 °C, with the inclusion of coating having YInFeO MIX ZnO / 850 °C pigment.

Pigments	NIR reflectance at 1100 nm (%)	Solar reflectance R* (%)
YInMnO-ZnO /850 °C	87.64	76.11
YInCuO-ZnO /850 °C	75.05	63.14
YInFeO-ZnO /850 °C	92.32	90.10
YInFeO MIX ZnO /850 °C	90.54	89.04

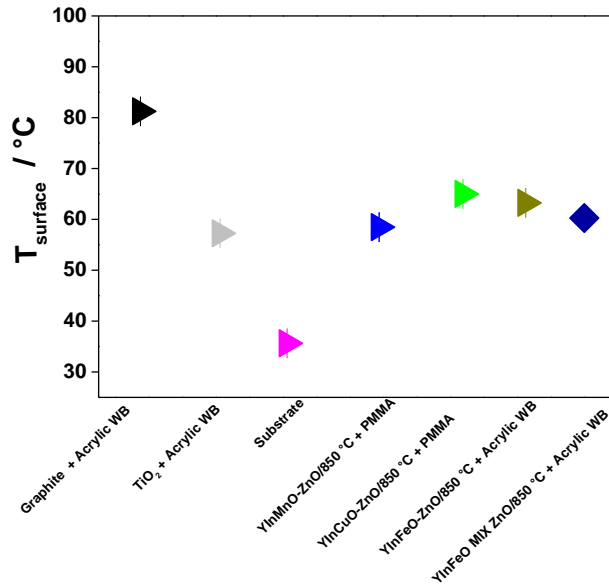


Figure 6. 2. T_{surface} of all coatings having pigments obtained after calcination of the dried gel at 850 °C, with the inclusion of coating having YInFeO MIX ZnO / 850 °C pigment.

Table 6. 2. . Recorded average temperatures produced by exposure to sunlight of all coatings having pigments obtained after calcination of the dried gel at 850 °C, with the inclusion of coating having YInFeO MIX ZnO / 850 °C pigment.

Sample	T_{panel} (°C)	T_{box} (°C)	ΔT (°C)	q_{12} (W/m ²)
Graphite + Acrylic WB	86.4 ± 1.3	43.0 ± 0.5	43.4	306.1
TiO ₂ + Acrylic WB	61.4 ± 0.2	35.2 ± 0.4	26.2	161.8
Substrate	46.7 ± 0.9	31.4 ± 0.4	15.3	86.7
YInMnO–ZnO /850 °C + PMMA	61.8 ± 0.7	33.9 ± 0.4	27.9	171.4
YInCuO–ZnO /850 °C + PMMA	64.3 ± 0.9	28.2 ± 0.2	36.1	218.8
YInFeO –ZnO / 850 °C+ Acrylic WB	66.3 ± 0.7	38.4 ± 0.4	27.9	178.4
YInFeO MIX ZnO / 850 °C + Acrylic WB	64.5±1.2	38.1±0.7	26.4	167.3

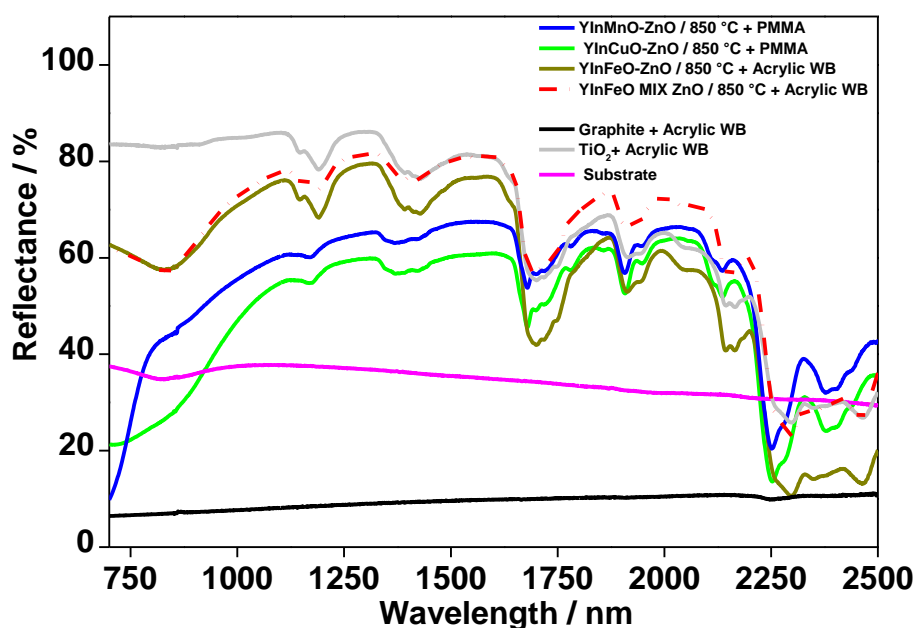


Figure 6. 3. NIR reflectance spectra of all coatings having pigments obtained after calcination of the dried gel at 850 °C, with the inclusion of coating having YInFeO MIX ZnO / 850 °C pigment.

Table 6. 3. NIR reflectance at 1100 nm and solar reflectance of the investigated coatings with pigments obtained after calcination of the dried gel at 850 °C, with the inclusion of coating having YInFeO MIX ZnO / 850 °C pigment.

Sample	IR reflectance at 1100 nm (%)	Solar reflectance, R* (%)
Graphite + Acrylic WB	8.11	7.76
TiO ₂ + Acrylic WB	85.89	82.32
Substate	37.76	35.90
YInMnO-ZnO /850 °C + PMMA	60.38	49.58
YInCuO-ZnO /850 °C + PMMA	54.72	41.04
YInFeO-ZnO /850 °C + Acrylic WB	75.93	66.07
YInFeO MIX ZnO /850 °C + Acrylic WB	77.04	68.95

7 Conclusions

The present thesis aimed to synthesize NIR reflective pigments and to produce NIR reflective coatings for cool coatings application. According to what was claimed in introductory section there are three widely used colors in NIR reflective pigments field: yellow, red, and shades tending to blue. In this thesis, excluding pigments having copper that are green, were synthesized pigments having yellow, red, and blue color.

In particular was synthesized a group of yellow pigments, having iron as doping element. A pigment with a red ochre color (YInMnO-ZnO /550 °C) was synthesized. Furthermore were synthesized pigments having two different shades of blue: YInMnO-ZnO /800 °C, and YInMnO-ZnO /850 °C.

YInFeO-ZnO pigments having yellow color have color coordinates similar to yellow pigments shown in Jose et al [70] paper. The highest value of NIR reflectance reached by Jose et al. is of about 88%. This value was observed in pigment having the following formulation: CeBi₂₀O₃₂. The YInFeO-ZnO based pigment having highest value of reflectance is YInFeO-ZnO/ 850 °C pigment. YInFeO-ZnO/ 850 °C pigment reaches a value of NIR reflectance equal to 90.10 %, which is comparable with value obtained by Jose et al.

The YInMnO-ZnO /550 °C pigment having red ochre color has color shade comparable with red brick pigments having general formula Bi_xLa_xFeO₃, synthesized by Yuan et al. [83]. Yuan

et al reach values of NIR reflectance of about 50 %, as the lowest value, while 75 % as the highest value. In YInMnO–ZnO /550 °C was obtained a value of reflectance of about 84 %.

About blue pigments shown in this thesis are obtained two different shades of blue: A cyan blue (YInMnO–ZnO /800 °C) and a deep blue (YInMnO–ZnO /850 °C).

Cyan blue pigment (YInMnO–ZnO /800 °C) has color coordinates near to pigments synthesized by Hedayati et al [56], with the general formula $\text{Co}_{1-x}\text{ZnCr}_{2-y}\text{Al}_y\text{O}_4$. In this case the highest value of NIR reflectance is of about 52 %, while YInMnO–ZnO /800 °C shows value of 76 %. It is interesting to note that the deep blue pigment (YInMnO–ZnO /850 °C), shows color coordinates near to the commercial cobalt blue discussed in the cited paper of Li et al.[89]. The cobalt blue reaches value of NIR reflectance of about 58 %, (it is not used as NIR reflective pigment). The YInMnO–ZnO /850 °C pigment has a value of NIR reflectance of about 87 %. So it can be claimed that YInMnO–ZnO /850 °C can easily act also as a substitute of a traditional pigment.

The Sol-Gel route resulted to be advantageous for the low temperatures employed and short times, together with low amount of expensive raw materials (rare earth oxides). Furthermore, the use of non-toxic reagents, in a process, which is known to be “waste-free”, helps to label the synthesis process used as environmentally friendly.

The obtained pigments show a wide variety of colors, just by tuning the calcination temperature and adding chromophores (Mn, Cu, Fe). Comparing NIR reflectance values of all pigments and related coatings, the ZnO (which imparts high reflectance values) is not the only agent able to increase reflectance value. As demonstrated before in the literature,

and confirmed in this work, the doping chromophore elements have a role in tuning reflectance value. According to data, pigments based on $\text{YIn}_{0.9}\text{Fe}_{0.1}\text{O}_3$ and ZnO are the pigments showing NIR reflectance values promising for cool coating application. Those pigments obtained by calcination at 850 °C are the most reflective. In particular, pigment having ZnO nanopowders added mechanically ($\text{YIn}_{0.9}\text{Fe}_{0.1}\text{O}_3$ MIX ZnO/ 850 °C) results the most reflective pigment. This is due to the higher active area of ZnO nanoparticles respect to the ripened ZnO particle in $\text{YIn}_{0.9}\text{Fe}_{0.1}\text{O}_3\text{-ZnO}$. This pigment shows a relevant photocatalytic action. For this reason $\text{YInFeO MIX ZnO/ 850 °C}$ can be defined a smart pigment combining NIR reflectance and photocatalytic activity. The high reflectance value of $\text{YIn}_{0.9}\text{Fe}_{0.1}\text{O}_3$ MIX ZnO/ 850 °C is maintained also after the addition of the pigment in the binder. Therefore, this pigment is a smart pigment for outdoor application combing high reflectance toward solar radiation and high photocatalytic activity. The pigments can be dispersed in the two selected binder forming a paste that is easy to apply and covering well the aluminum substrate. Looking at T_{surface} data of those coatings with pigments calcined at the highest temperature, they show a temperature higher of 4/ 5°C compared to T_{surface} of coatings with TiO_2 . The highest value of reflectance is obtained for yellow/ ochre coating having $\text{YInFeO MIX ZnO/ 850 °C}$. The reflectance values are comparable with the coating having TiO_2 . So the mechanical addition of ZnO, respect to the addition in the sol-gel bath, is able to increase reflectance for its higher active surface. The mechanical addition of ZnO also gives a pigment with high photocatalytic power, high NIR reflectance, and a different shade of yellow.

8 References

- [1] ONU, World Urbanization Prospects, Demogr. Res. 12 (2018) 197–236.
<https://population.un.org/wup/Publications/Files/WUP2018-Report.pdf>.
- [2] S. Akhtar, A. Matin, A. Madhan Kumar, A. Ibrahim, T. Laoui, Enhancement of anticorrosion property of 304 stainless steel using silane coatings, Appl. Surf. Sci. 440 (2018) 1286–1297.
<https://doi.org/10.1016/j.apsusc.2018.01.203>.
- [3] T. Kolås, A. Røyset, M. Grandcolas, M. ten Cate, A. Lacau, Cool coatings with high near infrared transmittance for coil coated aluminium, Sol. Energy Mater. Sol. Cells. 196 (2019) 94–104.
<https://doi.org/10.1016/j.solmat.2019.03.021>.
- [4] J. Jazaeri, R.L. Gordon, T. Alpcan, Influence of building envelopes, climates, and occupancy patterns on residential HVAC demand, J. Build. Eng. 22 (2019) 33–47.
<https://doi.org/https://doi.org/10.1016/j.job.2018.11.011>.
- [5] L. Kleerekoper, M. van Esch, T.B. Salcedo, How to make a city climate-proof, addressing the urban heat island effect, Resour. Conserv. Recycl. 64 (2012) 30–38.
<https://doi.org/https://doi.org/10.1016/j.resconrec.2011.06.004>.
- [6] Koppe, C., Sari Kovats, R., Menne, B., Jendritzky, G WHO.In, Health and global environmental change, 2 (2004) 123.
- [7] I.P.O.C. Change, Climate change 2007: the physical science basis: summary for policymakers, Geneva IPCC. (2007) 104–116.
- [8] A.J. Arnfield, Two decades of urban climate research: A review of turbulence, exchanges of energy and water, and the urban heat island, Int. J. Climatol. 23 (2003) 1–26. <https://doi.org/10.1002/joc.859>.
- [9] D. Yinfei, S. Qin, W. Shengyue, Bidirectional heat induced structure of asphalt pavement for reducing pavement temperature, Appl. Therm. Eng. 75 (2015) 298–306.
<https://doi.org/10.1016/j.applthermaleng.2014.10.011>.
- [10] R.L. Wilby, Past and projected trends in London's Urban heat island, Weather. 58 (2003) 251–260.
<https://doi.org/10.1256/wea.183.02>.
- [11] M. Santamouri, D.N. Asimakopoulos, V.D. Assimakopoulos, N. Chrisomallidou, N. Klitsikas, D. Mangold, P. Michel, M. Santamouris, A. Tsangrassoulis, Energy and climate in the urban built environment, Energy Clim. Urban Built Environ. (2013) 1–402. <https://doi.org/10.4324/9781315073774>.
- [12] D.N. Asimakopoulos, V.D. Assimakopoulos, N. Chrisomallidou, N. Klitsikas, D. Mangold, P. Michel, M. Santamouris, A. Tsangrassoulis, Energy and Climate in the Urban Built Environment, 1st Editio, Routledge, London, 2001. <https://doi.org/https://doi.org/10.4324/9781315073774>.
- [13] W. Wang, K. Liu, R. Tang, S. Wang, Remote sensing image-based analysis of the urban heat island effect in Shenzhen, China, Phys. Chem. Earth. 110 (2019) 168–175.
<https://doi.org/10.1016/j.pce.2019.01.002>.
- [14] L. Zhang, H. Fukuda, Z. Liu, The value of cool roof as a strategy to mitigate urban heat island effect: A contingent valuation approach, J. Clean. Prod. 228 (2019) 770–777.
<https://doi.org/10.1016/j.jclepro.2019.04.338>.

- [15] D. Guilbert, S. Caluwaerts, K. Calle, N. Van Den Bossche, V. Cnudde, T. De Kock, Impact of the urban heat island on freeze-thaw risk of natural stone in the built environment, a case study in Ghent, Belgium, *Sci. Total Environ.* 677 (2019) 9–18. <https://doi.org/10.1016/j.scitotenv.2019.04.344>.
- [16] U. Berardi, A.A. Gallardo, Properties of concretes enhanced with phase change materials for building applications, *Energy Build.* 199 (2019) 402–414. <https://doi.org/10.1016/j.enbuild.2019.07.014>.
- [17] S. Nandja, A. Haché, Attenuated internal reflection at an interface with a phase change material, *Opt. Commun.* 449 (2019) 63–68. <https://doi.org/10.1016/j.optcom.2019.05.029>.
- [18] Y. Huang, J. lei Niu, T. ming Chung, Comprehensive analysis on thermal and daylighting performance of glazing and shading designs on office building envelope in cooling-dominant climates, *Appl. Energy.* 134 (2014) 215–228. <https://doi.org/10.1016/j.apenergy.2014.07.100>.
- [19] I. Hernández-Pérez, J. Xamán, E. V. Macías-Melo, K.M. Aguilar-Castro, I. Zavala-Guillén, I. Hernández-López, E. Simá, Experimental thermal evaluation of building roofs with conventional and reflective coatings, *Energy Build.* 158 (2018) 569–579. <https://doi.org/10.1016/j.enbuild.2017.09.085>.
- [20] U. Berardi, A.H. GhaffarianHoseini, A. GhaffarianHoseini, State-of-the-art analysis of the environmental benefits of green roofs, *Appl. Energy.* 115 (2014) 411–428. <https://doi.org/10.1016/j.apenergy.2013.10.047>.
- [21] J. Liao, X. Tan, J. Li, Evaluating the vertical cooling performances of urban vegetation scenarios in a residential environment, *J. Build. Eng.* 39 (2021) 102313. <https://doi.org/10.1016/j.job.2021.102313>.
- [22] D. Armson, P. Stringer, A.R. Ennos, Urban Forestry & Urban Greening The effect of tree shade and grass on surface and globe temperatures in an urban area, *Urban For. Urban Green.* 11 (2012) 245–255. <https://doi.org/10.1016/j.ufug.2012.05.002>.
- [23] M. Hunger, A.G. Entrop, I. Mandilaras, H.J.H. Brouwers, M. Founti, The behavior of self-compacting concrete containing micro-encapsulated Phase Change Materials, *Cem. Concr. Compos.* 31 (2009) 731–743. <https://doi.org/https://doi.org/10.1016/j.cemconcomp.2009.08.002>.
- [24] F. Kuznik, J. Virgone, Experimental assessment of a phase change material for wall building use, *Appl. Energy.* 86 (2009) 2038–2046. <https://doi.org/https://doi.org/10.1016/j.apenergy.2009.01.004>.
- [25] B. He, F. Setterwall, Technical grade paraffin waxes as phase change materials for cool thermal storage and cool storage systems capital cost estimation, *Energy Convers. Manag.* 43 (2002) 1709–1723. [https://doi.org/10.1016/S0196-8904\(01\)00005-X](https://doi.org/10.1016/S0196-8904(01)00005-X).
- [26] Y. Wu, T. Wang, Hydrated salts/expanded graphite composite with high thermal conductivity as a shape-stabilized phase change material for thermal energy storage, *Energy Convers. Manag.* 101 (2015) 164–171. <https://doi.org/https://doi.org/10.1016/j.enconman.2015.05.006>.
- [27] A. Bland, M. Khzouz, T. Statheros, E.I. Gkanas, PCMs for Residential Building Applications: A Short Review Focused on Disadvantages and Proposals for Future Development, *Build.* 7 (2017). <https://doi.org/10.3390/buildings7030078>.
- [28] A.L. Pisello, V.L. Castaldo, C. Fabiani, F. Cotana, Investigation on the effect of innovative cool tiles on local indoor thermal conditions: Finite element modeling and continuous monitoring, *Build. Environ.* 97 (2016) 55–68.
- [29] A. Premier, Façade cool coatings: an experiment on colour and surface quality, *Intell. Build. Int.* 13 (2021) 293–310. <https://doi.org/10.1080/17508975.2019.1704207>.
- [30] M. Rawat, R.N. Singh, A study on the comparative review of cool roof thermal performance in

various regions, *Energy Built Environ.* (2021).
<https://doi.org/https://doi.org/10.1016/j.enbenv.2021.03.001>.

- [31] F. Kuznik, J. Virgone, Experimental assessment of a phase change material for wall building use, *Appl. Energy*. 86 (2009) 2038–2046. <https://doi.org/10.1016/j.apenergy.2009.01.004>.
- [32] A. Synnefa, M. Santamouris, K. Apostolakis, On the development, optical properties and thermal performance of cool colored coatings for the urban environment, *Sol. Energy*. 81 (2007) 488–497. <https://doi.org/10.1016/j.solener.2006.08.005>.
- [33] A. Synnefa, M. Saliari, M. Santamouris, Experimental and numerical assessment of the impact of increased roof reflectance on a school building in Athens, *Energy Build.* 55 (2012) 7–15. <https://doi.org/https://doi.org/10.1016/j.enbuild.2012.01.044>.
- [34] I. Hernández-Pérez, G. Álvarez, H. Gilbert, J. Xamán, Y. Chávez, B. Shah, Thermal Performance of a Concrete Cool Roof under Different Climatic Conditions of Mexico, *Energy Procedia*. 57 (2014) 1753–1762. <https://doi.org/https://doi.org/10.1016/j.egypro.2014.10.164>.
- [35] A.L. Pisello, State of the art on the development of cool coatings for buildings and cities, *Sol. Energy*. 144 (2017) 660–680. <https://doi.org/10.1016/j.solener.2017.01.068>.
- [36] R.F. Brady, L. V. Wake, Principles and formulations for organic coatings with tailored infrared properties, *Prog. Org. Coatings*. 20 (1992) 1–25. [https://doi.org/10.1016/0033-0655\(92\)85001-C](https://doi.org/10.1016/0033-0655(92)85001-C).
- [37] J. Song, J. Qin, J. Qu, Z. Song, W. Zhang, X. Xue, Y. Shi, T. Zhang, W. Ji, R. Zhang, H. Zhang, Z. Zhang, X. Wu, The effects of particle size distribution on the optical properties of titanium dioxide rutile pigments and their applications in cool non-white coatings, *Sol. Energy Mater. Sol. Cells*. 130 (2014) 42–50. <https://doi.org/https://doi.org/10.1016/j.solmat.2014.06.035>.
- [38] N. Kiomarsipour, R. Shoja Razavi, Hydrothermal synthesis of ZnO nanopigments with high UV absorption and vis/NIR reflectance, *Ceram. Int.* 40 (2014) 11261–11268. <https://doi.org/10.1016/j.ceramint.2014.03.178>.
- [39] V. Malshe, A. Bendiganavale, Infrared Reflective Inorganic Pigments, *Recent Patents Chem. Eng.* 1 (2012) 67–79. <https://doi.org/10.2174/2211334710801010067>.
- [40] M. Zhao, A. Han, M. Ye, T. Wu, Preparation and characterization of Fe³⁺ doped Y₂Ce₂O₇ pigments with high near-infrared reflectance, *Sol. Energy*. 97 (2013) 350–355. <https://doi.org/10.1016/j.solener.2013.08.007>.
- [41] A. Han, M. Ye, M. Zhao, J. Liao, T. Wu, Crystal structure, chromatic and near-infrared reflective properties of iron doped YMnO₃ compounds as colored cool pigments, *Dye. Pigment*. 99 (2013) 527–530. <https://doi.org/https://doi.org/10.1016/j.dyepig.2013.06.016>.
- [42] Y. Song, W. Chen, X.M. Lim, X. Hu, M. Liu, Q. Zhang, Electronic configuration in outset orbitals of doping elements plays as a key factor in tuning near infrared reflection of YMn_{0.9}M_{0.1}O₃ (M = Cr, Mn, Fe, Co, Al, Ga and In), *J. Solid State Chem.* 273 (2019) 81–84. <https://doi.org/10.1016/j.jssc.2019.02.040>.
- [43] Y. Mastai, Y. Diamant, S.T. Aruna, A. Zaban, TiO₂ nanocrystalline pigmented polyethylene foils for radiative cooling applications: Synthesis and characterization, *Langmuir*. 17 (2001) 7118–7123. <https://doi.org/10.1021/la010370g>.
- [44] Y. Qi, B. Xiang, J. Zhang, Effect of titanium dioxide (TiO₂) with different crystal forms and surface modifications on cooling property and surface wettability of cool roofing materials, *Sol. Energy Mater. Sol. Cells*. 172 (2017) 34–43. <https://doi.org/10.1016/j.solmat.2017.07.017>.

- [45] S. Wang, J. Zhang, Effect of titanium dioxide (TiO₂) on largely improving solar reflectance and cooling property of high density polyethylene (HDPE) by influencing its crystallization behavior, *J. Alloys Compd.* 617 (2014) 163–169. <https://doi.org/10.1016/j.jallcom.2014.07.191>.
- [46] S. Sadeghi-Niaraki, B. Ghasemi, A. Habibolahzadeh, E. Ghasemi, M. Ghahari, Nanostructured Fe₂O₃@TiO₂ pigments with improved NIR reflectance and photocatalytic ability, *Mater. Chem. Phys.* 235 (2019) 121769. <https://doi.org/10.1016/j.matchemphys.2019.121769>.
- [47] N. Kiomarsipour, R. Shoja Razavi, K. Ghani, M. Kioumarsipour, Evaluation of shape and size effects on optical properties of ZnO pigment, *Appl. Surf. Sci.* 270 (2013) 33–38. <https://doi.org/10.1016/j.apsusc.2012.11.167>.
- [48] M.M. Mikhailov, V. V Neshchimenko, C. Li, Optical properties of zinc oxide powders modified by nanoparticles ZrO₂, Al₂O₃, TiO₂, SiO₂, CeO₂ and Y₂O₃ with various concentrations, *Dye. Pigment.* 131 (2016) 256–263. <https://doi.org/https://doi.org/10.1016/j.dyepig.2016.04.012>.
- [49] L. Sandhya Kumari, P. Prabhakar Rao, A. Narayana Pillai Radhakrishnan, V. James, S. Sameera, P. Koshy, Brilliant yellow color and enhanced NIR reflectance of monoclinic BiVO₄ through distortion in VO₄³⁻ tetrahedra, *Sol. Energy Mater. Sol. Cells.* (2013). <https://doi.org/10.1016/j.solmat.2013.01.022>.
- [50] S.P. Radhika, K.J. Sreeram, B.U. Nair, Rare earth doped cobalt aluminate blue as an environmentally benign colorant, *J. Adv. Ceram.* 1 (2012) 301–309. <https://doi.org/10.1007/s40145-012-0029-6>.
- [51] S. Jose, A. Jayaprakash, S. Laha, S. Natarajan, K.G. Nishanth, M.L.P. Reddy, YIn_{0.9}Mn_{0.1}O₃-ZnO nanopigment exhibiting intense blue color with impressive solar reflectance, *Dye. Pigment.* 124 (2016) 120–129. <https://doi.org/10.1016/j.dyepig.2015.09.014>.
- [52] Y.F. Gomes, J. Li, K.F. Silva, A.A.G. Santiago, M.R.D. Bomio, C.A. Paskocimas, M.A. Subramanian, F. V Motta, Synthesis and characterization of Y(In, Mn)O₃ blue pigment using the complex polymerization method (CPM), *Ceram. Int.* 44 (2018) 11932–11939. <https://doi.org/https://doi.org/10.1016/j.ceramint.2018.04.152>.
- [53] W. Liu, T. Du, Q. Ru, S. Zuo, X. Yang, C. Yao, Y. Kong, Facile synthesis and characterization of 2D kaolin/CoAl₂O₄: A novel inorganic pigment with high near-infrared reflectance for thermal insulation, *Appl. Clay Sci.* 153 (2018) 239–245. <https://doi.org/10.1016/j.clay.2017.12.030>.
- [54] X. Wang, B. Mu, Z. Zhang, A. Wang, Insights into halloysite or kaolin role of BiVO₄ hybrid pigments for applications in polymer matrix and surface coating, *Compos. Part B Eng.* 174 (2019) 107035. <https://doi.org/https://doi.org/10.1016/j.compositesb.2019.107035>.
- [55] J. de O. Primo, K.W. Borth, D.C. Peron, V. de C. Teixeira, D. Galante, C. Bittencourt, F.J. Anaissi, Synthesis of green cool pigments (Co_xZn_{1-x}O) for application in NIR radiation reflectance, *J. Alloys Compd.* 780 (2019) 17–24. <https://doi.org/10.1016/j.jallcom.2018.11.358>.
- [56] H.R. Hedayati, A.A. Sabbagh Alvani, H. Sameie, R. Salimi, S. Moosakhani, F. Tabatabaee, A. Amiri Zarandi, Synthesis and characterization of Co_{1-x}Zn_xCr_{2-y}Al_yO₄ as a near-infrared reflective color tunable nano-pigment, *Dye. Pigment.* 113 (2015) 588–595. <https://doi.org/10.1016/j.dyepig.2014.09.030>.
- [57] C. Ding, A. Han, M. Ye, Y. Zhang, L. Yao, J. Yang, Solar Energy Materials and Solar Cells Synthesis and characterization of a series of new green solar heat-reflective pigments : Cr-doped BiPO₄ and its effect on the aging resistance of PMMA (Poly (methyl methacrylate)), 191 (2019) 427–436. <https://doi.org/10.1016/j.solmat.2018.12.007>.
- [58] J. Devoy, F. Cosnier, E. Bonfanti, G. Antoine, H. Nunge, A.M. Lambert-Xolin, M.J. Décret, L. Douteau, M. Lorcin, S. Sébillaud, S. Grossmann, S. Michaux, S. Müller, S. Viton, C. Seidel, L. Gaté, Intra-

erythrocyte chromium as an indicator of exposure to hexavalent chromium: An in vivo evaluation in intravenous administered rat, *Toxicol. Lett.* 314 (2019) 133–141.
<https://doi.org/10.1016/j.toxlet.2019.07.020>.

- [59] L. Leysens, B. Vinck, C. Van Der Straeten, F. Wuyts, L. Maes, Cobalt toxicity in humans – A review of the potential sources and systemic health effects, *Toxicology*. 387 (2017) 43–56.
<https://doi.org/10.1016/j.tox.2017.05.015>.
- [60] D. Schildhammer, G. Fuhrmann, L. Petschnig, N. Weinberger, H. Schottenberger, H. Huppertz, Synthesis and characterization of a new high NIR reflective ytterbium molybdenum oxide and related doped pigments, *Dye. Pigment.* 138 (2017) 90–99.
<https://doi.org/https://doi.org/10.1016/j.dyepig.2016.11.024>.
- [61] B. Huang, Y. Xiao, C. Huang, J. Chen, X. Sun, Environment-friendly pigments based on praseodymium and terbium doped $\text{La}_2\text{Ce}_2\text{O}_7$ with high near-infrared reflectance: Synthesis and characterization, *Dye. Pigment.* 147 (2017) 225–233. <https://doi.org/10.1016/j.dyepig.2017.08.004>.
- [62] G. George, V.S. Vishnu, M.L.P. Reddy, The synthesis, characterization and optical properties of silicon and praseodymium doped $\text{Y}_6\text{MoO}_{12}$ compounds: Environmentally benign inorganic pigments with high NIR reflectance, *Dye. Pigment.* 88 (2011) 109–115.
<https://doi.org/https://doi.org/10.1016/j.dyepig.2010.05.010>.
- [63] S. Jose, D. Joshy, S.B. Narendranath, P. Periyat, Recent advances in infrared reflective inorganic pigments, *Sol. Energy Mater. Sol. Cells.* 194 (2019) 7–27. <https://doi.org/10.1016/j.solmat.2019.01.037>.
- [64] A.K.V. Raj, P. Prabhakar Rao, S. Sameera, S. Divya, Pigments based on terbium-doped yttrium cerate with high NIR reflectance for cool roof and surface coating applications, *Dye. Pigment.* 122 (2015) 116–125. <https://doi.org/10.1016/j.dyepig.2015.06.021>.
- [65] S. Zhang, Z. Pan, Y. Wang, Synthesis and characterization of (Ni, Sb)-co-doped rutile ceramic pigment via mechanical activation-assisted solid-state reaction, *Particuology*. 41 (2018) 20–29.
<https://doi.org/https://doi.org/10.1016/j.partic.2017.12.016>.
- [66] V. Sarasamma Vishnu, M. Lakshmipathi Reddy, Near-infrared reflecting inorganic pigments based on molybdenum and praseodymium doped yttrium cerate: Synthesis, characterization and optical properties, *Sol. Energy Mater. Sol. Cells.* 95 (2011) 2685–2692.
<https://doi.org/https://doi.org/10.1016/j.solmat.2011.05.042>.
- [67] S. Jose, M.L. Reddy, Lanthanum–strontium copper silicates as intense blue inorganic pigments with high near-infrared reflectance, *Dye. Pigment.* 98 (2013) 540–546.
<https://doi.org/https://doi.org/10.1016/j.dyepig.2013.04.013>.
- [68] K. McLAREN, XIII – The Development of the CIE 1976 ($L^* a^* b^*$) Uniform Colour Space and Colour-difference Formula, *J. Soc. Dye. Colour.* 92 (1976) 338–341. <https://doi.org/doi:10.1111/j.1478-4408.1976.tb03301.x>.
- [69] J. Li, M.A. Subramanian, Inorganic pigments with transition metal chromophores at trigonal bipyramidal coordination: $\text{Y}(\text{In}, \text{Mn})\text{O}_3$ blues and beyond, *J. Solid State Chem.* 272 (2019) 9–20.
<https://doi.org/10.1016/j.jssc.2019.01.019>.
- [70] S. Jose, S.B. Narendranath, D. Joshy, N. V. Sajith, M.R. Prathapachandra Kurup, P. Periyat, Low temperature synthesis of NIR reflecting bismuth doped cerium oxide yellow nano-pigments, *Mater. Lett.* 233 (2018) 82–85. <https://doi.org/10.1016/j.matlet.2018.08.136>.
- [71] P.K. Thejus, K.G. Nishanth, Rational approach to synthesis low-cost BiVO_4 – ZnO complex inorganic

pigment for energy efficient buildings, *Sol. Energy Mater. Sol. Cells*. 200 (2019) 109999. <https://doi.org/https://doi.org/10.1016/j.solmat.2019.109999>.

- [72] D. Schildhammer, G. Fuhrmann, L. Petschnig, N. Weinberger, H. Schottenberger, H. Huppertz, Synthesis and characterization of a new high NIR reflective ytterbium molybdenum oxide and related doped pigments, *Dye. Pigment*. 138 (2017) 90–99. <https://doi.org/10.1016/j.dyepig.2016.11.024>.
- [73] A.K.V. Raj, P.P. Rao, T.S. Sreena, T.R.A. Thara, Pigmentary colors from yellow to red in $\text{Bi}_2\text{Ce}_2\text{O}_7$ by rare earth ion substitutions as possible high NIR reflecting pigments, *Dye. Pigment*. 160 (2019) 177–187. <https://doi.org/10.1016/j.dyepig.2018.08.010>.
- [74] Y. Shi, M. Zhong, Z. Zhang, D. Wang, Crystal structure and near-infrared reflective properties of Fe^{3+} doped AlPO_4 pigments, *Ceram. Int*. 43 (2017) 5979–5983. <https://doi.org/10.1016/j.ceramint.2017.01.131>.
- [75] V. Elakkiya, S. Sumathi, Effect of preparation methodology on the colour and the NIR reflectance of nickel doped manganese pyrophosphate, *J. Alloys Compd*. 768 (2018) 535–544. <https://doi.org/10.1016/j.jallcom.2018.07.236>.
- [76] M.S. Bernardo, T. Jardiel, M. Peiteado, A.C. Caballero, M. Villegas, Reaction pathways in the solid state synthesis of multiferroic BiFeO_3 , *J. Eur. Ceram. Soc*. 31 (2011) 3047–3053. <https://doi.org/https://doi.org/10.1016/j.jeurceramsoc.2011.03.018>.
- [77] X. Wang, B. Mu, A. Zhang, X. An, A. Wang, Effects of different pH regulators on the color properties of attapulgite/ BiVO_4 hybrid pigment, *Powder Technol.* (2019). <https://doi.org/10.1016/j.powtec.2018.11.003>.
- [78] D. Wang, D. Su, M. Zhong, Chromatic and near-infrared reflective properties of Fe^{3+} doped KZnPO_4 , *Sol. Energy*. 110 (2014) 1–6. <https://doi.org/10.1016/j.solener.2014.09.004>.
- [79] M. Llusar, A. García, C. Gargori, R. Galindo, J.A. Badenes, G. Monrós, Synthesis of diphosphate $\text{Mn}_{2-x}\text{Mg}_x\text{P}_2\text{O}_7$ solid solutions with thortveitite structure: New pink ceramic dyes for the colouration of ceramic glazes, *J. Eur. Ceram. Soc*. 32 (2012) 765–776. <https://doi.org/https://doi.org/10.1016/j.jeurceramsoc.2011.10.051>.
- [80] B. Boonchom, R. Baitahe, Synthesis and characterization of nanocrystalline manganese pyrophosphate $\text{Mn}_2\text{P}_2\text{O}_7$, *Mater. Lett*. 63 (2009) 2218–2220. <https://doi.org/10.1016/j.matlet.2009.07.028>.
- [81] R.G. Henderson, J. Durando, A.R. Oller, D.J. Merkel, P. Ann, H.K. Bates, Acute oral toxicity of nickel compounds, *Regul. Toxicol. Pharmacol*. 62 (2012) 425–432. <https://doi.org/10.1016/j.yrtph.2012.02.002>.
- [82] G. George, G. George, P.P. Rao, M.L. Reddy, Synthesis and Characterization of Environmentally Benign Nontoxic Pigments: $\text{RE}_2\text{Mo}_2\text{O}_9$ (RE = La or Pr), *Chem. Lett*. 34 (2005) 1702–1703. <https://doi.org/10.1246/cl.2005.1702>.
- [83] L. Yuan, A. Han, M. Ye, X. Chen, L. Yao, C. Ding, Synthesis and characterization of environmentally benign inorganic pigments with high NIR reflectance: Lanthanum-doped BiFeO_3 , *Dye. Pigment*. 148 (2018) 137–146. <https://doi.org/10.1016/j.dyepig.2017.09.008>.
- [84] G. Tian, W. Wang, B. Mu, Q. Wang, A. Wang, Cost-efficient, vivid and stable red hybrid pigments derived from naturally available sepiolite and halloysite, *Ceram. Int*. 43 (2017) 1862–1869. <https://doi.org/10.1016/j.ceramint.2016.10.145>.
- [85] S. Radhika, K.J. Sreeram, B.U. Nair, Effective synthesis route for red-brown pigments based on Ce - Pr - Fe - O and their potential application for near infrared reflective surface coating, *J. Chem. Sci*. 126 (2014) 65–73. <https://doi.org/10.1007/s12039-013-0559-7>.

- [86] Y. Xiao, B. Huang, J. Chen, X. Sun, Novel Bi³⁺ doped and Bi³⁺/Tb³⁺ co-doped LaYO₃ pigments with high near-infrared reflectances, *J. Alloys Compd.* 762 (2018) 873–880. <https://doi.org/10.1016/j.jallcom.2018.05.233>.
- [87] K.J. Sreeram, C.P. Aby, B.U. Nair, T. Ramasami, Colored cool colorants based on rare earth metal ions, *Sol. Energy Mater. Sol. Cells.* 92 (2008) 1462–1467. <https://doi.org/10.1016/j.solmat.2008.06.008>.
- [88] P. Šulcová, L. Vitásková, M. Trojan, Thermal analysis of the Ce_{1-x}Tb_xO₂ pigments, *J. Therm. Anal. Calorim.* 99 (2010) 409–413. <https://doi.org/10.1007/s10973-009-0129-x>.
- [89] J. Li, E.A. Medina, J.K. Stalick, A.W. Sleight, M.A. Subramanian, Colored oxides with hibonite structure: A potential route to non-cobalt blue pigments, *Prog. Solid State Chem.* 44 (2016) 107–122. <https://doi.org/https://doi.org/10.1016/j.progsolidstchem.2016.11.001>.
- [90] A.E. Smith, H. Mizoguchi, K. Delaney, N.A. Spaldin, A.W. Sleight, M.A. Subramanian, Mn³⁺ in trigonal bipyramidal coordination: A new blue chromophore, *J. Am. Chem. Soc.* 131 (2009) 17084–17086. <https://doi.org/10.1021/ja9080666>.
- [91] M.P. Pechini, Method of preparing lead and alkaline earth titanates and niobates and coating method using the same to form a capacitor, U.S. Patent No. 3,330,697. 11 Jul. (1967).
- [92] A.E. Danks, S.R. Hall, Z. Schnepf, The evolution of “sol-gel” chemistry as a technique for materials synthesis, *Mater. Horizons.* 3 (2016) 91–112. <https://doi.org/10.1039/c5mh00260e>.
- [93] P. Berdahl, S.K. Boocock, G.C.Y. Chan, S.S. Chen, R.M. Levinson, M.A. Zalich, High quantum yield of the Egyptian blue family of infrared phosphors (MCuSi₄O₁₀, M = Ca, Sr, Ba), *J. Appl. Phys.* 123 (2018). <https://doi.org/10.1063/1.5019808>.
- [94] A. Yurdakul, H. Gocmez, One-step hydrothermal synthesis of yttria-stabilized tetragonal zirconia polycrystalline nanopowders for blue-colored zirconia-cobalt aluminate spinel composite ceramics, *Ceram. Int.* 45 (2019) 5398–5406. <https://doi.org/10.1016/j.ceramint.2018.11.240>.
- [95] Y. Xie, L. Wang, B. Liu, L. Zhu, S. Shi, X. Wang, Flexible, controllable, and high-strength near-infrared reflective Y₂O₃ nanofiber membrane by electrospinning a polyacetylaceton-yttrium precursor, *Mater. Des.* 160 (2018) 918–925. <https://doi.org/10.1016/j.matdes.2018.10.017>.
- [96] S. Salem, Effect of calcination temperature on colorant behavior of cobalt-aluminate nano-particles synthesized by combustion technique, *J. Ind. Eng. Chem.* 20 (2014) 818–823. <https://doi.org/10.1016/j.jiec.2013.06.011>.
- [97] A. Aguilar-Elguézabal, M. Román-Aguirre, L. De la Torre-Sáenz, P. Pizá-Ruiz, M. Bocanegra-Bernal, Synthesis of CoAl₂O₄/Al₂O₃ nanoparticles for ceramic blue pigments, *Ceram. Int.* 43 (2017) 15254–15257. <https://doi.org/10.1016/j.ceramint.2017.08.062>.
- [98] M. De Boeck, M. Kirsch-Volders, D. Lison, Cobalt and antimony: Genotoxicity and carcinogenicity, *Mutat. Res. - Fundam. Mol. Mech. Mutagen.* 533 (2003) 135–152. <https://doi.org/10.1016/j.mrfmmm.2003.07.012>.
- [99] X. Wang, B. Mu, A. Hui, Q. Wang, A. Wang, Low-cost bismuth yellow hybrid pigments derived from attapulgite, *Dye. Pigment.* 149 (2018) 521–530. <https://doi.org/10.1016/j.dyepig.2017.10.041>.
- [100] A. Rosati, M. Fedel, S. Rossi, NIR reflective pigments for cool roof applications: A comprehensive review, *J. Clean. Prod.* 313 (2021) 127826. <https://doi.org/https://doi.org/10.1016/j.jclepro.2021.127826>.
- [101] G. Yang, S.-J. Park, Conventional and microwave hydrothermal synthesis and application of functional materials: A review, *Materials (Basel).* 12 (2019) 1177. <https://doi.org/10.3390/ma12071177>.

- [102] M. Yoshimura, H. Suda, Hydrothermal processing of hydroxyapatite: past, present, and future, in: *Hydroxyapatite Relat. Mater.*, CRC Press, 2017: pp. 45–72.
- [103] K. Nadeem Riaz, N. Yousaf, M. Bilal Tahir, Z. Israr, T. Iqbal, Facile hydrothermal synthesis of 3D flower-like La-MoS₂ nanostructure for photocatalytic hydrogen energy production, *Int. J. Energy Res.* 43 (2019) 491–499. <https://doi.org/10.1002/er.4286>
- [104] R.L. Penn, J.F. Banfield, Morphology development and crystal growth in nanocrystalline aggregates under hydrothermal conditions: Insights from titania, *Geochim. Cosmochim. Acta.* 63 (1999) 1549–1557. [https://doi.org/10.1016/S0016-7037\(99\)00037-X](https://doi.org/10.1016/S0016-7037(99)00037-X).
- [105] T. Sekiguchi, S. Miyashita, K. Obara, T. Shishido, N. Sakagami, Hydrothermal growth of ZnO single crystals and their optical characterization, *J. Cryst. Growth.* 214 (2000) 72–76. [https://doi.org/10.1016/S0022-0248\(00\)00065-8](https://doi.org/10.1016/S0022-0248(00)00065-8).
- [106] W. Zheng, W. Pang, G. Meng, Hydrothermal synthesis and characterization of perovskite-type Ba₂SbMO₆ (M=In, Y, Nd) oxides, *Mater. Lett.* 37 (1998) 276–280. [https://doi.org/https://doi.org/10.1016/S0167-577X\(98\)00105-0](https://doi.org/https://doi.org/10.1016/S0167-577X(98)00105-0).
- [107] F. Bondioli, A.M. Ferrari, L. Lusvardi, T. Manfredini, S. Nannarone, L. Pasquali, G. Selvaggi, Synthesis and characterization of praseodymium-doped ceria powders by a microwave-assisted hydrothermal (MH) route, *J. Mater. Chem.* 15 (2005) 1061–1066. DOI <https://doi.org/10.1039/B415628E>
- [108] Y. Hu, C. Liu, Y. Zhang, N. Ren, Y. Tang, Microwave-assisted hydrothermal synthesis of nanozeolites with controllable size, *Microporous Mesoporous Mater.* 119 (2009) 306–314. <https://doi.org/https://doi.org/10.1016/j.micromeso.2008.11.005>.
- [109] H. Cui, M. Zayat, D. Levy, Epoxide assisted sol–gel synthesis of perovskite-type LaM_xFe_{1-x}O₃ (M=Ni,Co) nanoparticles, *J. Non. Cryst. Solids.* 352 (2006) 3035–3040. <https://doi.org/https://doi.org/10.1016/j.jnoncrysol.2006.03.062>.
- [110] Y. Xiao, B. Huang, J. Chen, X. Sun, Novel Bi³⁺ doped and Bi³⁺/Tb³⁺ co-doped LaYO₃ pigments with high near-infrared reflectances, *J. Alloys Compd.* 762 (2018) 873–880. <https://doi.org/https://doi.org/10.1016/j.jallcom.2018.05.233>.
- [111] J. Zha, H. Roggendorf, *Sol–gel science, the physics and chemistry of sol–gel processing*, Ed. by CJ Brinker and GW Scherer, Academic Press, Boston 1990, xiv, 908 pp., bound—ISBN 0-12-134970-5, (1991).
- [112] S. Esposito, “Traditional” Sol-Gel Chemistry as a Powerful Tool for the Preparation of Supported Metal and Metal Oxide Catalysts, *Materials (Basel).* 12 (2019) 2–25. <https://doi.org/10.3390/ma12040668>.
- [113] Z. Yao, Y. Peng, C. Xia, X. Yi, S. Mao, M. Zhang, The effect of calcination temperature on microstructure and properties of FeNiMo@Al₂O₃ soft magnetic composites prepared by sol-gel method, *J. Alloys Compd.* 827 (2020) 154345. <https://doi.org/https://doi.org/10.1016/j.jallcom.2020.154345>.
- [114] J. Wu, M. Li, H. Jia, M. Wang, Z. Liu, Influences of calcination temperature and charge compensators on the properties of SrMoO₄:Sm³⁺ red phosphor prepared via the sol–gel method, *J. Lumin.* 214 (2019) 116607. <https://doi.org/https://doi.org/10.1016/j.jlumin.2019.116607>.
- [115] C.J. Brinker, G.W. Scherer, *Sol-gel science: the physics and chemistry of sol-gel processing*, Academic

press, 2013.

- [116] A. Fidalgo, M.E. Rosa, L.M. Ilharco, Chemical Control of Highly Porous Silica Xerogels: Physical Properties and Morphology, *Chem. Mater.* 15 (2003) 2186–2192. <https://doi.org/10.1021/cm031013p>.
- [117] Y. Hao, Q. Lai, D. Liu, Z. Xu, X. Ji, Synthesis by citric acid sol–gel method and electrochemical properties of $\text{Li}_4\text{Ti}_5\text{O}_{12}$ anode material for lithium-ion battery, *Mater. Chem. Phys.* 94 (2005) 382–387. <https://doi.org/https://doi.org/10.1016/j.matchemphys.2005.05.019>.
- [118] L. Dimesso, Pechini processes: an alternate approach of the sol–gel method, preparation, properties, and applications, *Handb. Sol-Gel Sci. Technol.* 2 (2016) 1–22. DOI 10.1007/978-3-319-19454-7_123-1.
- [119] W.-F. Chen, S.S. Mofarah, D.A.H. Hanaor, P. Koshy, H.-K. Chen, Y. Jiang, C.C. Sorrell, Enhancement of Ce/Cr Codopant Solubility and Chemical Homogeneity in TiO_2 Nanoparticles through Sol–Gel versus Pechini Syntheses, *Inorg. Chem.* 57 (2018) 7279–7289. <https://doi.org/10.1021/acs.inorgchem.8b00926>.
- [120] A. Kahoul, P. Nkeng, A. Hammouche, F. Naamoune, G. Poillierat, A Sol–Gel Route for the Synthesis of $\text{Bi}_2\text{Ru}_2\text{O}_7$ Pyrochlore Oxide for Oxygen Reaction in Alkaline Medium, *J. Solid State Chem.* 161 (2001) 379–384. <https://doi.org/https://doi.org/10.1006/jssc.2001.9346>.
- [121] L. Schwertmann, M. Wark, R. Marschall, Sol–gel synthesis of defect-pyrochlore structured CsTaWO_6 and the tribochemical influences on photocatalytic activity, *RSC Adv.* 3 (2013) 18908–18915.
- [122] D.T.T. Nguyet, N.P. Duong, T. Satoh, L.N. Anh, T.D. Hien, Temperature-dependent magnetic properties of yttrium iron garnet nanoparticles prepared by citrate sol–gel, *J. Alloys Compd.* 541 (2012) 18–22. <https://doi.org/https://doi.org/10.1016/j.jallcom.2012.06.122>.
- [123] O. Opuchovic, G. Kreiza, J. Senvaitiene, K. Kazlauskas, A. Beganskiene, A. Kareiva, Sol-gel synthesis, characterization and application of selected sub-microsized lanthanide (Ce, Pr, Nd, Tb) ferrites, *Dye. Pigment.* 118 (2015) 176–182. <https://doi.org/https://doi.org/10.1016/j.dyepig.2015.03.017>.
- [124] A.Z. Arsad, N.B. Ibrahim, The effect of Ce doping on the structure, surface morphology and magnetic properties of Dy doped-yttrium iron garnet films prepared by a sol–gel method, *J. Magn. Magn. Mater.* 410 (2016) 128–136. <https://doi.org/https://doi.org/10.1016/j.jmmm.2016.03.013>.
- [125] M.K. Cinibulk, Synthesis of Yttrium Aluminum Garnet from a Mixed-Metal Citrate Precursor, *J. Am. Ceram. Soc.* 83 (2000) 1276–1278. <https://doi.org/https://doi.org/10.1111/j.1151-2916.2000.tb01367.x>.
- [126] P. Hagenmuller, M. Pouchard, J.C. Grenier, Nonstoichiometry in the perovskite-type oxides: an evolution from the classical Schottky-Wagner model to the recent high T_c superconductors, *Solid State Ionics.* 43 (1990) 7–18. [https://doi.org/10.1016/0167-2738\(90\)90464-3](https://doi.org/10.1016/0167-2738(90)90464-3).
- [127] S. Malo, A. Maignan, Co-substitution at the Mn-site in YMnO_3 : Structural stability and physical properties, *Mater. Res. Bull.* 47 (2012) 974–979. <https://doi.org/https://doi.org/10.1016/j.materresbull.2012.01.015>.
- [128] C. Moure, D. Gutierrez, O. Peña, P. Duran, Structural Characterization of $\text{YMe}_x\text{Mn}_{1-x}\text{O}_3$ (Me=Cu, Ni, Co) Perovskites, *J. Solid State Chem.* 163 (2002) 377–384. <https://doi.org/https://doi.org/10.1006/jssc.2001.9367>.
- [129] S. Tamilarasan, D. Sarma, M.L.P. Reddy, S. Natarajan, J. Gopalakrishnan, $\text{YGa}_{1-x}\text{Mn}_x\text{O}_3$: A novel purple inorganic pigment, *RSC Adv.* 3 (2013) 3199–3202. <https://doi.org/10.1039/C2RA22400C>.
- [130] D.A. Rusakov, A.A. Belik, S. Kamba, M. Savinov, D. Nuzhnyy, T. Kolodiazhnyi, K. Yamaura, E.

Takayama-Muromachi, F. Borodavka, J. Kroupa, Structural Evolution and Properties of Solid Solutions of Hexagonal InMnO_3 and InGaO_3 , *Inorg. Chem.* 50 (2011) 3559–3566.
<https://doi.org/10.1021/ic102477c>.

- [131] J. Li, A.E. Smith, P. Jiang, J.K. Stalick, A.W. Sleight, M.A. Subramanian, True Composition and Structure of Hexagonal “ YAlO_3 ”, Actually $\text{Y}_3\text{Al}_3\text{O}_8\text{CO}_3$, *Inorg. Chem.* 54 (2015) 837–844.
<https://doi.org/10.1021/ic502027k>.
- [132] P. Jiang, J. Li, A.W. Sleight, M.A. Subramanian, New Oxides Showing an Intense Orange Color Based on Fe^{3+} in Trigonal-Bipyramidal Coordination, *Inorg. Chem.* 50 (2011) 5858–5860.
<https://doi.org/10.1021/ic200535c>.
- [133] J. Li, U.G. Singh, T.D. Schladt, J.K. Stalick, S.L. Scott, R. Seshadri, Hexagonal $\text{YFe}_{1-x}\text{Pd}_x\text{O}_{3-\delta}$: Nonperovskite Host Compounds for Pd^{2+} and Their Catalytic Activity for CO Oxidation, *Chem. Mater.* 20 (2008) 6567–6576. <https://doi.org/10.1021/cm801534a>.
- [134] A.E. Smith, A.W. Sleight, M.A. Subramanian, Synthesis and properties of solid solutions of hexagonal $\text{YCu}_{0.5}\text{Ti}_{0.5}\text{O}_3$ with YMO_3 ($\text{M}=\text{Mn, Cr, Fe, Al, Ga, and In}$), *Mater. Res. Bull.* 46 (2011) 1–5.
<https://doi.org/https://doi.org/10.1016/j.materresbull.2010.10.006>.
- [135] K. Bergum, H. Okamoto, H. Fjellvåg, T. Grande, M.-A. Einarsrud, S.M. Selbach, Synthesis, structure and magnetic properties of nanocrystalline YMnO_3 , *Dalt. Trans.* 40 (2011) 7583–7589.
<https://doi.org/10.1039/C1DT10536>
- [136] M. Ocaña, J.P. Espinós, J.B. Carda, Synthesis, through pyrolysis of aerosols, of $\text{YIn}_{1-x}\text{Mn}_x\text{O}_3$ blue pigments and their efficiency for colouring glazes, *Dye. Pigment.* 91 (2011) 501–507.
<https://doi.org/https://doi.org/10.1016/j.dyepig.2011.03.009>.
- [137] Y. Chen, Y. Ma, Z. Wang, X. Wang, H. Liu, G.J. Cheng, Molten salt synthesis of YMnO_3 powder with high near-infrared reflectivity, *Mater. Lett.* 229 (2018) 171–173.
<https://doi.org/https://doi.org/10.1016/j.matlet.2018.07.002>.
- [138] Y. Zhang, J. Yang, J. Xu, Q. Gao, Z. Hong, Controllable synthesis of hexagonal and orthorhombic YFeO_3 and their visible-light photocatalytic activities, *Mater. Lett.* 81 (2012) 1–4.
<https://doi.org/https://doi.org/10.1016/j.matlet.2012.04.080>.
- [139] A.E. Smith, M.C. Comstock, M.A. Subramanian, Spectral properties of the UV absorbing and near-IR reflecting blue pigment, $\text{YIn}_{1-x}\text{Mn}_x\text{O}_3$, *Dye. Pigment.* 133 (2016) 214–221.
<https://doi.org/10.1016/j.dyepig.2016.05.029>.
- [140] S. Sharifzadeh, L.H. Clemmensen, C. Borggaard, S. Støier, B.K. Ersbøll, Supervised feature selection for linear and non-linear regression of $L^*a^*b^*$ color from multispectral images of meat, *Eng. Appl. Artif. Intell.* 27 (2014) 211–227. <https://doi.org/https://doi.org/10.1016/j.engappai.2013.09.004>.
- [141] X. Zhang, Q. Wang, J. Li, X. Zhou, Y. Yang, H. Xu, Estimating spectral reflectance from camera responses based on CIE XYZ tristimulus values under multi-illuminants, *Color Res. Appl.* 42 (2017) 68–77. <https://doi.org/10.1002/col.22037>.
- [142] K.M.M. Krishna Prasad, S. Raheem, P. Vijayalekshmi, C. Kamala Sastri, Basic aspects and applications of tristimulus colorimetry, *Talanta.* 43 (1996) 1187–1206.
[https://doi.org/https://doi.org/10.1016/0039-9140\(96\)01871-1](https://doi.org/https://doi.org/10.1016/0039-9140(96)01871-1).
- [143] A. Chrismont, *Couleur & colorimétrie*, Editions 3, Paris, 1998.
- [144] B.C.K. Ly, E.B. Dyer, J.L. Feig, A.L. Chien, S. Del Bino, Research techniques made simple: cutaneous colorimetry: a reliable technique for objective skin color measurement, *J. Invest. Dermatol.* 140 (2020)

3–12. <https://doi.org/10.1016/j.jid.2019.11.003>.

- [145] E. Pawar, A review article on acrylic PMMA, *IOSR J. Mech. Civ. Eng.* 13 (2016) 1–4.
- [146] X. Ning, Z. Xiong, B. Yang, W. Lu, S. Wu, The Role of Nitrate on the Sol-Gel Spread Self-Combustion Process and Its Effect on the NH₃-SCR Activity of Magnetic Iron-Based Catalyst, *Catal.* 10 (2020). <https://doi.org/10.3390/catal10030314>.
- [147] S. Hosseini Vajargah, H.R. Madaah Hosseini, Z.A. Nemati, Preparation and characterization of yttrium iron garnet (YIG) nanocrystalline powders by auto-combustion of nitrate-citrate gel, *J. Alloys Compd.* 430 (2007) 339–343. <https://doi.org/https://doi.org/10.1016/j.jallcom.2006.05.023>.
- [148] M.R. Gilberg, N.J. Seeley, The identity of compounds containing chloride ions in marine iron corrosion products: a critical review, *Stud. Conserv.* 26 (1981) 50–56. <https://doi.org/10.1179/sic.1981.26.2.50>
- [149] H. Zhang, X. Li, C. Du, H. Qi, Y. Huang, Raman and IR spectroscopy study of corrosion products on the surface of the hot-dip galvanized steel with alkaline mud adhesion, *J. Raman Spectrosc.* 40 (2009) 656–660. <https://doi.org/https://doi.org/10.1002/jrs.2178>.
- [150] M.V. Diamanti, R. Paolini, M. Rossini, A.B. Aslan, M. Zinzi, T. Poli, M.P. Pedferri, Long term self-cleaning and photocatalytic performance of anatase added mortars exposed to the urban environment, *Constr. Build. Mater.* 96 (2015) 270–278. <https://doi.org/10.1016/j.conbuildmat.2015.08.028>.
- [151] S. Kinoshita, A. Yoshida, Investigating performance prediction and optimization of spectral solar reflectance of cool painted layers, *Energy Build.* 114 (2016) 214–220. <https://doi.org/10.1016/j.enbuild.2015.06.072>.
- [152] A.P. Werle, M.L. De Souza, K. Loh, R. Ando, V.M. John, The performance of a self-cleaning cool cementitious surface, *Energy Build.* 114 (2016) 200–205. <https://doi.org/10.1016/j.enbuild.2015.06.025>.
- [153] H. Badenhorst, N. Fox, A. Mutalib, The use of graphite foams for simultaneous collection and storage of concentrated solar energy, *Carbon N. Y.* 99 (2016) 17–25. <https://doi.org/10.1016/j.carbon.2015.11.071>.
- [154] M. Chandrashekar, A. Yadav, Experimental study of exfoliated graphite solar thermal coating on a receiver with a Scheffler dish and latent heat storage for desalination, *Sol. Energy.* 151 (2017) 129–145. <https://doi.org/10.1016/j.solener.2017.05.027>.
- [155] Lutterotti, L., S. Matthies, and H. R. Wenk. “MAUD: a friendly Java program for material analysis using diffraction.” *IUCr: Newsletter of the CPD* 21.14-15 (1999), 1999. <http://www.ccp14.ac.uk/ccp/web-mirrors/lutterotti/~luttero/maud/Installers/maudInstallers.html>.
- [156] L. Lutterotti, M. Bortolotti, Object Oriented programming and fast computation techniques in Maud , a program for powder diffraction analysis written in Java TM, 2 (2003) 43–50. <https://www.iucr.org/resources/commissions/computing/newsletters/1/object-oriented-programming-in-maud>.
- [157] ASTM, Standard Tables for Reference Solar Spectral Irradiances : Direct Normal and, *Astm.* 03 (2013) 1–21. <https://doi.org/10.1520/G0173-03R20.2>.
- [158] J. Zou, Y. Chen, P. Zhang, Influence of crystallite size on color properties and NIR reflectance of TiO₂@NiTiO₃ inorganic pigments, *Ceram. Int.* 47 (2021) 12661–12666. <https://doi.org/https://doi.org/10.1016/j.ceramint.2021.01.126>.

- [159] A.L. Pisello, V.L. Castaldo, G. Pignatta, F. Cotana, M. Santamouris, Experimental in-lab and in-field analysis of waterproof membranes for cool roof application and urban heat island mitigation, *Energy Build.* 114 (2016) 180–190. <https://doi.org/https://doi.org/10.1016/j.enbuild.2015.05.026>.
- [160] A. Dominguez-Delgado, H. Domínguez-Torres, C.-A. Domínguez-Torres, Energy and economic life cycle assessment of cool roofs applied to the refurbishment of social housing in southern Spain, *Sustainability.* 12 (2020) 5602.
- [161] M. Zinzi, S. Agnoli, G. Battistini, G. Bernabini, Retrofit of an Existing School in Italy with High Energy Standards, *Energy Procedia.* 48 (2014) 1529–1538. <https://doi.org/https://doi.org/10.1016/j.egypro.2014.02.173>.
- [162] T. Sinsel, H. Simon, A.M. Broadbent, M. Bruse, J. Heusinger, Modeling impacts of super cool roofs on air temperature at pedestrian level in mesoscale and microscale climate models, *Urban Clim.* 40 (2021) 101001. <https://doi.org/https://doi.org/10.1016/j.uclim.2021.101001>.
- [163] W. Zhang, Z. Song, Y. Shi, J. Song, J. Qu, J. Qin, T. Zhang, Y. Li, W. Ji, L. Xu, X. Xue, The effects of manufacturing processes and artificial accelerated weathering on the solar reflectance and cooling effect of cool roof coatings, *Sol. Energy Mater. Sol. Cells.* 118 (2013) 61–71. <https://doi.org/10.1016/j.solmat.2013.07.039>.
- [164] J. Anand, D.J. Sailor, A. Baniassadi, The relative role of solar reflectance and thermal emittance for passive daytime radiative cooling technologies applied to rooftops, *Sustain. Cities Soc.* 65 (2021) 102612. <https://doi.org/10.1016/j.scs.2020.102612>.
- [165] K.L. Uemoto, N.M.N. Sato, V.M. John, Estimating thermal performance of cool colored paints, *Energy Build.* 42 (2010) 17–22. <https://doi.org/https://doi.org/10.1016/j.enbuild.2009.07.026>.
- [166] J. Nijskens, J. Deltour, S. Coutisse, A. Nisen, Heat transfer through covering materials of greenhouses, *Agric. For. Meteorol.* 33 (1984) 193–214. [https://doi.org/https://doi.org/10.1016/0168-1923\(84\)90070-4](https://doi.org/https://doi.org/10.1016/0168-1923(84)90070-4).
- [167] R. Yang, A. Han, M. Ye, X. Chen, L. Yuan, The influence of Mn/N-codoping on the thermal performance of ZnAl₂O₄ as high near-infrared reflective inorganic pigment, *J. Alloys Compd.* 696 (2017) 1329–1341. <https://doi.org/https://doi.org/10.1016/j.jallcom.2016.12.100>.
- [168] P.W. Fairey, Radiant energy transfer and radiant barrier systems in buildings, Florida Solar Energy Center, 1986.
- [169] E. Coser, V.F. Moritz, A. Krenzinger, C.A. Ferreira, Development of paints with infrared radiation reflective properties, *Polimeros.* 25 (2015) 305–310. <https://doi.org/10.1590/0104-1428.1869>.
- [170] P. Meenakshi, M. Selvaraj, Bismuth titanate as an infrared reflective pigment for cool roof coating, *Sol. Energy Mater. Sol. Cells.* 174 (2018) 530–537. <https://doi.org/10.1016/j.solmat.2017.09.048>.
- [171] A. Han, M. Ye, L. Liu, W. Feng, M. Zhao, Estimating thermal performance of cool coatings colored with high near-infrared reflective inorganic pigments: Iron doped La₂Mo₂O₇ compounds, *Energy Build.* 84 (2014) 698–703. <https://doi.org/https://doi.org/10.1016/j.enbuild.2014.08.024>.
- [172] M. Tian, C. Chen, A. Han, M. Ye, X. Chen, Estimating thermal insulation performance and weather resistance of acrylonitrile-styrene-acrylate modified with high solar reflective pigments: Pr³⁺/Cr³⁺ doped BaTiO₃, *Sol. Energy.* 225 (2021) 934–941. <https://doi.org/https://doi.org/10.1016/j.solener.2021.08.009>.
- [173] L. Yuan, A. Han, M. Ye, X. Chen, C. Ding, L. Yao, Preparation, characterization and thermal performance evaluation of coating colored with NIR reflective pigments: BiVO₄ coated mica-titanium oxide, *Sol. Energy.* 163 (2018) 453–460. <https://doi.org/https://doi.org/10.1016/j.solener.2018.01.009>.

- [174] C. Zhu, W. Lin, L. Chen, J. Lv, J. Zhang, J. Feng, Deep color, heat-reflective, superhydrophobic and anti-soiling coatings with waterborne silicone emulsion, *Sol. Energy Mater. Sol. Cells*. 199 (2019) 129–135. <https://doi.org/https://doi.org/10.1016/j.solmat.2019.04.029>.
- [175] A. Rosati, M. Fedel, S. Rossi, Laboratory scale characterization of cool roof paints: Comparison among different artificial radiation sources, *Prog. Org. Coatings*. 161 (2021) 106464. <https://doi.org/10.1016/j.porgcoat.2021.106464>.
- [176] J. Lei, K. Kumarasamy, K.T. Zingre, J. Yang, M.P. Wan, E.-H. Yang, Cool colored coating and phase change materials as complementary cooling strategies for building cooling load reduction in tropics, *Appl. Energy*. 190 (2017) 57–63. <https://doi.org/https://doi.org/10.1016/j.apenergy.2016.12.114>.
- [177] W. Wang, B. Laumert, Simulate a ‘sun’ for solar research: a literature review of solar simulator technology, (2014).
- [178] R.J. Cicerone, Human forcing of climate change: Easing up on the gas pedal, *Proc. Natl. Acad. Sci.* 97 (2000) 10304 LP – 10306. <https://doi.org/10.1073/pnas.97.19.10304>.
- [179] M. Tawfik, X. Tonnellier, C. Sansom, Light source selection for a solar simulator for thermal applications: A review, *Renew. Sustain. Energy Rev.* 90 (2018) 802–813. <https://doi.org/10.1016/j.rser.2018.03.059>.
- [180] D.S. Codd, A. Carlson, J. Rees, A.H. Slocum, A low cost high flux solar simulator, *Sol. Energy*. 84 (2010) 2202–2212. <https://doi.org/https://doi.org/10.1016/j.solener.2010.08.007>.
- [181] R.J. Matson, K.A. Emery, R.E. Bird, Terrestrial solar spectra, solar simulation and solar cell short-circuit current calibration: A review, *Sol. Cells*. 11 (1984) 105–145. [https://doi.org/https://doi.org/10.1016/0379-6787\(84\)90022-X](https://doi.org/https://doi.org/10.1016/0379-6787(84)90022-X).
- [182] P.N.M. Dos Anjos, E.C. Pereira, Y.G. Gobato, Study of the structure and optical properties of rare-earth-doped aluminate particles prepared by an amorphous citrate sol-gel process, *J. Alloys Compd.* 391 (2005) 277–283. <https://doi.org/10.1016/j.jallcom.2004.08.058>.
- [183] S. Vivekanandhan, M. Venkateswarlu, N. Satyanarayana, Synthesis and characterization of nanocrystalline $\text{LiNi}_{0.5}\text{Co}_{0.5}\text{VO}_4$ powders by citric acid assisted sol-gel combustion process, *J. Alloys Compd.* 462 (2008) 328–334. <https://doi.org/10.1016/j.jallcom.2007.08.055>.
- [184] S. Yu, W. Jing, M. Tang, T. Xu, W. Yin, B. Kang, Fabrication of Nd:YAG transparent ceramics using powders synthesized by citrate sol-gel method, *J. Alloys Compd.* 772 (2019) 751–759. <https://doi.org/10.1016/j.jallcom.2018.09.184>.
- [185] J. Li, Y. Pan, C. Xiang, Q. Ge, J. Guo, Low temperature synthesis of ultrafine $\alpha\text{-Al}_2\text{O}_3$ powder by a simple aqueous sol-gel process, *Ceram. Int.* 32 (2006) 587–591. <https://doi.org/https://doi.org/10.1016/j.ceramint.2005.04.015>.
- [186] Y.S. Hong, C.M. Ho, H.Y. Hsu, C.T. Liu, Synthesis of nanocrystalline $\text{Ba}(\text{MnTi})_x\text{Fe}_{12-2x}\text{O}_{19}$ powders by the sol-gel combustion method in citrate acid-metal nitrates system ($x=0, 0.5, 1.0, 1.5, 2.0$), *J. Magn. Magn. Mater.* 279 (2004) 401–410. <https://doi.org/https://doi.org/10.1016/j.jmmm.2004.02.008>.
- [187] Q. Xiao, Y. Liu, Y. Zhong, W. Zhu, A citrate sol-gel method to synthesize Li_2ZrO_3 nanocrystals with improved CO_2 capture properties, *J. Mater. Chem.* 21 (2011) 3838–3842. DOI <https://doi.org/10.1039/C0JM03243C>.
- [188] J. Li, Y. Pan, F. Qiu, Y. Wu, J. Guo, Nanostructured Nd:YAG powders via gel combustion: The influence of citrate-to-nitrate ratio, *Ceram. Int.* 34 (2008) 141–149. <https://doi.org/https://doi.org/10.1016/j.ceramint.2006.09.002>.

- [189] G.V. Rama Rao, D.S. Surya Narayana, U.V. Varadaraju, G.V.N. Rao, S. Venkadesan, Synthesis of $\text{YBa}_2\text{Cu}_3\text{O}_7$ through different gel routes, *J. Alloys Compd.* 217 (1995) 200–208. [https://doi.org/10.1016/0925-8388\(94\)01317-B](https://doi.org/10.1016/0925-8388(94)01317-B).
- [190] S. Senthilkumaar, K. Rajendran, S. Banerjee, T.K. Chini, V. Sengodan, Influence of Mn doping on the microstructure and optical property of ZnO, *Mater. Sci. Semicond. Process.* 11 (2008) 6–12. <https://doi.org/10.1016/J.MSSP.2008.04.005>.
- [191] J.F.Q. Rey, T.S. Plivelic, R.A. Rocha, S.K. Tadokoro, I. Torriani, E.N.S. Muccillo, Synthesis of In_2O_3 nanoparticles by thermal decomposition of a citrate gel precursor, *J. Nanoparticle Res.* 7 (2005) 203–208. <https://doi.org/10.1007/s11051-004-7899-7>.
- [192] M. Blosi, S. Albonetti, M. Dondi, A. Costa, M. Ardit, G. Cruciani, Sol–gel combustion synthesis of chromium doped yttrium aluminum perovskites, *J. Sol-Gel Sci. Technol.* 50 (2009) 449–455. <https://doi.org/10.1007/s10971-009-1906-5>.
- [193] B.C.B.S. Balamurugan, The effect of post annealing treatment on the citrate sol – gel derived nanocrystalline $\text{BaFe}_{12}\text{O}_{19}$ powder : structural , morphological , optical and magnetic properties, *Appl. Nanosci.* 6 (2016) 1199–1210. <https://doi.org/10.1007/s13204-016-0531-1>.
- [194] R.I. Olivares, The thermal stability of molten nitrite/nitrates salt for solar thermal energy storage in different atmospheres, *Sol. Energy.* 86 (2012) 2576–2583. <https://doi.org/10.1016/j.solener.2012.05.025>.
- [195] X. Wang, Q. Cui, Y. Pan, G. Zou, X-Ray photoelectron and infrared transmission spectra of manganite system $\text{La}_{0.5-x}\text{Bi}_x\text{Ca}_{0.5}\text{MnO}_3$ ($0 \leq x \leq 0.25$), *J. Alloys Compd.* 354 (2003) 91–94. [https://doi.org/https://doi.org/10.1016/S0925-8388\(02\)01350-6](https://doi.org/https://doi.org/10.1016/S0925-8388(02)01350-6).
- [196] T.H. Dolla, K. Pruessner, D.G. Billing, C. Sheppard, A. Prinsloo, E. Carleschi, B. Doyle, P. Ndungu, Sol-gel synthesis of $\text{Mn}_x\text{Ni}_{1-x}\text{Co}_2\text{O}_4$ spinel phase materials: Structural, electronic, and magnetic properties, *J. Alloys Compd.* 742 (2018) 78–89. <https://doi.org/10.1016/j.jallcom.2018.01.139>.
- [197] N. Brahme, A. Gupta, D.P. Bisen, U. Kurrey., Thermoluminescence Study of Y_2O_3 : Tb, *Recent Res. Sci. Technol.* 4 (2012) 130–132. <https://updatepublishing.com/journal/index.php/rrst/article/view/955>.
- [198] A.J. Abdulghani, W.M. Al-Ogedy, Preparation and Characterization of Yttrium Oxide Nanoparticles at Different Calcination Temperatures from Yttrium Hydroxide Prepared by Hydrothermal and Hydrothermal microwave Methods, *Ogedy Iraqi J. Sci.* 56 (2015) 1572–1587.
- [199] A. Kajbafvala, M.R. Shayegh, M. Mazloumi, S. Zanganeh, A. Lak, M.S. Mohajerani, S.K. Sadrnezhad, Nanostructure sword-like ZnO wires: Rapid synthesis and characterization through a microwave-assisted route, *J. Alloys Compd.* 469 (2009) 293–297. <https://doi.org/10.1016/j.jallcom.2008.01.093>.
- [200] X. Lü, J. Xie, H. Shu, J. Liu, C. Yin, J. Lin, Microwave-assisted synthesis of nanocrystalline YFeO_3 and study of its photoactivity, *Mater. Sci. Eng. B Solid-State Mater. Adv. Technol.* 138 (2007) 289–292. <https://doi.org/10.1016/j.mseb.2007.01.003>.
- [201] S.R. Naik, A. V Salker, Variation in the magnetic moment of Indium doped $\text{Ce}_{0.1}\text{Y}_{2.9}\text{Fe}_5\text{O}_{12}$ garnet relative to the site inversion, *J. Alloys Compd.* 600 (2014) 137–145. <https://doi.org/https://doi.org/10.1016/j.jallcom.2014.02.101>.
- [202] P. Vaqueiro, M.A. López-Quintela, Influence of Complexing Agents and pH on Yttrium–Iron Garnet Synthesized by the Sol–Gel Method, *Chem. Mater.* 9 (1997) 2836–2841. <https://doi.org/10.1021/cm970165f>.
- [203] R. Shukla, V. Grover, S.K. Deshpande, D. Jain, A.K. Tyagi, Synthesis and structural and electrical investigations of a hexagonal $\text{Y}_{1-x}\text{Gd}_x\text{InO}_3$ ($0.0 \leq x \leq 1.0$) system obtained via metastable C-type

intermediates, *Inorg. Chem.* 52 (2013) 13179–13187. <https://doi.org/10.1021/ic402085w>.

- [204] Y. He, The structural, electronic, elastic and thermodynamics properties of 2D transition-metal electride Y_2C via first-principles calculations, *J. Alloys Compd.* 654 (2016) 180–184. <https://doi.org/https://doi.org/10.1016/j.jallcom.2015.09.133>.
- [205] M. Atoji, M. Kikuchi, Crystal Structures of Cubic and Trigonal Yttrium Hypocarbides; A Dimorphically Interphased Single-Crystal Study, *J. Chem. Phys.* 51 (1969) 3863–3872. <https://doi.org/10.1063/1.1672603>
- [206] O. Polat, M. Coskun, F.M. Coskun, Z. Durmus, M. Caglar, A. Turut, Os doped $YMnO_3$ multiferroic : A study investigating the electrical properties through tuning the doping level, *J. Alloys Compd.* 752 (2018) 274–288. <https://doi.org/10.1016/j.jallcom.2018.04.200>.
- [207] C.W.F.T. Pistorius, G.J. Kruger, Stability and structure of noncentrosymmetric hexagonal $LnInO_3$ ($Ln = Eu, Gd, Tb, Dy, Ho, Y$), *J. Inorg. Nucl. Chem.* 38 (1976) 1471–1475. [https://doi.org/https://doi.org/10.1016/0022-1902\(76\)90011-7](https://doi.org/https://doi.org/10.1016/0022-1902(76)90011-7).
- [208] S.C. Abrahams, J.L. Bernstein, Remeasurement of the structure of hexagonal ZnO , *Acta Crystallogr. Sect. B.* 25 (1969) 1233–1236. <https://doi.org/10.1107/S0567740869003876>.
- [209] H. Sowa, H. Ahsbabs, High-pressure X-ray investigation of zincite ZnO single crystals using diamond anvils with an improved shape, *J. Appl. Crystallogr.* 39 (2006) 169–175. <https://doi.org/10.1107/S0021889805042457>.
- [210] M. Schreyer, L. Guo, S. Thirunahari, F. Gao, M. Garland, Simultaneous determination of several crystal structures from powder mixtures: the combination of powder X-ray diffraction, band-target entropy minimization and Rietveld methods, *J. Appl. Crystallogr.* 47 (2014) 659–667. <https://doi.org/10.1107/S1600576714003379>.
- [211] A. Rosati, M. Fedel, S. Rossi, $YIn_{0.9}Mn_{0.1}O_3$ – ZnO NIR reflective nano-pigment exhibiting three different colors: ochre, cyan blue, and deep blue, *J. Solid State Chem.* (2021) 122176. <https://doi.org/https://doi.org/10.1016/j.jssc.2021.122176>.
- [212] R. Shukla, F.N. Sayed, V. Grover, S.K. Deshpande, A. Guleria, A.K. Tyagi, Quest for Lead Free Relaxors in $YIn_{1-x}Fe_xO_3$ ($0.0 \leq x \leq 1.0$) System: Role of Synthesis and Structure, *Inorg. Chem.* 53 (2014) 10101–10111. <https://doi.org/10.1021/ic5009472>.
- [213] C.C. Huang, Y.H. Hung, J.Y. Huang, M.F. Kuo, Performance improvement of S-band phase shifter using Al, Mn and Gd doped $Y_3Fe_5O_{12}$ and sintering optimization, *J. Alloys Compd.* 643 (2015) S193–S198. <https://doi.org/10.1016/j.jallcom.2014.12.123>.
- [214] M.S. Kim, J.B. Yang, J. Medvedeva, W.B. Yelon, P.E. Parris, W.J. James, Electronic structure of $La_{0.7}Sr_{0.3}Mn_{1-x}Cu_xO_3$ ($0.0 \leq x \leq 0.30$), *J. Phys. Condens. Matter.* 20 (2008) 255228. <http://iopscience.iop.org/0953-8984/20/25/255228>.
- [215] A. De Bonis, G. Cultrone, C. Grifa, A. Langella, A.P. Leone, Different shades of red : The complexity of mineralogical and physico- chemical factors influencing the colour of ceramics, 43 (2017) 8065–8074. <https://doi.org/10.1016/j.ceramint.2017.03.127>.
- [216] L.M. Schabbach, D.L. Marinoski, S. Güths, A.M. Bernardin, M.C. Fredel, Pigmented glazed ceramic roof tiles in Brazil : Thermal and optical properties related to solar reflectance index, *Sol. Energy.* 159 (2018) 113–124. <https://doi.org/10.1016/j.solener.2017.10.076>.
- [217] A.M. Gueli, S. Gallo, S. Pasquale, Optical and colorimetric characterization on binary mixtures prepared with coloured and white historical pigments, *Dye. Pigment.* 157 (2018) 342–350.

<https://doi.org/https://doi.org/10.1016/j.dyepig.2018.04.068>.

- [218] R.S. Azis, S. Sulaiman, I.R. Ibrahim, A. Zakaria, J. Hassan, N.N.C. Muda, R. Nazlan, N.M. Saiden, Y.W. Fen, M.S. Mustaffa, K.A. Matori, Influence of pH Adjustment Parameter for Sol–Gel Modification on Structural, Microstructure, and Magnetic Properties of Nanocrystalline Strontium Ferrite, *Nanoscale Res. Lett.* 13 (2018) 160. <https://doi.org/10.1186/s11671-018-2562-x>.
- [219] G. Amin, M.H. Asif, A. Zainelabdin, S. Zaman, O. Nur, M. Willander, Influence of pH, precursor concentration, growth time, and temperature on the morphology of ZnO nanostructures grown by the hydrothermal method, *J. Nanomater.* 2011 (2011) 5. <https://doi.org/10.1155/2011/269692>.
- [220] L. Zhang, P. Wu, H. Chen, L. Yuan, G. Yang, H. Xie, D. Liang, J. Xie, L. Deng, Effect of calcination temperature on visible near-infrared reflectance of aluminum-doped chromium, *Mater. Sci. Semicond. Process.* 105 (2020) 104672. <https://doi.org/https://doi.org/10.1016/j.mssp.2019.104672>.
- [221] P. Berdahl, S.E. Bretz, Preliminary survey of the solar reflectance of cool roofing materials, *Energy Build.* 25 (1997) 149–158. [https://doi.org/https://doi.org/10.1016/S0378-7788\(96\)01004-3](https://doi.org/https://doi.org/10.1016/S0378-7788(96)01004-3).
- [222] Y. Li, Y. Ma, W. liu, Z. Wang, H. Liu, X. Wang, H. Wei, S. Zeng, N. Yi, G.J. Cheng, A promising inorganic YFeO₃ pigments with high near-infrared reflectance and infrared emission, *Sol. Energy.* 226 (2021) 180–191. <https://doi.org/https://doi.org/10.1016/j.solener.2021.08.047>.
- [223] N. Zhou, J. Luan, Y. Zhang, M. Li, X. Zhou, F. Jiang, J. Tang, Synthesis of high near infrared reflection wurtzite structure green pigments using Co-doped ZnO by combustion method, *Ceram. Int.* 45 (2019) 3306–3312. <https://doi.org/10.1016/j.ceramint.2018.10.241>.
- [224] C. Ferrari, A. Libbra, F. Maria, L. De Maria, S. Marchionna, M. Barozzi, C. Siligardi, A. Muscio, A composite cool colored tile for sloped roofs with high ' equivalent ' solar reflectance, *Energy Build.* 114 (2016) 221–226. <https://doi.org/10.1016/j.enbuild.2015.06.062>.
- [225] T. Ihara, B.P. Jelle, T. Gao, A. Gustavsen, Accelerated aging of treated aluminum for use as a cool colored material for facades, *Energy Build.* 112 (2016) 184–197. <https://doi.org/10.1016/j.enbuild.2015.12.014>.
- [226] ABET technologies, Sun 2000 Class A, <https://Abet-Technologies.Com>. (2021). <https://abet-technologies.com/solar-simulators/sun-2000-class-a/> (accessed February 26, 2022).
- [227] F. Parrino, C. De Pasquale, L. Palmisano, Influence of Surface-Related Phenomena on Mechanism, Selectivity, and Conversion of TiO₂-Induced Photocatalytic Reactions, *ChemSusChem.* 12 (2019) 589–602. <https://doi.org/10.1002/cssc.201801898>
- [228] H. Lachheb, F. Ajala, A. Hamrouni, A. Houas, F. Parrino, L. Palmisano, Electron transfer in ZnO–Fe₂O₃ aqueous slurry systems and its effects on visible light photocatalytic activity, *Catal. Sci. Technol.* 7 (2017) 4041–4047. <https://doi.org/10.1039/C7CY01085K>
- [229] A. Hamrouni, N. Moussa, A. Di Paola, L. Palmisano, A. Houas, F. Parrino, Photocatalytic activity of binary and ternary SnO₂–ZnO–ZnWO₄ nanocomposites, *J. Photochem. Photobiol. A Chem.* 309 (2015) 47–54. <https://doi.org/https://doi.org/10.1016/j.jphotochem.2015.05.001>.
- [230] A. Hamrouni, H. Azzouzi, A. Rayes, L. Palmisano, R. Ceccato, F. Parrino, Enhanced solar light photocatalytic activity of Ag doped TiO₂–Ag₃PO₄ composites, *Nanomaterials.* 10 (2020) 795. <https://doi.org/10.3390/nano10040795>.
- [231] M. Pirhashemi, A. Habibi-Yangjeh, S. Rahim Pourn, Review on the criteria anticipated for the fabrication of highly efficient ZnO-based visible-light-driven photocatalysts, *J. Ind. Eng. Chem.* 62 (2018) 1–25. <https://doi.org/https://doi.org/10.1016/j.jiec.2018.01.012>.

- [232] H. Tada, Q. Jin, H. Nishijima, H. Yamamoto, M. Fujishima, S. Okuoka, T. Hattori, Y. Sumida, H. Kobayashi, Titanium(IV) Dioxide Surface-Modified with Iron Oxide as a Visible Light Photocatalyst, *Angew. Chemie Int. Ed.* 50 (2011) 3501–3505. <https://doi.org/https://doi.org/10.1002/anie.201007869>.
- [233] J. Liu, S. Yang, W. Wu, Q. Tian, S. Cui, Z. Dai, F. Ren, X. Xiao, C. Jiang, 3D Flowerlike α -Fe₂O₃@TiO₂ Core-Shell Nanostructures: General Synthesis and Enhanced Photocatalytic Performance, *ACS Sustain. Chem. Eng.* 3 (2015) 2975–2984. <https://doi.org/10.1021/acssuschemeng.5b00956>.
- [234] M. Shekofteh-Gohari, A. Habibi-Yangjeh, M. Abitorabi, A. Rouhi, Magnetically separable nanocomposites based on ZnO and their applications in photocatalytic processes: A review, *Crit. Rev. Environ. Sci. Technol.* 48 (2018) 806–857. <https://doi.org/10.1080/10643389.2018.1487227>.
- [235] M. Ismael, E. Elhaddad, D.H. Taffa, M. Wark, Solid state route for synthesis of YFeO₃/g-C₃N₄ composites and its visible light activity for degradation of organic pollutants, *Catal. Today.* 313 (2018) 47–54. <https://doi.org/https://doi.org/10.1016/j.cattod.2018.02.003>.
- [236] M. Fortuño-Morte, P. Serna-Gallén, H. Beltrán-Mir, E. Cordoncillo, A new series of environment-friendly reddish inorganic pigments based on AFeO₃ (A = Ln, Y) with high NIR solar reflectance, *J. Mater.* 7 (2021) 1061–1073. <https://doi.org/https://doi.org/10.1016/j.jmat.2021.02.002>.
- [237] S.D. Dolić, D.J. Jovanović, D. Štrbac, L.Đ. Far, M.D. Dramićanin, Improved coloristic properties and high NIR reflectance of environment-friendly yellow pigments based on bismuth vanadate, *Ceram. Int.* 44 (2018) 22731–22737. <https://doi.org/10.1016/j.ceramint.2018.09.057>.
- [238] M.-K. Lee, T.-H. Shih, P.-C. Chen, Zinc Oxide and Zinc Hydroxide Growth Controlled by Nitric Acid in Zinc Nitrate and Hexamethylenetetramine, *J. Electrochem. Soc.* 156 (2009) H268. <https://doi.org/10.1149/1.3077567>.
- [239] S. Kim, U. Kim, W.-S. Cho, Color Formation Mechanism of Ceramic Pigments Synthesized in the TiO₂-SnO-ZnO Compounds, *J. Korean Ceram. Soc.* 55 (2018) 368–375. <https://doi.org/10.4191/kcers.2018.55.4.12>
- [240] J.B. Baxter, E.S. Aydil, Epitaxial growth of ZnO nanowires on a-and c-plane sapphire, *J. Cryst. Growth.* 274 (2005) 407–411. <https://doi.org/10.1016/j.jcrysgro.2004.10.014>.
- [241] Q. Kuang, Z.-Y. Jiang, Z.-X. Xie, S.-C. Lin, Z.-W. Lin, S.-Y. Xie, R.-B. Huang, L.-S. Zheng, Tailoring the optical property by a three-dimensional epitaxial heterostructure: a case of ZnO/SnO₂, *J. Am. Chem. Soc.* 127 (2005) 11777–11784. <https://doi.org/10.1021/ja052259t>.
- [242] X. Yan, T. Ohno, K. Nishijima, R. Abe, B. Ohtani, Is methylene blue an appropriate substrate for a photocatalytic activity test? A study with visible-light responsive titania, *Chem. Phys. Lett.* 429 (2006) 606–610. <https://doi.org/https://doi.org/10.1016/j.cplett.2006.08.081>.
- [243] F. Parrino, V. Loddo, V. Augugliaro, G. Camera-Roda, G. Palmisano, L. Palmisano, S. Yurdakal, Heterogeneous photocatalysis: guidelines on experimental setup, catalyst characterization, interpretation, and assessment of reactivity, *Catal. Rev.* 61 (2018) 163–213. <https://doi.org/10.1080/01614940.2018.1546445>